UNIVERSITY OF SOUTHAMPTON

Faculty of Engineering and Physical Sciences
School of Engineering
nCATS

Nano-scale Frictional Properties of 2D Materials

by

Aleš Rapuc

MSc

ORCiD: 0000-0001-6231-3369

A thesis for the degree of
Doctor of Philosophy

June 2022

University of Southampton

Abstract

Faculty of Engineering and Physical Sciences
School of Engineering
nCATS

Doctor of Philosophy

Nano-scale Frictional Properties of 2D Materials

by Aleš Rapuc

Nano and atomic-scale frictional properties of various 2D transition metal dichalcogenide systems (monolayers, multilayers, thin-film coatings) were analysed by atomic force microscopy. All the analysed monolayer samples (MoS_2, WS_2, $MoSe_2$, WSe_2) exhibited very low friction when free of surface contamination. The chalcogenide atom was found to have a larger effect on friction than the metal atom, and selenides experienced lower friction than sulphides. All the layers provided superior wear resistance, and no layer rupture could be observed even at very high loads up to 10 μN.

A shift in load-dependent behaviour was observed in the multilayered samples, and the difference was contributed to the contact area gain due to adhesion and a decrease in contact shear strength due to interlayer coupling. A numerical model was used to study the problem, and a new model for fitting experimental data was developed.

Nanotribological analysis of the W-S-C coatings and the corresponding wear tracks revealed a two-phase structure of the coatings. The two phases experienced entirely different frictional responses and were assigned to an amorphous solution of WS_2 and carbon (high friction phase, $\mu > 1$) and nanocrystalline WS_2 (low friction phase, $\mu \approx 0.15$). The two-phase structure was confirmed by Raman spectroscopy and Raman mapping, which identified the regions with high concentrations of either carbon or crystalline WS_2. WS_2 tribofilm in the form of multilayer flakes was identified within the wear tracks. The coverage of the wear tracks with such features was much lower than initially expected, thus indicating that the tribo-film formation is localised and occurs only when contact pressure exceeds the formation threshold.

Contents

List of Figures

List of Tables

List of Accompanying Material

Dataset to support the thesis (10.5258/SOTON/D2262)

Declaration of Authorship

I declare that this thesis and the work presented in it is my own and has been generated by me as the result of my own original research.

I confirm that:

1. This work was done wholly or mainly while in candidature for a research degree at this University;
2. Where any part of this thesis has previously been submitted for a degree or any other qualification at this University or any other institution, this has been clearly stated;
3. Where I have consulted the published work of others, this is always clearly attributed;
4. Where I have quoted from the work of others, the source is always given. With the exception of such quotations, this thesis is entirely my own work;
5. I have acknowledged all main sources of help;
6. Where the thesis is based on work done by myself jointly with others, I have made clear exactly what was done by others and what I have contributed myself;
7. Parts of this work have been published as: A. Rapuc, K. Simonovic, T. Huminiuc, A. Cavaleiro, and T. Polcar, "Nanotribological Investigation of Sliding Properties of Transition Metal Dichalcogenide Thin Film Coatings," *ACS Applied Materials & Interfaces*, vol. 12, pp. 54191–54202, 12 2020
   A. Rapuc, H. Wang, and T. Polcar, "Nanotribology of transition metal dichalcogenide flakes deposited by chemical vapour deposition: The influence of chemical composition and sliding speed on nanoscale friction of monolayers," *Applied Surface Science*, vol. 556, p. 149762, 8 2021

Signed:..... Date:.....

Acknowledgements

In the first place, I would like to thank my supervisors, Prof Tomas Polcar and Dr Richard Cook, for their supervision and professional help during the project. They provided good guidance and helped me by discussing the ideas about the work and the interpretation of the obtained results. I would like to thank Dr Kosta Simonovic, from the *Czech Technical University in Prague*, for the assistance with experimental work during my secondment in Prague and for performing additional Raman mapping experiments, Dr He Wang, from the *University of Southampton*, for providing the monolayer samples and their chemical characterisation, Prof Albano Cavaleiro and his group from the *University of Coimbra*, for manufacturing W-S-C coatings, Dr Egor Ukraintsev, from the *Czech Technical University in Prague*, for the assistance with setting up the atomic force microscopy experiments during my secondment in Prague, Dr Teodor Huminiuc, from the *University of Southampton*, for obtaining transmission electron microscopy images, and Paola Torche, from the *University of Southampton*, for collaboration on the development of the machine fitting procedure for experimental data analysis.

I want to thank the nCATS and Engineering Materials groups at the *University of Southampton* for their support and assistance with lab work, especially everyone in office 5/3025 for providing a relaxed and welcoming workplace. I want to thank Advanced Materials Group at the *Czech Technical University in Prague* for the welcoming environment and assistance during the secondment in Prague. Furthermore, I would like to acknowledge all researchers and coordinators of the Solution ITN project for the fruitful discussions during project meetings and summer schools.

Last but not least, the thanks go to my parents, Mirjana and Goran, for providing their unconditional support. I must also thank Katy for her patience and encouragement during my research and writing of this thesis.

This work was funded by H2020 MSCA ITN project Solution No. 721642.

Definitions and Abbreviations

AFM	Atomic Force Microscopy
CVD	Chemical Vapour Deposition
DC	Direct Current
DLC	Diamond-Like Carbon
DMT	Derjaguin-Muller-Toporov
EM	Electro-magnetic
FET	Field Effect Transistor
FFM	Friction Force Microscopy
FFT	Fast Fourier Transform
FK	Frenkel-Kontorova
FKT	Frenkel-Kontorova-Tomlinson
GUI	Graphical user interface
JKR	Johnson-Kendall-Roberts
LFM	Lateral Force Microscopy
MEMS	Micro-Electro-Mechanical Systems
NEMS	Nano-Electro-Mechanical Systems
NSM	Nano-Structured Materials
PLD	Pulsed Laser Deposition
PT	Prandtl-Tomlinson
PVD	Physical Vapour Deposition
QCM	Quartz Crystal Microbalance
r.f.	Radio Frequency
SEM	Scanning Electron Microscope
SFA	Surface Forces Apparatus
SPM	Scanning Probe Microscope
STM	Scanning Tunneling Microscope
TEM	Transmission Electron Microscope
TMDs	Transition Metal Dichalcogenides
UHV	Ultra-High Vacuum
XRD	X-Ray Diffraction

Chapter 1

Introduction

1.1 Background

1.1.1 Introduction

Reduction of friction in mechanical contacts is one of the key elements in modern engineering applications, driven by the aim to reduce fuel consumption and emissions, extend the lifetime of the components and comply with strict environmental regulations (1). Friction and wear cause significant energy losses globally (2), with estimates that up to 11% of energy in transportation could be saved by further improvements in reducing friction (3). Friction can be reduced through fluid lubrication or solid lubrication. In the first case, fluid viscosity and chemical interactions between the fluid and the surface play a major role in surface separation and friction reduction. In the second case, however, the contacting bodies are in constant contact and protected only by a thin, solid and low-shear layer between them. Fluid lubricants are usually the easiest and most convenient solution for lubrication problems. However, applications under extreme environmental conditions or strict regulations may limit their usability. For instance, in the vacuum of outer space, solid lubricants in the form of thin films are more applicable (4).

To better understand and adequately describe the physical behaviour of solid lubricants at the macro-scale, we first need to analyse their intrinsic frictional properties at both the nano and atomic scales. The study of atomic and nano-scale sliding, friction and wear is called nanotribology (5, 6). It has started receiving increasing attention since the late 1980s and early 1990s, with the introduction of experimental techniques, such as atomic force microscopy (AFM) (7), quartz crystal microbalance (QCM) (5, 8) and surface forces apparatus (SFA) (9). In contrast to macro-tribology, where the overall performance of the sliding system is studied under

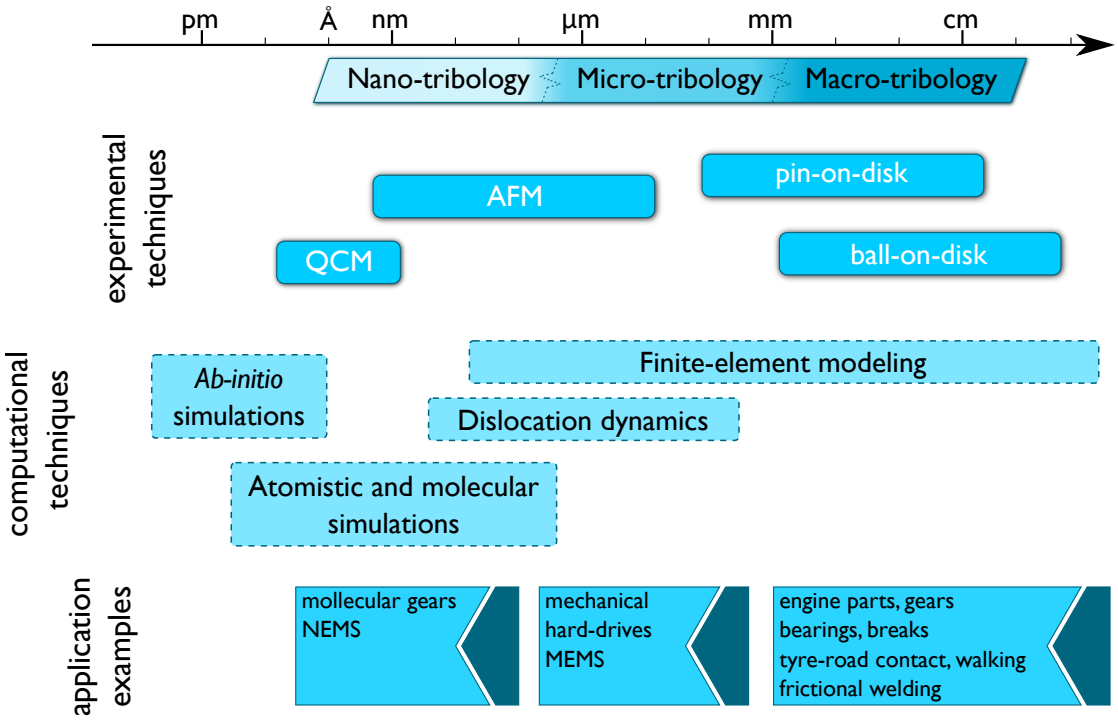

Figure 1.1: A comparison of scales in tribology.

operational conditions using a macroscopic tribometer in various configurations (i.e. ball-on-disc, pin-on-disc, flat-on-flat, ... (10)), nanotribology studies the fundamental frictional properties and concerns contacts ranging from a few to hundreds of nanometres (11). The main differentiation between nanotribology and conventional macro-scale tribology arises from the influence of surface forces on the adhesion and friction of the system at a small scale (12). The gap between nano and macro-tribology is occupied by micro-tribology, where the frictional behaviour is dictated by some effects from nanotribology, such as adhesion and stiction, and some effects from macro-tribology, such as contact geometry and roughness. It is important to note that the boundaries between the scales are not clearly defined, and the regimes can often overlap. Figure 1.1 shows a comparison between the scales, a correlation between different experimental and simulation approaches in tribology, and some application examples at each scale. Essentially, the behaviour of any realistic sliding contact combines the effects from all scales and, therefore, needs to be studied from different perspectives.

For consistency, we refer to nano-scale when the applied load ranges from a few to 100 nN, the contact size is below 100 nm, and the friction data does not explicitly display atomic influence. On the other hand, we refer to the atomic scale when the load conditions are the same as at the nano-scale, contact sizes are a few nanometres, and the signal displays the influence of the atomic structure. Furthermore, for the measurements at the nano-scale, the measured area is generally larger (a few 100 nm), whereas the atomic-scale scans are usually taken over only a few nm.

Recent advancements in the engineering design of small contacts have surpassed the limits of the macro-scale, and several fully functional mechanical systems that operate in micro and nanotribology regimes are already readily available. For example, the emergence of micro and nano-electro-mechanical systems (MEMS/NEMS) (13), the development of molecular-scale mechanical systems (such as molecular gears (14)) and the ever-increasing performance demand of mechanical hard drives (15) have resulted in a growing interest in tribological behaviour of components and materials at a much smaller scale. While storage systems have started steadily transitioning to alternative solid-state drives with no moving parts (16, 17), the desire to improve the performance of mechanical hard drives still persists. A good understanding of the frictional behaviour of materials at the nano-scale and their incorporation in the component design could, therefore, eventually lead to increased performance of such systems. Furthermore, the results from nano and micro-scale analysis can help with understanding the macro-scale systems better, which is essential for future development and advancements in providing sufficiently low friction contacts.

1.1.2 Solid lubricants

As mentioned above, specific operational conditions sometimes do not allow the use of liquid lubricants and, therefore, require solid lubricants to provide sufficient performance. Good lubricating properties in a solid lubricated contact are achieved by appropriate material selection of the contacting surfaces. Any chemical bond formation between the surfaces presents an undesirable effect on the friction and performance of such systems. For example, when two flat metal surfaces come in contact, long-range van der Waals forces are formed first, followed by strong metallic bonds when the separation decreases (18). Bonding between metals can be assessed by mutual solubility. A compatibility chart (Figure 1.2), developed by E. Rabinowicz (19), can be used for an initial general estimation of the contact properties of a metal-metal pair; adhesion and friction are expected to increase with increased solubility.

Materials that meet low friction and low wear criteria seldom possess good mechanical and physical properties. To achieve good tribological properties of a mechanical system, a third material, in the form of a solid lubricant, can be introduced in an otherwise structurally stable system (18). For example, materials with a lamellar crystal structure usually exhibit good lubricating properties. The most important technical materials with such crystal structures are graphene (20) and transition metal dichalcogenides (TMDs) (21, 22). Additionally, hard coatings such as diamond-like-carbon (DLC) (23) or TiN and Ti-Al-N systems (24) rely on low wear, low deformation of the contact or inert surfaces to provide good tribological properties.

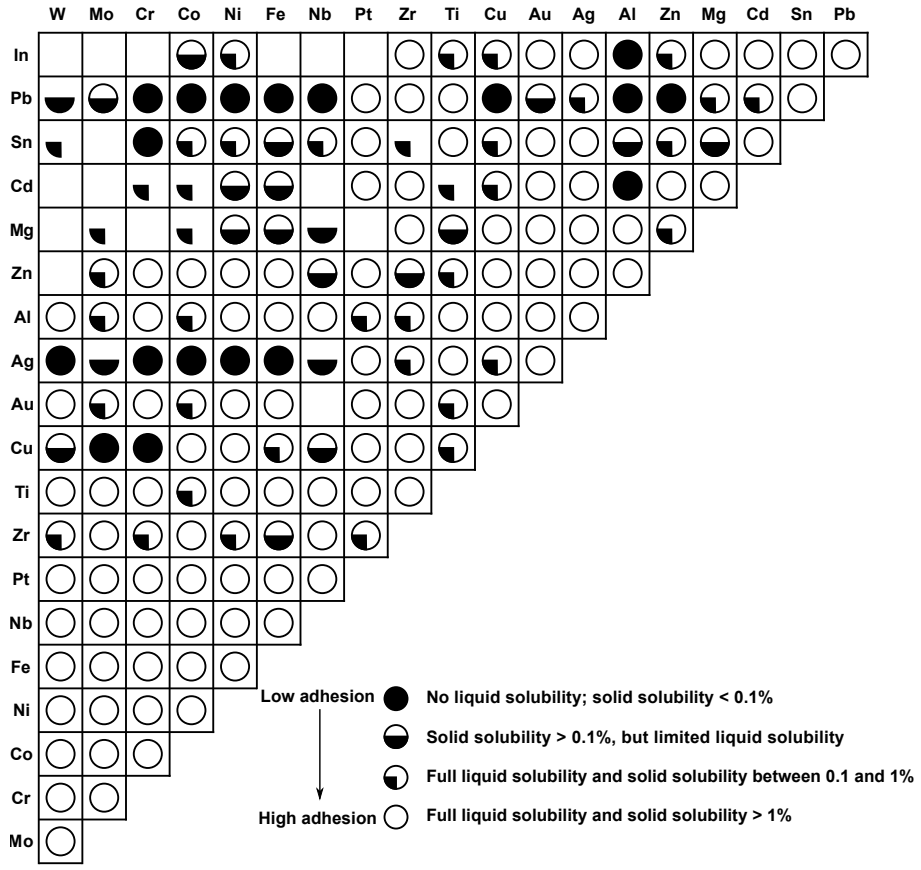

Figure 1.2: Compatibility chart between metals (19).

1.1.3 Transition metal dichalcogenides

Group 6 transition metal dichalcogenides (TMDs) are known for their exceptional tribological properties, especially in dry air and vacuum (21, 25). Their good lubricating behaviour arises from their lamellar crystal structure, which results in low shear between the basal planes.

The general formula of transition metal dichalcogenides is MeX_2, where "Me" represents a transition metal atom with an oxidation state +4 (e.g. Mo, W, Nb) and "X" is a chalcogen atom (e.g. S, Se, Te) (26). The most widely studied compounds from these groups are MoS_2 and WS_2. The interaction between the metal and dichalcogenide atoms is strong covalent bonding, while only weak Van der Waals forces act between the lattice layers (21). TMDs have been widely applied in many areas of science and technology; they have been used as catalysts, in fuel cells, in microelectronics (e.g. single layer transistors and photodetectors), and as solid lubricants (21, 27).

In tribology, TMDs are mainly used as solid thin-film coatings (21, 28) or as oil additives (29). Thin-film coatings can be prepared by various physical vapour deposition (PVD) or chemical vapour deposition (CVD) techniques, which produce

either amorphous or nano-crystalline structures. The main PVD methods include sputtering and pulsed laser deposition (PLD) (30). The coatings form low shear tribo-films during tribo-chemical reactions induced by the sliding process (31). The amorphous TMD films are sensitive to environmental attacks, as they tend to oxidise rapidly while sliding in the air (21), thus significantly increasing friction and wear rates in the presence of oxygen and air humidity (28). Pure sputtered TMDs are therefore restricted only to high vacuum applications (28). Furthermore, the hardness of TMD coatings is low and is usually in the range of 0.3-2 GPa (21). For comparison, DLC coatings can achieve hardness values as high as 10-20 GPa (23). Adhesion of pure TMDs to the substrate is weak, which results in a relatively low load-bearing capacity, and the coatings can peel off quickly under high-pressure applications (21).

1.2 Definition of a research problem

Despite recent advancements in tribology, which include the ever-expanding experimental capabilities and the increasing computational capacity, gaps in knowledge persist in understanding the coupling between frictional behaviour at different scales. Due to the complexity of the conventional experimental systems, the formulation of mathematical models that would include and accurately describe all aspects involved in sliding is still nearly impossible.

In this work, we investigate the possibilities of bridging a gap between the scales, by focusing on the comparison between the results obtained by atomic force microscopy (AFM) and macro-scale tests. We examine nano-scale friction properties of different TMD systems, including sputtered thin-film coatings and pure crystalline TMD flakes deposited by chemical vapour deposition, and correlate the observed nano-scale properties to the previously reported behaviour of these materials at the macro-scale. We used AFM to study the nanotribological properties. AFM probe can accurately mimic a single nano-scale asperity contact (32), which offers a controllable environment, contact size and high precision, and allows for a wide array of nanotribological investigations. Lateral force microscopy (LFM), or friction force microscopy (FFM), which utilises measuring lateral forces of the AFM probe in contact with the sample, has previously been successfully employed to study nano and atomic scale tribological properties of 2D materials: graphite (33), graphene (34, 35), exfoliated TMDs (35, 36), sputtered TMDs (37, 38), and h-BN (35). This work expands on previously reported studies, with an attempt to reduce the gap between different scales, materials and approaches by comparing the frictional values measured at different scales and on various systems with different degrees of crystallinity. The obtained results are correlated with simulations, namely predictive contact models and a machine learning approach to analyse the atomic scale frictional data.

1.2.1 Research hypothesis

2D materials are known to exhibit low friction, and a significant number of them have already been applied in practical applications as thick or thin-film coatings (21, 28). They experience similarly low yet observably different frictional behaviour (39), but the differences in their practical performance are further affected by external factors, such as environment, contact size, coating quality, adhesion and stoichiometry. The majority of the research is still focused on MoS_2 and graphene. However, higher-order TMDs, such as WS_2, $MoSe_2$ and WSe_2, have a strong potential of having lower friction than MoS_2. Our first hypothesis is that the TMD monolayers would experience very low friction, and there would be observable differences in frictional response between materials, with higher-order TMDs resulting in lower friction.

The nano-scale frictional behaviour is correlated to the macro-scale, though the same behaviour may not be observed at both scales (40). Due to small-size effects (i.e. dangling bonds, electrostatic forces, meniscus formation, ...), the behaviour at the nano-scale can be skewed, whereas, at the larger scales, these effects would cancel out. Nonetheless, we predict that the correlation between the scales can still be observed by carefully considering the contact parameters.

The fundamental mechanism of operation of TMD-based coatings is the reorientation of basal planes parallel to the direction of sliding (31, 41). So far, the formation of such tribofilm has been successfully observed using transmission electron microscopy (TEM) (21, 31). However, the sample preparation and operation of TEM are expensive and demanding. We hypothesise that atomic force microscopy could provide a simple and non-destructive alternative for detecting easy-sliding tribofilms on the surface. Due to the small size of the contact, any dangling bonds in the non-reoriented coating would result in a significantly higher frictional signal than the oriented platelets.

1.2.2 Main objectives

The primary objective of this work is to assess the frictional properties of TMDs at the nano and atomic scales and correlate them to their macro-scale behaviour. Frictional characteristics at the atomic scale were measured by atomic force microscopy in lateral mode (lateral force microscopy), which represents a single asperity contact. We investigate how friction differs between the main materials from the group, their anti-wear properties, and how the layer thickness and orientation affect the friction and adhesion properties of the TMD layers.

Furthermore, the origin of the formation of ordered TMD structures from sputtered TMD thin-film coatings is analysed by the means of atomic force microscopy. J. R.

Lince and P.D. Fleichauer (41) showed that sliding causes crystallites in sputtered MoS_2 films to orient their basal planes parallel to the sliding direction. The matter has been widely studied since (21, 31, 42, 43), but the true nature of the recrystallisation/reorientation remains unknown. Assessment of recrystallisation includes AFM analysis of the wear tracks and AFM analysis of sputtered TMD coatings.

TMD mono and multilayers were prepared by chemical vapour deposition (CVD), and the TMD thin films were deposited by magnetron sputtering. Some of the materials were provided by the partners in the Solution ITN project.

1.2.3 Research approach

The thesis follows a mixed approach. The work started as 'top-down', with clearly defined hypotheses, objectives and expected outcomes. However, interesting results, such as a shift in frictional behaviour between mono and multilayer TMDs and observation of fully crystalline features in the wear tracks, led to new hypotheses to be tested. The new hypotheses were: (i) the frictional behaviour on multilayered samples is influenced by higher adhesion between the probe and the surface than between the surface and the layer below, and (ii) recrystallisation and reorientation occur only locally within the wear track when the contact conditions exceed the formation threshold.

1.3 Thesis structure

The thesis begins with the literature review (Chapter 2), which outlines the important theoretical definitions of friction on a small scale. The review includes (i) a comparison of the major adhesive contact models, (ii) an overview of atomic force microscopy (AFM) and challenges related to imaging, (iii) an introduction to 2D nanomaterials, and (iv) an overview of transition metal dichalcogenides (TMDs) used as solid lubricants.

The results are divided into four separate chapters, dealing with the frictional behaviour of monolayer TMDs (Chapter 4), the influence of the number of layers on the nano-scale frictional response of WSe_2 (Chapter 5), atomic-scale friction of WS_2 (Chapter 6), and a nanotribological approach to the analysis of thin-film coatings and wear-tracks (Chapter 7).

The thesis concludes with the discussion and conclusion, which correlate the results from the main four chapters and comment on the frictional behaviour across different scales.

The appendices include supplementary information on the in-situ calibration of AFM tips (Appendix A), the description of the custom method developed for Raman mapping (Appendix B), additional friction maps for Chapter 6 (Appendix C) and nanotribological analysis of sputtered MoS_2 coatings (Appendix D).

1.4 Solution ITN project

Solution ITN is a Horizon 2020 (Marie Sklodowska-Curie Actions) project dealing with the development and analysis of novel solid lubrication, combining theoretical and experimental approaches at different scales. The project included a total of 14 early-stage researchers, and the consortium consisted of several European universities, research institutes and industrial partners.

I worked closely with Paola Torche (University of Southampton), who was developing a machine learning algorithm for the analysis of atomic force microscopy data, and with Czech Technical University, where I did my secondment, which included deposition and macro-scale testing of some of the samples and atomic-scale measurements of the flakes.

1.5 Publications

Rapuc A, Wang H, Polcar T. Nanotribology of transition metal dichalcogenide flakes deposited by chemical vapour deposition: The influence of chemical composition and sliding speed on nanoscale friction of monolayers. Appl Surf Sci 2021;556:149762. https://doi.org/10.1016/j.apsusc.2021.149762.

Rapuc A, Simonovic K, Huminiuc T, Cavaleiro A, Polcar T. Nanotribological Investigation of Sliding Properties of Transition Metal Dichalcogenide Thin Film Coatings. ACS Appl Mater Interfaces 2020;12:54191–202. https://doi.org/10.1021/acsami.0c16789.

Chapter 2

Literature review

2.1 Friction at the nano-scale

2.1.1 Coefficient of Friction

The coefficient of friction is a widely used quantity in science and engineering. By its most basic definition, it is easy to measure and define - as the factor correlating the tangential frictional force to the applied normal force. It is convenient for quantifying the relative ease with which two surfaces can slide against one another. However, the property is not as easy to describe on a more fundamental level (44).

Two types of macroscopic (i.e. conventional, large scale) friction coefficients exist (44): (i) static coefficient of friction, which represents the resistance opposing the onset of relative motion and (ii) kinetic coefficient of friction, which represents the friction opposing the continuance of relative motion during sliding.

Three main friction laws are generally accepted at the macro-scale and apply to a large number of macroscopic contacts. The first friction law, described by G. Amontons, states that the friction force F_f is linearly proportional to the applied load $F_f = \bar{\mu}L$, where $\bar{\mu}$ stands for the macroscopic coefficient of friction (i.e. an average coefficient of friction across the entire contact area) (45). Another observation of Amontons was that friction is independent of the apparent contact area (44). Furthermore, the third friction law, described by C. Coulomb, states that the macroscopic coefficient of friction is also independent of sliding velocity (46).

For general engineering use, the coefficients of friction for different combinations of materials have been widely tabulated and used within the engineering handbooks and were sufficient for designing machines and structures in the past (44). However, with the increasing complexity of modern tribological contacts and the emergence of

new nano-mechanical devices, the tabulated coefficients of friction are not adequate anymore. We, therefore, need to investigate the frictional behaviour of materials at smaller scales more thoroughly and understand how small scale behaviour influences friction on larger scales.

F.P. Bowden and D. Tabor (47) assumed adhesion to be the primary mechanism of friction between solids; in a tribological contact, the asperity junctions appear as a result of contact pressure and adhesion. The combination of all the asperity junctions constitutes the real contact area ($A_r = F_n/p$, where p is the yield pressure of the contact material); the frictional force was defined by the shear strength of the contact and the real contact area, as shown in Equation 2.1:

$$F = SA_r = \frac{F_n S}{p}, \tag{2.1}$$

where S is the shear strength of the asperity junction. The coefficient of friction can then be defined as (47):

$$\mu = \frac{S}{p}. \tag{2.2}$$

Shearing usually occurs within the softer material, meaning that S and p are approximately equal to the shear strength and yield pressure of the softer material, respectively (47). It is important to note that the above law is independent of contact geometry and is based only on the material properties of the contacting surfaces.

2.1.2 Describing friction at the nano-scale

Tribological properties of a specific system depend on its dimension; the dominant mechanisms within the nano-scale contracts are therefore not the same as at the macro-scale (15). Effects, such as sudden non-linear stick-slip motion (48), adhesion (49) and stiction (15), contribute significantly to nano-scale friction and cannot be described using the traditional theoretical approaches. Hence, the macroscopic laws of friction may not fully apply at the nano-scale (45).

When two atomically flat rigid bodies, where one of the surfaces is elastically deformable in the sliding direction, slide against each other, the total lateral force F_{lat} acting on the surfaces is equal to the sum of the individual contributions from all atoms j in the contact (50):

$$F_{lat}(t) = -\kappa \sum_{j=1}^{n} \xi_j(t), \tag{2.3}$$

where κ is the elastic constant of the deformable surface, and ξ_j is the relative displacement of a single atom.

L. Prandtl (51) and G.A. Tomlinson (52) introduced the first atomistic friction models in 1928 and 1929, respectively. In the so-called 'Prandtl-Tomlinson' (PT) model, they portrayed the atoms as spheres and assumed that the surfaces are atomically flat. The spacing between the atoms was represented by the lattice constant. The model did not describe all aspects of the atomic-scale friction accurately, but it provided the first insight into the processes involved in friction at the atomic scale, namely the atomic-scale stick-slip effect (15). The model also explained why the friction in dry contact does not vanish when the sliding velocity approaches zero (50). The molecule of one surface can get temporarily pinned to the other surface, thus increasing static friction. When the surface is moved forward, the molecule suddenly detaches and releases its energy through dampened vibrations. This principle of movement is called stick-slip and is the main mode of frictional energy dissipation at the atomic scale.

The next attempt at describing atomic-scale friction was by J. Frenkel and T. Kontorova (53), presented in 1938. The 1-dimensional Frenkel-Kontorova (FK) model was based upon the interaction between the substrate atoms and a harmonic chain of surface atoms linked by springs; a periodic potential force is applied to the particles. The model described the effect of commensurability on friction; in a commensurate case, the contributions from each atomic pair are maximised, while in an incommensurate case, the individual contributions may cancel out (see Figure 2.1) (15). Furthermore, a combined Frenkel-Kontorova-Tomlinson (FKT) model was presented more recently (50). The FKT model extends the Prandtl-Tomlinson model by including next-neighbour interactions between the molecules, thus combining it with the Frenkel-Kontorova model. The FKT model allows the investigation of the ground-state (i.e. each atom lies in the potential well underneath the support of its spring), meta-stable states, static friction and kinetic friction.

2.1.3 Superlubricity

As the atomic-scale stick-slip motion is the primary source of energy dissipation in a dry contact, reducing it to negligible levels is highly desirable. Different definitions for superlubricity exist. From a purely theoretical perspective, superlubricity occurs when two incommensurate surfaces slide in absence of stick-slip motion (48). Another definition states that superlubricity is the state in which contacting surfaces exhibit no

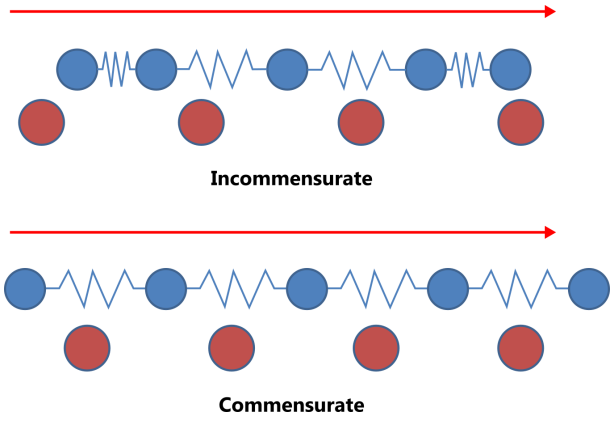

Figure 2.1: A comparison of commensurate and incommensurate sliding in the Frenkel-Kontorova model (15).

resistance to sliding (54), also referred to as the state of zero friction (55). A significant reduction of friction can therefore be expected when compared to a similar commensurate sliding condition (48). On the other hand, from an engineering perspective, superlubricity stands for super low friction, with a coefficient of friction below 0.01 (56).

The main conditions for achieving superlubricity are that the energy of the interacting incommensurate surfaces is independent of their relative position and that the surfaces are sufficiently hard (48). Superlubricity is, therefore, reached when the sum of all atomic contributions to the lateral force is equal to zero (see Equation 2.1.2) (57). Incommensurate contact is achieved when two crystals contact at a certain lattice misfit angle θ (54); altering the lattice misfit angle changes the degree of commensurability and alters the frictional response. Typical solid superlubric materials include diamond-like carbon (DLC), transition metal dichalcogenides (TMDs), graphite and carbon nitrides (CN_x) (58).

2.1.4 Contact models and their relation to friction

2.1.4.1 Hertz model

We begin this section with a description of a simple model describing the contact of two elastic bodies. H. Hertz developed this model in 1882, and it still serves as a starting point in many more complex models. For a point contact of two elastic spheres (with radii R_1 and R_2), the contact radius a_0 is described as (59):

$$a_0^3 = \frac{3R^*F}{4E^*}, \tag{2.4}$$

where E^* is the reduced Young's modulus, F is the applied load, and R^* is the reduced radius of the contacting spheres. The reduced Young's modulus E^* for the contacting materials (with their corresponding Young's moduli E_1, E_2 and Poisson coefficients ν_1, ν_2) is defined as (60):

$$E^* = \left\{ \frac{1-\nu_1^2}{E_1} + \frac{1-\nu_2^2}{E_2} \right\}^{-1}, \tag{2.5}$$

and the reduced radius R* of the contacting spheres as:

$$R^* = \left\{ \frac{1}{R_1} + \frac{1}{R_2} \right\}^{-1}. \tag{2.6}$$

The relationship between the applied normal force and contact radius can be rewritten as (60):

$$F_{Hertz} = \frac{4E^* a_0^3}{3R^*}. \tag{2.7}$$

Deformation (i.e. the relative approach between two distant points in the contacting spheres) according to the Hertz theory is defined as (59):

$$\delta = \frac{a_0^2}{R^*}. \tag{2.8}$$

Hertz verified his theory experimentally using an optical microscope, where he observed the contact behaviour between glass spheres (59).

2.1.4.2 Adhesive contact: Johnson, Kendall and Roberts

As the size of the contact gets smaller, the influence of surface-related phenomena on contact properties increases. At the nanometre scale, which usually includes light loads and smooth surfaces, the adhesion between solid surfaces becomes a significant parameter contributing to contact properties (61). Adhesion is a collective term, represented as the work of adhesion - that is, work required to separate a unit area of the interface. It incorporates different physical phenomena, such as intermolecular forces, electrostatic forces and capillary action (meniscus forces) (61). The adhesion models are based upon the Hertz approach with additional consideration of adhesion (60), where the adhesive stress is typically represented by the Lennard-Jones potential

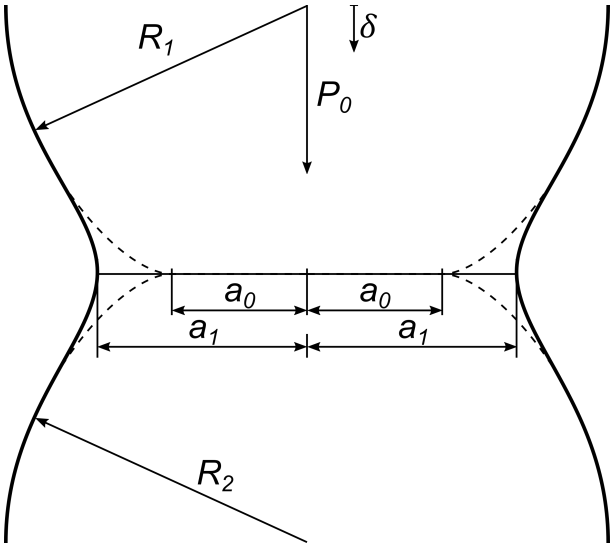

Figure 2.2: Contact geometry between two elastic bodies in the presence (a_1) or absence (a_0) of surface forces, according to the JKR model (59).

(62). The effect of adhesion on the contact properties was first studied in the 1930s by R.S. Bradley and B. Derjaguin independently (63).

The first major model to include adhesion in the contact of two deformable elastic bodies was the Johnson-Kendall-Roberts (JKR) model, presented in 1971 (59). The contact geometry of the two contacting spheres is shown in Figure 2.2. They experimentally identified that the contact area between two spheres at low loads was considerably larger than predicted by Hertz, while results at higher loads appeared closer to the Hertz theory. That indicated that attractive forces act between the surfaces and become very important at low loads. The model proposed a method for determining the interfacial surface energy of solids when one of the solids is highly deformable.

The presence of attractive surface forces results in a larger contact radius a_1, as shown in Figure 2.2. The model describes surface attraction in terms of surface energy. The apparent Hertz load (e.g. the load required for a Hertzian contact to reach contact radius a_1) acting between two elastic bodies with a total surface energy $\Delta\gamma$ ($\Delta\gamma = \gamma_1 + \gamma_2 - \gamma_{12}$, where γ_1, γ_2 and γ_{12} are the corresponding surface energies (62)) is, therefore, larger than the applied load F (59):

$$F_{Hertz} = F + 3\Delta\gamma\pi R^* + \sqrt{6\Delta\gamma\pi R^* F + (3\Delta\gamma\pi R^*)^2}, \tag{2.9}$$

which can be rewritten as:

$$F_{JKR} = F_{Hertz} - \sqrt{8\Delta\gamma\pi E^* a_1^2}. \tag{2.10}$$

The resulting equation for the contact radius with included surface energy effect is (59):

$$a_1^3 = \frac{3R^*}{4E^*}\left(F + 3\Delta\gamma\pi R^* + \sqrt{6\Delta\gamma\pi R^* F + (3\Delta\gamma\pi R^*)^2}\right). \tag{2.11}$$

In the case of negative applied load in (2.9), there is a limiting case in the term $\sqrt{6\Delta\gamma\pi R^* F + (3\Delta\gamma\pi R^*)^2}$; the equation can only have a real solution if (59):

$$6\Delta\gamma\pi R^* F \leq (3\Delta\gamma\pi R^*)^2. \tag{2.12}$$

The contacting bodies would therefore separate at (59):

$$F_{JKR,pull-off} = -1.5\Delta\gamma\pi R^*. \tag{2.13}$$

2.1.4.3 Adhesive contact: Derjaguin, Muller, Toporov

An alternative adhesion theory was proposed by Derjaguin, Muller and Toporov (DMT) in 1975 (64). In the model, the authors considered a contact between an elastic ball and an absolute rigid surface ($E_{ball}/E_{surf} < 1$). However, E_{ball} should not be too small, so the deformation shape can be assumed as in the Hertz theory (i.e. adhesion forces do not change the shape of the contacting bodies). The model applies to the contact between smooth particles of small sizes. Adhesion is considered in the form of attractive long-range forces acting over a gap outside the contact area (60, 64). The force of adhesion is equal to the pull-off force and is defined as:

$$F_{DMT} = 2\pi R^* \Delta\gamma. \tag{2.14}$$

The expression is equivalent to the one obtained by R. S. Bradley (65) in the 1930s for the separation of two rigid spheres. A similar expression had also been proposed by B. Derjaguin (66) for relating the force law $F(D)$, between two curved surfaces, to the free energy of interaction per unit area $w(D)$, and is commonly referred to as the Derjaguin approximation (67):

$$F(D) \approx 2\pi R^* w(D), \tag{2.15}$$

where D is the separation distance and w is the work of adhesion.

As the contact geometry in the DMT model is assumed to be the same as in Hertz theory, we can define the contact radius as (64):

$$a = \left(\frac{3R^*}{4E^*} (F + 2\pi R^* w) \right)^{1/3}. \tag{2.16}$$

2.1.4.4 Transition regime

JKR and DMT theories were thought to be contradictory at first, but as was later indicated by D. Tabor (68), the two models were just the two opposite extremes of a general solution. D. Tabor proposed a dimensionless parameter μ_{Tabor}, defined as (68):

$$\mu_{Tabor} = \frac{h}{Z_0} = \left(\frac{R^* w^2}{E^{*2} {Z_0}^3} \right)^{1/3}, \tag{2.17}$$

where h is the neck height around the contact zone (see Figure 2.3), and Z_0 is the equilibrium separation between the surfaces. Small values of μ_{Tabor} resemble small rigid solids (DMT), while large values correspond to large radius compliant solids (JKR) (61). The transitional regime between the two models was numerically described by incorporating the Lennard-Jones potential by Muller, Yushchenko and Derjaguin (69).

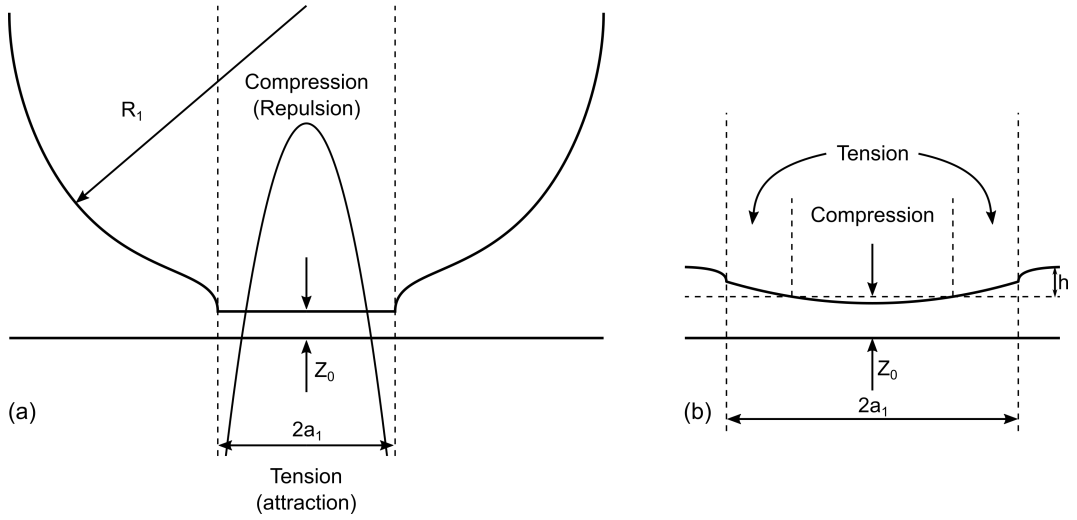

Figure 2.3: Interaction between an elastic sphere and a rigid flat surface. (a) Contact geometry and the resulting internal pressures within the contact diameter $2a_1$ according to the JKR model. (b) An exaggerated shape of the contact (68).

D. Maugis (70) presented a generalised model for the transition regime in 1992, in which he included the Dugdale model for yielding of steel slits (71). The model allowed analytical solutions by approximating the adhesion stress σ_0 to be constant (and equal to the yield strength of the material) up to a maximum separation between

the surfaces h_0. The maximum work of adhesion is therefore defined as $w = \sigma_0 h_0$. Maugis parameter λ defines the elasticity of the contacting surfaces and can be expressed as (70):

$$\lambda = \frac{\sigma_0}{\left(\frac{\pi w E^{*2}}{R}\right)^{1/3}} \tag{2.18}$$

The transition parameter can be used to evaluate the nature of the contact regime. The JKR model is valid when $\lambda > 5$ and DMT when $\lambda < 0.1$, while the transition regime between 0.1 and 5 should be calculated by the Maugis-Dugdale model (60). Furthermore, the Maugis-Dugdale model allows for the exact reproduction of the influence of capillary forces due to meniscus formation on adhesion (61). K. Johnson (72) presented an adhesion map (Figure 2.4) showing which model applies to the elasticity and load parameters. The adhesion map serves as a more complete alternative to using a single parameter for the determination of the appropriate contact model.

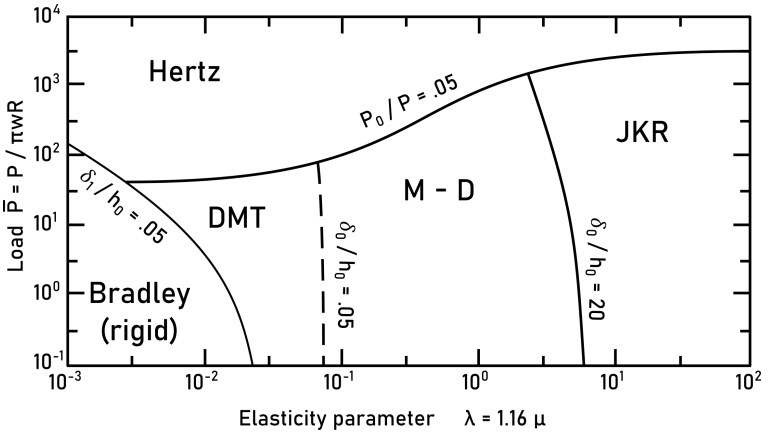

Figure 2.4: Adhesion map (72).

2.1.5 Nano-scale contact models

2.1.5.1 Hertz-plus-offset model and the effective coefficient of friction for point-contact-like single-asperity friction

The models presented above were developed for and validated by well defined macro-scale contacts. However, a similar approach can be taken when analysing the nano-scale contacts. If the Tabor parameter is low enough (i.e. $\mu_{Tabor} < 0.1$, DMT regime), which means that the effect of the attractive forces inside the contact area is negligible, a simplification can be considered. An effective normal force ($F_n = F_L + F_0$, where F_L is the applied load and F_0 is the sum of all attractive forces and can be

approximated by the measured pull-off force) can be introduced. This, in turn, leads to a formulation for contact area (73):

$$A = \pi \left(\frac{R(F_L + F_0)}{K} \right)^{2/3} = \pi \left(\frac{RF_n}{K} \right)^{2/3}. \tag{2.19}$$

The above expression has been successfully used to describe the contact between the AFM tip and the surface. K is an effective elastic modulus of the contact ($K = {}^3/_4 E^*$).

U. D. Schwarz et al. (73) have further derived the expression for the correlation between the load on the AFM tip and the resulting frictional force. They have introduced the effective friction coefficient for point-contact-like single-asperity friction $\tilde{\mu}$, which is independent of the size effects (e.g. tip radius). The resulting friction law was defined as:

$$F_f = \tilde{\mu} R^{\frac{2}{3}} F_n^{\frac{2}{3}}. \tag{2.20}$$

The benefit of using $\tilde{\mu}$ for nano-scale contacts over the conventional coefficient of friction is that it only depends on the intrinsic frictional and mechanical properties of the materials in the contact:

$$\tilde{\mu} = \pi \frac{S}{K^{2/3}}, \tag{2.21}$$

where S is the contact shear strength. The actual value of K in the nano-scale contacts may be difficult to determine due to the presence of contamination layers or composite contact structures. Therefore, presenting the values of $\tilde{\mu}$ is usually preferable to the exact values of the contact shear strength. Further analysis by U.D. Schwarz et al. (73) has shown that a small force offset F_{off}, which should be much smaller than the measured total adhesion force ($|F_{off}| \ll |F_0|$), had to be introduced to fit the data more accurately. The need for the force offset arises from the uncertainty in the determination of F_0 (73); the total force of adhesion F_0 is only approximated by the pull-off force obtained from the force-distance (FD) curve. Consequently, we can rewrite Eq. (2.20) as:

$$F_f = \tilde{\mu} R^{2/3} (F_n - F_{off})^{2/3}, \tag{2.22}$$

which is called the Hertz-plus-offset model (73). The effective friction coefficient for point-contact-like single-asperity friction, obtained from Equation 2.22 can be used to independently compare the contact and frictional properties of different materials

regardless of their geometry. However, we must note that the $^2/_3$ power law applies only to perfectly spherical tip apex, which is not always the case with commercial AFM probes. If the portion of the tip apex in contact with the sample is not completely spherical, the contact would exhibit a slightly different power law at low loads, with a power coefficient m in the range $0.4 < m < 1.2$ (73):

$$F_f = \tilde{\mu} R^m (F_n - F_{off})^m = \pi \left(\frac{S}{K}\right)^m (F_n - F_{off})^m. \tag{2.23}$$

2.1.5.2 Other nano-scale contact models for the description of AFM contact

Even though the Hertz-plus-offset model presents an easy and straightforward model for describing AFM contacts and can be applied to many different materials (73, 74), it is only valid when the Tabor parameter is below 0.1. More general models for fitting load-dependent friction measurements were presented by R. Carpick et al. (75) and U. D. Schwarz (76), which tackle the entire range of interaction forces but offer a simplified solution compared to the Maugis-Dugdale model.

R. Carpick et al. (75) presented a general equation for fitting contact area and load-dependent friction measurements. They introduced a new dimensionless parameter α; when $\alpha = 1$, the model is equivalent to the JKR model, and when $\alpha = 0$, it is equivalent to the DMT model, while for intermediate cases ($0 < \alpha < 1$), the generalised equation closely corresponds to the transition regime in the Maugis-Dugdale model. They define the equation for the contact radius as:

$$\frac{a}{a_{0(\alpha)}} = \left(\frac{\alpha + \sqrt{1 - \frac{L}{L_{c(\alpha)}}}}{1 + \alpha}\right)^{2/3}, \tag{2.24}$$

where a is the contact radius at a given load L, $a_{0(\alpha)}$ is the contact radius at no applied load, and $L_{c(\alpha)}$ is the critical separation force (pull-off force). The parameter α can be correlated to the elasticity parameter using an empirical conversion relation $\lambda = -0.924 \ln(1 - 1.02\alpha)$.

Considering the assumption that friction is directly proportional to the contact area, we can replace all instances of a in Eq. (2.24) with $\sqrt{F_f}$. Therefore, the above equation can be used for both, fitting contact area and load-dependent friction measurements. The measured data is fit to the equation, leaving a_0 (or $\sqrt{F_{f0}}$), L_c and α as fitting parameters. L_c can alternatively be approximated by the measured pull-off force. Having obtained the values of a_0 (or $\sqrt{F_{f0}}$), L_c and α, we can then determine the value

of λ and the dimensionless values of $\hat{L}_c(\lambda)$ and $\hat{a}_0(\lambda)$. These can be further used to determine the values of γ and K, provided that we know the value of the tip radius R:

$$\hat{L}_c(\lambda) = \frac{L_c}{\pi\gamma R} = -\frac{7}{4} + \frac{1}{4}\left(\frac{4.04\lambda^{1.4} - 1}{4.04\lambda^{1.4} + 1}\right) \tag{2.25}$$

$$\hat{a}_0(\lambda) = a_0\left(\frac{K}{\pi\gamma R}\right)^{1/3} = 1.54 + 0.279\left(\frac{2.28\lambda^{1.3} - 1}{2.28\lambda^{1.3} + 1}\right). \tag{2.26}$$

Additionally, for friction measurements, we can use Eq. (2.26) to determine a_0 and contact shear $\tau = {}^{F_0}/_{\pi a_0^2}$. Both values of K and R must be known to determine interfacial shear strength.

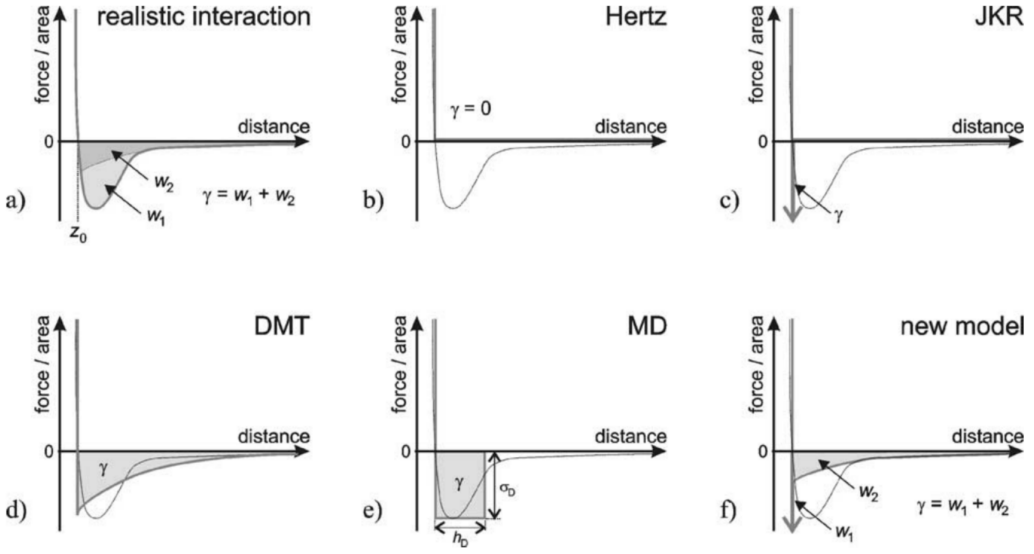

Figure 2.5: A comparison of force-distance relationships according to different models. (a) realistic interaction (such as Lennard-Jones potential), (b) Hertz model (no adhesion), (c) JKR model (adhesion represented by only short-range forces), (d) DMT model (adhesion represented by only long-range forces), (e) Maugis-Dugdale model (constant force σ_0 acting up to h_0), (f) combined JKR-DMT transition model (combined effect of short-range forces w_1 and long-range forces w_2) (76).

U. D. Schwarz (76) developed a simple analytical solution for the transition regime. This model is based on the fact that the JKR model accurately models short-range forces, and the DMT model accurately describes long-range forces. As shown in Figure 2.5f, the model combines the interaction energy of short-range forces w_1, similar to the JKR model (Figure 2.5c), and long-range forces w_2, similar to the DMT model (Figure 2.5d). Therefore, the resulting contact radius according to this model is:

$$a = \left(\frac{R}{K}\right)^{1/3}\left(\sqrt{3F_c + 6\pi R\gamma} \pm \sqrt{F_1 - F_c}\right)^{2/3} \tag{2.27}$$

where F_1 is the value of the externally applied force, and $F_c = {}^{-3}/_{2}\pi R w_1 - 2\pi R w_2$ is the critical separation force. The advantage of the model is that it is purely analytical and contains only independently measurable physical quantities. There is no need for the introduction of a specific transition parameter, as the critical force F_c already serves as a transition parameter. Furthermore, the DMT and JKR equations can be obtained from the model by substituting w_1 or w_2 with 0 respectively.

Despite the model being entirely analytical, the practical applications may call for an introduction of a transition parameter that would directly indicate whether the contact is closer to the DMT or JKR regime. Thus, an alternative parameter τ_1 has been introduced:

$$\tau_1 = \sqrt{\frac{w_1}{\gamma}} = \sqrt{\frac{2F_c}{\pi\gamma R} + 4}, \tag{2.28}$$

which takes values between 0 (DMT) and 1 (JKR). Further forms for the contact radius, additional transition parameters and correlation of the model to the empirical model by R. Carpick et al. can be found in Ref. (76).

Further models incorporating plastic deformation of the contacting bodies or a description of multi-asperity contacts can be found in the literature (77, 78). However, plastic deformation and multi-asperity contacts are mainly applicable to macro-scale cases. In the framework of this work, we are only dealing with small well-defined surfaces and low loads, for which we expect only elastic deformation and, therefore, good agreement between our data and the presented models. Regardless, plastic deformation is manifested differently at the nano-scale; therefore, scaling the plastic-elastic models to the nano-scale may not be feasible (79, 80).

2.2 Atomic Force Microscopy as a nanotribology technique

2.2.1 Atomic Force Microscope

Atomic force microscopy (AFM) is a convenient tool for imaging surfaces and probing fundamental surface forces, such as van der Waals, electrostatic and frictional forces, down to atomic resolution (81). The AFM belongs to the group of scanning probe microscopy (SPM) surface analysis techniques (82).

The first atomic force microscope was developed in 1986 by G. Binnig, C.F. Quate and C. Gerber (83) as a modification of scanning tunnelling microscopy (STM). STM, developed in 1981 by G. Binnig et al. (84), is an SPM technique for observing surface

topography at the atomic scale based on vacuum tunnelling (85). The main operating principle of STM is based upon scanning a metal tip over the sample surface while maintaining a constant tunnelling current. A constant tunnelling current is achieved through manipulation of the displacement of the metal tip by a piezo-drive; recording the applied voltages to the piezo-drive results in a topographic image of the surface (85). The high resolution of the method allowed the investigation of the individual surface atoms for the first time (85, 86). The main limitation of STM is that it requires electrically conductive samples to allow the tunnelling current to flow between the metal tip and the sample (83, 86).

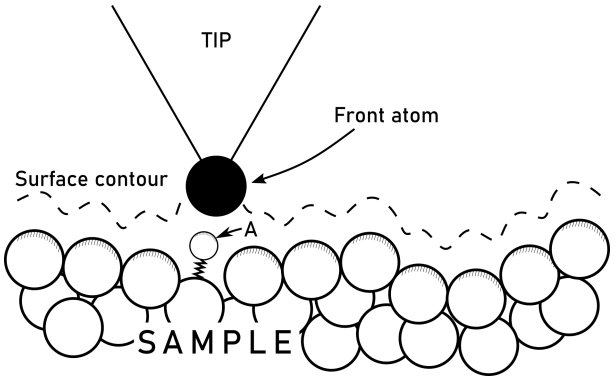

Figure 2.6: AFM working principle. The tip follows the surface contour by keeping the contact force constant. "A" shows an adatom on the sample surface and its interaction with the tip. A non-linear spring is an approximation of the chemical bond (83).

The invention of AFM has enabled atomic-scale surface probing on any solid material, regardless of its conductivity (83). The images are obtained by measuring forces acting on the sharp tip as it is dragged across the surface. The applied load is usually kept constant through a feedback mechanism; hence, when the tip moves across the surface it follows the surface contour, as shown in Figure 2.6 (83). Long-range (van der Waals, electrostatic and magnetic forces) and short-range (chemical forces due to orbital overlap) forces between the tip and the sample are formed when the sharp tip is close to the surface. The interaction between the tip and the surface atoms can be theoretically summarised using the Morse potential or Lennard-Jones potential (LJP) (87, 88). In addition, operation in ambient conditions may result in the presence of adsorbed water or hydrocarbon molecules on the surface (89). This may, in turn, result in the formation of additional adhesive meniscus forces (86).

In the initial AFM design, a cantilever beam with an ultra-small mass and an attached sharp diamond tip was placed between the sample and the STM tip. The cantilever, therefore, acted as an STM sample. The STM tip and the AFM sample were assigned to separate feedback mechanisms to keep a constant force acting on the surface by keeping the tunnelling current constant. More precisely, the authors presented four different operating modes in the original design - see Ref. (83) for a more detailed

description. The cantilever was attached to a modulating piezo element used to oscillate the cantilever at its resonant frequency (83).

Even though the STM is very sensitive to the detection of position changes, it is difficult to precisely align a tunnelling probe with a very small area at the end of the cantilever. Furthermore, the STM tip exerts additional forces on the cantilever, which contribute to the total deflection and are impossible to distinguish from surface forces. The lateral position of the tip shifts with the deflection of the cantilever and the roughness of the cantilever results in a non-linear signal (86).

More common approaches for measuring the deflection of a cantilever are utilising the reflection of a laser beam. The two techniques that are mainly used are (i) measuring the phase of the reflected laser light from the back of the cantilever and (ii) measuring the deflection of a laser beam that reflects off the back of the cantilever with the photodiode (the optical-lever technique) (90). A schematic presentation of the optical-lever technique is shown in Figure 2.7.

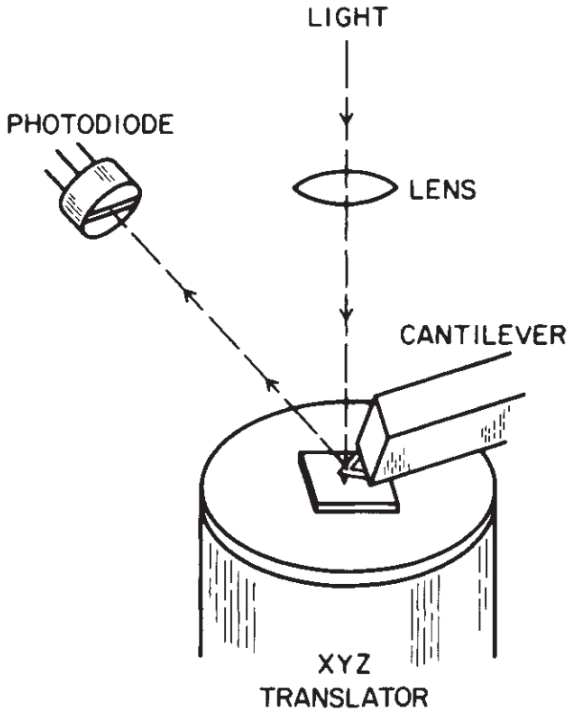

Figure 2.7: AFM deflection detection. The schematic shows the positioning of the laser, AFM probe and photodetector (90).

In the basic principle, AFM operation can be divided into contact and non-contact modes (67, 91). Contact modes utilise the repulsive forces between the tip and the sample when the tip is in contact with the surface. Generally, it is used on hard surfaces that would not be affected by the contact force (67). Contact mode, for example, is required for lateral force microscopy (LFM) measurements. On the other hand, non-contact modes are preferable on softer surfaces. In this case, the tip

oscillates at a frequency near its resonant frequency, and the attractive forces between the surface and the tip are monitored (67). A special regime of the non-contact mode is the tapping mode, where the oscillating frequency is set to be the resonant frequency of the tip. Consequently, the oscillation amplitude increases and the tip briefly touches the surface in its lowest position. This mode can achieve high resolution and does not damage the surface (67).

2.2.2 Common artefacts in AFM imaging

An important aspect in any analysis involving AFM is distinguishing between the features of interest and potential artefacts that arise from the physical nature of the method, interference due to external noise, defects in the probe shape or surface contamination (92). Some artefacts are very common for the technique and have therefore been widely documented (92, 93), making them easy to discover and correct. However, some artefacts may only arise under specific conditions, and it requires the operators' experience to successfully recognise them and not mistake them for an actual sample feature. One such example would be the geometrical structure of the tip, which can, under specific conditions, significantly alter the shape of the final scanned image without any indication that the scanned image is false. Here we summarise some common artefacts and discuss how they can be recognised and corrected. Different types of measurement artefacts and their detection and correction approaches are collected in Table 2.1.

The most common artefacts in the AFM include sample tilt, light interference and scanner bow. Some degree of sample tilt can always be expected when mounting the sample. Due to the very high resolution of the technique (sub-nm), the human eye cannot ensure that the surface is parallel to the scanning plane. Nevertheless, sample tilt is very easy to correct through 1st order plane levelling, and most AFM systems already employ levelling algorithms that automatically correct it. An example of sample tilt is shown in Figure 2.8.

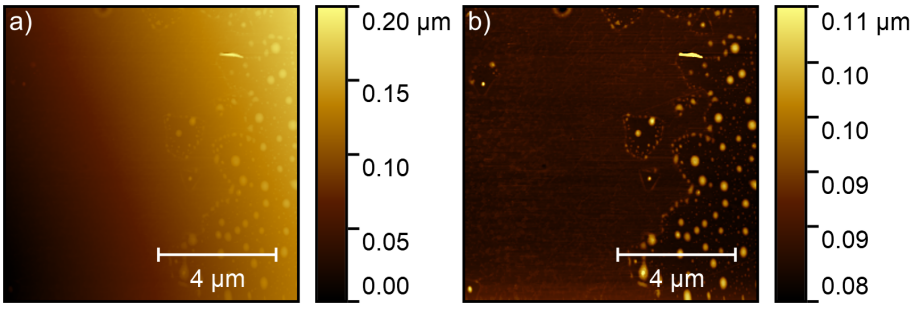

Figure 2.8: An example of sample tilt: (a) original uncorrected scan, (b) sample tilt corrected using plane levelling.

Table 2.1: An overview of different types of artefacts

Artefact	Detection	Correction	Correction methods
Sample tilt	Easy	Easy	1^{st} order plane levelling
Light interference	Easy	Moderately easy	Line levelling
Scanner bow	Easy	Easy	2^{nd} order plane levelling
Thermal drift	Moderately difficult	Difficult	Re-scanning the surface when the temperature stabilises, increased scan rates
Creep	Moderately easy	Moderate	Creep path extraction and aligning of the scans
Piezo ageing	Moderately difficult	Easy (once detected)	System calibration
Edge overshoot	Moderate	Moderate	Scan rate reduction, gain correction
Edge elevation	Moderate	Very difficult	Modifying the contact chemistry (e.g. coating the surfaces) or changing the operation mode, which are in most cases not feasible
External and internal noise	Easy to difficult	Easy to difficult	Active/passive acoustic isolation, correct tuning of the system, performing the measurements when there are fewer external fluctuations (electrical grid, temperature, vibrations), cleaning or changing the probe
Cross-talk	Difficult	Very difficult	Similar to edge elevation, it would require modifying the surface chemistry or a different operation mode (the artefact disappears in non-contact mode)
Probe and sample wear	Easy to moderate	Moderate to difficult	Replacing the probe, modifying the measuring parameters, probe shape examination

Light interference artefacts commonly occur in the AFMs that use the optical lever technique for the detection of the cantilever deflection (93). The artefact appears when the reflected light from the sample surface interferes with the laser beam reflected from the cantilever surface. As shown in Figure 2.9, the artefact appears as periodic waviness on the image. The resulting oscillations typically have a period comparable to the wavelength of the laser (93). Once identified, this artefact can be corrected by an appropriate levelling algorithm; an appropriate plane or line levelling algorithm can be applied to correct the artefact; the orientation and period of the oscillations determine the order of the correction function.

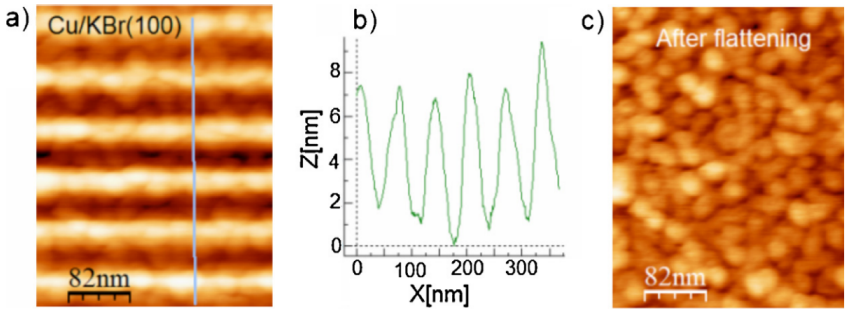

Figure 2.9: An example of light interference: (a) surface topography showing interference waves, (b) height profile following the line, showing false sample topography and (c) levelled surface using line flattening (93)

The lateral movement of the piezo scanner can deviate from an ideally level *xy* plane; the movement of a common tube scanner follows the parabolic/spherical shape and produces an effect called scanner bow (94). Whereas this effect does not present a problem on a smaller scan area, it has to be taken into account when scanning larger samples. As shown in Figure 2.10, the artefact is very apparent and easy to spot and can be easily corrected by 2nd order flattening.

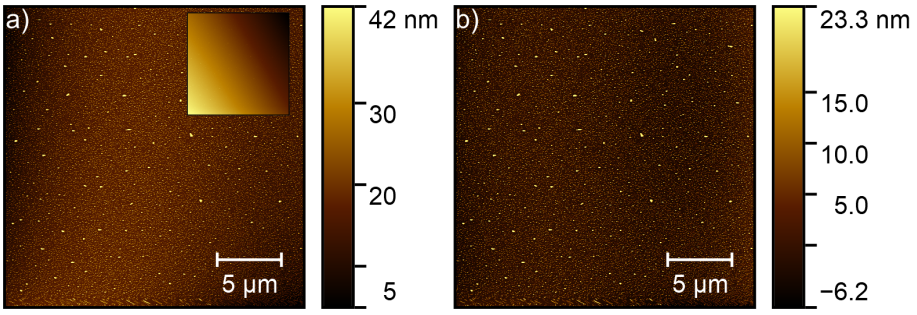

Figure 2.10: An example of scanner bow: (a) corrected tilt (the inset shows the original scan), (b) scanner bow corrected using 2nd order plane levelling.

The small sizes and masses of the AFM cantilevers[1] mean that they have limited heat capacity. Therefore, shining a light (laser or light from the optical system) on the cantilever or a tip coming in contact with the sample may change the temperature and cause thermal expansion, resulting in thermal drift distortion of the image (93). The effect is further amplified when using coated cantilevers, as the dissimilarity of the thermal expansion coefficients between materials causes bending and twisting of the cantilever. Thermal drift may be difficult to recognise unless the topography of the surface is known before the measurement. Since the effect of thermal drift is minimised by allowing sufficient time to reach thermal equilibrium (93), another way of detecting the defect is by performing subsequent scans on the same area and comparing the shape of the features; if the shapes are the same that indicates no

[1]The dimensions of a standard contact mode cantilever are L: 450 µm, W: 50 µm and T: 2 µm (source: www.nanosensors.com)

thermal drift has occurred. The effect can also be minimised by increasing scan rates (93).

A similar effect is a piezo scanner creep when the scanner continues to move in a certain direction for some time after the signal has stopped, which usually occurs when the scanner is rapidly moved to a new location (93, 94). The scanner creep can usually be easily recognised, by examining the lines at the beginning of the scan, especially when measuring the samples with well defined straight edges, such as the one shown in Figure 2.11. The distortion can be corrected after the measurement by extracting the creep path and laterally aligning the lines or by re-scanning the area once the system reaches equilibrium (see Figure 2.11). Note that, when using the first method, we either need to crop the excess area at the edges of the scan or interpolate over the missing data. Scanner creep can occur in all axes of movement and depends on the total distance moved, rate of movement and time from when the applied signal stopped, which makes it difficult to predict and remove by calibration.

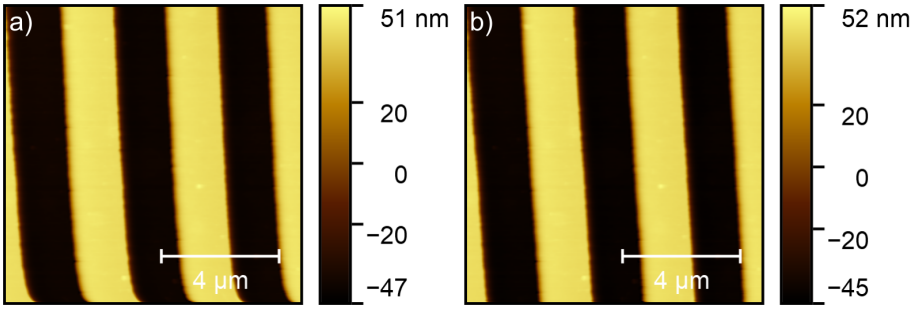

Figure 2.11: An example of scanner creep: (a) original scan, (b) corrected creep in post-processing.

Edge overshoot and edge elevation are common artefacts when scanning surfaces with step edges (93). Both effects appear as artificial narrow elevations or depressions near the edge step. Overshoot is a consequence of the scanner hysteresis and inertia of the sample/cantilever holder and can be minimised by reducing the scanning speed. On the other hand, edge elevation occurs when attractive forces have a significant effect on the tip-sample interaction and do not change with scanning speed (93). A schematic of edge overshoot is shown in Figure 2.12.

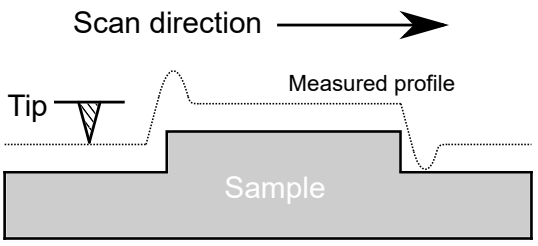

Figure 2.12: Edge overshoot (93).

Many different sources can contribute to the total external noise, such as acoustic noise, electromagnetic noise, mechanical vibrations, airflow and temperature

instability (93). Most modern AFM systems include some form of acoustic isolation, which is usually an active acoustic isolation table or a passive system using dissipative elements. The active acoustic isolation table usually takes up less space, but it can introduce some additional noise to the system itself. Additionally, the design of the components usually includes heavy elements and a windowless enclosure to further minimise the acoustic noise, airflow, light and temperature instability. The location of the AFM apparatus in the building can also influence the level of noise that the system experiences. Despite the effectiveness of the listed protective measures, some measurements might require further steps, such as performing the measurements at night or over the weekends when the mechanical vibrations and electrical grid fluctuations are generally lower (93). On the other hand, the sources of potential internal noise include all system components, including the sensing tip and cantilever, piezoelectric scanner, amplifiers and the rest of the electronic system, the laser and the optical system. Furthermore, tip contamination can introduce additional noise in the system (93). It is, therefore, important to keep the tip clean throughout the measurement and monitor the raw signals to minimise the effects of internal noise. The significance of noise increases when measuring very smaller areas with periodic features, such as the atomic stick-slip measurements.

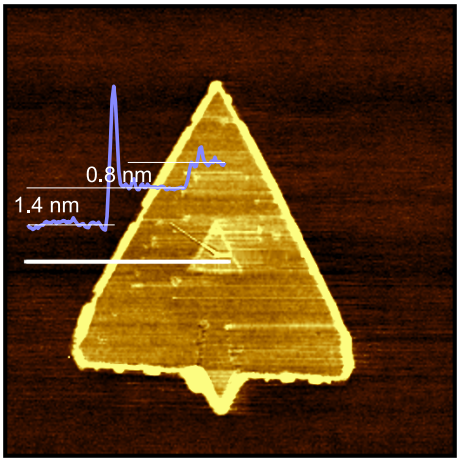

Figure 2.13: An example of cross-talk.

Friction forces can have a significant contribution to the total tip-sample interaction forces. Due to torsion of the cantilever during sliding in a lateral direction, these forces can manifest themselves as height variation on the detector (93). Additionally, even a slight misalignment between the laser deflection axes and the detector can also result in (i) lateral signal influencing the height signal, (ii) topography influencing measured friction, or (iii) a set-point shift can modify the friction signal, resulting in significantly higher or lower apparent friction. This effect is commonly referred to as cross-talk (95). Frictional artefacts may appear when measuring samples with significantly different frictional properties in contact mode; therefore, a good understanding of the sample is required, as well as observing multiple channels simultaneously when

analysing the sample. Constant monitoring of the frictional response when measuring topography can identify whether certain features correspond to the actual changes in topography or are just a consequence of the frictional difference. Likewise, a large difference in adhesional properties between parts of the sample could manifest in a similar artefact. Figure 2.13 shows an example of a friction-induced artefact; a much larger height difference can be observed between the 1st layer and the substrate, whereas the thickness of the 2nd layer on top agrees well with the expected value for the thickness of a single WSe_2 layer (96).

When using contact mode on soft materials, or when high contact loads are required, there is a high possibility of surface deformation or even sample damage and alteration. Elastic deformation can significantly reduce resolution due to increased contact area (93). The resulting height profiles can be altered, and the measured heights are much lower than the true ones. An additional drawback with softer materials is sample alteration through the removal of the surface layers of the material (wear) by the tip pushing the material to the sides of the scanned area. An example is shown in Figure 2.14. Material transfer from the tip to the sample is also possible when using contaminated tips (93).

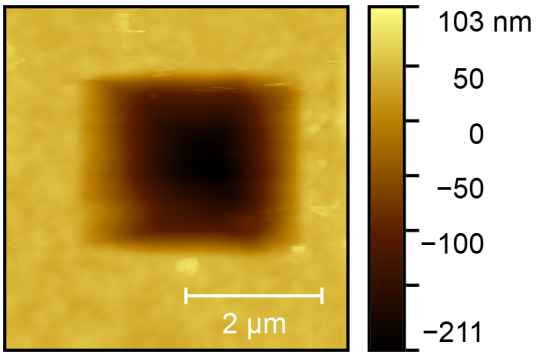

Figure 2.14: Sample damage due to wear, which occurred after prolonged continuous sliding on the same area.

On the other hand, measuring on very hard and adhesive samples and using high loads can cause extensive tip wear or even rupture, resulting in altered tip shape, which can be an increased radius of the apex or a completely altered geometry. Increased contact radius may result in lower resolution and alteration of the shape of the measured features (see Figure 2.15a), while a completely altered geometry can result in the features that were not a part of the sample appearing on the image (see Figure 2.15b). Some initial wear, however, and therefore a slight increase in contact radius, is usually expected upon the initial contact of the tip with the sample (97, 98), but keeping the scanning speed and applied load relatively low can preserve the tip shape for longer. A good indicator of tip damage is when repeated features with an identical shape appear on the image (see Figure 2.15c).

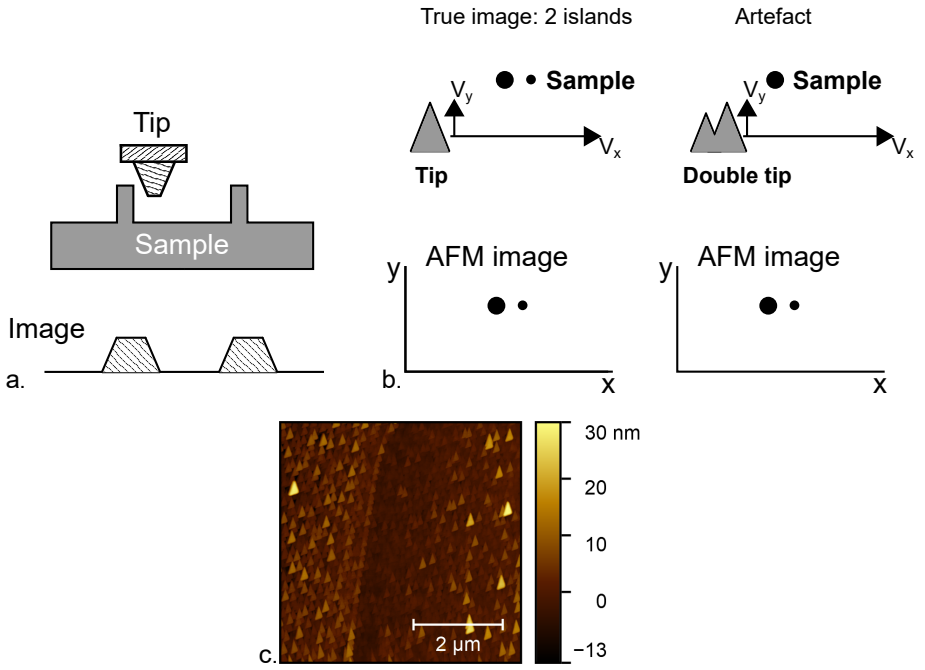

Figure 2.15: The influence of tip shape on the AFM image. (a) Features that are sharper than the tip are distorted in the image (93). (b) A damaged tip can introduce features in the image that are not part of the sample (93). (c) Repeated features of identical shape appearing on the scan are a good indicator of a damaged tip that needs replacing.

2.2.3 Friction Force Microscopy

Friction force microscopy (FFM), or lateral force microscopy (LFM), allows an insight into understanding the fundamental mechanisms of friction and adhesion at the nano and atomic scales (95). LFM is essentially an extension of contact mode AFM, where a lateral deflection signal is collected simultaneously with the topography.

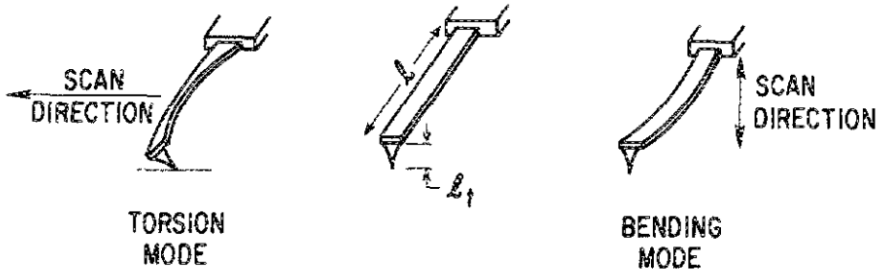

Figure 2.16: Bending modes of the AFM cantilever. Torsional and normal bending modes are the representative and most prominent bending modes of a common rectangular cantilever. Additional bending modes include lateral in-plane bending (not detectable using the optical lever technique) and torsional bending mode when sliding in the parallel direction to the cantilever (can be detected, but it creates the same signal as normal bending) (99).

C. Mate et al. (7) were the first to utilise the AFM for observing the atomic-scale friction and stick-slip behaviour of a tungsten tip on a graphite surface in 1987. The deflection of the tip was measured in the parallel direction to the surface using the interference technique, which, in turn, hindered the ability to detect topography and normal force.

The optical-lever technique has become the preferred method for detecting cantilever deflection, as it allows simultaneous measurements of both lateral and normal forces (99, 100). Frictional force, which arises during scanning the surface in the lateral direction, results in the torsion of the cantilever, as shown in Figure 2.16, whereas the normal force on the tip causes bending (99).

A more detailed schematic drawing, showing the corresponding coordinate system, forces acting on the cantilever, a reflection of a laser beam and a quadrant photodiode detector, is presented in Figure 2.17. The friction force causes deflection of the laser beam in the x-direction, while the normal force deflects the laser beam in the y-direction. Thus, the precisely aligned quadrant detector allows simultaneous detection of normal and lateral forces (100).

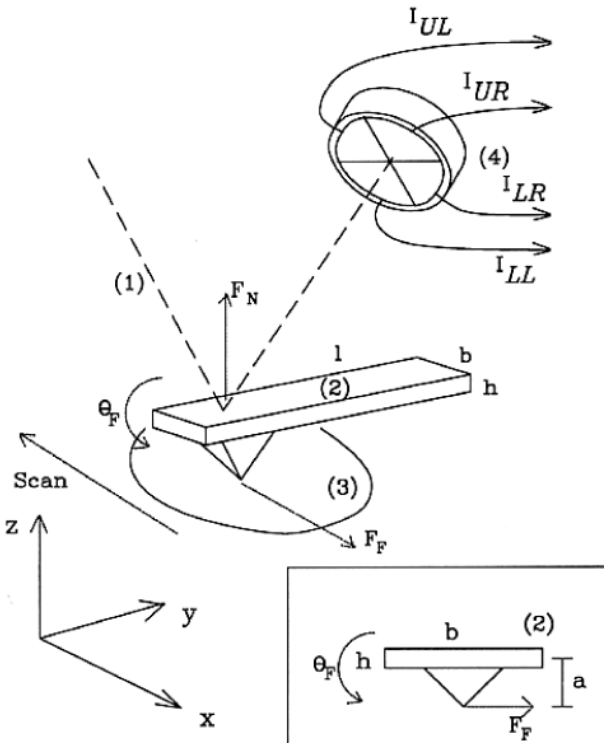

Figure 2.17: The forces acting on the AFM tip and the corresponding output signals from the quadrant photodetector. (1) Laser beam, (2) cantilever, (3) sample surface, (4) photodiode detector. Normal force F_N results in a signal vertical direction $(I_{UL} + IUR) - (I_{LL} + I_{LR})$, and friction force F_F, which causes torsion angle Θ_F, results in a signal in the lateral direction $(I_{UR} + ILR) - (I_{UL} + I_{LL})$ (99).

2.2.4 Recent advances in atomic force microscopy

Being a relatively new technique, atomic force microscopy is receiving increasing interest in different fields of science, including biology, chemistry, physics and engineering. Researchers are still finding new ways of implementing AFM to study different phenomena. For example, in their recent publications, N. Gosvami et al. (101, 102) operated contact mode AFM in oil containing ZDDP additive to investigate the formation of a protective tribofilm *in-situ* at different contact loads and temperatures on Fe coated and uncoated Si substrates. They discovered the power-law dependency of tribofilm thickness on the number of sliding cycles and the exponential relation between the growth rate and pressure or temperature. The limiting tribofilm thickness was 30-40 nm, at which point they started detecting substantial wear of the grown film.

2.3 2D materials and their frictional behaviour

2.3.1 What are 2D nanomaterials?

Nano-structured materials (NSM) are low dimensional materials that have at least one dimension in the nanometre range (less than 100 nm) (26, 63). V.V. Pokropivny and V.V. Skorokhod (63) have fully classified NSMs based on their dimension:

- 0D (molecules, fullerenes, nanoparticles, ... (63)),
- 1D (nanotubes, nanowires, nanorods, ... (26, 63)),
- 2D (layered materials: nanoplates, nanosheets, ... (26, 63)) and
- 3D (nanopillars, hetero layers, nanocones, ... (26, 63)).

The primary interest of this work is focused on two-dimensional (2D) nanomaterials. 2D materials are known to exhibit particular electrical and optical properties, lack of interlayer interaction, low interlayer forces and high surface-to-volume ratio (26). 2D nano-structured materials can be further divided into three categories (26):

1. *Layered van der Waals solids* are the most common layered 2D nanomaterials. They express strong covalent bonding in-plane and weak van der Waals forces between the planes. They are usually a few μm in size and less than 1 nm thick. Graphene, transition metal dichalcogenides (TMDs), h-BN, SiC and vanadium oxide are some of the representative materials from the group.

2. *Layered ionic solids* are composed of a charged polyhedral layer sandwiched between hydroxide or halide layers by electrostatic forces; either single or few-layered materials can be easily obtained by liquid exfoliation methods. The main materials from the group are europium hydroxide, Perovskite-type oxides and metal hydroxides.

3. *Surface assisted non-layered solids* are represented by an atomically thin layer of a material, artificially synthesized on a substrate via chemical vapour deposition or epitaxial growth. Silicene, ZrB_2, Al_2O_3, Cu_2N, MgO and TiO_2 nanosheets are some of the representative materials of this type. Their main application is for energy storage, field-effect transistors (FET) and for controlling the charge density of nanoparticles.

There are over 150 2D materials that can form atomically thin layers with exceptional properties already available. They can be classified as metallic, semi-metallic, semi-conductive, insulating or superconductive (103).

2.3.1.1 Graphene

Graphene, i.e. a single atomic layer of carbon atoms in a hexagonal sp^2 structure, was first isolated in 2004 by K. Novoselov et al. (104) using mechanical scotch-tape exfoliation from graphite and has since become the most widely studied 2D material and a leading material in nanotechnology (26). Mono and bilayer graphene are zero band gap semiconductors (105), which potentially limits their applicability in electronics; however, introducing strain in the structure (strain engineering) by stretching, shearing, or periodic rippling has been shown to increase the band gap (106).

Graphene has soon gained the status of a prospective future lubricant (20), as it exhibits favourable frictional and anti-wear characteristics. A single layer of graphene is ultra-thin, offers extreme mechanical strength (107), and can conformally coat nano and micro-scale contacts, making it an ideal solid lubricant for even the most precisely engineered contacts in MEMS/NEMS devices (20). The presence of water has been shown to improve the frictional properties of graphene (20), unlike a plethora of other materials, including TMDs, which are negatively affected by humidity (108, 109).

The main techniques for synthesis and production of monolayer graphene include mechanical exfoliation (104), chemical exfoliation (110), unrolling of carbon nanotubes (111), chemical vapour deposition (CVD) (112), arc discharge, epitaxial growth (113) and reduction of graphene oxide (114).

2.3.1.2 Transition Metal Dichalcogenides

The structure of transition metal dichalcogenides (TMDs) can be compared to that of graphene/graphite; they form strong covalent interlayer bonds and weak van der Waals forces between the layers (26). TMDs have a general formula MeX_2, where Me presents a transition metal (with the oxidation state +4) and X a chalcogenide (group VI) atom (27). Three different stacking poly-types for the crystallisation of TMDs exist: (i) 1T (tetragonal symmetry), (ii) 2H (hexagonal symmetry) and (iii) 3R (rhombohedral symmetry), and are shown in Figure 2.18 (26, 115). 2H phase is usually the most stable stacking phase of the three. In total, 40 different combinations of TMDs exist (26). The majority of 2D TMDs are semi-conductive and present a possible future material for the fabrication of ultra-small and low power transistors (26, 103). The main physical property distinguishing them from graphene and other 2D materials is the direct band gap of monolayer TMDs (103) and a transition to an indirect band gap for bulk phases, making them an ideal material for high-performance flexible transistors (116).

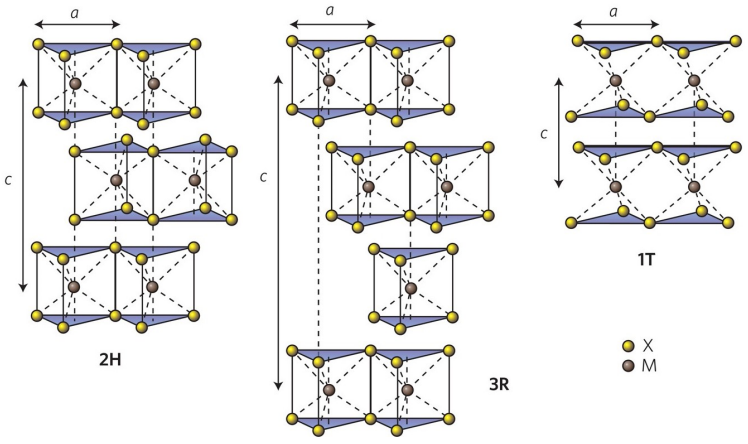

Figure 2.18: Different possible stacking poly-types for the crystallisation of TMDs; (2H) hexagonal symmetry, (3R) rhombohedral symmetry and (1T) tetragonal symmetry (115).

The available methods for obtaining mono and few-layer thick flakes of TMDs include (i) micromechanical exfoliation, (ii) liquid exfoliation, (iii) chemical vapour deposition (CVD), (iv) epitaxial growth, (v) hydrothermal synthesis (26) and alternative methods such as sulfurisation of transition metal foils (117, 118).

2.3.2 Applications of 2D materials

The discovery of graphene has sparked immense research interest in 2D materials and unveiled a vast array of potential applications in electronics, microscopy, bendable devices, resonators, sensing, composites, data storage and friction reduction (35, 105, 119). According to predictions, graphene may replace Si as the base material

for electronic applications (119), and it has already seen some applications in commercial products such as touch panels of smartphones and cooling components (106). As determined by C. Lee et al. (107), graphene is one of the strongest materials ever measured, with an intrinsic strength of a defect-free sheet at the atomic scale of 130 GPa.

Two-dimensional transition metal dichalcogenides have first found their application in the field of nano-electronics, photonics, sensing, energy storage, optoelectronics, etc. (103). Monolayer MoS_2 has shown a potential to be implemented in ultra-sensitive photodetectors, as it possesses a high absorption coefficient under photo-excitation (120). This could be directly applied in light sensing applications, optoelectronic circuits, video recording, biomedical imaging, and spectroscopy (26). Moreover, the extraordinary mechanical properties of MoS_2 (e.g. Young modulus is 270 ± 100 GPa, the average breaking strength is 23 ± 4 GPa at the effective strain between 6 and 11%) make it suitable for the fabrication of flexible electronic applications and as reinforcing elements in composite materials (121). For instance, highly flexible MoS_2 thin-film transistors have already been fabricated on flexible polyimide substrates (122). Gas sensing (e.g. detection of NO concentrations down to 0.8 ppm) is another field for the application of MoS_2 (123).

Besides the broad potential of 2D materials in the field of electronics and their extraordinary electrical and mechanical properties, their layered structure also presents them as suitable solid lubricants for frictional applications. Ultra-low friction has been observed on sputtered MoS_2 in the absence of water vapour and oxygen, which makes it extremely suitable for use in vacuum conditions, such as in space (4). Furthermore, 2D materials, in general, present a particularly interesting material for lubrication of nano-scale contacts, such as nano-scale storage devices, nanocomposites and nano-electro-mechanical systems (NEMS) (35). The tribological properties of TMDs are further discussed in Section 2.4.

2.3.3 Frictional properties of 2D materials

2D materials experience favourable frictional properties, which are a consequence of their unique lamellar structure, as they form strong covalent bonds within layers and only weak van der Waals interactions between the layers (21, 124). Additionally, strong covalent bonding within the layers results in extreme mechanical strength of single layers, making them very wear-resistant (20). The three-layer structure of TMDs offers slightly lower mechanical strength than graphene; nonetheless, they are still among some of the strongest materials known to us (121).

The three most widely studied 2D materials for frictional applications are graphene, Transition Metal Dichalcogenides and h-BN (20, 39, 109, 125). Graphene is an

attractive material for achieving low friction and low wear systems. It can easily be applied to micro and nano-scale contacts and, therefore, be considered a potential low-friction and wear-resistant coating for MEMS/NEMS (20). According to simulations (126) and AFM measurements (127), the frictional force on graphene decreases with the number of layers. It is believed that puckering in front of the AFM tip contributes to friction; with the increase of graphene layers, the interlayer forces reduce puckering and, therefore, lower friction. On the other hand, if the graphene layer is strongly attached to the substrate, the dependence of friction on the number of layers could not be observed (127). Similar characteristics were also observed for other 2D materials (35).

2.3.4 Atomic force microscopy studies on 2D materials

M. Dienwiebel et al. (33) have studied the superlubric properties of a tungsten tip sliding over a graphite surface in dry contact. They have implemented a custom friction force microscope, which allowed them to study forces as low as 15 pN. They have discovered that ultra-low friction between graphite layers results from incommensurability between rotated layers. They observed angle dependence of friction; the sample experienced noticeably higher friction at 0°and 60°, whereas the friction in other orientations remained low and exhibited similar values. The strong angle dependence was attributed to a single graphene flake being attached to the tip during sliding. Their observations were backed by G. Verhoeven et al. (128), who simulated a sliding contact between a single graphene flake (N_{atoms} = 6, 24, 54, 96, 150) and a graphite substrate. The model allowed them to rotate the flake as well as change pulling directions; they found that the misalignment angle between the flakes has a major effect on friction, whereas the effect of pulling direction reduces with increasing misalignment.

K. Miura and S. Kamiya (129) analysed the sliding of a bare tip and a MoS_2 flake on top of a MoS_2 substrate. They observed conservation of Amontons-Coulomb law at the nano-scale for MoS_2 on MoS_2 sliding, whereas the bare tip exhibited either straight stick-slip or zig-zag stick-slip motion when slid along different directions. Similarly, for the flake-on-flake system, they observed that the stacking of sulphur atoms is preserved during sliding, but the absolute values of friction change substantially when sliding in different directions.

C. Lee et al. (35) compared frictional characteristics of four different exfoliated 2D materials – graphene, MoS_2, $NbSe_2$ and h-BN. They observed the decrease in friction with the increase in the number of layers. They attributed the behaviour to mechanical characteristics of layers – compliance of material increases when they approach atomic thickness (flexural rigidity of a material is inversely proportional to its thickness

cubed). They confirmed the hypothesis by comparing the friction of sheets on different substrates; the friction of the material suspended on weakly bonded material (such as SiO_2) was higher than on the materials that are strongly adhered to the substrate (such as mica). Local adhesion between the AFM tip and the sample causes the layer to pucker locally; puckering becomes much more prominent when the sheet becomes thinner. They concluded that the behaviour is characteristic of all atomically thin layers. Furthermore, they discussed that, due to potential stretching of the layers in the scanning direction, it is sometimes more advisable to calculate the relative frictional energy dissipated per unit cell E instead of presenting the average or maximum friction force; this can be achieved by integrating over the forward and backward scans (F_{tr} and F_{re}) and dividing them by the total number of apparent unit cells scanned N:

$$E = \int_0^{x_1} \frac{F_{tr}(x) - F_{re}(x)}{2N} dx. \tag{2.29}$$

L. Fang et al. (36) confirmed the results from Lee et al. (Ref. (35)) and observed a similar trend of increasing friction with the decrease in the number of layers when they used a sharp AFM tip on MoS_2, WS_2 and WSe_2. However, when they used a flattened pre-worn tip, they observed an increase in friction with the increasing number of layers; the exception was the MoS_2 sample, where the friction decreased from monolayer to bilayer and then increased. They presented the total friction as a combination of intrinsic friction per unit area f_i and puckering friction f_p, for a certain number of layers n. Factor c accounts for the puckering strength of the material:

$$f(n) = f_i(n) + cf_p(n). \tag{2.30}$$

With the increase in the contact area, the intrinsic friction also increases, meaning that the effect of puckering becomes less noticeable. The decrease in friction of MoS_2 from monolayer to bilayer was attributed to the high puckering strength of the system.

J. Zekonyte et al. (37, 38) have performed LFM studies on sputtered composite tungsten-sulphur-carbon (W-S-C) and tungsten-sulphur-carbon doped with chromium (W-S-C-Cr) coatings. They observed the non-linear dependence between the load, contact area and frictional force on W-S-C-Cr coatings and utilised the Hertz-plus-offset model to fit the data (37). On W-S-C coatings, they observed the formation of a WS_2 tribolayer at the surface-tip interface, which had consequently peeled off and attached to the tip surface (38). However, on W-S-C-Cr coatings they did not see the formation of WS_2 film on the tip (37). The calculated contact shear strength was relatively low (around 90 MPa for W-S-C-Cr (37) and between 36 and 90 MPa for W-S-C (38)), which they attributed to the formation of a tribo-film in the AFM

contact.

P. Gallagher et al. (130) have studied how the self-assembled environmental adsorbates influence friction on top of a graphene flake. Leaving the flake in an uncontrolled environment results in adsorption and self-assembly of adsorbates into regular stripes with a period of 4-6 nm. They have demonstrated how such structures can be reversibly and precisely manipulated using an AFM tip, creating a patterned surface with varying frictional properties; high normal force and unidirectional sliding can force the adsorbates into a specific orientation, whereas rapid back-and-forth scanning destabilises the surface domains and results in the most stable structure. When scanning over the surface at a lower normal force, the adsorbates are not affected and the sliding behaviour is therefore governed by their orientation. The ability to tune and control frictional behaviour *in-situ* could have an immense effect on the future development of MEMS.

2.3.5 Recent advances in 2D materials

Increasing interest in flexible portable electronic devices presents many challenges in material selection; the materials need to be able to bend, fold and stretch without changing their properties (131, 132). As brittle silicon-based electrical components become unsuitable for flexible applications, scientists have been forced to look for alternative highly elastic materials. Materials such as inorganic ceramics (132), metallic materials (133, 134), conductive polymers (131, 135) and nanomaterials (e.g. carbon nanotubes (136), nanofibres (137) and 2D materials (138)) have previously been explored for fabricating flexible devices. However, the devices manufactured from these materials were only able to withstand very limited amounts of mechanical strains ($< 5\%$) (133, 134), which is relatively low for practical applications. W. Zheng et al. (132) have demonstrated a 'Kirigami' inspired approach to the fabrication of flexible MoS_2 devices, using photolithography and wet etching of large-area monolayer MoS_2 grown by CVD. With this approach, they reached the reversible stretchability of $\sim$15 %.

2.4 Transition metal dichalcogenides as solid lubricants

While many combinations of transition metal and chalcogenide atoms are obtainable, only a certain number of them are thermodynamically stable (139), and even a lower number of them are suitable for friction applications (21, 27). So far, only sulphides (MoS_2 (4, 140) and WS_2 (4)) and selenides ($MoSe_2$ (140), $NbSe_2$ (4, 140) and WSe_2 (141–143)) have been shown to have sufficient frictional characteristics.

TMD coatings show excellent self-lubricating properties in dry air and vacuum, but their tribological performance is severely reduced in the presence of moisture and oxygen (144). Furthermore, the hardness of such coatings is low, and they usually experience poor adhesion to the surface, which, in turn, results in low load-bearing capacity and limits their usability for engineering applications (28). Adding functional groups (i.e. doping) to the TMDs results in changes in the chemical and physical properties of the material (26). Doping the TMD coatings with different metallic or non-metallic elements results in a significant improvement of their properties. Metals, such as Ti, Cr, Pb and Au, have been used to improve the density and strength of TMD films (28). Furthermore, non-metallic elements, mainly C and N, also improved the mechanical properties of the coatings (22, 28, 145). Moreover, co-sputtering of TMDs and amorphous carbon results in combined good frictional properties of TMDs in a vacuum with excellent tribological behaviour of DLC coatings in humid air (28, 145). For instance, aerospace systems are usually subjected to extreme operating conditions; they are exposed to moisture and oxygen during manufacturing and launch, come in contact with atomic oxygen in low orbit and finally operate in the high vacuum in space (146). This calls for the development of self-adaptive 'chameleon' coatings, consisting of three phases, (i) hard carbide (such as WC), (ii) diamond-like carbon and (iii) transition metal dichalcogenide (such as WS_2) (43, 146). In such coatings, the self-adaptive behaviour is driven by friction and the environment. In humid air, a graphite-like transfer film is formed between the contacting bodies, whereas, in a vacuum and dry nitrogen, the TMD phase crystallises in the contact (43).

In this section, we will look at the common coatings deposition techniques, a chronological overview of the commonly used TMD thin-film coatings in tribology and the description of the commonly accepted principle of operation of these coatings.

2.4.1 TMD coating preparation techniques

TMD-based solid lubricants are normally prepared as thick or thin-film coatings (22). Thick-film processes include burnishing (147), electroplating (148) and reverse pulse plating (149), where TMD particles are co-deposited in a composite coating. Thin-film processes include the production of either pure TMD coatings (150), doped TMDs (21, 151) or nano-composite TMD containing coatings (22, 43). Deposition processes for thin TMD coatings are mainly from the physical vapour deposition (PVD) category and include DC (direct current) (38) or r.f (radio frequency) (21, 22, 145) magnetron sputtering and pulsed laser deposition (PLD) (141).

Sputtering is considered to be the most suitable method for the deposition of self-lubricating TMD films and usually results in highly disordered structures (140). Such thin-film coatings have been observed to reorient their basal planes parallel to

the sliding direction when used in a tribo-contact. This phenomenon is further explained in Section 2.4.2.3. The main advantage of sputtering lies in the relative ease of doping the TMD coating by co-sputtering with another material (152).

2.4.2 Common TMD-based thin-film solid lubricants

The use of TMD based thin-film coatings for friction reduction dates back to the 1960s. MoS_2 has been used as a lubricant much sooner (124, 153). Because of its appearance, naturally occurring MoS_2 (molybdenite) was often mistaken for graphite in the past and has, therefore, been used interchangeably (153). In this subsection, we will focus on thin-film coatings produced by vacuum based processes, which are, by far, the most common methods used for the deposition of high-quality TMD coatings today (154). Throughout the years, several different TMD systems have been produced and analysed. The research started with pure coatings; however, the first coatings suffered from poor adhesion and oxidation. Therefore, newer approaches included co-deposition with metallic or non-metallic elements or even more advanced structuring to achieve better performance. This subsection will follow the research progress and will, therefore, present pure and complex structures separately.

2.4.2.1 Pure TMD films

The first MoS_2 films have been produced by using binders, such as resins, and by burnishing the substrates with MoS_2 powder (124, 147, 155). Binding agents are usually undesirable for tribological applications, as the binders that are present in the tribo-chemical reactions in the contact can alter the performance. On the other hand, burnished coatings suffer from poor bonding to the surface, higher coefficient of friction and poor uniformity of coating thickness (147, 155).

Vacuum deposition methods have received intensive interest in the late 1960s, with the pioneering works by T. Spalvins and J.S. Przybyszewski at Lewis Research Center (147, 156). Vacuum physical vapour deposition techniques, such as thermal evaporation and DC sputtering resulted in coatings with stronger adhesion to the substrate, longer endurance life and allowed precise thickness control. T. Spalvins and J. S. Przybyszewski (147, 156) produced some of the first sputtered MoS_2 films, using a triode DC sputtering apparatus. They deposited coatings on different metal substrates and obtained stoichiometric films with strong bonding to the substrate. The coatings were durable and had a coefficient of friction in ultra-high vacuum (UHV) ranging from 0.01 to 0.1, except for copper substrate (156), where they observed incompatibility between the materials in terms of low adherence. T. Spalvins (156) compared the lifetime of MoS_2 coatings prepared by DC sputtering to burnished or

resin bonded commercially available films; they observed much longer lifetimes, despite the much lower thickness of the films.

In the next decade, r.f. sputtering (156–158) and r.f. reactive sputtering (159) became the primary deposition techniques for the deposition of thin MoS_x coatings [2]. The principal advantage of r.f. sputtering is the ability to sputter conductive, semi-conductive or isolating materials and the ability to coat more complex geometries (156). In contrast, DC sputtering can only sputter conductive and semi-conductive materials. Subsequent interest in the materials and further improvement of the deposition techniques resulted in increasingly better coatings.

H. Dimigen et al. (160) observed the effect of coating stoichiometry on the structure of MoS_2 films. They demonstrated that the lowest friction coefficient in dry nitrogen is obtained at a slight sulphur deficiency, while reasonably low friction can be expected down to a 1:1 ratio between Mo and S.

The first use of pure sputtered WS_2 appears in 1970. T. Spalvins (156) reported DC sputtering of MoS_2 and WS_2 films on Ni, Ni-Cr and Nb substrates. They obtained a similar coefficient of friction on MoS_2 and WS_2 in a vacuum (μ = 0.055), together with very good durability of over a million cycles. However, WS_2 film performed much worse in atmospheric conditions with the coefficient of friction reaching 0.22 and coating failure after only 1500 cycles. They attributed the fast degradation of the film to the formation of corrosive H_2SO_4, which forms as a result of the reaction of sulphur and sulphur dioxide in the film with air moisture.

Diselenides have been studied as solid lubricants since the early 1970s (161). However, they have only received limited attention until recently (141–143, 162–164). W. Jamison and S. Cosgrove (161) have investigated several bulk disulphides and diselenides of transition metals from the 2^{nd} and 3^{rd} rows, obtained from commercial sources or synthesised in the lab by heating powders of elements in the vacuum. They performed the tribotests under environmental conditions and obtained a stable low coefficient of friction on $NbSe_2$, MoS_2, $MoSe_2$, WS_2 and WSe_2. The obtained values of coefficient of friction (μ = 0.037 - 0.075) are comparable with sputtered films in the vacuum, indicating that oxygen and humidity inhibit recrystallisation of the sputtered film and do not directly increase friction between the layers. Furthermore, their results show that the best lubricating performance of bulk TMD crystals is achieved with materials that have the 2H structure.

E. Bergmann et al. (140) presented the first comparative study of frictional properties of sputter-deposited TMD solid lubricants, namely MoS_2, WS_2, $MoSe_2$, $MoTe_2$, $NbSe_2$ and $TaSe_2$. They used the same deposition procedure for all the coatings, which was expected to eliminate the influence of the deposition procedure on the coating quality.

[2] subscript 'x' stands for the ratio of sulphur in the final structure of the coating

They noted that the comparison of tribological properties with previously available deposition procedures was not possible due to differences in the shape and size of the particles or incompatibility with the binders. They reported that there is a clear correlation between coating crystallinity and frictional behaviour of the coatings and that the two very important properties in evaluating TMDs tribological properties are adhesion to the substrate and coating brittleness. Therefore, they conclude that as long as the tribological interaction does not interfere with the substrate/coating interface, we can expect good solid lubricant properties from any sputtered TMD included in the study. However, only MoS_2, $MoSe_2$ and $NbSe_2$ can be considered consistently good solid lubricants on any substrate. On the other hand, WS_2 appeared incompatible with some substrates, while performing well with the others. They also proposed the idea of the reorientation of crystallites parallel to the surface during sliding and local recrystallisation due to frictional heat.

J.R. Lince and P.D. Fleischauer (41) investigated the idea of reorientation of crystallites during sliding further by employing X-Ray diffraction (XRD) and transition electron microscopy (TEM) analysis on the wear track. They observed that when the film is worn in, the only major change in crystallinity is the reorientation of crystallites. XRD analysis has shown that on the as-deposited films the (h k 0) crystallite planes were oriented parallel with the substrate surface, while the (0 0 1) plane was constrained perpendicularly to the surface. Analysis of sliding wear has shown that the reorientation of crystallites occurs during sliding, as the basal planes of the crystallites become oriented parallel to the surface plane.

E. W. Roberts (4) reviewed the applicability of several thin solid lubricant films in space, including MoS_2 and soft metals. They pointed out that the main disadvantage of all thin films may be their limited durability. Once the films are worn through, they cannot be replaced, which significantly impacts the lifetime of the components the films are applied to. Therefore, only low-duty components with short-to-medium term duration can be lubricated with such a mechanism. However, proper substrate selection can significantly increase adhesion to the substrate and consequently prolong the lifetime of the films. They assessed the possibility of applying thin solid lubricating films to ball bearings, gears and purely sliding mechanisms, such as screws, cams, journal bearings and slides. For gears lubricated with MoS_2, they reported significant improvement in gear transmission efficiencies and slightly reduced lifetime compared to lead lubricated gears. In the case of ball bearings, the lowest torque was obtained when only races were lubricated by MoS_2. On the other hand, coating the balls resulted in a slight increase in bearing torque and a five-fold increase in bearing lifetime. They concluded that MoS_2 would be the most suitable candidate for purely sliding components, as it provides the highest durability under pure sliding.

In the 1990s, J. M. Martin et al. (108) and C. Donnet et al. (165) achieved super-low friction with r.f. sputtered MoS_2 coatings in ultra-high vacuum (μ = 0.002) and dry nitrogen (μ = 0.003). They compared the UHV results with the coefficient in high vacuum, which was 0.013, and in air, which was 0.150. The onset of super-low friction was attributed to superlubric sliding between the basal planes. They attributed the mechanism of superlubricity to frictional anisotropy – incommensurate sliding of contacting surfaces due to a certain misfit angle. The main criterion for the onset of such behaviour is the absence of reactive species – therefore, only UHV and nitrogen environments result in extremely low coefficients of friction.

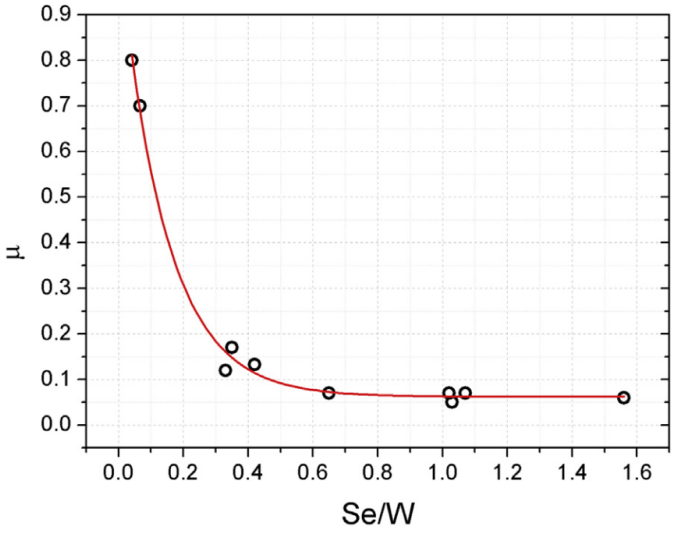

Figure 2.19: The effect of stoichiometry on the frictional properties of the W-Se system in ambient air. The Se/W ratio as low as 0.6 is sufficient for achieving coefficient friction below 0.1 (142).

D.V. Shtansky et al. (141) analysed WSe_x coatings deposited by pulsed laser deposition (PLD). The results showed that the WSe_x crystallites within these coatings were oriented either parallel or perpendicular to the substrate surface. They discovered that double-layer coatings (WSe_x/TiSiN, WSe_x/TiC, WSe_x/TiCN) achieve superior tribological properties in air and underwater. The presence of a hard under-layer was shown to be necessary for achieving low friction. A possible reorientation of WSe_2 nano-crystallites was proposed by the authors but was not assessed further.

Similar to the work of H. Dimigen et al. (160), S. Dominguez-Meister et al. (142) indicated that it is not necessary to produce stoichiometric WSe_2 coatings to achieve ultra-low friction; as shown in Figure 2.19, a Se-W ratio of 0.6 is adequate to reduce friction coefficient in ambient air below 0.1. The coatings exhibited decreased sensitivity to humidity and good wear resistance. Wear resistance can be improved by modifying the coating morphology or carbon incorporation. Similarly to Ref. (141), they proposed the reorientation of WSe_2 basal planes. The Raman analysis showed the presence of WSe_2 peaks, but the authors did not assess the hypothesis further (142).

2.4.2.2 Composite, alloyed and doped structures

TMD coatings co-deposited with metals: B.C. Stupp (166) analysed a wide array of co-sputtered metals and alloys with MoS_2 – aluminium, brass, bronze, chromium, cobalt, molybdenum, nickel, platinum, gold, silver, tantalum and tungsten. They have found that some metal additives can increase the size of crystallites, reduce and stabilise friction and improve endurance. The best improvements were reached at 5-7 % concentration of the co-deposited metal. Nickel and tantalum performed the best out of the metals tested. However, the authors presented no exact mechanism for the improvement of tribological properties.

T. Spalvins (167) reported MoS_2 films co-sputtered with gold (5 wt.% Au). The films resulted in a lower friction coefficient, a higher degree of frictional stability and less wear debris than pure MoS_2 films. Better tribological characteristics were attributed to the effective film thickness and more densely packed columnar structure.

D. Teer et al. (168) prepared composite titanium/MoS_2 coatings (MoST^{TM}) by closed field magnetron sputtering with the purpose of improving cutting tools. Due to the deposition procedure (rotating substrates between three MoS_2 and one Ti target (168)), the MoST^{TM} coating was initially assumed to be a multilayer coating with alternating layers of MoS_2 and titanium. However, a later analysis by XRD and TEM did not show any evidence of the multilayered structure (169). However, the addition of titanium has resulted in denser and harder coatings than pure MoS_2, while the coefficient of friction remained low. Furthermore, the titanium-containing coatings showed improved wear resistance and reduced susceptibility to humidity (168).

V. Fox et al. (169) have continued working on and further improved the MoST^{TM} coatings. They have achieved even better wear resistance and have tested the coatings in several industrial applications, such as the ejector pins and dry drills. TEM analysis of the coatings revealed that the coatings were quasi-amorphous, and no crystalline structure could have been observed. Furthermore, the authors deposited a forced multilayer coating, which resulted in inferior tribological properties. XRD on these multilayers showed a titanium peak, which indicated that if titanium is present as atomic titanium in the coating it can be detected. However, XRD analysis on MoST^{TM} did not show atomic titanium within the coating. They have also predicted that the MoS_2 lattice may be distorted and concluded that a mixed molybdenum-titanium disulphide or a solid solution of titanium in MoS_2 could have been formed.

X. Wang et al. (170) analysed composite MoST^{TM} coatings with different titanium contents, deposited by DC magnetron sputtering. The composite coatings consisted of nanocrystalline and amorphous phases, with the degree of crystallisation increasing with titanium content. The hardness and tribological properties of the coatings increased with the increasing titanium content and reached the maximum values at

19.5 at.% Ti. A similar study by X. Qin et al. (171), in which they utilised a high-power impulse magnetron sputtering on a Ti-target and DC magnetron sputtering on a MoS_2 target, showed comparable results. The hardness and tribological properties increased with increasing titanium content up to 13.5 at.% Ti. Above that point, the hardness decreased slightly, while the coating resulted in lubrication failure.

S. Xu et al. (172) showed that the presence of silver in WS_2 coatings changes morphology from amorphous to nanocrystalline. Furthermore, the presence of silver improved adhesion and helped with the formation and rearrangement of the compact transfer layer. However, high levels of silver resulted in worsened adhesion and tribological properties due to film brittleness.

S. Xu et al. (151) studied the performance of nickel doped WS_2 coatings. They reported an improved S/W ratio with the presence of Ni. The coatings showed low hardness but had a high tendency to form a lubricating transfer layer and exhibited low brittleness and good wear life in vacuum conditions.

TMD coatings co-deposited with carbon and nitrogen: As discussed earlier, the good performance of TMD coatings in a vacuum makes them a suitable coating material for sliding applications in space (4). However, before the components are introduced into their standard environment in space, they may have to endure some operation in the atmosphere, where the performance of TMDs is poor due to oxidation and consequent rapid deterioration of the coating. A. A. Voevodin and J. S. Zabinski (43) presented the coatings with 'chameleon' surface adaptation, combining the good performance of amorphous carbon in environmental conditions with low friction of TMDs in a vacuum. They designed a composite W-S-C system, consisting of dichalcogenide and nanocrystalline carbon phases encapsulated in an amorphous DLC matrix. The coatings were grown by either magnetron assisted pulsed laser deposition or by laser ablation of a composite graphite/WS_2 target (146). They proposed a mechanism where friction would induce readjustment of the structure – graphite-like transfer film is the dominant surface chemistry in ambient environments, and recrystallised hexagonal WS_2 is formed in a vacuum. They have demonstrated the recovery behaviour, by alternating between dry N_2 and humid air environments and correlated both trends to WS_2 and DLC lubrication, respectively.

A. Nossa et al. (173) analysed the improvements in hardness of r.f. sputtered WS_2 films when alloyed with carbon and nitrogen. Increased hardness was attributed to the densification of the morphology, decrease of grain size and precipitation of harder phases. Additionally, a combination of carbon and nitrogen with the titanium interlayer resulted in the formation of either TiC or TiN, which increased adhesion and resulted in a significant reduction of wear rates.

T. Polcar et al. (174) deposited carbon-doped $MoSe_2$ coatings using r.f. magnetron

sputtering. The addition of carbon significantly improved hardness compared to pure $MoSe_2$. Increasing carbon content improved Se/Mo ratio, reaching an ideal Se/Mo ratio of 2.0 at 68 at.% C. The structure of the coating consisted of nanometre-sized $MoSe_2$ grains embedded in the carbon matrix, without any trace of carbides. The Mo-Se-C coatings exhibited low friction and wear rates, which decreased with increasing load (28).

T. Yaqub et al. (175) used DC magnetron sputtering to deposit Mo-Se-C coatings from separate $MoSe_2$ and C targets, in an attempt toward an industrial up-scaling of the deposition procedure. They found the best quality of the coating when a negative bias was applied to the substrate; the produced coatings displayed a slightly lower sub-stoichiometric Se/Mo ratio but resulted in a more compact and thus harder structure. The coatings with 90V applied bias showed superior tribological properties in humid air and dry nitrogen environments, with the coefficient of friction as low as 0.025 and a specific wear rate of 2.4e-8 mm^3/Nm in a vacuum. In the subsequent studies (176, 177), they compared tribological properties of DC and r.f. magnetron sputtered Mo-Se-C coatings. In both cases, the addition of carbon reduced porosity and slightly reduced Se/Mo ratio, with a lower Se/Mo ratio observed on r.f. sputtered samples. They were able to obtain consistently low coefficients of friction and wear rates at different loading conditions and environments (vacuum and humid air), regardless of deposition method, indicating a great potential for Mo-Se-C coatings to be used as a universal dry lubricant. T. Vuchkov et al. (178) have presented yet another approach to the deposition of Mo-Se-C coatings aimed at the industrial scale - closed-field unbalanced magnetron sputtering. The coatings produced by this method had similar tribological and mechanical properties to previously reported Mo-Se-C systems, with an added possibility to coat more complex 3D geometries commonly found in mechanical systems.

T. Polcar et al. (179) have compared the tribological behaviour of two self-lubricating systems – r.f. sputtered W-S-C and Mo-Se-C. Unlike Mo-Se-C, W-S-C contained traces of WC. Similarly to A. A. Voevodin and J. S. Zabinski (43), they alternated the environment between dry nitrogen and humid air. However, unlike reported in Ref. (43), they have not observed significant graphitisation on the W-S-C coating or any increased carbon content in either the wear track or the counter-body. They observed TMD tribolayer formation in all conditions and suggested that the thin TMD tribolayer is the main factor affecting the frictional properties of sputtered TMD-C coatings. T. Yaqub et al. (180) have observed similar behaviour on Mo-Se-C coatings with low carbon content, where they concluded that low friction of the analysed system is governed by $MoSe_2$ tribofilm formation in all environments. Unlike T. Polcar et al. (179) and A.A. Voevodin and J. S. Zabinski (43), they did not alternate the environment during the experiment and compared the results of different tests performed in separate environments.

M. Evaristo et al. (162, 163) have shown that sputtered W-Se-C coatings have very similar frictional properties to other TMD coatings alloyed with carbon. Friction tests in air showed a decrease in friction with increased contact pressures, which is characteristic of pure and C-alloyed TMD films. The obtained friction coefficient for these films was as low as 0.05. However, pure W-Se sputtered films peeled off almost immediately upon starting the tribotest (162).

T. Vuchkov et al. (181) have reported that substrate placement in the sputtering chamber has an important role in the structure, stoichiometry, mechanical and tribological properties of W-S-C coatings, thus presenting a challenge when coating larger objects. They determined that the W/S ratio of at least 1.5 needs to be achieved for sufficient tribological performance.

T. Hudec et al. (182) have analysed Mo-S-N coatings with increasing content of nitrogen. They discovered that doping MoS_2 with nitrogen results in significantly harder and denser coatings, with better wear resistance and similar frictional behaviour in humid air than MoS_2. Higher percentages of nitrogen result in the nanocrystalline structure of MoS_2 grains embedded in a nitrogen-molybdenum matrix, whereas lower nitrogen content produces fully amorphous coatings. Similarly, they observed improved tribological performance of doped coatings in nitrogen and vacuum environments and at elevated temperatures (183). Mo-Se-N coatings showed a similar increase in hardness and densification of the coatings, with an even lower coefficient of friction (184). On the other hand, K. H. Kannur et al. (185) found Mo-S-N coatings deposited by reactive DC magnetron sputtering to only perform well in the vacuum, whereas they observed a much higher coefficient of friction and increased wear rates in air, where oxidation and moisture prevented the formation of a protective tribofilm.

Multilayered coatings: S. Watanabe et al. (186, 187) presented multilayered WS_2/MoS_2 films prepared by r.f. magnetron sputtering. The thickness of each layer was 5 nm, and the total thickness of the coating reached 500 nm. Such super-lattice structured films are expected to show good mechanical properties, namely high hardness and stiffness, which result in reduced friction and improved endurance. They observed a significant reduction of wear rates in the air compared to a single layer WS_2 or MoS_2 by approximately seven times while sustaining a low coefficient of friction of 0.05 until the end (186). Similar trends were observed in the vacuum and at elevated temperatures, where the multilayered films significantly outperformed single layers in all tests (187).

2.4.2.3 Friction induced reorientation of basal planes

Observations of the wear tracks by transmission electron microscopy (TEM) have indicated that the deposited thin TMD films undergo a wear-induced reorientation of basal planes in the first cycles of sliding (31). As shown in Figure 2.20, a buffer layer (c) is formed between the bulk film (d) and the counter body (a). Effective lubrication is achieved due to the complex relative motion between the crystallites in the buffer layer (31).

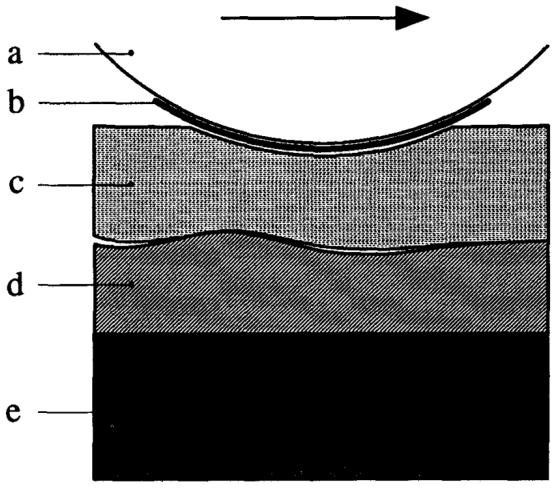

Figure 2.20: MoS_2 film under sliding. The figure presents five main elements of a dry lubricated contact: a counter body (a), a tribofilm (b), a buffer layer (c), bulk coating (d) and the substrate (e) (31).

J. S. Zabinski et al. (42) compared the effects of thermal and laser annealing to the mechanically induced recrystallisation of WS_2, using Raman spectroscopy and X-Ray Diffraction (XRD). They concluded that mechanical energy input through rubbing induces crystallisation similarly to the thermal energy input from thermal or laser annealing.

2.5 Summary

In this literature review, we have covered the principles of nano-scale friction, contact models, atomic force microscopy, transition metal dichalcogenides, the current state of the art of TMD-based thin-film coatings and the mechanism of lubrication with thin-film coatings.

A significant number of contact models have been developed over the years for different types of contacts. The most relevant ones were reviewed in Section 2.1.4. The contact models were used in data analysis, for fitting the measured AFM data to extract useful information about the samples and sliding properties. The correct

contact model depends on the contact conditions. The hertz-plus-offset model is used for monolayers in the air (Chapter 4, Chapter 5) and multilayers in water (Chapter 6). The models are also applied in the analysis of the multilayer sliding in the air (Chapter 5). The numerical model for simulating the contact behaviour is built on top of the Hertz contact model and the new model for fitting the data is formulated as a modification of the Hertz-plus-offset model.

Atomic force microscopy (AFM) is a relatively new measurement technique. It allows probing the surface properties specifically, which gives it an advantage over other microscopy and spectroscopy techniques, where the resulting signal is likely to include information from below the surface. It has a very high vertical resolution, as it can resolve height differences as low as 0.1 nm. This makes AFM an ideal technique to study atomically thin 2D materials. Understanding how the AFM works, how different modes of operation can be applied and how to identify different types of artefacts are necessary for the successful operation and setup. AFM was used in all chapters of this work.

More than 150 different 2D materials have already been synthesised, among which graphene, transition metal dichalcogenides (TMDs) and h-BN are the most widely studied for frictional applications. A combination of high layer strength and weak van der Waals interaction between the layers allows easy sliding. The inertness of the layer faces allows low friction between the monolayer and another material. TMDs are the main focus of study in this work.

A lot of improvements have been done on the thin film coatings in the past years, and it is well known that reoriented/recrystallised tribofilm is formed in a tribo-contact. However, the precise mechanisms that occur at the atomic level and cause tribofilm formation remain unknown. Furthermore, only a limited number of nanotribological studies have been done on the TMD tribofilms, and atomic force microscopy is still relatively rarely used to study the wear tracks after the tribotests. As AFM offers non-destructive surface probing, it is suited to study the properties of low-friction tribofilms within the wear tracks and the coverage of such tribofilms.

Chapter 3

Materials and Methodology

3.1 Materials

A range of different pure TMD and TMD-based materials were used in this work. In the first part (Chapters 4-6), mono and multilayered fully crystalline flakes were used, which were deposited by chemical vapour deposition (CVD). In the second part (Chapter 7), composite coatings doped with carbon (TMD-C) were deposited by DC magnetron sputtering. Additionally, MoS_2 coatings in Appendix D were deposited by r.f. magnetron sputtering.

3.1.1 Sample preparation and deposition

Four different TMD monolayers (MoS_2, WS_2, $MoSe_2$, WSe_2) were deposited by chemical vapour deposition (CVD) on Si substrates coated with 300 nm SiO_2. The reaction was operated under atmospheric pressure in a 3 cm diameter quartz tube. The SiO_2/Si substrates were loaded on a boat containing MoO_3 (or WO_3) (Alfa Aescar, 99.9995% purity) and placed in the tube centre before the reaction. NaCl was added during some depositions to reduce the high melting point of WO_3 and facilitate vaporisation. Afterwards, another boat with sulphur (or selenium) (Alfa Aescar, 99.9995% purity) was placed upstream. After a 10-minute purge with 300 standard cubic centimetres per minute (sccm) Ar (or H_2/Ar) (BOC, 99.999% pure with additional purifications), the flow rate was decreased to 30 sccm, and the furnace was subsequently programmed (T_1 in Table 3.1) to heat substrates. In the meantime, sulphur (or selenium) was heated (T_2 in Table 3.1), allowing its vapour to be transported to the substrate. After 15 minutes of deposition, the furnace was switched off for a natural cooling-down. The samples were mostly monolayer flakes, with WS_2 and WSe_2 also containing some multilayer regions. The monolayers were used in

Chapter 4 and multilayers in Chapter 6, whereas Chapter 5 contains data measured on both monolayers and bilayers.

Table 3.1: CVD deposition parameters

Material	Precursors		Temperature for precursors T_1(°C)	T_2(°C)	Gas inlet	Note
MoS_2	MoO_3	S	700	200	Ar	
$MoSe_2$	MoO_3	Se	750	300	H_2/Ar	
WS_2	WO_3	S	900	200	Ar	NaCl used
WSe_2	WO_3	Se	900	300	H_2/Ar	

Composite W-S-C coatings were used in the final part of this work instead. The coatings were deposited by DC magnetron sputtering (Teer, UK) on polished tungsten carbide discs. The substrates were cleaned before the coating deposition, by establishing the plasma close to the substrate electrode for 30 minutes. Four targets were used: chromium (Cr, purity 99,9%), two carbon/graphite targets (C, purity 99.6%) and one WS_2 target (purity 99%). After plasma etching, the substrates were first coated by a thin bonding layer, consisting of Cr with an increasing amount of W-S-C, with the final layer deposited at a pressure of 0.3 Pa and an applied substrate bias of -50 V. Finally, the W-S-C layer was deposited at a pressure of 0.45 Pa (without bias) by using two graphite and one WS_2 target. The thickness of the functional W-S-C coating with homogeneous composition was 1 µm.

MoS_2 coatings were deposited by non-reactive r.f. magnetron sputtering (AJA International, Inc., United States) from a single MoS_2 target onto polished 100Cr6 steel samples in an argon atmosphere at 10 mTorr. Sputtering power was 80 W, with no applied bias. Before the deposition, substrates were sputter cleaned for 45 min by plasma etching. The final thickness of the coatings was 1 µm.

3.1.2 Methodology

Due to a range of specific characterisation techniques and different equipment used for separate studies, the exact description of the methodology and measurement parameters is included in the specific chapters. Only an overview of the sample characterisation techniques and macro and nanotribological techniques is summarised here.

3.1.2.1 Sample characterisation

Raman spectroscopy (InVia Raman Spectrometer, Renishaw, UK and XPlora, Horiba Scientific, France, both excited at $\lambda_{laser} = 532\,\text{nm}$) has been used to determine the

sample structure (layer thickness, composition, crystallinity) of TMD layers in Chapter 4 and Chapter 7. Photoluminescence (PL, InVia Raman Spectrometer) spectroscopy and X-Ray photoelectron spectroscopy (XPS, Thermo Scientific Theta Probe XPS System MC03, Al Kα source) were employed to further examine the crystal quality and chemical composition of the monolayer flakes in Chapter 4. Scanning electron microscopy (SEM, FEI Verios 460L and FEI Helios Nanolab, Thermo Fisher Scientific, United States) was used to characterise the topography of the wear tracks in Chapter 7. The cross-sections of the selected areas on the wear tracks in Chapter 7 were analysed by transmission electron microscopy (TEM, FEI Titan Themis Cubed, Thermo Fisher Scientific, United States).

Atomic force microscopy (AFM) was used to obtain the majority of the measurements in this work. Images were predominantly obtained in contact mode using soft probes unless otherwise noted. Friction force measurements were performed exclusively in contact mode, using both soft and stiff probes (see the following section for more details). Two different AFM systems were used (Agilent/Keysight AFM5500, USA and ND-MDT nTegra, Russia). The Agilent system was used to acquire the majority of the topographic images and friction measurements in Chapter 4, Chapter 5 and Chapter 7, whereas the superior sub-nanometre resolution of the ND-MDT system allowed for measuring atomic-scale friction in Chapter 6.

3.1.2.2 Tribology and nanotribology

Macro-scale tests on the composite W-S-C coatings in Chapter 7 and MoS_2 coatings in Appendix D were performed in a vacuum on a custom-built unidirectional ball-on-disk tribometer (VacTrib03, Advanced Materials Group, Czech Republic).

Nano-scale friction measurements were performed by lateral force microscopy (LFM) on a commercial AFM system (Agilent AFM5500, USA), using commercial probes (NanoSensors PPP-LFMR and PPP-NCHR). Normal forces were calibrated before each experiment using the built-in thermal-K method. Lateral forces were calibrated using the Wedge calibration method (95).

Atomic-scale measurements were performed using a different AFM system (ND-MDT nTegra, Russia). The experiments were operated in an aqueous environment to reduce adhesion between the tip and the surface. Both the sample and the probe were fully submerged in water. Commercial ND-MDT CSG01 contact mode probes were used. Normal forces were calibrated according to the Sader method, using a built-in script, and lateral forces according to the Wedge calibration method (95).

Chapter 4

Nanotribology of TMD flakes

4.1 Introduction

The experimental discovery of graphene in 2004 (104) and increased fabrication capabilities in the following years (188, 189) have led to an increasing research interest related to atomically thin 2D nanomaterials, including carbon compounds, transition metal dichalcogenides (TMDs) and hexagonal boron nitride (105). Besides their more conventional applications in nano-electronics, photonics and sensing (26, 103, 123), 2D nanomaterials have also emerged as a promising candidate for modifying friction at the nano-scale (190). In particular, the undesirable properties of Si-Si contacts present operational challenges in the performance of micro/nano-electro-mechanical systems (MEMS/NEMS) (13, 191–193). Coating the contacting surfaces of such systems with 2D materials can provide a solution due to their favourable adhesional and frictional properties (194). Understanding the behaviour of such materials within the small-scale contacts, namely the effects of friction and adhesion on their performance and wear, will help with the further development of related materials and with the design of new components and systems incorporating them.

It was not until recently (35) that the TMDs have started receiving increasing interest as a material for reducing friction at the nano-scale. The low friction of bulk and multilayered TMD systems is a result of their lamellar structure, where weak van der Waals forces between the layers provide low shear resistance (21, 124). On the other hand, low friction between a TMD surface and a second body results from surface inertness (195).

Most of the previous nanotribological studies on 2D materials (33–36) have only focused on a specific normal force and solely observed the trends within the same sample, such as the influence of the number of layers on friction (35, 36), sample orientation (33), or the effect of substrate morphology (125). A recent review presented

an extensive and comprehensive insight into the macro and nano-scale frictional properties of MoS_2 (109). However, transition metal dichalcogenides beyond MoS_2 are still rarely explored in terms of their nano-scale frictional properties. Despite recent attempts (196, 197), an in-depth quantitative comparison between different TMD monolayers beyond MoS_2 is still lacking in the literature. M. Vazirisereshk et al. (196) have studied the role of the chalcogen atom on the friction of bulk and monolayer TMDs and found that atoms with a higher atomic number contribute to lower friction in a vacuum environment.

In this chapter, we have utilised the AFM to study how the elemental composition of the TMD monolayer (metal and chalcogen atoms) influences nano-scale friction between a bare silicon tip and the TMD surface. Because of different tools, methods, equipment, and sample preparation being used in various studies, a direct quantitative comparison between the frictional response of TMD materials from different sources of literature is almost impossible. We used bare silicon tips, which offer a good standard depiction of a nano-scale tribo-system and accurately represent a contact in MEMS (193). Furthermore, we examined the influence of sliding speed on nano-scale friction and compared how wear resistance and maximum applicable load differ between the TMD sample and the bare SiO_2 substrate.

To quantitatively compare the data of different TMD samples, we deposited MoS_2, WS_2, $MoSe_2$ and WSe_2 monolayer flakes by an almost identical CVD procedure and performed the analysis using the same AFM setup (i.e. using the same probe and performing the measurements in a single session), thus minimising the external effects on the measurement. The quantitative values of load-dependent friction behaviour on the three major TMD monolayers ($MoSe_2$, WS_2 and WSe_2) are analysed according to the Hertz-plus-offset model (73), which has been previously successfully applied to study nano-scale frictional properties and contact shear strength of many different materials (see Table 4.1). The MoS_2 sample, on the other hand, suffered from extensive surface contamination. Despite the best attempts to remove the adsorbed surface contaminants without damaging the sample, the contamination persisted. Therefore, the MoS_2 sample was excluded from the main comparison and quantitative analysis using the Hertz-plus-offset model.

The work presented in this chapter was published in *Applied Surface Science* (Ref. (198)). The sample preparation and chemical analysis were performed by Dr He Wang (*University of Southampton*).

Table 4.1: Nano-frictional properties of different materials from literature

Material	Atmosphere	$\tilde{\mu}$ [1] ($GPa^{1/3}$)	τ [2] (MPa)	Ref.
Amorphous carbon	Air	0.450±0.042	/	(73)
Amorphous carbon	Argon	0.158±0.022	/	(73)
Diamond	Air	0.158±0.061	/	(73)
Diamond	Argon	0.263±0.060	/	(73)
C60	Argon	0.67±0.22	/	(73)
HOPG	Argon	0.0012±0.0009	/	(73)
GeS	Air	0.50±0.21	/	(74)
Mica	Air	0.14±0.05	/	(74)
Mica	Argon	0.16±0.04	/	(74)
W-S-C coating	Air	/	36-91.2	(38)
W-S-C-Cr coating	Air	/	71-99.3	(37)

[1] Effective coefficient of friction for point-like contact
[2] Contact shear strength

4.2 Experimental details

4.2.1 Characterisation of synthesised TMDs

An optical microscope (Nikon LV200) and AFM (Agilent 5500, Agilent Technologies, USA) were employed to observe the surface morphology. The thickness of the flakes was measured in non-contact AFM mode. Raman spectroscopy (InVia Raman Spectrometer, excited with 532 nm laser) was used to characterise the vibrational modes as well as photoluminescence (PL) spectra, and X-ray photoelectron spectroscopy (XPS, Thermo Scientific Theta Probe XPS System MC03, Al Kα source) was used to analyse the chemical composition.

4.2.2 Friction and nano-scale wear measurement by AFM

Surface friction maps and corresponding topography images were collected simultaneously by AFM (Agilent 5500, Agilent Technologies, USA) in contact mode. Frictional maps were used to examine the qualitative frictional contrast between the sample and the substrate. We used a PPP-LFMR (Nanosensors, USA) probe at low contact loads (up to 30 nN) and 1 ln/s scan rate.

Load-dependent frictional behaviour was measured using the same setup. A single PPP-LFMR probe was used to perform all the measurements to reduce measurement error due to discrepancies in the probe shape, calibration factors, or probe mounting. The measurements were performed in atmospheric conditions in a single session, thus minimising the influence of air humidity and temperatures on the final results. The

experiments with incrementally increasing or decreasing normal load were performed at three different sliding speeds (0.5, 1.0 and 1.5 µm s^{-1}) over a 0.5 x 0.5 μm^2 area, at the resolution of 256 x 256 px. A total of 10 different loads were used, including negative loads to study the behaviour between the tip and the sample in the adhesive regime (see Table 4.2 for the range of minimum and maximum applied loads per sample). At least 25 lines were scanned at each applied load. The value of minimum load was determined empirically on each sample, as the lowest load at which the tip did not lose contact with the surface during continuous sliding. Note that the value of applied negative load had to be lower than the force of adhesion to ensure that the tip does not snap out of contact due to local differences in adhesion, contact area, or surface roughness. The normal spring constant (k = 0.109 N m^{-1}) was determined in-situ using a built-in thermal noise method (199). Lateral forces were calibrated according to the wedge calibration method (95) on commercial TGF11 (µMasch, Bulgaria) gratings (calibration factor α = 278 nN V^{-1}). Friction was evaluated as a difference between trace and retrace signals divided by two. We developed a custom script to automatically control the contact loads and sliding speeds during the experiments.

Table 4.2: LFM experimental parameters

Sample	F_{min} (nN)	F_{max} (nN)	$F_{pull-off}$ (nN)
WS_2	$-0.6F_{pull-off}$	30	7.5
$MoSe_2$	$-0.7F_{pull-off}$	30	11.4
WSe_2	$-0.7F_{pull-off}$	30	7.5

Nano-scale wear was evaluated in terms of surface damage and wear caused to the tip. We used stiffer probes (PPP-NCH, k = 51 N m^{-1}), which allowed reaching the much higher contact pressure required to induce changes at the surface. The loads up to 10 µN were used. Wear measurements were performed over a 0.75 x 0.75 μm^2 scan size, and the surface topography was obtained after each scan over a larger area (1.5 x 1.5 μm^2) at a lower load. As a reference, the scans on the TMD flakes were compared to sliding on SiO_2.

4.3 Results

4.3.1 Sample characterisation

WS_2: The sizes of the WS_2 nanoflakes deposited on SiO_2/Si substrate by the CVD method reached up to ∼10 µm. Raman spectrum, displayed in Figure 4.1a_0, shows the 353.1 cm^{-1} 2LA and 420.1 cm^{-1} A_{1g} peaks, which are characteristic for monolayers. A slight red shift of 2LA and a blue shift of A_{1g} mode would be expected at a higher

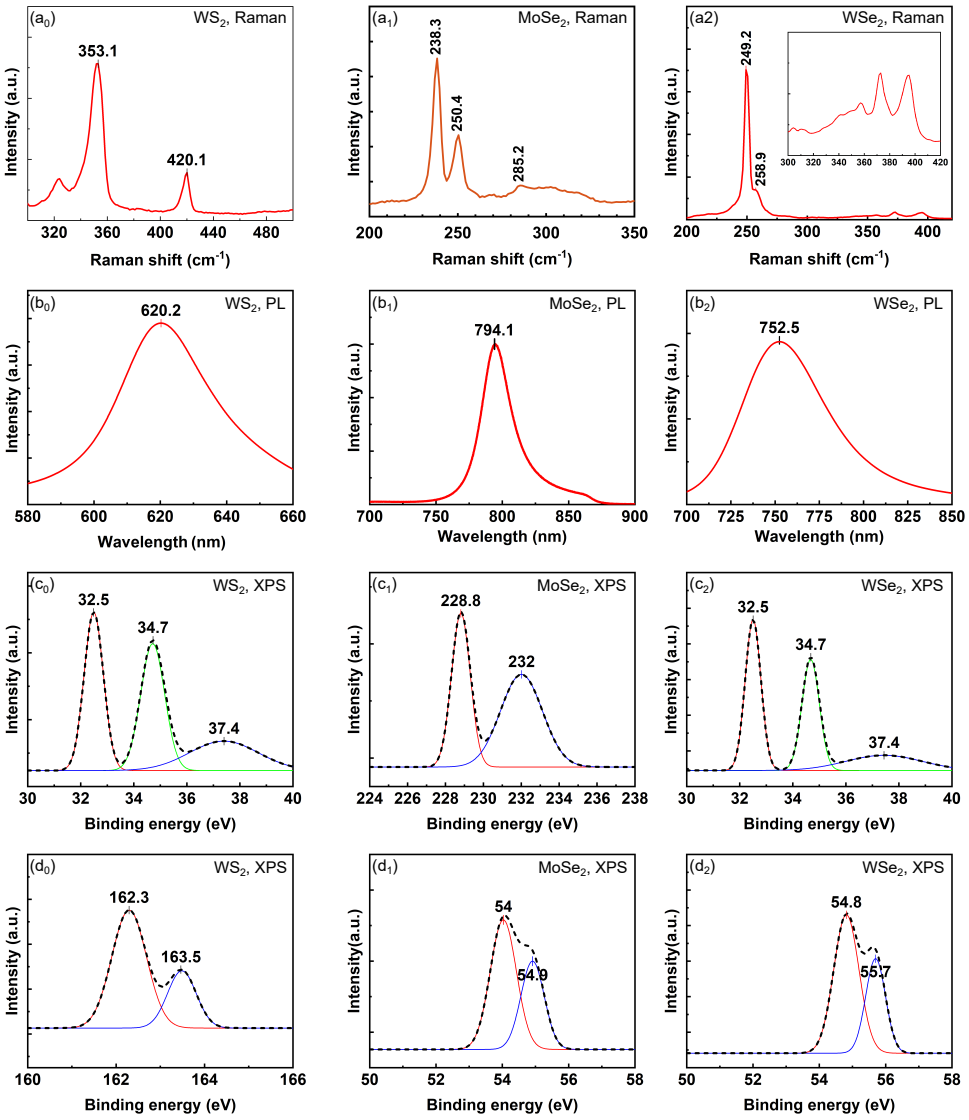

Figure 4.1: Characterisation of TMD nanoflakes. (a) Raman spectra and (b) PL spectra with 532 nm laser excitation. XPS spectra of the corresponding metal (c) and chalcogen (d) orbitals.

layer number (200, 201). In addition, the PL spectrum in Figure 4.1b_0 shows an emission peak at 620.2 nm, indicating monolayer WS_2.

According to the XPS spectra of monolayer WS_2 flakes in Figures 4.1c_0 and d_0, the W 4f peaks at 34.7 and 32.5 eV are assigned to the $4f_{5/2}$ and $4f_{7/2}$ orbitals of WS_2, respectively (202, 203); the W 5p core level at 37.6 eV suggests the existence of W^{6+}, likely residual WO_3 on the as-deposited sample (204). 163.5 and 162.3 eV peaks belong to the S doublets: $2p_{1/2}$ and $2p_{3/2}$ (202). All the binding energies are indicative of WS_2 crystal, and the atomic ratio between S and W is ∼2:1.

$MoSe_2$: The lateral sizes of the CVD deposited $MoSe_2$ nanoflakes were between 10 and 30 µm. Raman peaks at 238.3 cm^{-1} and 285.2 cm^{-1} (Figure 4.1a_1) were related to A_{1g} and E_{2g} modes, respectively (205, 206). Additionally, we observed an unknown

peak at 250.4 cm^{-1}. This peak can be often seen in the literature (see (206), (207) and (208)), but the authors did not comment on it. The 794.1 nm peak in the PL spectrum (Figure 4.1b_1) belongs to monolayer $MoSe_2$ (209, 210).

As evident from the XPS spectra in Figure 4.1c_1 and d_1, the 232 and 228.8 eV peaks correspond to the Mo $3d_{3/2}$ and $3d_{5/2}$ orbitals, respectively; the Se 3d peaks at 54.9 and 54 eV originate from the $3d_{3/2}$ and $3d_{5/2}$ doublets (211, 212). An atomic ratio of 1:2.05 was extracted for Mo and Se. Note that Raman spectroscopy was performed on the same sample as used later in AFM analysis, while PL and XPS spectra were obtained on a separate monolayer $MoSe_2$ produced by the identical procedure.

WSe_2: The lateral sizes of the CVD deposited triangular WSe_2 nanofilms were 5-20 µm. Two Raman peaks at 249.2 and 258.9 cm^{-1} in Figure 4.1a_2 belong to the E_{2g} and A_{1g} modes of WSe_2, respectively. As the van der Waals force can induce the interactions between neighbouring layers, a peak at ∼308 cm^{-1} would be detected for multilayered WSe_2, and the absence of this specific peak was used to confirm the single-layer nature of WSe_2 instead of the frequency difference between E_{2g} and A_{1g} modes (96, 213). There is no B^1_{2g} peak at ∼308 cm^{-1}, as demonstrated by the inset in Figure 4.1a_1. We can, therefore, conclude that the as-grown WSe_2 consists of a single layer. Additionally, the emission peak at 752.5 nm also indicates the single-layer nature of the WSe_2 sample (Figure 4.1b_2) (96).

The XPS spectra in Figure 4.1c_2 and d_2 show the peaks at 32.5 and 34.7 eV, which correspond to the W $4f_{7/2}$ and W $4f_{5/2}$ doublets; the weak peak at 37.4 eV may result from the WO_3 residues on the sample surface; the 54.8 and 55.7 eV peaks are ascribed to the Se $3d_{5/2}$ and Se $3d_{3/2}$ orbits; the atomic ratio of W and Se was calculated to be 1:1.98, which is close to the stoichiometric 1:2 (214).

MoS_2: The sizes of MoS_2 flakes reached up to 100 µm in size. Two characteristic Raman peaks were observed, E_{2g} mode at 383.1 cm-1 and A_{1g} mode at 404.1 cm-1, indicating monolayer or bilayer MoS_2 (215) as shown in Figure 4.2a. Additionally, a clear PL peak at 675.3 nm (Figure 4.2b) confirms the monolayer structure (216).

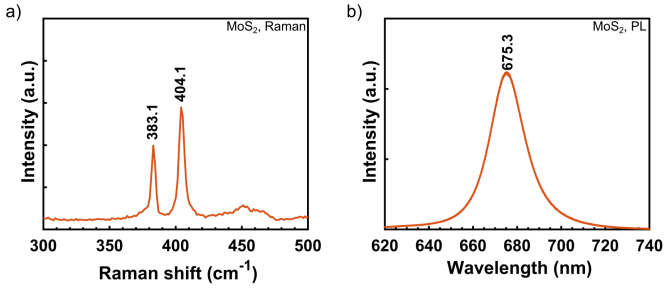

Figure 4.2: Characterisation of MoS_2 nanoflakes. (a) Raman spectrum and (b) PL spectrum with 532 nm laser excitation.

4.3.2 Nanotribology: Friction maps and load-dependent frictional behaviour

4.3.2.1 WS_2, $MoSe_2$, WSe_2

The topography of the WS_2, $MoSe_2$ and WSe_2 flakes chosen for nanotribological analysis is shown in Figure 4.3, together with their corresponding friction maps and load-dependent frictional response. Note that the flakes presented in this section are not the same monolayers used for characterisation in the previous section due to their small size and different methods used to characterise the samples. However, the flakes used for frictional experiments were taken from the same sample (i.e. from the same substrate or CVD batch) unless otherwise noted.

The surface topography of the specific flakes was obtained just before performing each friction experiment. As shown in Figure 4.3a, WS_2 and WSe_2 formed triangular crystals, indicating well-controlled crystal growth, while $MoSe_2$ resulted in a

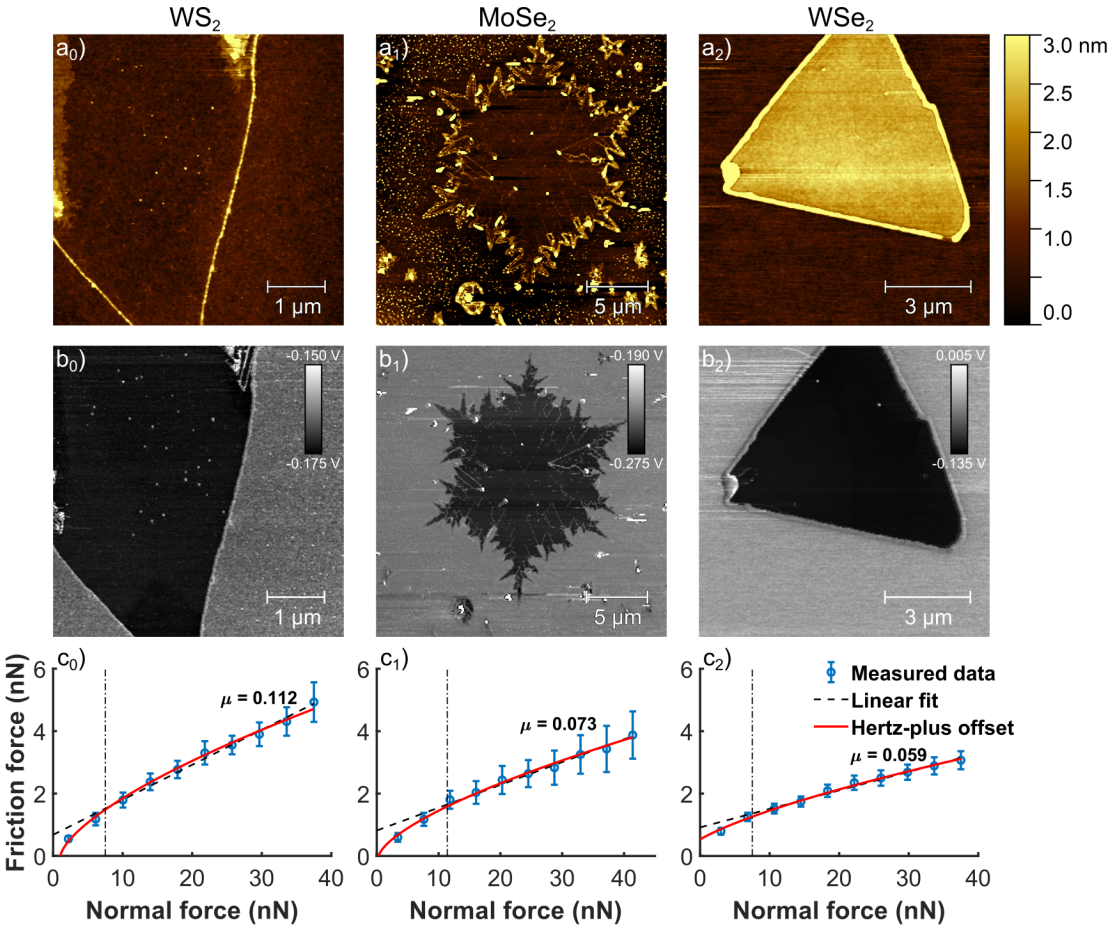

Figure 4.3: Surface characterisation of the analysed monolayer WS_2, $MoSe_2$ and WSe_2 flakes. Topography (a_0-a_2), corresponding friction maps (b_0-b_2) and load-dependent friction (c_0-c_2). Normal force represents the combined force of adhesion and applied load. Zero applied load is marked by a dotted dashed line.

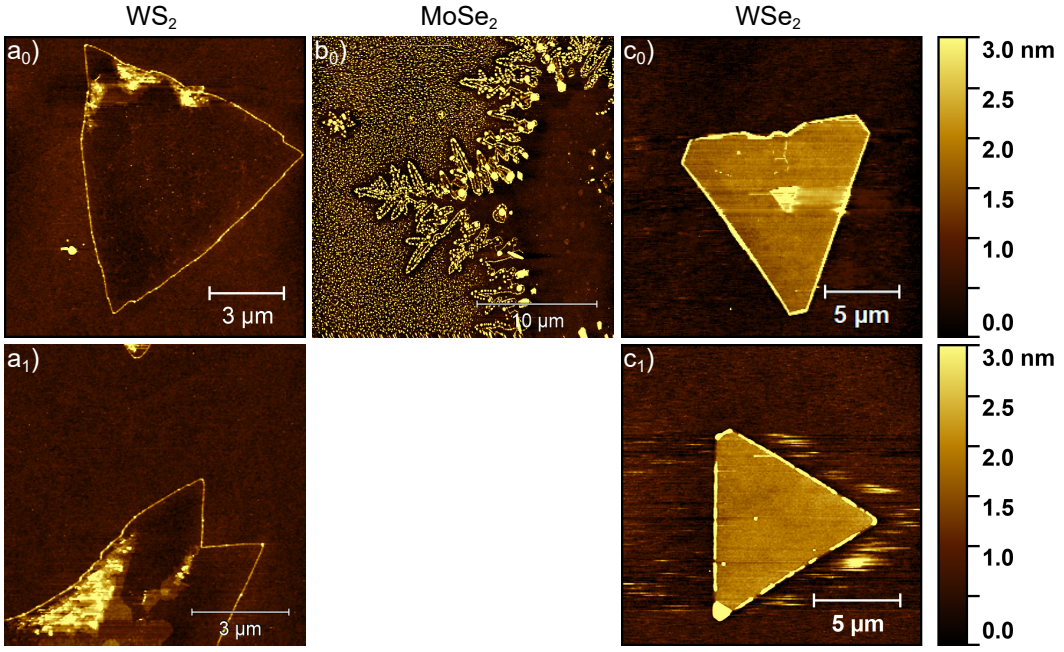

Figure 4.4: Topography scans of additional monolayer WS_2 (a), $MoSe_2$ (b) and WSe_2 flakes (c).

'snowflake-like' shape. Nevertheless, the AFM scan on $MoSe_2$ displays triangular grain boundaries within the flake, thus indicating that the single grains are, in fact, triangular. The 'snowflake-like' shape is a consequence of recrystallisation due to a longer deposition time (208). Raman spectroscopy (see Figure 4.1e) confirms the monolayer structure. Furthermore, friction measurements on $MoSe_2$ (Figure 4.3c) are comparable with the other two (in absolute value and load-dependent behaviour), further validating the quality and crystallinity of the surface. For example, poor crystallinity or low crystal quality should result in increased friction due to the presence of dangling bonds.

The measured flake thicknesses in contact mode vary substantially between the samples. WS_2 and $MoSe_2$ flakes display almost no height difference compared to the substrate, while the measured thickness of WSe_2 was 1.10 ± 0.12 nm. The same thicknesses were observed on additional WS_2, WSe_2 and $MoSe_2$ flakes (see Figure 4.4), showing that the structure is comparable between the flakes on the same sample. Note that the measured thickness can differ from the true value because these measurements were performed in contact mode. The discrepancy arises from the cross-talk between the lateral and normal signals. Due to the low spring constant of the AFM probe, the observed frictional contrast between the sample and the substrate can either mask or amplify small height differences. Cross-talk is a common artefact experienced in contact mode (see Chapter 2, Section 2.2.2).

The sample thicknesses were also measured in tapping mode (Figure 4.5), which avoids the effect of friction-induced cross-talk and thus provides more meaningful

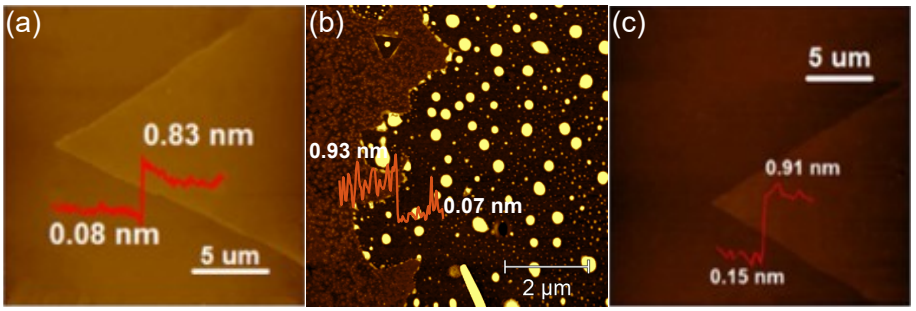

Figure 4.5: Tapping mode topography scans of WS_2 (a), $MoSe_2$ (b) and WSe_2 flakes (c).

values of the thickness. Note that the flakes are not the same as those used in contact mode. The obtained thickness values of ∼0.75 nm, ∼0.86 nm and ∼0.76 nm for WS_2, $MoSe_2$, and WSe_2, respectively, agree well with the reported values for monolayer flakes (96, 217–221).

Friction maps (Figure 4.3b) show high friction contrast between the flakes and the SiO_2 substrate. All the analysed TMD flakes experienced much lower friction than the substrate, indicating superior frictional characteristics. This shows that coating a single surface in the MEMS/NEMS contacts with a TMD monolayer could offer a significant performance improvement.

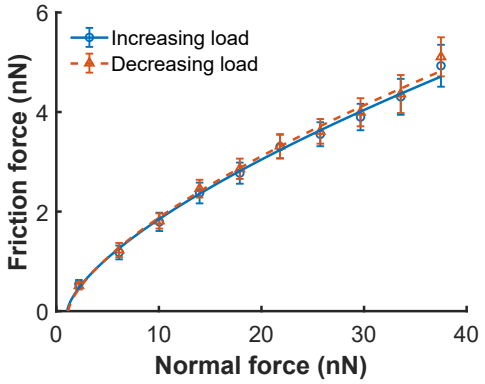

Figure 4.6: Load-dependent frictional behaviour at the increasing and decreasing loads on the WS_2 sample.

Load-dependent frictional behaviour of the three samples is shown in Figure 4.3c. Only the results obtained at 1 µm s^{-1} are shown here, despite performing the measurements at various sliding speeds; the speed-dependent behaviour is discussed later. No stick-slip motion was observed on any of the samples under the tested conditions. The measurements were consistent across a total of three different WS_2 and WSe_2 flakes and two separate locations on the $MoSe_2$ flake. No significant difference was observed between the loading and unloading curves on any of the samples, which can be expected for an elastic contact, where the layer is adhered to the substrate well. An example of this, obtained from the measurement on the WS_2 flake,

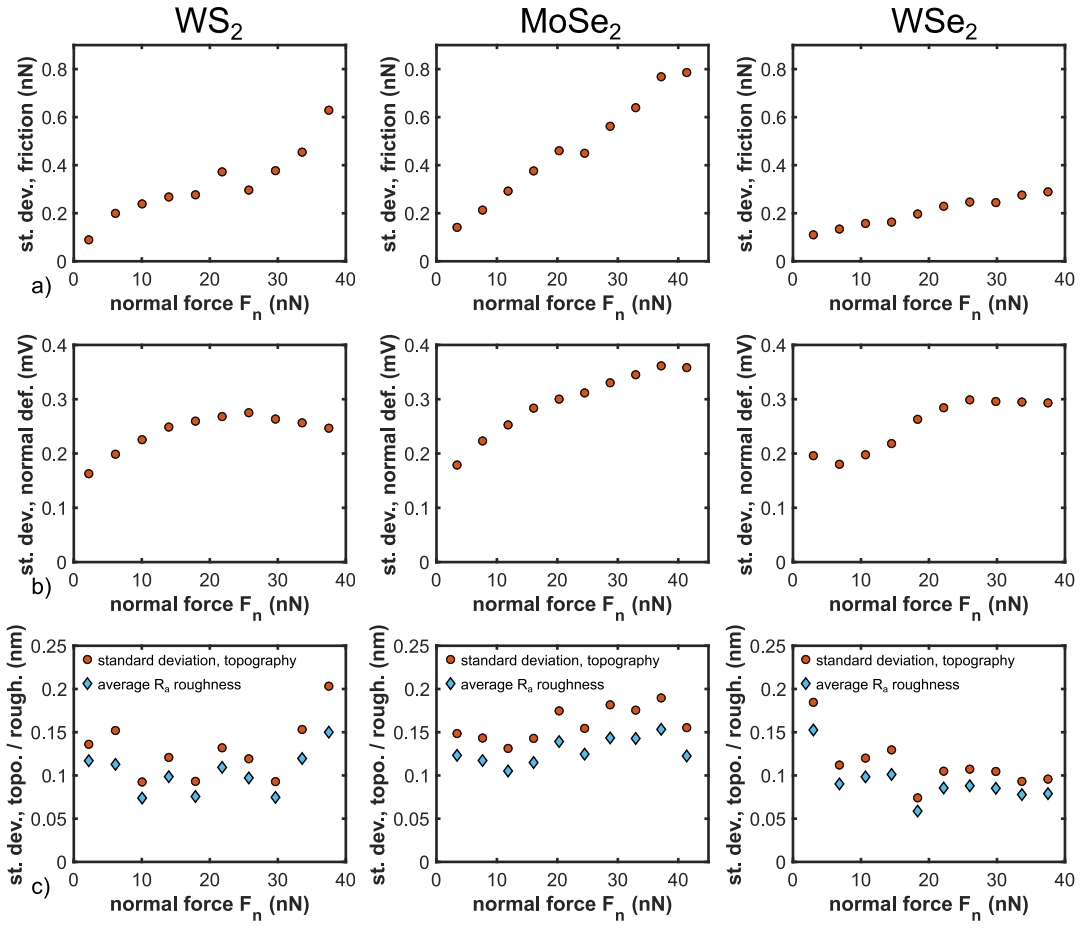

Figure 4.7: Standard deviations representing the magnitudes of error bars of friction (a), normal deflection (b) and topography/roughness (c) at different loads

is shown in Figure 4.6. The values are within the experimental error of each other. Thus, only the data with increasing normal force are included in Figure 4.3c for clarity.

The error bars in Figure 4.3c, which represent the standard deviation of friction force within the analysed region, are increasing with the load on all samples. Even if no stick-slip motion was observed on the samples, local stick events are still possible within the contact area and can, therefore, contribute to probe fluctuations. Examining the magnitude of error bars (Figure 4.7) reveals additional information about the surface quality and the frictional properties of the samples. Furthermore, single trace and retrace lines at the highest and lowest loads are displayed in Figure 4.8. $MoSe_2$ exhibits the largest fluctuations among the three samples, which indicates the possibility of a higher number of surface defects within the flake compared to the other two. In fact, a similar signal shape can be seen on both trace and retrace signals on $MoSe_2$ in Figure 4.8b, which confirms that the fluctuations are a direct response of the features on the sample surface.

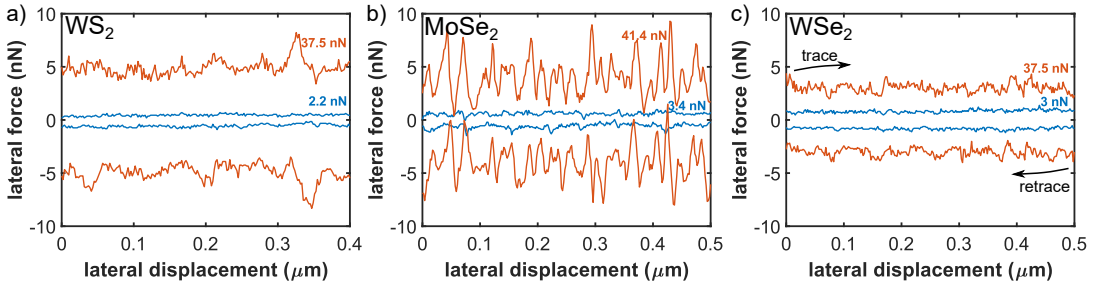

Figure 4.8: Single trace and retrace lines extracted from the friction measurements. (a) WS_2, (b) $MoSe_2$, (c) WSe_2. Note that WS_2 measurement was taken closer to the edge of the flake, therefore, only the proportion of the signal that was measured on top of the flake is shown here.

An increase in standard deviation was also observed in the normal deflection signal (Figure 4.7b); however, it does not follow the same trend as friction. This further points to random probe fluctuations and reveals that the fluctuations occur in all directions and not just in the direction of motion. Furthermore, the standard deviation of the topography and surface roughness (Figure 4.7c) display slightly higher values on $MoSe_2$ and indicate that increased fluctuations can also be due to higher roughness. Similarly, an increase in the fluctuations on WS_2 at higher loads can be explained by locally higher roughness.

Careful observation of Figures 4.3 and 4.4 reveals different orientations of triangular WS_2 and WSe_2 flakes. Individual friction measurements were taken on the differently oriented flakes and are shown in Figure 4.9. The insets in Figure 4.9 show the rotation angle of the flake edge compared to the sliding direction. The angles are considered in an anti-clockwise direction from the left-to-right scanning direction for consistency. The data displays frictional anisotropy, i.e. varying frictional behaviour with the sliding angle. Because the measurements were performed in humid air, there is a possibility of a thin adsorbed layer on top of the flakes, which could significantly affect friction and mask the effects of angle dependence. Consequently, the friction does not decrease as much as would be expected. The probe has probably undergone some wear before these measurements, contributing to an increased contact size. Therefore, the contact is incommensurate at any angle due to lattice mismatch between the Si and TMD crystals. Nonetheless, different degrees of incommensurability can still exist at different sliding angles.

Only a minor variation of friction with sliding speed was observed across the analysed range (Figure 4.10), which can mainly be attributed to measurement uncertainty and internal equipment error. The only obvious difference in the response is on the $MoSe_2$ sample at increasing load (Figure 4.10b) at 0.5 Hz (0.5 µm s^{-1}). However, as it is the only measurement that deviates from the rest, and it was the first measurement taken on that sample, we can conclude that the difference in response was a consequence of surface or tip contamination. The amount of contamination was

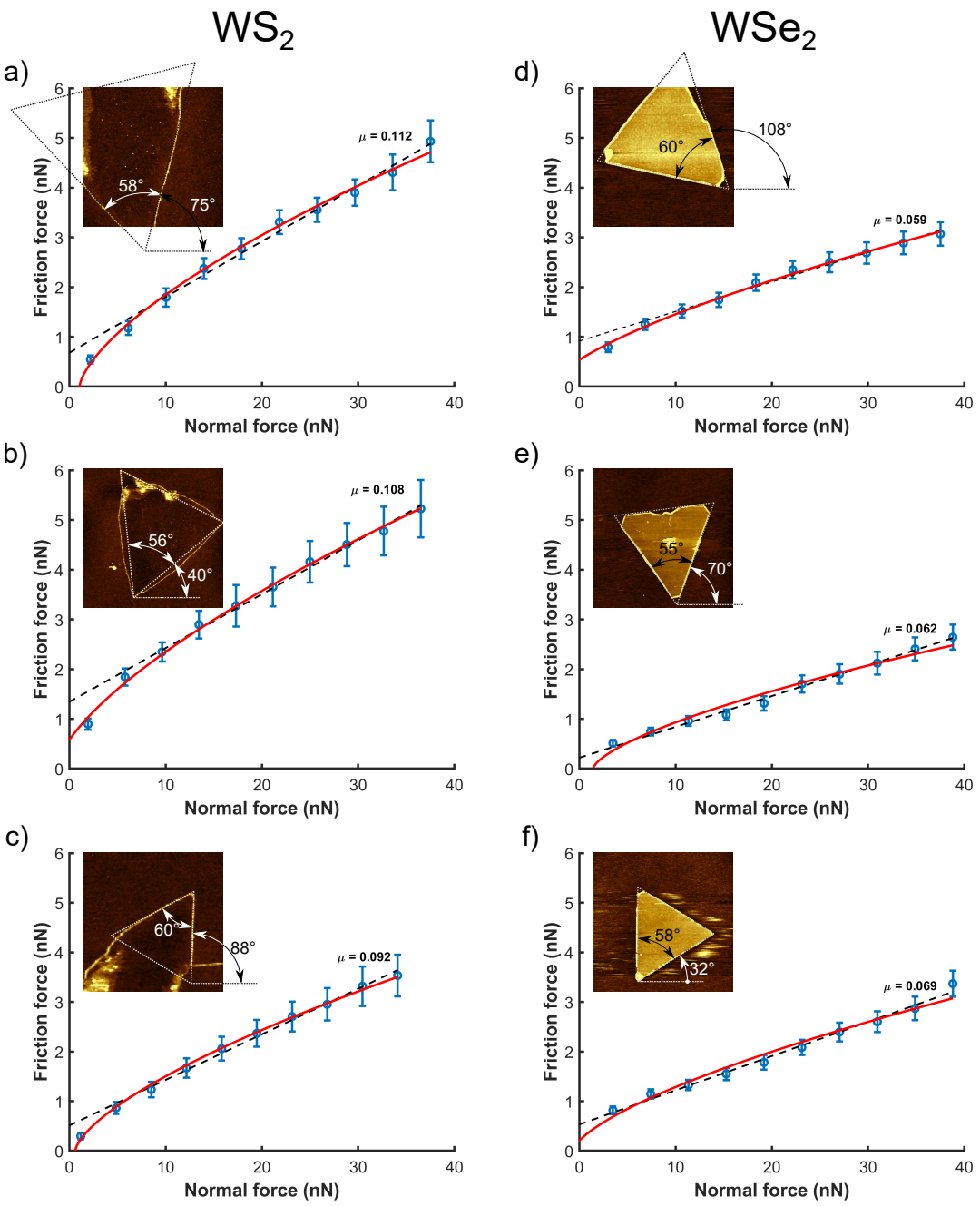

Figure 4.9: Dependence of friction of TMDs on the flake rotation.

low, and it was completely removed after the initial scan, which is evident from the other measurements on the same sample. Even the measurement with decreasing load (Figure 4.10e) at 0.5 Hz, performed right after within the same area, did not show any deviation between the sliding speeds anymore. Besides that, all three samples exhibit the same behaviour, indicating that nano-scale friction of TMDs is independent of sliding speed within the analysed range.

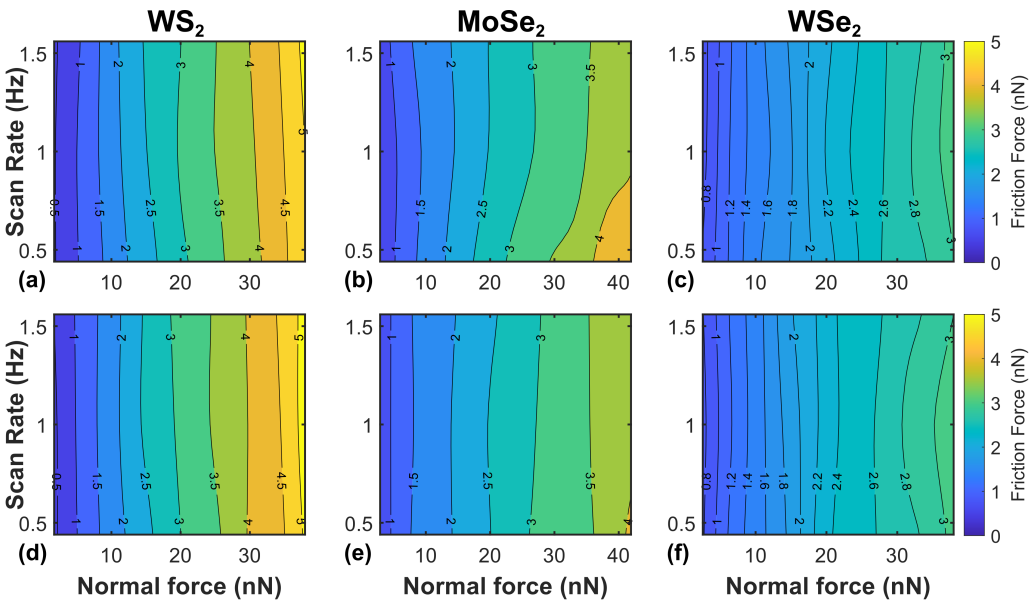

Figure 4.10: Contour plots showing the dependence of friction of TMDs on load and sliding speed. No significant difference in friction related to sliding speed was observed. Increasing (a-c) and decreasing (d-f) load.

4.3.2.2 MoS_2

The topography of the MoS_2 sample (Figure 4.11a) displays triangular growth and a clear height difference to the substrate (1.57 ± 0.35 nm). Unlike the other samples, the friction map shows similar values on the flake as the substrate. Furthermore, the behaviour on the MoS_2 flake is less uniform, namely increased friction in the bottom 10 - 45% of the image. This indicates high levels of contamination on the surface, which results in material transfer from the sample to the tip and, therefore, a significantly altered sliding interface. This is further highlighted by the load-dependent frictional behaviour (Figure 4.11c). The slope (μ = 0.074) is comparable with the other TMDs (μ = 0.112, 0.073 and 0.059 for WS_2, $MoSe_2$ and WSe_2 respectively), but the values are shifted in the positive direction. The absolute value of friction force at zero normal force, F_0, is double compared to the other samples, implying a substantial adhesion contribution to friction. The friction, in this case, is therefore principally driven by adhesion, with the contact area and contact geometry taking a secondary role. Note that two points are missing at the lower loads because the probe lost contact with the surface, pointing to a high adhesion discrepancy across the surface.

Surface contamination was further confirmed by re-scanning the same area after the friction measurement. As seen in Figures 4.11d and e, the scanning caused the removal of the adsorbed material from the scanned area and its accumulation at the sides. Additionally, we can see different surface heights at different locations of the sample, corresponding to previous measurements being performed at this location, as each subsequent scan removed some contamination from the surface. This showed

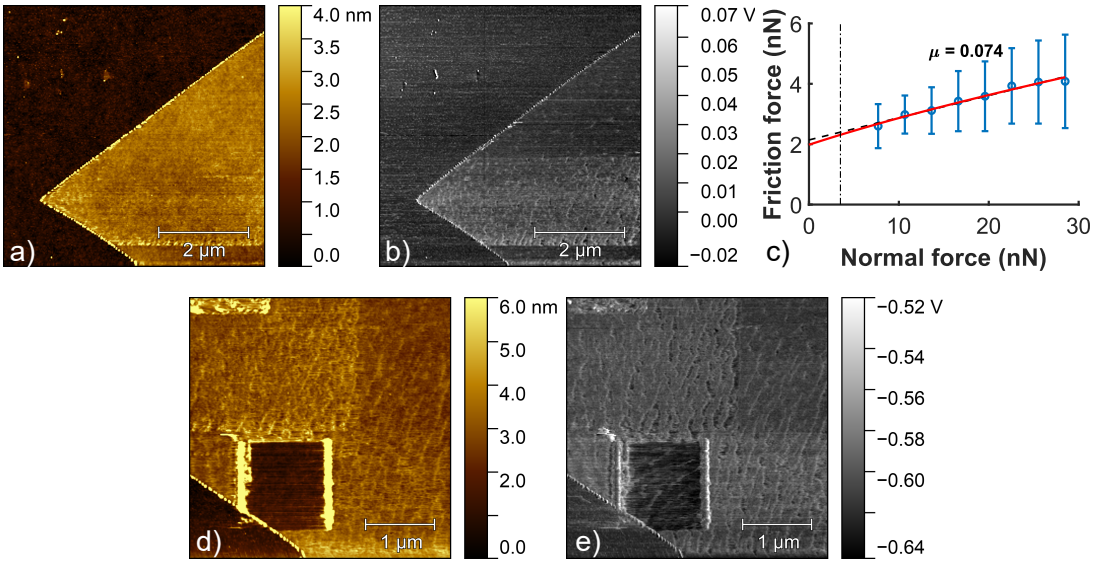

Figure 4.11: Nanotribology of MoS_2. (a) Topography and (b) friction map, showing a thicker layer of an adsorbed material on top of the layer. (c) Frictional behaviour. (d) Topography and (e) friction map obtained after the friction measurement, displaying removal of adsorbed material from the surface.

that the contamination layer is very soft and poorly adhered to the surface. The probe was able to scratch the surface despite low applied loads (note that the probe had a spring constant of $\sim$0.2 N m^{-1} and the applied loads were in the 0 – 30 nN range). As reported in Ref. (89), TMD flakes are susceptible to the adsorption of hydrocarbons, water, or other species from the surrounding air with time. However, we observed similar contamination levels on several MoS_2 samples, even those deposited just a few days before the measurement. Even though there is a possibility that the samples were contaminated by the adsorption from the environment, the most probable reason for the contamination arose from the deposition procedure.

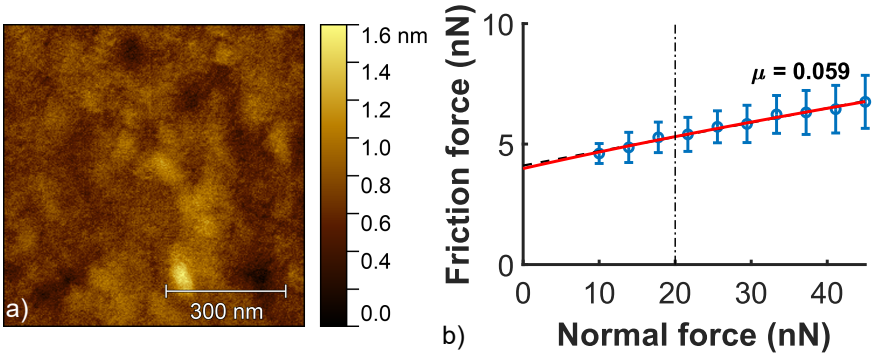

Figure 4.12: Surface of MoS_2 after a test on another MoS_2 sample (a) and the corresponding friction measurement (b).

An additional measurement on a different flake of the MoS_2 sample is presented in Figure 4.12. In this case, the removal of the surface material was not observed (Figure 4.12a), but the values of friction force showed an even larger positive shift. The

value of F_0 was almost five-fold larger than on the other TMD flakes, whereas the slope remained low at 0.059.

4.3.3 Nanotribology: Wear resistance

The experiments above were performed at relatively low loads to prevent excessive damage to the tip or the substrate. Hence, no changes were observed on the WS_2, $MoSe_2$ and WSe_2 samples after the friction tests at low loads. Following that, we increased the maximum load up to 10 µN to analyse the WS_2 monolayers for potential rupture and tip wear. A pre-worn probe was used to prevent the tip shattering solely due to high contact pressures, which could give inconsistent results. The pre-worn probe was obtained by incrementally increasing the load on the fresh sharp probe up to the maximum measurement load of 10 µN on the WS_2 sample, which resulted in the probe apex shattering at 6 µN on WS_2 (Figure 4.13). The event happened after 80 scanned lines and occurred mainly due to high internal pressures. In a subsequent scan with the same (shattered) probe, no additional probe wear could be detected. This ensured that no additional wear occurred from the probe shattering, and the general geometry of the contact remained consistent between the experiments. Therefore, only the results obtained by the pre-worn probe can be used to assess the behaviour. Additional reference scans were performed on the SiO_2 substrate.

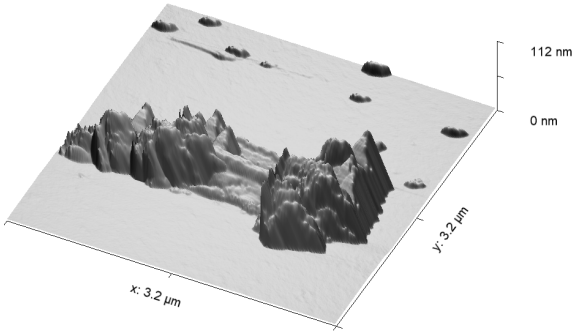

Figure 4.13: 3D topography after the first wear measurement on the WS_2 surface with a sharp probe.

We have not observed any sample wear on WS_2, including at the highest applied load of 10 µN. However, high friction between the tip and the SiO_2 surface caused the tip to start wearing off above 1000 nN, which resulted in the transfer of material from the tip to the surface (see the insets in Figure 4.14a). No removal of the SiO_2 substrate was observed and the wear solely occurred on the tip. Probe wear is quantitatively evaluated in Figure 4.14a; the total volume difference was determined between the surface topography after each wear measurement and the initial topography scan at 0

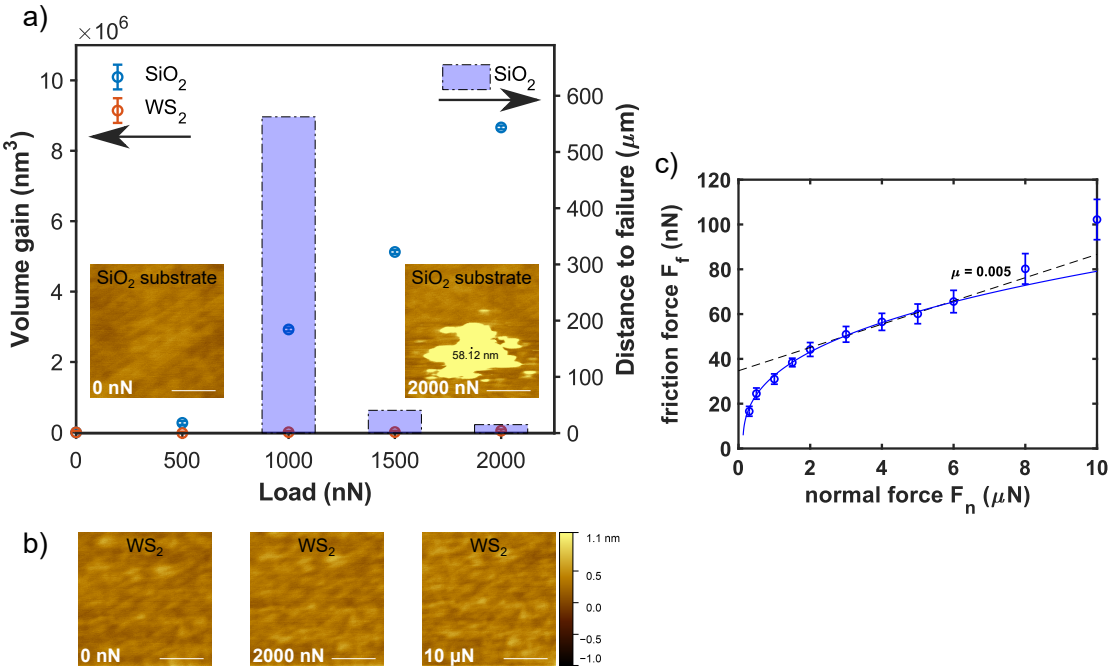

Figure 4.14: Tip wear on the SiO_2 substrate and WS_2 sample. (a) Sample volume gain and distance to failure. The insets show the surface topography after the experiments performed on SiO_2 substrate at 0 nN and 2000 nN. (b) WS_2 monolayer surface topography after the experiments at 0 nN, 2000 nN and 10 µN. The height bar applies to all topography scans. The lateral scale bars correspond to 500 nm. (c) Corresponding load-dependent frictional behaviour at the analysed loads.

nN. As expected, the volume differences are negligible on WS_2, but we see an almost linear increase on the SiO_2 above 500 nN.

The bars in Figure 4.14a show the distance to failure (i.e. the point at which we could visually notice the changes on the surface) at the loads where tip wear was observed. The total scanned distance at each load was 768 µm, indicating that even though we detected noticeable amounts of tip wear at 1000 nN, it only occurred towards the end of the experiment. The distance reduced significantly at higher loads; at 1500 nN it reduced down to 40 µm whereas at 2000 nN the transfer of the material occurred after only 15 µm of sliding. Therefore, the limit of usable loads on SiO_2 is around 1000 nN. On the other hand, sliding on WS_2 did not result in similar behaviour; even near the technical limit of our setup at 10 µN, there was no observable tip wear (Figure 4.14b). Friction during the experiment (Figure 4.14b) follows the m-power law up to 6 µN, indicating deviation from the spherical shape of the probe (73). Above 6 µN the friction starts increasing faster than the model predicts, which can be attributed to the plastic deformation of the tip.

4.4 Discussion

The standard approach to frictional analysis is to obtain the slope μ of the increasing friction with applied load L, similar to linear Amontons' law at the macro-scale (47). As discussed in Chapter 2, Section 2.1, at the nano-scale, the friction does not vanish at zero load due to the effects of adhesion; therefore, the friction force at zero load F_0 needs to be considered. Adhesion is initially included in total normal force $F_N = L + F_{adh}$ (73), leading to a formulation of adhesion-correlated Amontons' law:

$$F_f = \mu F_N + F_0. \tag{4.1}$$

The formulation is straightforward and readily comparable with the approach to understanding friction at the macro-scale. However, it can only serve as an initial assessment of the analysed measurements and can only be applied in cases where the observed behaviour is linear. Its major drawbacks include general inapplicability at low loads and its dependence on the contact geometry. Furthermore, it is only applicable to qualitatively compare the measurements obtained with the same set-up.

By observing the friction graphs in Figure 4.3c, we notice a linear trend from ∼10 nN onward, whereas, at lower loads, the frictional response deviates from linear behaviour. Note that below 10 nN we are already entering the adhesive regime, where the surfaces are kept in contact solely by adhesion. By assuming the onset of linear behaviour at higher loads, we have only considered the data above 10 nN normal load when fitting the linear model. The resulting values of μ and F_0 are collected in Table 4.3.

Because adhesion plays a major role in the contact properties of nano-scale contacts, a more suitable approach is to utilise adhesive contact models from solid mechanics (see Chapter 2, Section 2.1.4.2). Several models have been suggested to study the contact interactions in the AFM contact (73, 75, 76), proposing either JKR (59), DMT (64), or transition regime to model the adhesive contact. The benefit of these models is that they incorporate contact geometry (usually approximated by a sphere-on-flat contact) and adhesion and thus allow for a more accurate quantitative comparison between the measurements performed using different probes and systems.

One of such models, which is commonly (37, 38) used to fit lateral force data, is the Hertz-plus-offset model for a sphere on flat contact (73) (see Equation 2.22). The Hertz-plus-offset model is equivalent to the DMT contact model, which is consistent with many AFM measurements, when the sample surfaces are atomically flat, sufficiently hard, and can be approximated by a sphere-on-flat contact (73). The radius of the probe was determined by scanning a standard calibration grating TGT1

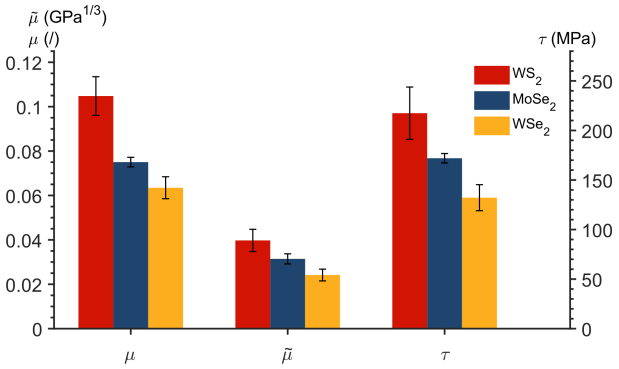

Figure 4.15: Averaged frictional and contact parameters.

(ND-MDT, Russia) and calculated using the envelope method (222). The obtained radius was 33.4 nm. As the manufacturer specified radius for a new probe is less than 10 nm, this indicates that some wear occurred throughout the measurements. However, because no visible signs of wear were observed on the scans during friction measurements, we can assume that the majority of the probe wear occurred during the initial contact of the tip with the sample and throughout the initial topography measurements. As reported by J. Liu et al. (97) and D.S. Grierson et al. (223), the sharp apex of Si tip could shatter almost immediately after contact with the surface. A slight increase of the probe radius after the measurements is therefore expected.

The results of the fit to the selected model are summarised in Table 4.3. We observe a very good fit to the model ($R^2 > 0.99$, $|F_{off}| < F_{adh}$) for all three samples, which further confirms wear-less friction and fully elastic contact, and thus shows that the nano-scale friction of TMDs is proportional to the contact area.

Table 4.3: Contact properties of TMD samples measured by LFM

Sample	μ (/)	F_0 (nN)	$\tilde{\mu}$ (GPa$^{1/3}$)	τ (MPa)	F_{off} (nN)	F_{adh}(nN)	R_2 (/)
WS_2	0.112	0.7	0.0413 ± 0.0014	226.1	1.1	7.5	0.9947
$MoSe_2$	0.073	0.8	0.0308 ± 0.0015	168.6	0.3	11.4	0.9910
WSe_2	0.059	0.9	0.0255 ± 0.0009	139.6	-2.9	7.5	0.9955

The averaged frictional parameters of the measurements on all three WS_2 and WSe_2 flakes and on both regions of the $MoSe_2$ flake are shown in Figure 4.15. All three samples exhibit low friction, but there are observable differences between them. Both selenium-containing samples experienced lower friction than the sulphur-based monolayer ($WS_2 > MoSe_2 > WSe_2$), which is in good agreement with the results obtained by M. Vazirisereshk et al. (196) on molybdenum based TMDs in a vacuum. This indicates that the chalcogenide atom has a major influence on the friction of TMD monolayers, although the influence of the metal atom is not negligible. We have found that tungsten-based monolayer exhibits lower friction than molybdenum based one. These results differ from those reported by Zhou et al. (197), who reported lower

friction on $MoSe_2$ than on WSe_2; however, a direct comparison between our results and theirs is not possible. Their samples were exfoliated bulk multilayers and they attributed the difference in friction to the elastic response of the structure. On the other hand, due to the atomically thin nature of our samples, the majority of the elastic response comes from the Si/SiO_2 substrate and is, therefore, expected to be similar between the samples. Thus, we can conclude that friction of clean layers is mainly driven by the interatomic forces between the contacting bodies, with structural properties of the layers taking a secondary role.

Since there were no large differences in measured pull-off forces among the three TMD samples, we can conclude that the difference in friction between different samples is not correlated to the observed small difference in adhesion. In fact, the same pull-off force was measured on samples with the highest and the lowest measured friction.

Comparing our measured values with the values of $\tilde{\mu}$ from the literature, we see that the values obtained on TMDs are substantially lower than the majority of materials collected in Table 4.1, except for highly oriented pyrolytic graphite (HOPG) measured in an argon atmosphere. Due to the high quality of HOPG crystals, they contain fewer surface defects than CVD grown monolayers, which are more prone to defects due to the shorter time scales used for deposition (224). Furthermore, our measurements were performed in air; therefore, we can expect some degree of organics and water adsorbed on the surfaces (89). Both effects can contribute significantly to the final frictional response. Therefore, eliminating them on the TMD surfaces could further decrease friction and make them potentially more comparable with HOPG. Nevertheless, the quantitative friction observed on all the TMD samples was very low.

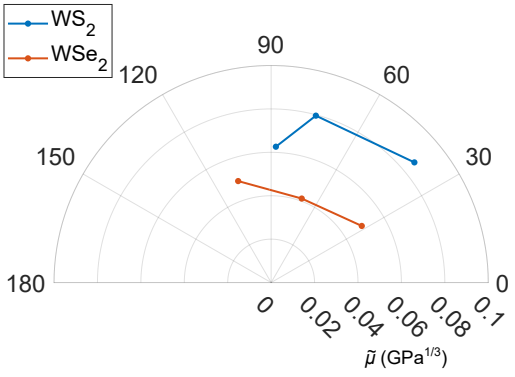

Figure 4.16: Dependence of friction on flake orientation.

The values of frictional properties obtained at differently oriented WS_2 and WSe_2 flakes are summarised in Figure 4.16. The data indicates a strong influence of sliding direction on frictional behaviour of TMDs and can be compared to the recent publication by V.E.P. Claerbout et al. (225), who computationally analysed the onset of superlubricity between two TMD layers in regards to relative sliding direction using molecular dynamics simulations. They observed a significant increase of friction for a

very limited range of angles; the friction variation we observe is much lower, but it is important to note that the analysed systems are not the same. Our system is incommensurate at any angle due to the different lattice constants of the tip and the sample. Similarly, M. Vazirisereshk et al. (226) studied 360° rotation on monolayer and bulk MoS_2 and found significant friction reduction only at specific rotation angles (60° and 240°, resulting in 180° symmetry).

4.5 Conclusions

We have shown that all the measured TMD monolayer samples exhibited low nano-scale friction, thus indicating good tribological behaviour. The exact elemental structure of the clean samples had some effect on the frictional response; however, all three monolayers showed similar behaviour. WS_2 monolayer experienced the highest values of the lateral force, and WSe_2 experienced the lowest. The results indicate that the selenides would generally result in lower friction than sulphides. The samples also did not show any dependence on sliding speed within the analysed range. Furthermore, we have shown that the TMD monolayers can significantly reduce and delay the onset of wear in high load applications beyond the onset of plastic deformation of the tip and demonstrated angle dependence of friction by analysing differently oriented flakes. MoS_2 sample experienced similarly low values of friction force; however, comparison with the other flakes is not possible due to different frictional behaviour resulting from substantial surface contamination.

We can conclude that precisely selecting a specific TMD monolayer for a specific sliding application is less important than ensuring that the deposited monolayer crystal would be of high quality, contain a low number of defects and be free of contamination.

Chapter 5

The effect of layer thickness on frictional behaviour of 2D materials

5.1 Introduction

Due to the high sensitivity and instability of nano-scale sliding systems, even minor differences in the sliding setup can significantly change the resulting frictional behaviour. Therefore, some key factors affecting friction may not be apparent while performing frictional experiments, and yet they could yield two seemingly similar measurements incomparable. Characterising frictional behaviour, i.e. the load-dependent frictional response of the system, instead of only comparing absolute values at a specific load, allows for a more thorough comparison between different systems. The standard parameters involved in the analysis of the nano-scale frictional contacts include sample chemistry, mechanical properties of the contacting bodies and the cantilever, crystalline orientation, contact quality, probe geometry, sliding speeds, contact pressures, and adhesive interaction between the probe and the sample.

The direct effect of adhesion on contact properties becomes increasingly noticeable at small scales. Decreasing the dimensions of the sliding bodies results in significantly higher surface to volume ratios (227). Consequently, surface phenomena, such as adhesion, become essential components in any nano-scale sliding contact, particularly in the case of supported 2D materials, where we need to consider three separate sites of local adhesion: (i) between the sample and the substrate, (ii) between the sample and the slider and (iii) internally between the layers of the sample. The chemical composition within each of these pairs can be different, thus resulting in locally different chemical and, therefore, also adhesional properties. Different magnitudes of attractive forces within each of the three adhesion sites mean that the contact

properties can be predominantly affected by the substrate, the slider or both (resulting in separation within the sample)

The commonly accepted nano-scale frictional behaviour of multilayered 2D materials is that the frictional response decreases with the number of layers, where the decrease in friction results from reduced puckering (35, 36). C. Lee et al. (35) explained that the total stiffness of an unsupported layer increases with the number of layers, which reduces the out-of-plane deformation during sliding. This reduced deformation, in turn, reduces sample puckering and, therefore, lowers friction. Similarly, L. Fang et al. (36) presented a model for correlating the number of layers with friction force, in which the final frictional behaviour is presented as a superposition of the contributions from intrinsic friction and puckering friction. They introduced a corrective factor for puckering strength, which allows the model to be applied to a wide array of materials. In general, intrinsic friction increases with the number of layers, while puckering friction decreases. The above studies have only reported the measurements obtained at a single load and have relativised the obtained measurements to the monolayer value. Alternatively, in the case of graphene films, T. Filleter et al. (228, 229) reported an approximately two-fold reduction of load-dependent nano-scale friction between a monolayer and a bilayer in an ultra-high vacuum.

In this work, we present a study of the nano-scale frictional behaviour of the supported monolayer and bilayer WSe_2 samples in air. The bilayer samples experience different load-dependent behaviour, thus strongly indicating altered adhesional properties. The observed frictional response indicates more complex behaviour, for which a simple 'bigger-smaller' comparison is not sufficient. To complement the measured data, we applied a numerical model to independently analyse the effects of adhesion on the contact properties in different locations. The results reveal that the resulting friction is driven by two independent phenomena – a reduction of interfacial shear strength at a higher number of layers and an increased contact area due to adhesion. A new model for fitting the friction measurements on samples that exhibit this behaviour was developed based on the findings from the numerical model. The new model is an expansion of the Hertz-plus-offset model, which was used with the monolayers in Chapter 4.

5.2 Experimental and computational details

The WSe_2 flakes were obtained from the same sample as those in Chapter 4. Monolayer and bilayer regions on the samples were identified by atomic force microscopy (AFM, Agilent Technologies, USA) in contact mode. Friction measurements were obtained on the same system by performing load-dependent

measurements over a total of 10 different loads, including negative loads, where the surfaces were kept in contact by adhesion alone; the lowest load was determined as a fraction of adhesive force to ensure no separation of the contact during sliding.

The numerical model for calculating the contact behaviour was based on the 3D Hertz model for a sphere-on-flat contact. An atomically thin 2D layer, with the atoms arranged in a specific lattice configuration, was then introduced between the two deformed surfaces; covalent bonding between the particles in the layer was modelled by a linear spring model and the van der Waals interactions with the surrounding surfaces by the Lennard-Jones potential (LJP). The parameters of the LJP were varied, and the simulation ran until the system reached equilibrium for each set of parameters. After the relaxation, each atom in the layer is either touching the upper surface, the bottom surface or is in an equilibrium state between the two.

5.3 Results

The topography of the measured WSe_2 flake is shown in Figure 5.1. The corresponding monolayer (1L) and bilayer (2L) regions are marked accordingly. The measured frictional response of monolayer and bilayer regions of the WSe_2 sample is displayed in Figure 5.2a. The monolayer measurement has been fit to a well-known and widely used nano-scale Hertz-plus-offset model (Eq. (2.22), (73)) and shows good agreement between the measured values and the $^2/_3$ power law (R^2=0.989). This directly indicates that the contact is in the DMT regime, high quality (compliance), and the probe shape is close to spherical.

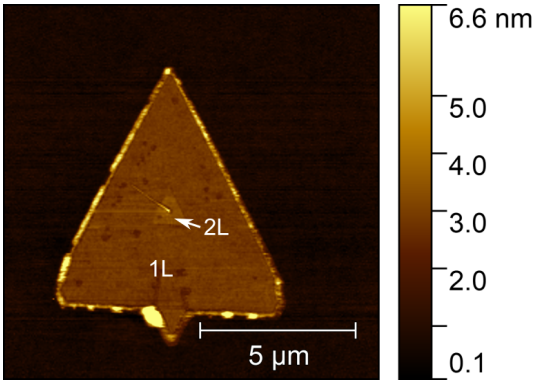

Figure 5.1: Topography of the monolayer (1L) and bilayer (2L) regions.

A contrasting situation can be observed on the bilayer; the load-dependent frictional response follows an altered behaviour. The friction of the bilayer is significantly larger at lower loads, but it flattens out and reaches a considerably lower slope at higher loads. The observation is particularly interesting, considering that the shape of the

probe and the chemistry of the contact stayed the same, which indicates a large influence of the structure below the contact.

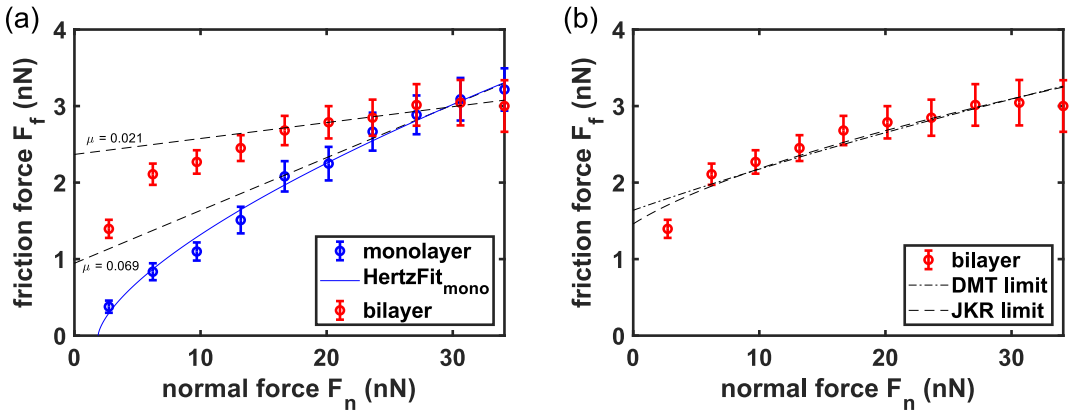

Figure 5.2: Frictional response of the monolayer and bilayer samples (a). DMT and JKR limits, displaying the best fit of the two models to the bilayer data (b).

Figure 5.2b displays a range of the JKR-DMT transition regime. The best fit of each of the models to the bilayer data is shown for each limit. The measured data falls outside the limits of the two models, thus indicating a more complex behaviour that can not be analysed by the standard contact models. Even at the JKR limit, the model still does not describe the bilayer behaviour accurately and, therefore, implies the need for an extended theory to encompass the frictional response.

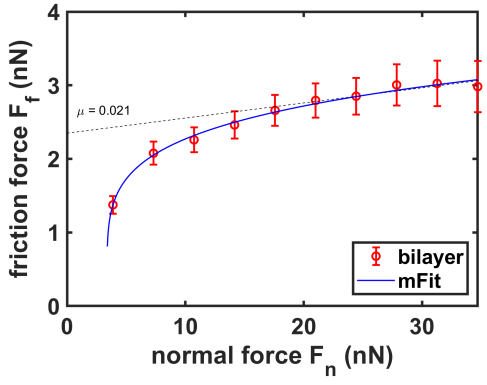

Figure 5.3: m-power law fit of the measured bilayer data.

The m-power law (Equation 2.23, (73)), where the exponent corrects for any deviations from the spherical shape, can provide a mathematically acceptable fit (Figure 5.3; m = 0.1955, R^2 = 0.99). However, according to Ref. (73), the reason for the deviation from the 2/3 power law would mean a deviation from an ideally spherical shape of the slider. Substantial changes in tip geometry between two subsequent measurements are unlikely, thus yielding the model insufficient to describe our data. This is further backed by the repeatability of the measurements.

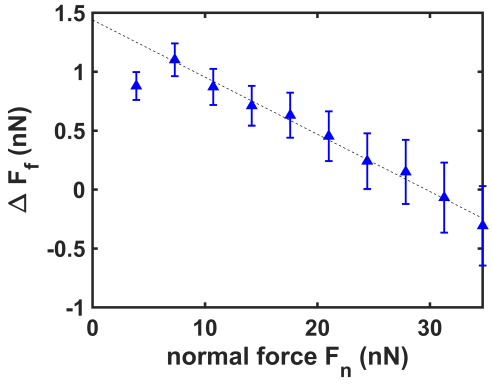

Figure 5.4: The difference between the monolayer and bilayer frictional responses, showing a linear relationship.

To identify the source of the observed discrepancy, we first examine the difference between the measurements on the monolayer and bilayer samples, as displayed in Figure 5.4. The difference between the monolayer and the bilayer response follows a linear relationship within the analysed range, except at the lowest load. It is important to note that the first point has the highest uncertainty in terms of normal load and contact size, as the surfaces are only held together by adhesion.

As the currently available analytical models are not sufficient to model and describe the presented data or explain the origin of the observed discrepancies in behaviour, it is necessary to model the contact properties numerically by studying the effect of attractive forces at the atomic level on the layer deformation.

5.4 Modelling the contact problem at the atomic level

To analyse the discrepancies observed between the monolayer and multilayer systems, we explore a simple numerical model, which allows us to study the effects of differing adhesional properties on the frictional response between an arbitrary slider (AFM tip) and the 2D material layer. The model presented here includes basic assumptions from similar models based upon the adhesive Hertz contact. The initial deformation geometry is calculated according to the sphere-on-flat Hertz contact (230). The height profiles of the deformed surfaces are $u_1(x, y)$ and $u_2(x, y)$ for the half-sphere and the flat surface, respectively. The deformed surfaces are then separated by a double separation distance ($2z_0$), and a single atomic layer, with the profile u_L, is introduced between them so that $u_L - u_2 = z_0$. From here on, subscript '1' denotes the half-sphere (tip), subscript 'L' the layer, and subscript '2' the flat surface below the layer (substrate) unless otherwise noted. The layer is assumed to be incompressible, has no dimension in the z-direction and has the lateral positions of the atoms fixed. Each particle in the layer exhibits two independent Lennard-Jones

interactions, with the sphere surface above and the substrate surface below. Note that the substrate here denotes the structure directly below the top layer, which could be (i) an actual substrate on which the sample is deposited, (ii) another layer of the same material or (iii) another layer of a different material. The cross-section of the starting point of the model (i.e. before loading and applying adhesion) is shown in Figure 5.5.

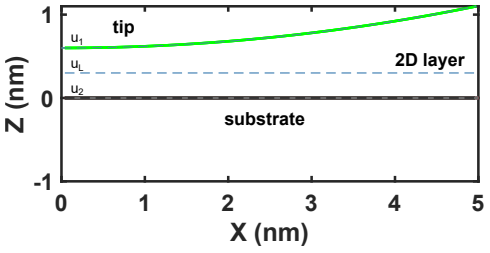

Figure 5.5: A cross-section of the starting point of the model before loading and without adhesion.

Two versions of the model were utilised: 1D, using a linear chain of atoms, separated by an interatomic distance a, and 2D, with the implementation of an appropriate lattice structure. Note that the dimension here corresponds to the number of independent coordinates of the lattice. Three different 2D atomic configurations that were tested are hexagonal, rhombical ($\theta = 60°$) and square ($\theta = 90°$), as shown in Figure 5.6.

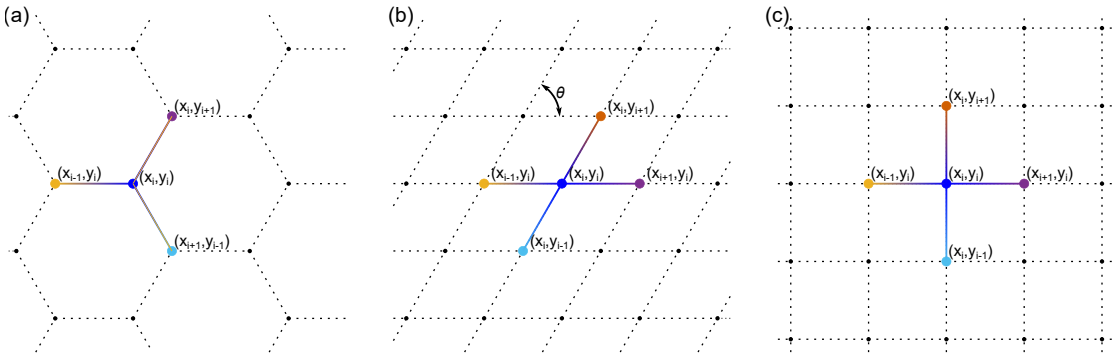

Figure 5.6: Different atomic lattice configurations: hexagonal (a), rhombical (b), and square (c).

Two types of forces act on each atom in the layer. The first one is van der Waals force between an atom in the layer and the atoms in each surface (f_1 and f_2), modelled by Lennard-Jones potential (LJP) (231):

$$f_m = 4\epsilon_{LJ_m} r\left(\frac{12\sigma_m^{12}}{r^{12}} - \frac{6\sigma_m^6}{r^6}\right); m = 1, 2, \tag{5.1}$$

where ϵ_{LJ_m} is the depth of the energy well, σ_m is the zero-energy distance between the particles, and r is the distance between the particles. The second force is the elastic

force arising from the elastic stretching of the covalent bonds with the neighbouring atoms in the layer $F_{1..N}$, represented by a linear harmonic spring (232):

$$F_i = E_{1D}\delta, \tag{5.2}$$

where δ is strain along the axis of the bond, and E_{1D} is the linear elastic constant. As we assume the fixed position of the atoms in the xy-plane, only the force component along the z-direction can be considered. It, therefore, follows that:

$$F_{z_i} = \frac{\sin\phi d(1-\cos\phi)}{\cos\phi} E_{1D}, \tag{5.3}$$

where ϕ is the angle between the analysed atom and the neighbouring atom i and d is the lateral distance between the two atoms.

The force balance in each point between u_1 and u_2 is:

$$F = -f_1 + f_2 - \sum_{i}^{I} F_{z_i}. \tag{5.4}$$

Each atom in the layer at the point (x, y) is allowed to assume any position in the range ($u_1(x, y)$ - $0.9z_0$, $u_2(x, y)$ + $0.9z_0$). Note the strong repulsive force when the distance between the surface and the atom is below z_0. Therefore, limiting the range in the repulsive regime to $0.1z_0$ is sufficient. The forces acting on the atom at different positions are shown in Figure 5.7b. Positive force denotes the force acting towards surface 1. Note that, in the attractive regime in the LJ potential formulation, the force is negative.

The new position of the atom is determined by finding the equilibrium point. In cases where there are multiple points where F = 0 nN, the equilibrium point is determined based on the value of the force in the initial position; if the force is above 0 nN, then the nearest zero towards surface 1 is selected, i.e. the layer is pulled towards the surface 1 until it assumes the correct position in the corresponding point. Similarly, when the net force is below 0, the layer is pulled towards surface 2 and assumes the nearest point where the net force is 0.

Procedure for the determination of the layer profile when subjected to two adhesive surfaces therefore follows:

1. Calculate the Hertzian profile without adhesion – as if the layer was not there

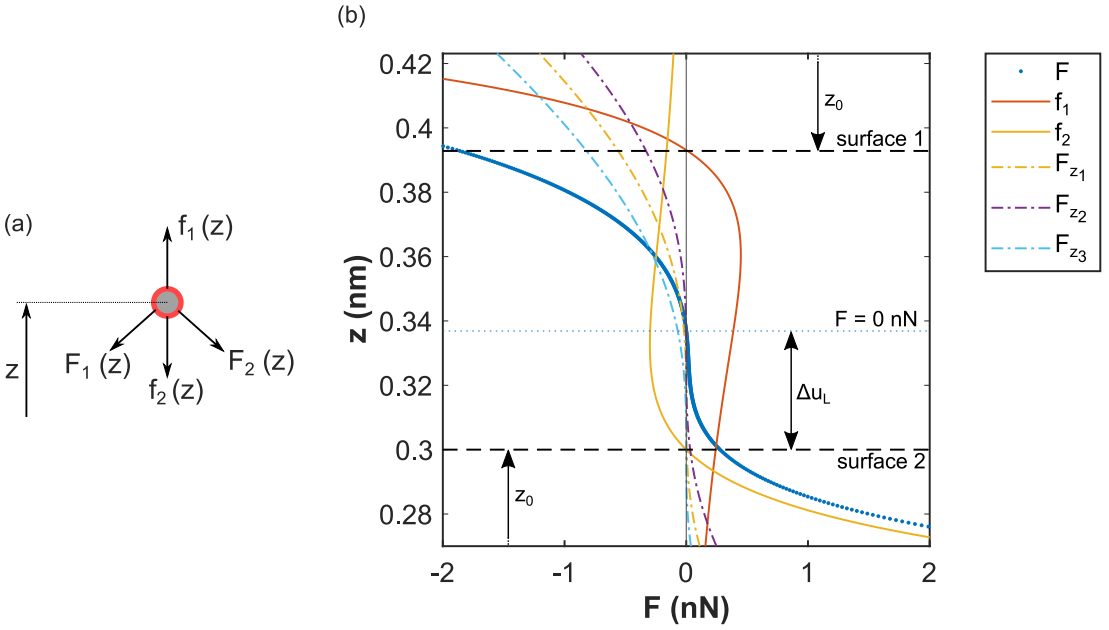

Figure 5.7: Forces acting on an atom (a) and the magnitude of each force along the z-axis (b). The atom in the layer assumes the equilibrium position at Δu_L ($F = 0$ nN)

2. Separate the profiles by the appropriate interatomic distance $2z_0$ and insert the layer in between
3. For each atom (point) determine the force profile between $(u_1(x, y) - 0.9z_0$, $u_2(x, y) + 0.9z_0)$
4. Find the equilibrium point. If there are multiple select the one that is the closest to the initial point
5. Repeat steps (3) and (4) until the profile does not change anymore between the cycles
6. Categorise the atoms as (a) in contact with the bottom surface, (b) in contact with the top surface or (c) in between

The result of a generic 1D instance of the model is shown in Figure 5.8, which shows the deformation of the layer in the form of a lip around the initial contact area. The thicker line on the substrate shows the Hertzian contact area at the given load. Note that the model parameters used to generate Figure 5.8 were exaggerated to amplify the observed effects. The actual results of the 2D instance are presented below.

Figure 5.9 demonstrates the evolution of contact area with normal load for a contact where $\epsilon_1 > \epsilon_2$ ($R_1 = 10$ nm, $\epsilon_1 = 0.5$ meV, $\epsilon_1/\epsilon_2 = 1.5$, $E_{1D} = 50$ N/m, $c = 0.2$ nm, $\sigma = z_0/2^{1/6}$). A_1 marks the total computed contact area, and A_0 represents the Hertzian contact area. A_0, therefore, also corresponds to the region where the layer is in contact with both the substrate and the slider. ΔA is the contact area gained by the

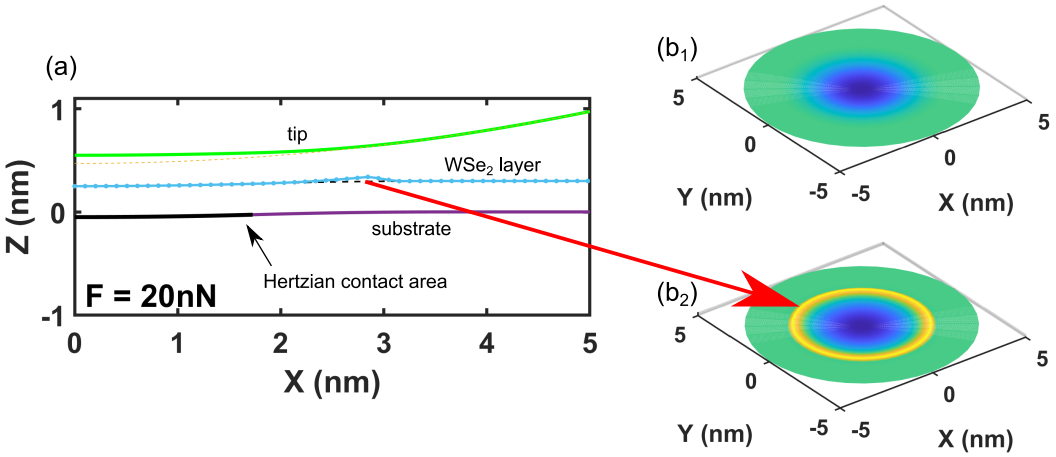

Figure 5.8: A cross-section of the contact at 20 nN load showing the layer wrapping around the tip (a). 3D drawing of the layer surface before considering adhesion (b_1) and after (b_2).

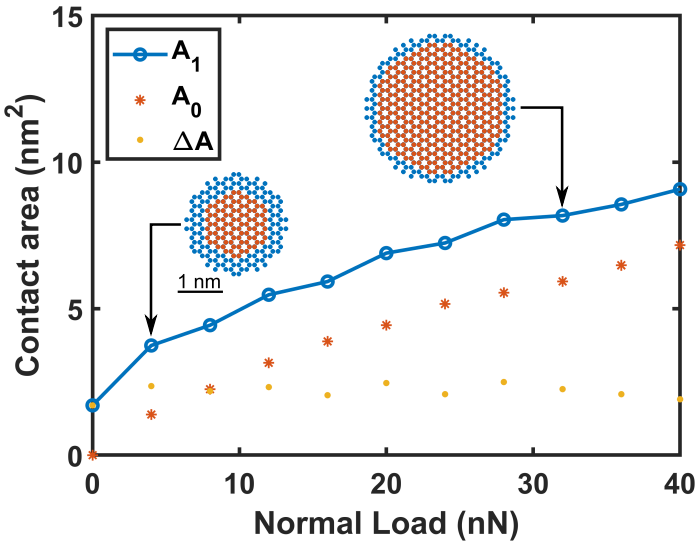

Figure 5.9: The total contact area A_1 (blue) of an adhesive layered contact is much larger than Hertzian contact area A_0 (red). The difference between the two contact areas ΔA (green) is almost constant within the tested range.

layer wrapping around the tip due to local adhesion. Consequently, it corresponds to an unsupported region of the layer. Interestingly, ΔA experiences the largest growth at very low loads and remains almost constant above 4 nN - a behaviour which could indicate a larger contribution of ΔA to friction in the case of the bilayer sample. The insets represent the atoms in contact with the slider at two different loads (4 nN and 32 nN).

Different lattice configurations (Figure 5.10) result in significantly different results for the contact area; the rhombical lattice results in the largest contact area and the square lattice the smallest. This is a consequence of the square lattice being stiffer (each atom

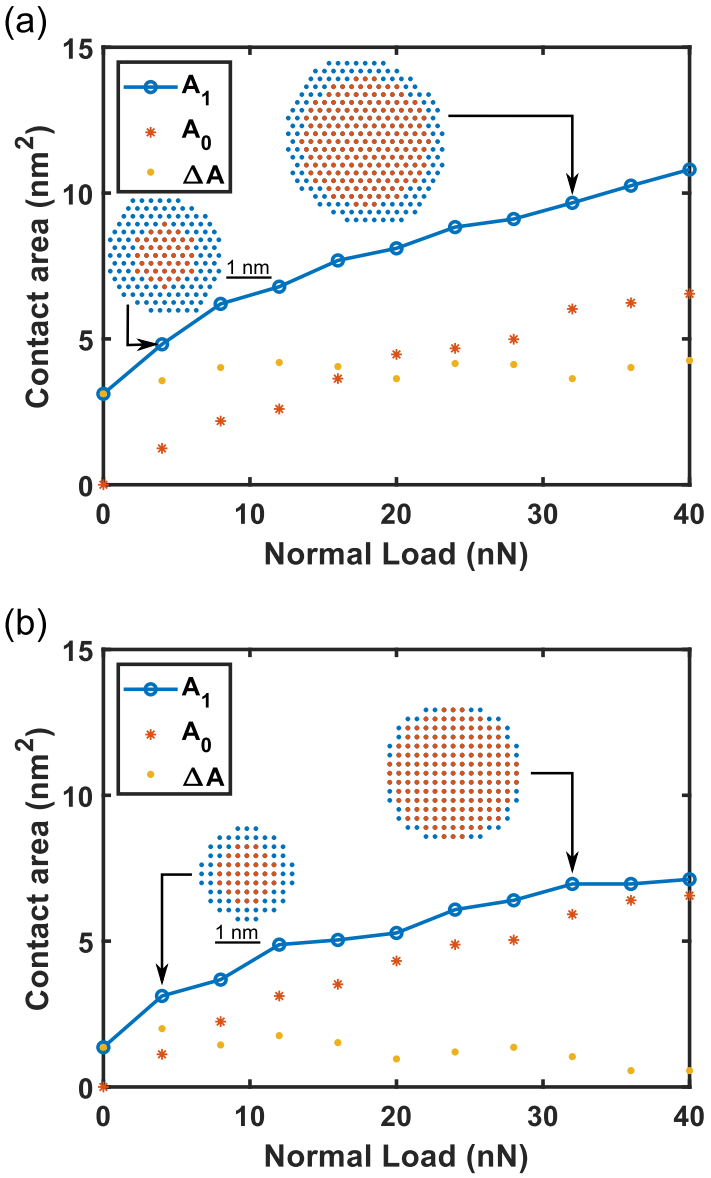

Figure 5.10: Contact areas for rhombical (a) and square (b) lattice configurations, showing a large influence of lattice geometry on the resulting contact area.

connected to one additional atom, thus further restricting vertical movement) and the rhombical lattice having a higher density of atoms. Furthermore, hexagonal and square lattices provide six-fold and four-fold symmetry, respectively, whereas rhombical lattice displays only two-fold symmetry.

The evolution of the contact area with increasing strength of interatomic forces is shown in Figure 5.11. As expected, when $\epsilon_1 < \epsilon_2$, the contact area is identical to the Hertzian contact, i.e. the layer is not in contact with the sphere outside the initial contact area. However, this does not mean that the layer remains undeformed. In fact, as demonstrated in the 3D profile of the deformed layer in Figure 5.12b, the layer still undergoes substantial deformation. Figure 5.11 also shows that 0.5 meV is the lowest value of ϵ_1 where the increase in contact area can still be observed.

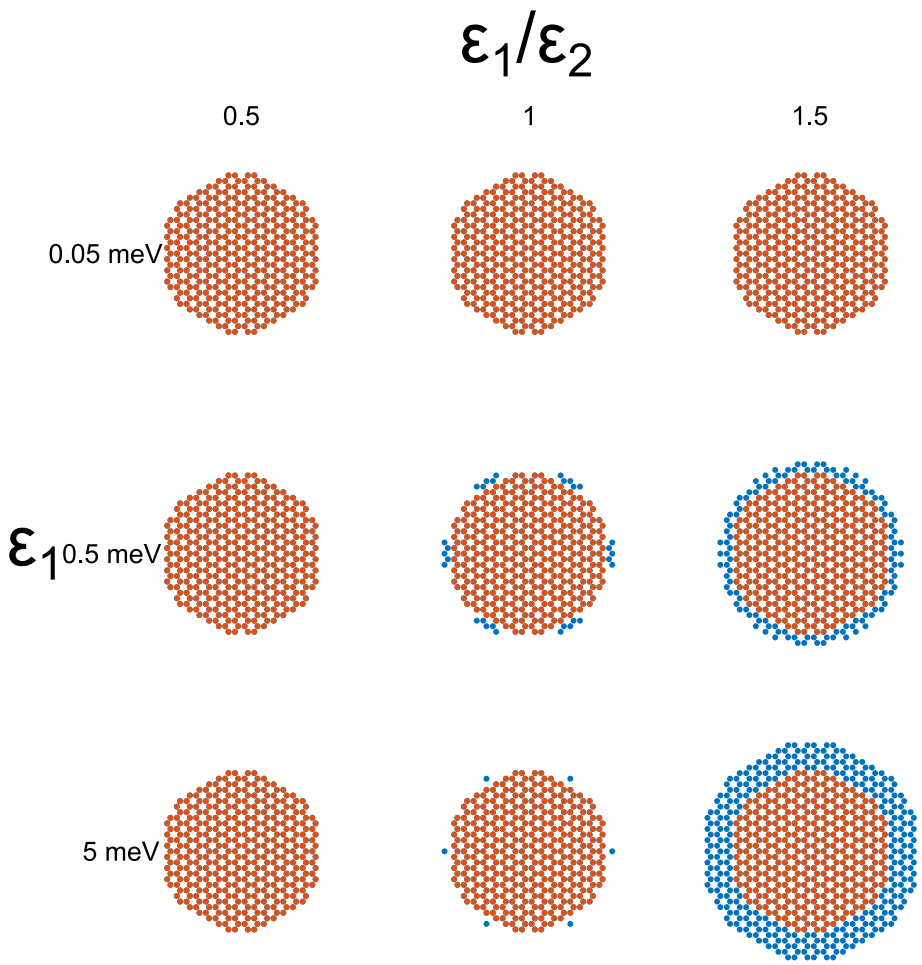

Figure 5.11: The atoms in contact at different values of input parameters.

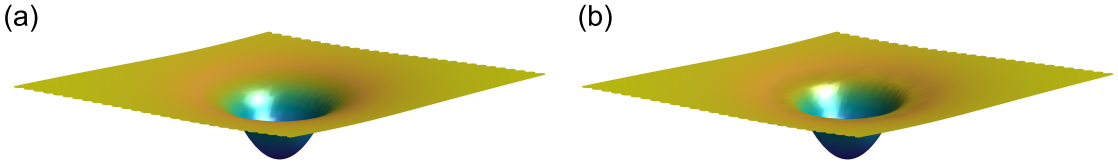

Figure 5.12: 3D surface of the undeformed (a) and deformed (b) layer at $\epsilon_1/\epsilon_2 = 0.5$.

5.5 Discussion

As mentioned in the introduction, a general consensus in the literature is that friction of 2D layered materials should decrease with an increasing number of layers, which is only partially true in the case presented in this chapter. For example, T. Filleter et al. (228, 229) report friction of multilayer graphene as only ½ of the friction of a monolayer and attribute the decrease in friction to better phonon coupling between the layers and, therefore, lower energy dissipation in multilayered systems. Our results further expand on the matter and display the increased effect of adhesion on friction, where on one hand, the samples experience a reduction of friction due to better phonon coupling and, on the other hand, an increase in contact area due to the

top layer conforming to the sliding body, which occurs only when the adhesion between the layer and the slider is larger than that between the layers.

The results in Figure 5.9, Figure 5.10 and Figure 5.11 demonstrate a significant influence of adhesion on the contact area when the attractive potential of the slider (i.e. the tip in the AFM experiments) is larger than the attractive potential of the substrate. The effect decreases with increasing load, thus illustrating that the highest differences should be observed at low loads, which complies with the experimental observations of friction. Four distinct regions can be identified between the layer and the slider: (i) the layer is in contact with both surfaces, (ii) the layer is in contact only with the top surface, (iii) the intermediate region where the layer is not in contact with either of the surfaces or (iv) the layer is in contact only with the substrate. Only points (i) and (ii) were considered to be a part of the contact area; however, point (iii) might also have a substantial effect on friction by promoting puckering.

There is also a considerable difference in the contact area between the regions (i) and (ii). Region (i) corresponds to a fully supported layer under compression, whereas region (ii) is unsupported and essentially under tension. We can, therefore, separate the contact area into two contact areas, the contact area in contact with both surfaces A_0, which is equivalent to the Hertz contact area, and the contact area that is only in contact with the slider ΔA. Consequently, the commonly accepted notion that $F_f = A\tau$ does not suffice in this situation. Nonetheless, we can redefine the expression as:

$$F_f = A_0\tau_0 + A_\Delta\tau_{unsupported}[+F_{pucker}(A_\Delta, N, v)], \tag{5.5}$$

where τ_0 and $\tau_{unsupported}$ are the contact shear strengths of the supported and unsupported layers, respectively. The magnitude of the puckering force cannot be directly determined from our model, as it depends on the affected area, number of layers and sliding speed and would require more advanced dynamic modelling. Nonetheless, we expect the puckering force to closely resemble the behaviour of $A_\Delta\tau_{unsupported}$, as the puckering force correlates to the out-of-plane deformation of the layer. We can, therefore, introduce a puckering coefficient $c_p \geq 1$ to the above expression so that:

$$F_f = A_0\tau_0 + c_pA_\Delta\tau_{unsupported}. \tag{5.6}$$

From the experimentally measured data, it is obvious that the friction of the bilayer sample is lower than the monolayer above 30 nN. As the final contact area from the model is at least as large as the Hertzian contact area, it follows that the contact shear strength needs to decrease for the multilayer sample to have lower friction.

Considering the results from T. Filleter et al. (228, 229) on graphene we can assume the contact shear strength of the bilayer and multilayer regions as approximately $1/2$ of that of the monolayer. If the friction measurement on the monolayer follows the characteristic $2/3$ power law, the contact shear strength of the monolayer can be obtained using the Hertz-plus-offset model (73). Furthermore, we can consider the findings of C. Lee et al. (35), who reported that the friction of supported graphene is the same as that of suspended. By taking A_0 and A_Δ from Figure 5.9 and assuming $\tau_{unsupported} = \tau_{monolayer-supported}$ and therefore $\tau_0 = {}^{\tau_{unsupported}}/_2$, we can predict the frictional response, as shown in Figure 5.13a. The result from the model very closely resembles the measured behaviour (Figure 5.13b), which confirms that the difference in adhesion between the layer and its immediate surfaces is the main cause of the observed frictional discrepancy.

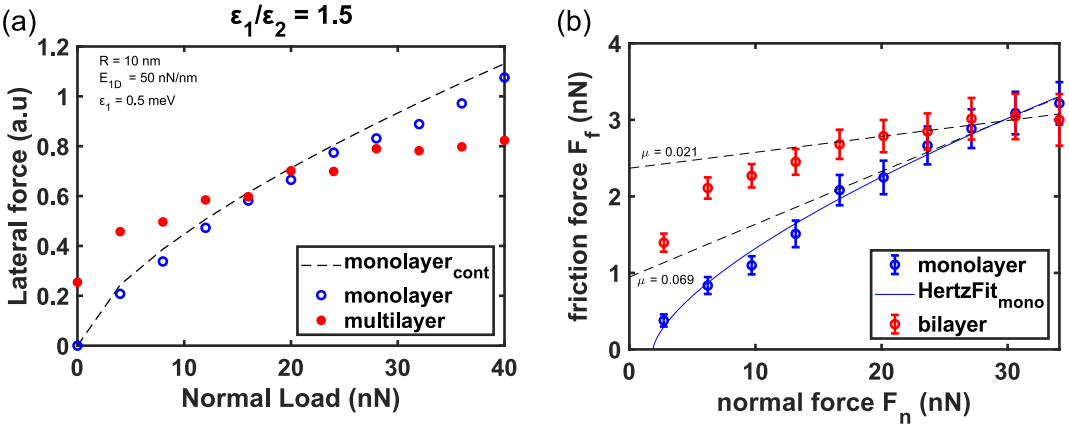

Figure 5.13: Predicted friction of the mono and multilayer samples according to the presented model (a), compared to the experiment (b).

The presented model does not directly differentiate between bilayer and multilayer systems beyond the possibility of changing the substrate elastic modulus to approximate the composite system. The layer exclusively interacts with the substrate/layer below and the surface above it. The values of the elastic modulus can effectively range from $E \approx E_{substrate}$ for a monolayer where the majority of the elastic deformation happens within the substrate, to $E = E_{2D,bulk}$ for a bulk multilayer ($Nt >$ Hertzian interaction depth, N is the number of layers and t is the thickness of a single layer), where all the deformation occurs in the sample.

The obtained results imply a large difference between the inter-particle interaction between two layers and between the layer and another material, i.e. Si or SiO_2 in this case. The results suggest that the interaction between the layer and the SiO_2 substrate would be at least as large as the interaction between the layer and the Si tip. Likewise, both interactions are larger than the interlayer interaction between two WSe_2 layers.

Due to finite distances between the particles in the layer, the resulting contact area appears discretised and slightly deviates from the perfectly circular shape of the

(a)

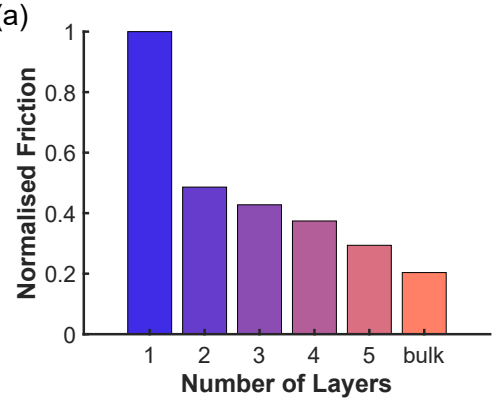

(b)

N° layers	$E_2\,(GPa)$	ε_2	τ_0
1L	2.5	0	$\tau_{unsupported}$
2L	5	$\varepsilon_1/_5$	$\tau_{unsupported}\,/_2$
3L	7.5	$\varepsilon_1/_4$	$\tau_{unsupported}\,/_2$
4L	10	$\varepsilon_1/_3$	$\tau_{unsupported}\,/_2$
5L	12.5	$\varepsilon_1/_2$	$\tau_{unsupported}\,/_2$
bulk	25	$\varepsilon_1/_{1.5}$	$\tau_{unsupported}\,/_2$

$R_1 = 10\ nm$ $\quad c = 0.2\ nm$ $\quad \tau_{unsupported} = 150\ MPa$

$E_{1D} = 50\,{}^{N}/_{m}$ $\quad \varepsilon_1 = 0.5\ meV$

Figure 5.14: Dependence of friction on the number of unsupported layers (a). Input parameters used in the simulation of each layer thickness (b).

contact area. In the model, we assumed that the particles in the substrate, the layer and the slider are perfectly aligned. Consequently, the forces only act along the z-direction. However, this is not the case in a realistic system, where it is likely that the contacting surfaces have different lattice geometry and lattice constants, where the lattices would overlap during sliding. We can, therefore, expect the results from the realistic system to resemble the continuous system more closely.

Ultimately, the presented model can also be used to describe the case of unsupported 2D layers, where the literature reports a reduction of friction with the number of layers. The generally accepted theory for unsupported layers attributes the decrease of friction to reduced puckering due to higher total stiffness (35, 36); stiffer layers deform less and, therefore, contribute less to the total friction. Our model lays out an alternative explanation and provides additional insight into the contact behaviour. The unsupported system can be studied by configuring the model parameters as $\epsilon_2 = 0$ for an unsupported monolayer or $\epsilon_2 > 0$ for an unsupported multilayer and gradually increasing the substrate elastic modulus with the number of layers (Figure 5.14). For the unsupported monolayer, the contact shear strength across the entire contact area was considered as $\tau_{unsupported}$, whereas for the higher layer numbers, friction was calculated using the same procedure as for the supported layers. Even without considering puckering in the simulation, the results show reduced contact area and, therefore, reduced friction with the increasing number of layers.

5.5.1 A model for fitting experimental data

Based on the findings from the numerical model presented above, we can derive a new model for fitting experimental data. As displayed in Equation 5.5, the friction of 2D layered materials comprises two independent components: (i) a Hertzian component $A_0(F_n)\tau_0$ and (ii) an additional adhesive component $A_\Delta(F_n)\tau_{unsupported}$. The Hertzian component is equivalent to the Hertz-plus-offset model (73), whereas

the additional adhesive component is also a function of load, but it depends on the adhesive conditions in the contact. The adhesive component can, therefore, be applied as a correction to the Hertz-plus-offset model:

$$F_f = \tau_0 \left\{ \pi \left[\frac{R}{K} \right]^{2/3} \left[F_n - F_{off} \right]^{2/3} \right\} + A_\Delta(F_n) \tau_{unsupported}. \tag{5.7}$$

As described earlier, τ_0 corresponds to the supported multilayer region of the contact and $\tau_{unsupported}$ to the region outside the initial contact area, which is approximately double τ_0. The appropriate function describing $A_\Delta(F_n)$ depends on the specific contact conditions and can differ between different systems. Considering that the difference between the measured bilayer and monolayer frictional responses follows a linear relationship (Figure 5.5) we define a function as:

$$A_\Delta(F_n) = \left[1 + \alpha F_n \right] A_{\Delta 0}, \tag{5.8}$$

where α and $A_{\Delta 0}$ are the correction factor and contact area difference at zero-load, respectively.

Equation 5.7 can, therefore, be rewritten as:

$$F_f = \tau_0 \left\{ \pi \left[\frac{R}{K} \right]^{2/3} \left[F_n - F_{off} \right]^{2/3} \right\} + n\tau_0 \left\{ \left[1 + \alpha F_n \right] A_{\Delta 0} \right\}; n = 2, \alpha \leq 0. \tag{5.9}$$

τ_0, F_{off}, α and $A_{\Delta 0}$ are fitting parameters. n is the ratio between the two contact shear strengths and is set before fitting. A factor of $n = 2$ is equivalent to the ratio used in the numerical model. It is important to note that n and $A_{\Delta 0}$ are mathematically dependent ($nA_{\Delta 0} = const.$). Therefore, fixing the ratio does not influence the final fitting result. Consequently, $A_{\Delta 0}$ obtained from the model is only accurate if n is accurate. Nevertheless, an optimisation for n can be performed during fitting by comparing the resulting τ_0 with the reference monolayer shear strength ($\tau_{unsupported} = \tau_{monolayer,supported}$). An equally valid approach would be to obtain $A_{\Delta 0}$ from the numerical model and leave n as a fitting parameter.

The formulation in Equation 5.9 is essentially only valid across a limited range of normal loads, as a negative linear term results in the function decreasing at higher loads. It is, therefore, mandatory to ensure the function is monotonically increasing, at least within the range of experimental data.

The fitting of the bilayer data to the presented model is shown in Figure 5.15a and shows that the model follows the data sufficiently ($R^2 = 0.9755$). The function is

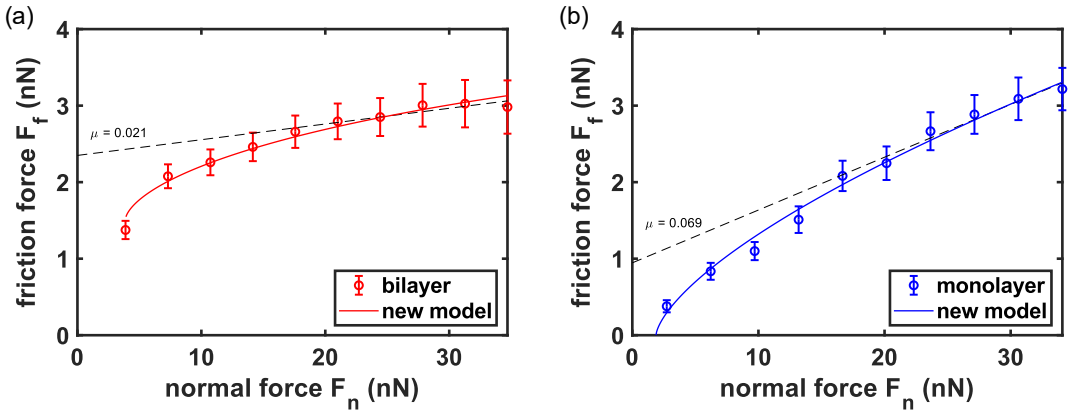

Figure 5.15: Experimental data fit to the new model: bilayer (a) and monolayer (b).

monotonically increasing up to $5F_{max}$ (175 nN). The monotonicity criterion reduced the quality of the fit slightly, but it is necessary to ensure the viability of the function.

The model remains valid for monolayer samples and reverts to the Hertz-plus-offset model when no deviation from the $^2/_3$ power law exists, as displayed in Figure 5.15b. For comparison, the fitting parameters are collected in Table 5.1 alongside the Hertz-plus-offset fit, which returns the same results for the monolayer. The only difference between the models is in marginally wider confidence intervals of the new model, resulting from a larger number of fitting parameters.

Table 5.1: Contact properties

	τ (MPa)	F_{off} (nN)	R^2 (/)	α (nN^{-1})	$A_{\Delta 0}$ (nm^2)	n (/)
monolayer	242.5 ± 13.6	1.9	0.9885	0	0	/
monolayer$_{\text{Hertz}}$	242.5 ± 12.4	1.9	0.9885	/	/	/
bilayer	195.6 ± 10.4	3.9	0.9755	-0.0193	6.78	1.24

5.6 Conclusions

In summary, we have shown that nano-scale friction of 2D materials differs significantly between supported monolayer and multilayer systems, not only in magnitude, as previously reported in the literature, but also in load-dependent behaviour. We attribute the frictional discrepancy between the two systems to the differences in adhesive behaviour between the slider, layer and substrate, which, in turn, increases the contact area. The observations were supported by a simple static numerical model, which allowed to separately model the inter-particle interactions between the analysed topmost layer and the probe or the top layer and the substrate. The model confirmed that when the adhesion to the probe is higher than to the

substrate, the total contact area increases significantly. The relative effect of adhesion decreases rapidly with the load.

Furthermore, some out-of-plane deformation of the layer around the contact area can even be observed when the adhesion to the probe is lower than to the substrate. However, it is not high enough to bring the layer within the influence of the slider. Nonetheless, such deformation can still manifest itself in increased friction as increased puckering. However, the behaviour can be challenging to analyse and would require advanced and computationally expensive dynamic modelling.

Finally, we have introduced a new model for fitting experimentally measured multilayer data by combining the established Hertz-plus-offset with a correction component for the contact area gain. The new model has been shown to work well with the presented data set and provides a comprehensive tool for obtaining the contact properties of a more complex multilayer system.

Chapter 6

Atomic-scale friction of WS_2 multilayers

6.1 Introduction

By further decreasing the measurement scale, we enter the regime of the AFM tip interacting with only a few atoms or even just a single surface atom at the time. Certain conditions need to be met to successfully perform measurements at this scale, including low adhesion, very sharp and well-defined probe geometry, absence of external noise, and precise tuning of the measurement parameters. To meet those challenging conditions, the measurements presented in this chapter were performed with a different atomic force microscope (AFM). Adhesion was managed by cleaning the samples through pre-scanning, which effectively removed any potential adsorbed species from the scanned area[1]. The measurements were performed in an aqueous environment, which reduced adhesion and fluctuations by removing meniscus forces around the contact. A fresh probe was used, and special care was taken to prevent excessive probe wear, such as only scanning over a small area and using slow scanning speeds and low loads. Lastly, the measurements were performed overnight, which minimised mechanical vibrations interfering with the system and ensured the best possible temperature stability.

The work presented in this chapter was undertaken in collaboration with the *Czech Technical University in Prague*, the *Institute of Physics of the Czech Academy of Sciences* and colleagues from the *University of Southampton*. I have performed the measurements during the secondment at *Czech Technical University in Prague*. Dr Egor Ukraintsev (*Czech Technical University*) assisted with the measurements and AFM setup.

[1] We did not observe any measurable levels of contamination, but some molecules could still be present on the surface and interfere with the main experiment.

Computational fitting to the modified Prandtl-Tomlinson model and the model development were done by Paola Torche (*University of Southampton*), and the results of the fitting are briefly summarised at the end of this chapter. A manuscript for a paper focused on fitting the experimental data to the model is currently in preparation.

6.2 Methodology

The atomic-scale friction measurements on a WS_2 multilayer were performed in an aqueous environment on nTegra (ND-MDT, Russia) atomic force microscope using commercial ND-MDT CSG01 contact mode probes. Normal stiffness was determined according to the Sader method (233), using the built-in script, and lateral force constant according to the wedge calibration method (95), using a commercial TGF11 grating. The obtained values of k_N and α were 0.078 $\mathrm{N\,m^{-1}}$ and 628 $\mathrm{nN\,nA^{-1}}$, respectively. Measurements were performed in water to reduce the adhesive forces. Consequently, very low sliding speeds ($\leq$ 25 $\mathrm{nm\,s^{-1}}$) had to be used to avoid hydrodynamic effects interfering with the measurements.

Large multilayer regions were identified using the optical system of the AFM, and the probe was centred on the selected region before approaching. The area chosen for analysis was initially scanned multiple times at a low normal load ($<$ 10 nN) and 50x50 $\mathrm{nm^2}$ scan size to remove any adsorbed species on top of the sample. The actual measurements were performed on a 10x10 $\mathrm{nm^2}$ area unless otherwise noted. Three different scan rates were used: 0.33 Hz, 0.75 Hz and 1.25 Hz corresponding to 6.6 $\mathrm{nm\,s^{-1}}$, 15 $\mathrm{nm\,s^{-1}}$ and 25 $\mathrm{nm\,s^{-1}}$, respectively. The scan rates showed a good correlation between the duration of the scan and the quality of the signal. The experiments were taken at a low gain setting (0.1) to reduce the influence of system vibrations interfering with the measurement.

A custom script was used during the measurements to correct for the drift in the z-direction by readjusting the set-point every 256 lines. The script was provided by the ND-MDT software development team.

6.3 Results

6.3.1 Friction maps

An optical image of the analysed WS_2 sample is shown in Figure 6.1. WS_2 experiences multilayer growth around the nucleation sites, resulting in a conglomeration of the flakes, which gets thinner further away from the nucleation site. The number of layers

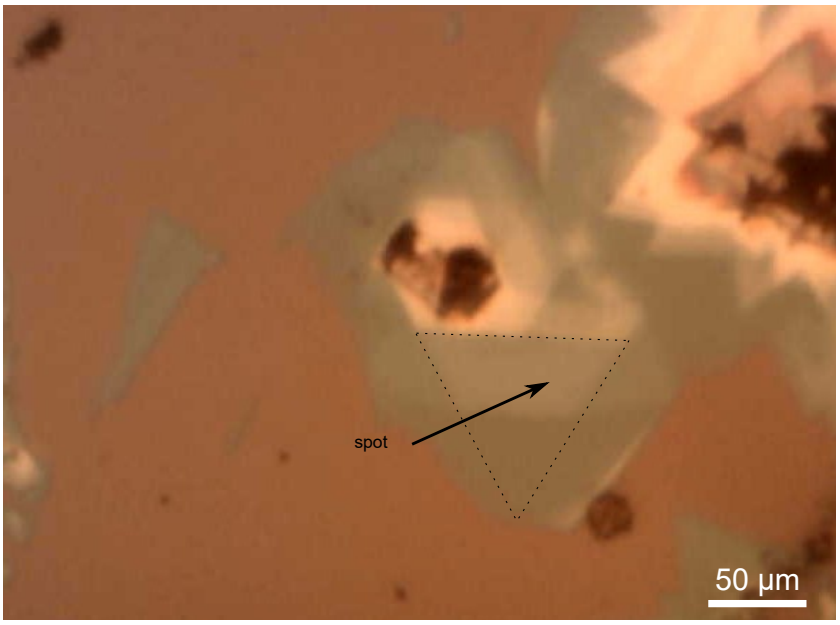

Figure 6.1: Optical image of the WS_2 sample and the spot in which the following measurements were taken.

can be estimated from the variation in the colour of the flakes on the substrate. While the WS_2 monolayer is almost transparent and shows a dark cyan colour, the multilayer is brighter, and the yellow colour can be seen for thicker flakes (234). The thickness of the spot selected for the analysis was at least three layers. An outline of a potential flake orientation is highlighted by the triangle extending around the edges of the measured layer. However, considering that the other flakes are oriented at various angles the actual crystal orientation can not be determined from the shape of the displayed flake alone.

The friction maps obtained on the multilayer WS_2 sample are shown in Figure 6.2a and Figure 6.3a. Both forward, i.e. left-to-right, and backward, i.e. right-to-left, scans are included. Figure 6.2 displays stick-slip behaviour at different normal loads, and Figure 6.3 shows the same behaviour at a fixed load and different sliding speeds. The images were levelled using a 1^{st} degree polynomial flattening, and a single pass of a conservative de-noise algorithm (2 px) was applied to all images (unedited images in Appendix C). The smoothing algorithm removed a significant amount of noise at 6.6 $nm\,s^{-1}$, thus making the surface features clearer. The smoothing was less effective at higher sliding speeds due to a lower spatial frequency of the noise.

No clear patterns, which would unambiguously indicate the lattice orientation, can be seen on any of the scans, despite a very clear stick-slip signal on every single line of the scan, as displayed in Figure 6.2b and Figure 6.3b. The friction loops were obtained from unedited friction maps. Different lengths of stick-slip events can be identified from visual inspection of the scans. Large deviations can even be observed within the same scans, thus, strongly indicating that some probe jumps occur over multiple

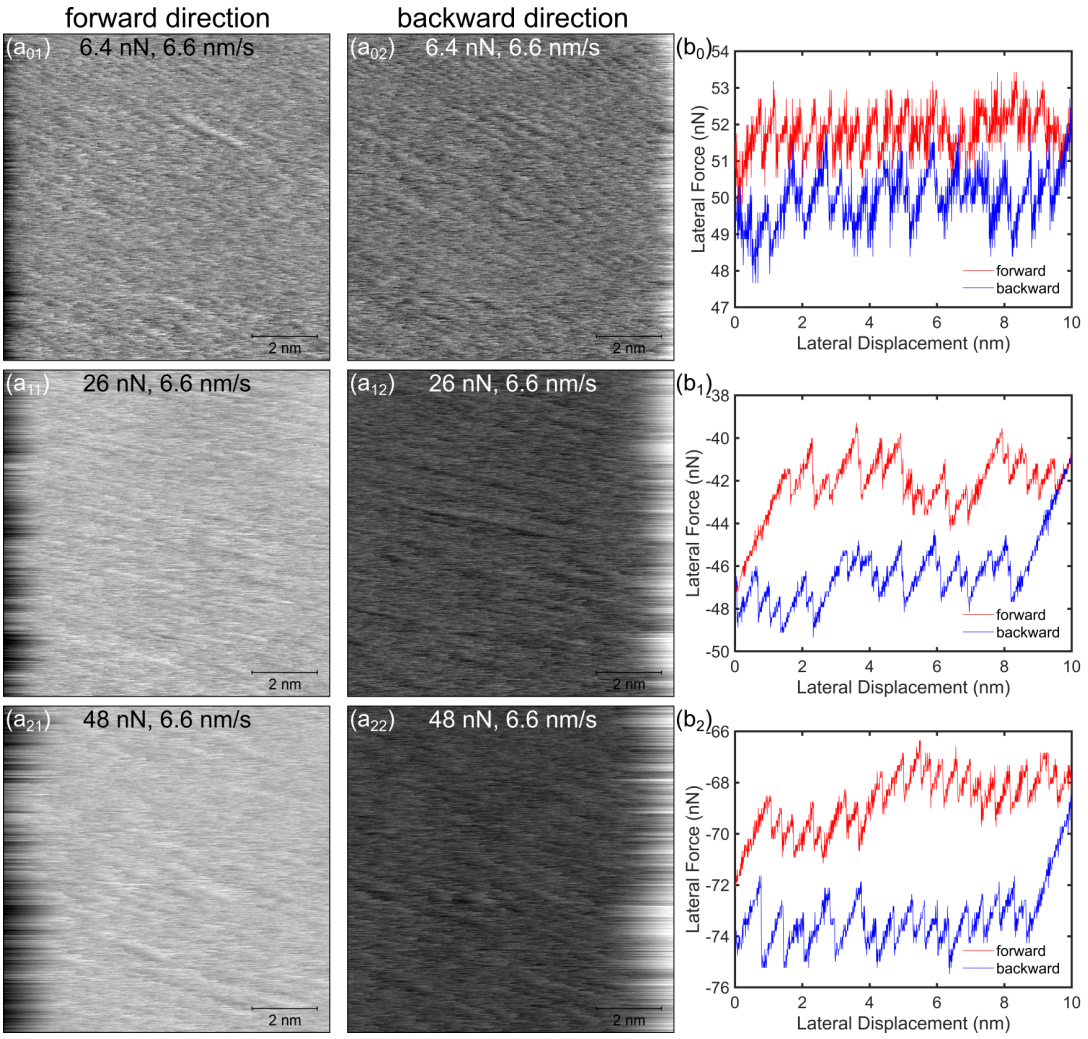

Figure 6.2: Friction maps obtained at different normal loads on multilayer WS_2.

lattice distances. In an ideal system, we would expect the 'peak-to-peak' distances to precisely correspond to the lattice constant of WS_2, which is 0.31 - 0.33 nm (235, 236).

Nevertheless, more careful observation of the scans reveals occasional patches with a clear pattern. The measurement obtained at 6.4 nN (see the top of Figure 6.2a_{01} and a_{02}) contains a number of lines ($\sim$ 1.5 nm wide) with a well-defined characteristic stick-slip pattern. Cropped and enlarged region is shown in Figure 6.4a, where the characteristic pattern is visible.

2D FFT (Fast Fourier Transform) filtering revealed additional information about the underlying lattice structure (Figure 6.4b). The lattice appears compressed in the y-direction, and the corresponding distances between the sulphur atoms a_1, a_2 and a_3 are 0.33 nm, 0.28 nm and 0.48 nm, respectively. This observed deformation could be a consequence of the piezo drift in the y-direction (see Section 2.2.2), improper system

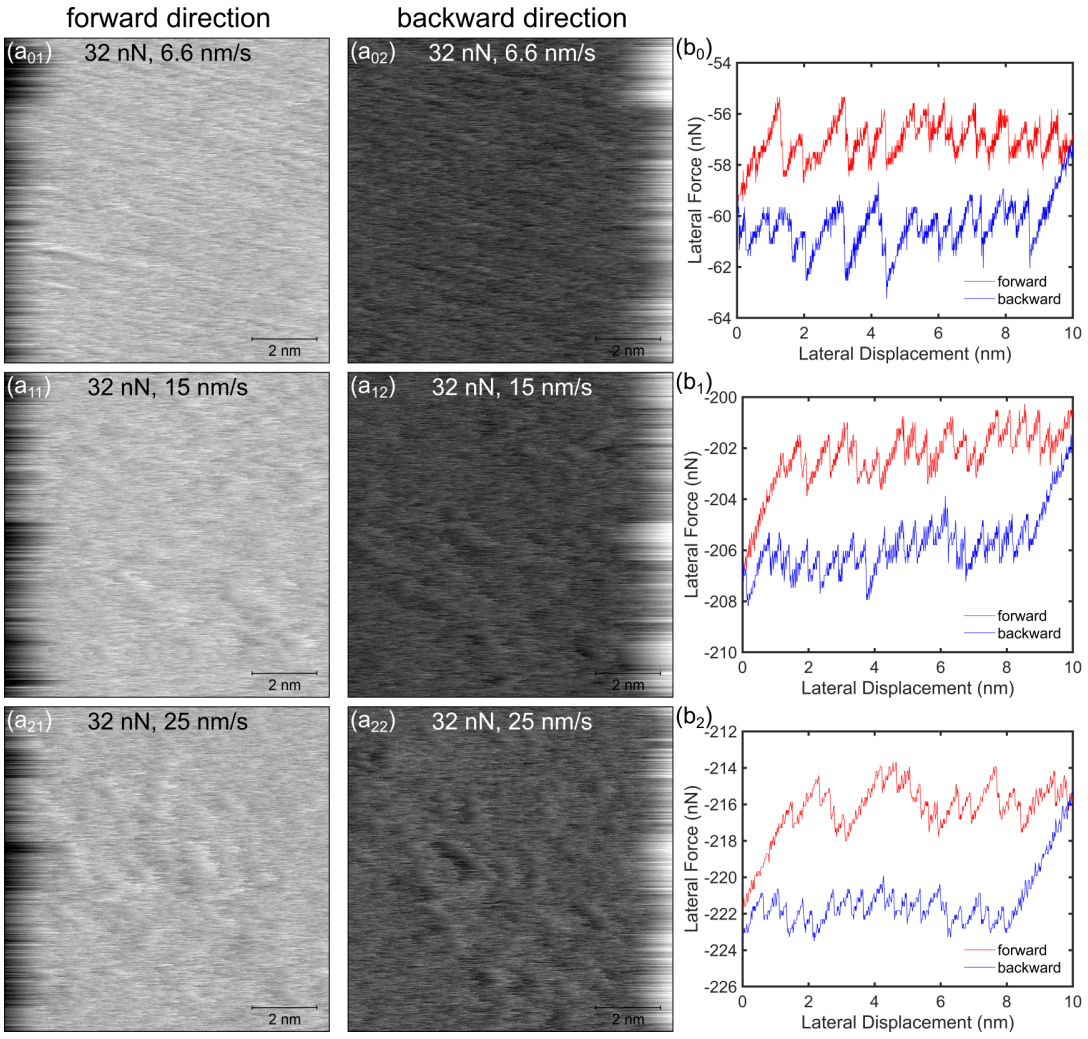

Figure 6.3: Friction maps obtained on multilayer WS_2 at different scanning speeds.

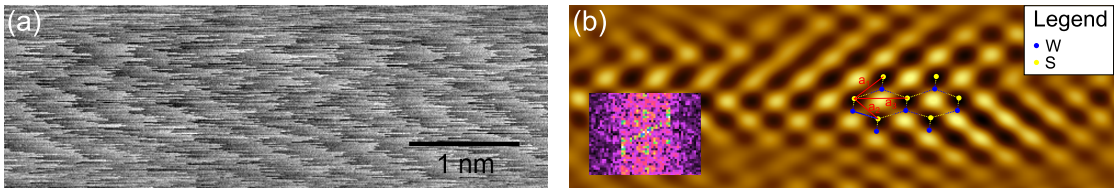

Figure 6.4: Enlarged detail of the backward scan at 6.4 nN (a). The same area after 2D FFT filtering (b). The inset shows the 2D FFT transformation of the scan in (a).

calibration[2], or lattice orientation. Due to low probe stiffness, the tip can jump to a minimum that is not aligned with the scanning line, which would also explain the discrepancies observed in the jump distances during the slip events. This is further highlighted as the lattice appears to be slightly tilted (7 deg), whereas the minima appear perfectly aligned along the x-axis. The effect of this phenomenon is discussed further in Section 6.3.4

[2]The setup in which we measured only allowed up to 1 µm scan size, which is smaller than most commonly available calibration gratings. We, therefore, had to rely on the factory calibration, which could potentially result in some discrepancies.

6.3.2 Peak detection algorithm

To analyse and deconstruct the measured stick-slip data, we have developed an algorithm that detects and counts stick-slip events. Let $line_k$ be the scan along the k-th line of the entire measured area. A schematic of a single scan line representing a noise-free stick-slip signal is shown in Figure 6.5. z-axis represents a lateral force in friction maps, and x and y are spatial coordinates. We choose the x-axis to be in the direction of the scan. A general 'z-axis' is used here as the algorithm can be adapted to analyse any data that show similar behaviour. The points X_{0i} correspond to the location of stick events, that is the position in which the tip apex is stationary and only the lateral force is increasing. A slip event is represented by a rapid decrease in lateral force when the probe snaps from one position to the next. The distances between the two points, therefore, correspond to the entire stick-slip event. x_f is the scan distance (10 nm).

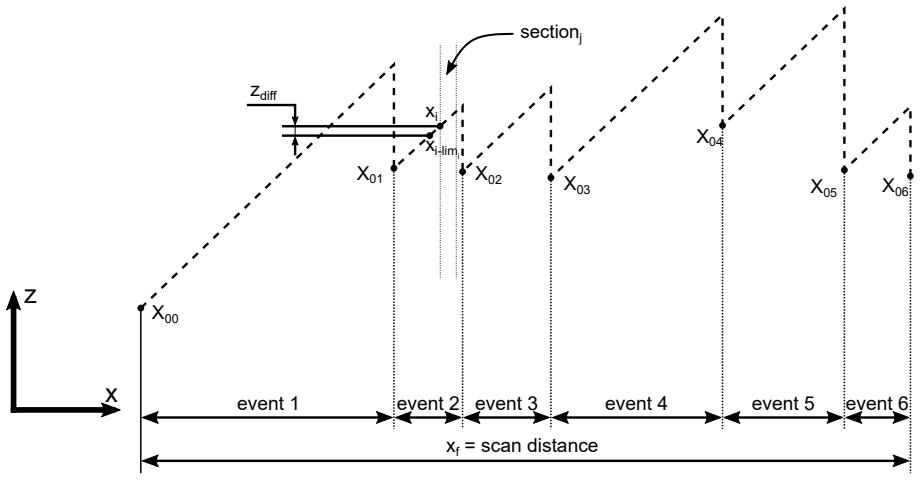

Figure 6.5: A schematic representation of a single line exhibiting stick-slip behaviour, with the corresponding points used in the algorithm for data evaluation.

The flowchart of the stick-slip analysis algorithm is shown in Figure 6.6. Each line of the scan is analysed independently and k marks the line number. Each scan line is first split into smaller sections and a minimum z_{min} of each section is determined. Next, a maximum in the interval between the limiting point x_{i-lim_i} and the location of the local minimum x_i is determined and the difference z_{diff} between them is calculated. The interval limit $lim_i > 1$ is one of the input parameters in the algorithm and is used to reduce the errors that may arise due to noise in experimental data; just comparing two neighbouring points could increase the chance of missing a significant number of the events. Values of up to 10 were used for lim_i when analysing data presented in this chapter.

The difference between the values is compared against the threshold lim_{diff}, which determines whether the difference between the two points is large enough to correspond to the stick-slip event. The validity is confirmed by the sum of all the

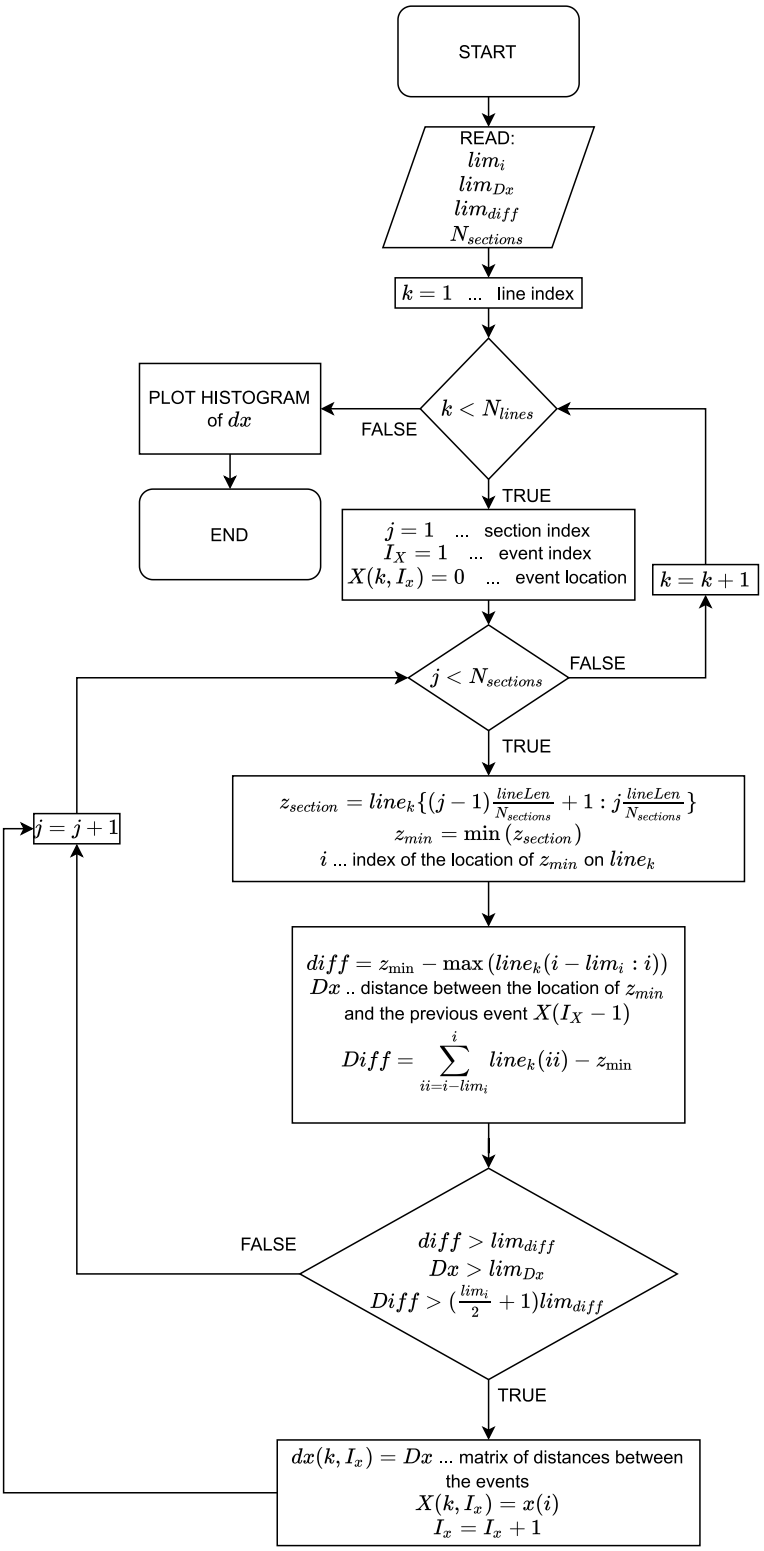

Figure 6.6: Algorithm for the analysis of stick-slip data.

differences $Diff$ in the range $(i - lim_i, i)$; the point is only considered to be a location of the stick-slip event if $Diff > (lim_i/2 + 1)lim_{diff}$. This additional criterion significantly reduces the number of false positives arising from noisy data and, therefore, allows tightening of the input parameters. Furthermore, a lateral limit lim_{Dx}

is used to remove potential double evaluation of a single event when there are two apparent minima due to noise. lim_{Dx} limits the smallest distance between the two neighbouring events. When two events are identified with the lateral separation $< lim_{Dx}$, only the one with lower z_{min} is stored. The algorithm was optimised to work with noisy data and is, therefore, a preferred method to the standard peak detection algorithms available in commercial software.

6.3.3 Distribution of stick-slip event distances

Upon completion of the algorithm, the distances between each pair of stick-slip events are saved, and the data of all the lines is displayed in the histogram showing the occurrence of each stick-slip distance in the range (lim_{Dx}, 2 nm). Histograms for the data from Figures 6.2a$_{01}$ and a$_{02}$ are shown in Figure 6.7a. Separate histograms are drawn for the forward and backward scans. A probability density function is then fit to the obtained data. A sum of multiple Gaussians, where each peak displays jumps over a single, double or many lattice distances, was chosen as a suitable probability density function. The insets in the histograms show the positions of the stick-slip events along a characteristic single scan line, as determined by the algorithm, thus

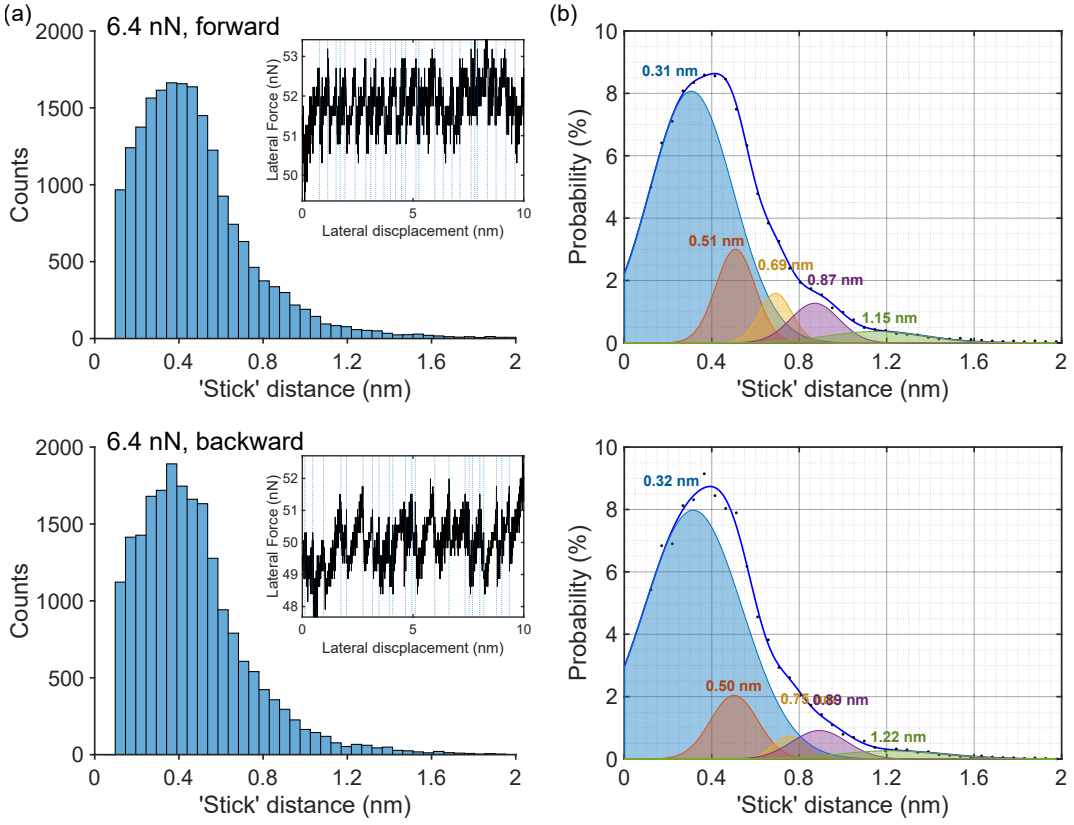

Figure 6.7: Histograms (a) and probability density functions (b) for the measurement at 6.4 nN and 6.6 nm s^{-1}. The insets in (a) show the corresponding stick-slip signal (single line) and the locations of the identified events.

demonstrating the ability of the algorithm to accurately detect the events. The algorithm correctly identifies the events despite a large amount of noise in the data. There are no falsely identified or missed events.

The distribution shown in Figure 6.7 displays a large number of separate underlying peaks. There is not much difference between the forward and backward scans; all peaks but one appear at almost the same location and are of similar magnitude. The peaks located at 0.31 - 0.32 nm, 0.87 - 0.89 nm and 1.15 - 1.22 nm correspond to the jumps over a single, triple and quadruple lattice distance, which is expected, being this the only data set that displays atomic lattice pattern. Additionally, the peaks at 0.50 - 0.51 nm and 0.69 - 0.77 nm are either a result of the probe jumping to minima not directly on the scanned line or correspond to the jumps over a dual lattice constant. The peaks are very broad, indicating a high degree of thermal activity on the surface.

The highest difference between the forward and backward scans can be seen in the 3rd peak, where the magnitude of the backward scan is much lower, and the peak is positioned 0.08 nm higher than the forward scan. However, note that fitting the 5th degree Gaussian is non-trivial due to a large number of free parameters (15), meaning that even a minor difference in the data caused by the underlying noise could result in

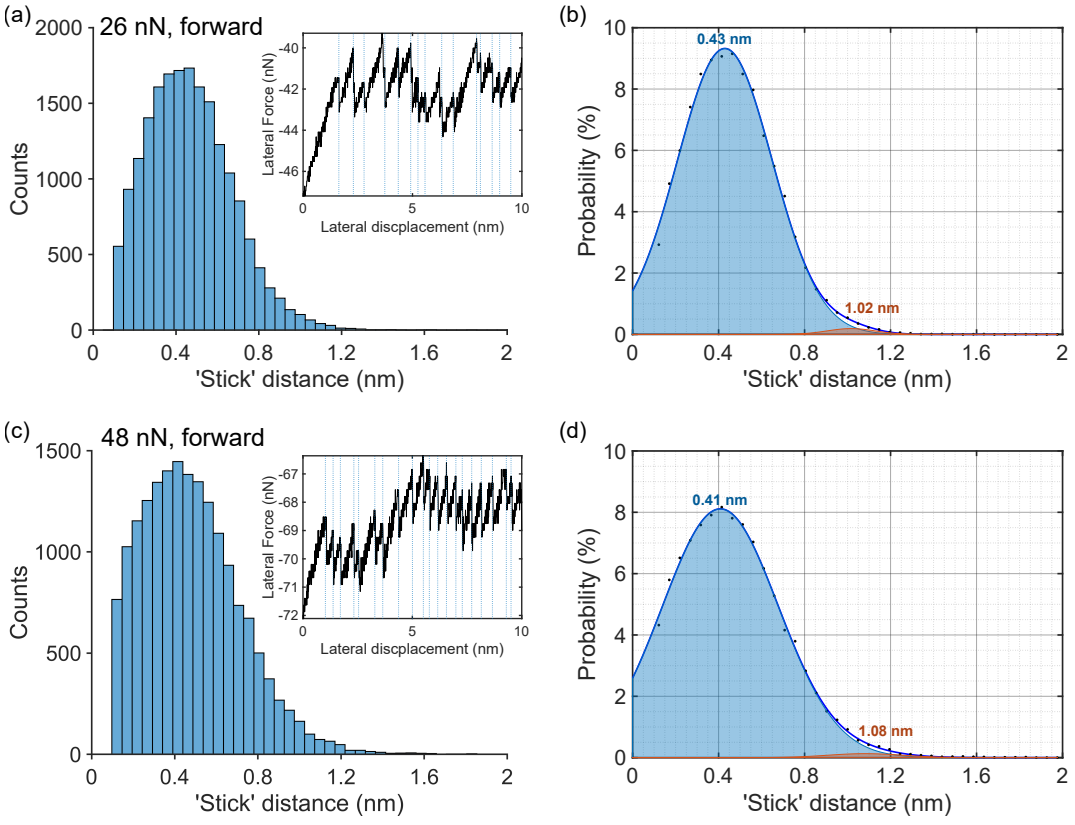

Figure 6.8: Histograms and probability density functions for the measurements at 26 nN (a and b) and 48 nN (c and d) obtained at 6.6 nm s^{-1}. The insets in (a) and (c) show the corresponding stick-slip signal (single line) and the locations of the identified events.

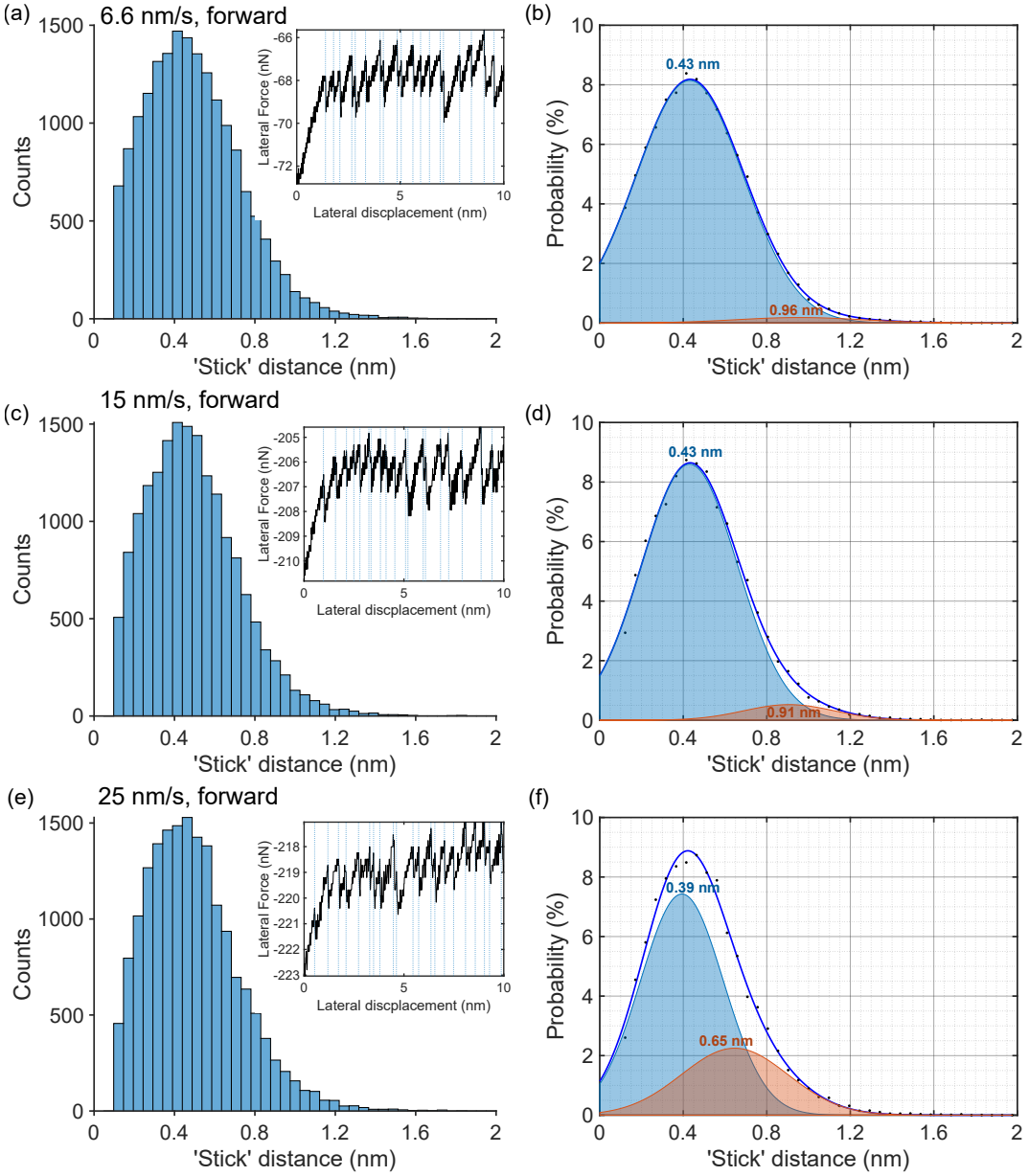

Figure 6.9: Histograms (a, c, e) and probability density functions (b, d, f) for the measurements at 32 nN. The insets in (a), (c) and (e) show the corresponding stick-slip signal (single line) and the locations of the identified events.

a substantially different fitting result. In fact, relying solely on the mathematical fitting methods, such as non-linear least squares, produced significant discrepancies even between the forward and backward scans. Therefore, fitting was performed in stages by manually tightening the range of possible positions of each peak and comparing the results between forward and backward scans to obtain the best agreement between the two.

The data obtained at higher loads (26 and 48 nN) is shown in Figure 6.8 and does not display much difference in the behaviour between the scans. The total number of events is lower at a higher load, as the initial slope until the first event is longer. The

average number of events (see Table 6.1) at 48 nN is 18±2, whereas at 26 nN is 19±2. Only two broad peaks are observed; the main peak at 0.41 - 0.43 nm, corresponding to a jump over a single lattice constant and a smaller peak at 0.95 - 1.08 nm, resulting from higher-order jumps.

The measurements at 32 nN in Figure 6.9 exhibit similar distribution to 26 and 48 nN. At 6.6 nm s^{-1}, the position of both peaks is identical to the other two measurements at the same sliding speed, whereas increasing the sliding speed to 15 nm s^{-1} increases the magnitude of the 2nd peak slightly and causes it to move to 0.84 - 0.91 nm. This effect is even more pronounced at 25 nm s^{-1}, as the magnitude of the 2nd peak increases significantly, and the peak is seen at 0.65 - 0.78 nm. The position of the main peak is also shifted slightly; however, a difference of only 0.04 nm is not significant, as it is caused by the 2nd peak width reaching further into the region of the 1st peak.

Table 6.1: Averaged event distances and number of events for each scan

v (nm s^{-1})	F_n (nN)	$\bar{D}$ (nm)	σ_D (nm)	$\bar{N}$	σ_N
6.6	6.4	0.49	0.10	20	4
6.6	26	0.47	0.04	19	2
6.6	32	0.49	0.05	18	2
6.6	48	0.48	0.05	18	2
15	32	0.49	0.05	18	2
25	32	0.51	0.07	18	2

Observing the main peak at almost the same position confirms that the signal originates from the surface and is not influenced by external noise. Increasing sliding speed substantially reduces the system relaxation time, thus increasing the probability of higher degree jumps and resulting in a more pronounced 2nd peak. As the sliding speed increases, the behaviour transitions from mainly jumps over a single lattice constant and occasional higher degree jumps to more dual lattice constant jumps, thus bringing the 2nd peak closer to 0.62 nm. This is in contrast with the observations from Chapter 5, where the effect of sliding speed on friction was negligible.

6.3.4 Potential energy surface and lattice orientation

From the histograms and friction maps, we can gather enough information to deduce that the scanning direction was not aligned with the sample orientation; however, accurate determination of the orientation from the images is not possible due to a lack of clear patterns and wide distributions. As mentioned above, only a crop of an area of one of the scans revealed a pattern and indicated a rotation angle of 7^{o}.

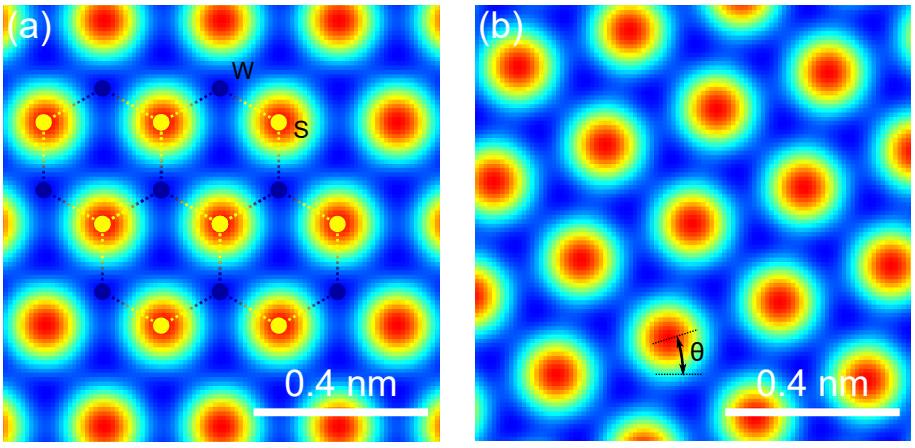

Figure 6.10: Potential energy surface of WS_2 (a). The same potential energy surface rotated by an angle θ (b).

To further examine the effect of the sliding direction on the resulting signal, we define a simple periodic surface, with the peaks corresponding to the position of sulphur atoms in the WS_2 lattice (Figure 6.10a). The potential energy surface is defined as (237):

$$E = \frac{1}{3}\left[\cos\left(\frac{4\sqrt{3}\pi v}{3a}\right) + 2\cos\left(\frac{6\pi u}{3a}\right)\cos\left(\frac{2\sqrt{3}\pi v}{3a}\right)\right], \tag{6.1}$$

where a is the lattice constant, and $u = \cos(\theta)x + \sin(\theta)y$ and $v = -\sin(\theta)x + \cos(\theta)y$ are the coordinate axes rotated by an angle θ. The rotated surface is displayed in Figure 6.10b. Squares with 10 nm sides are created (note that the surfaces shown in Figure 6.10 are cropped for clarity), and the spatial resolution is set to resemble the measured scans (i.e. 1024x1024 points), meaning that any resolution effects are matched with the measurements. A point attached to a spring is dragged over the potential surface (Prandtl-Tomlinson model) to resemble the AFM measurement. The force of the spring required to move across the energy barrier resembles the lateral

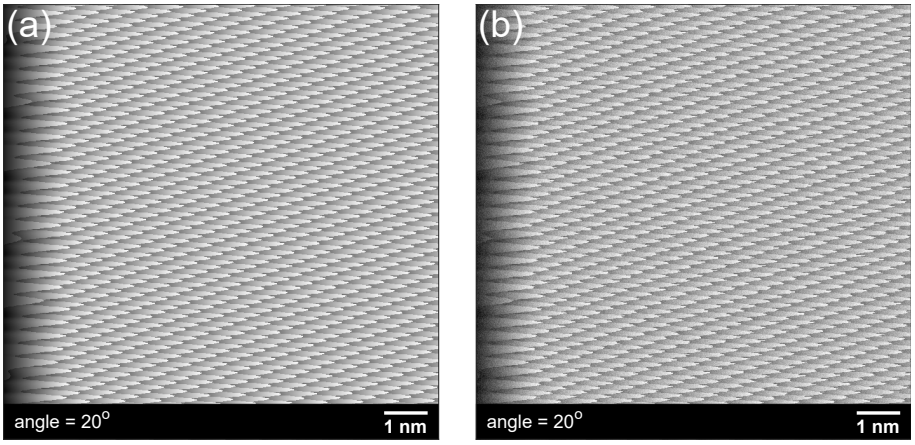

Figure 6.11: Generated friction force map without noise (a) and with noise (b).

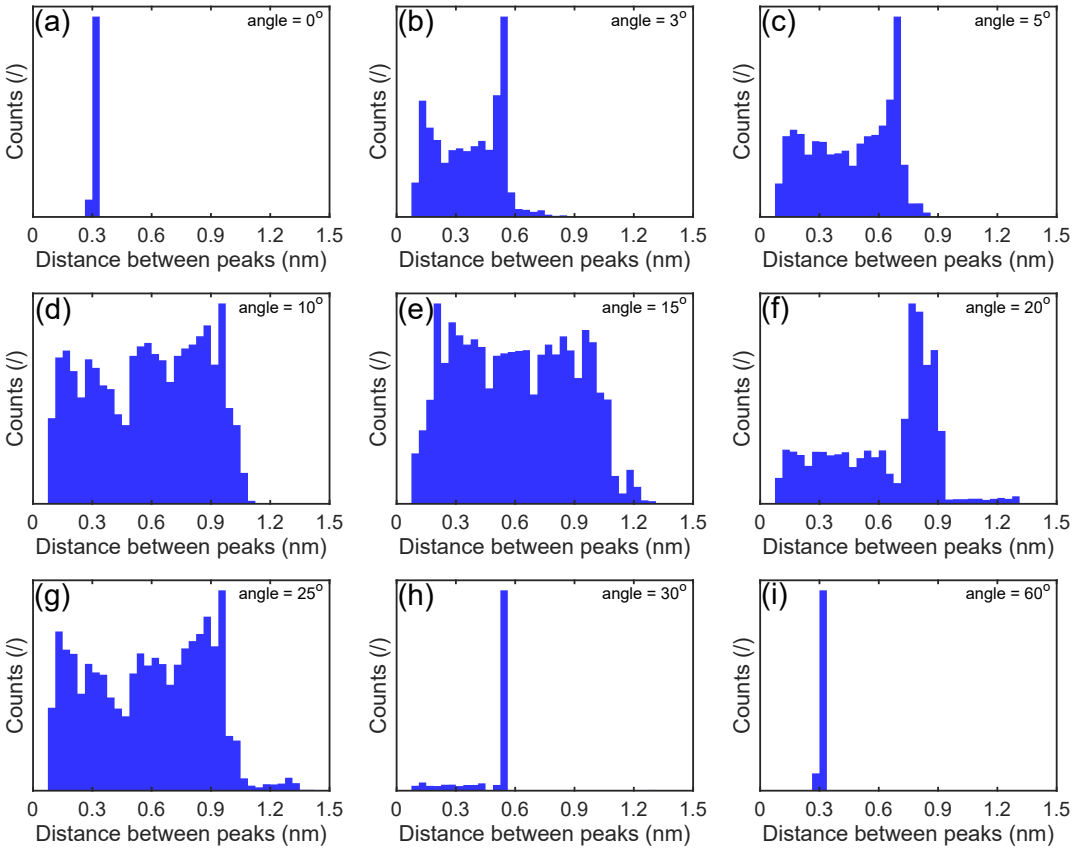

Figure 6.12: Distances between the peaks on single lines of the calculated force map rotated by a certain angle. Note that the histograms are scaled to the highest bar at each angle.

force in the AFM scans. An example of the resulting force map is shown in Figure 6.11. The data in Figure 6.11b contains added additional random noise, thus better representing realistic AFM measurements at finite temperatures.

Figure 6.12 displays the distances between the force peaks on single lines at nine different rotation angles between 0° and 60°, which is analogous to the stick-slip behaviour of a realistic system.

From the histograms, it follows that the stick-slip events are separated by an exact lattice constant only when the angle is $n60°$ (Figure 6.12a, i). Note that there is still a distribution of values around the exact value of the lattice constant, resulting from the finite resolution of the force map. At 30° (Figure 6.12h) the majority of jumps are $\sqrt{3}a$ = 0.54 nm (the lattice constant in the armchair direction). Therefore, only the lines aligned with the lattice have all distances between the local minima precisely matching the lattice constants, i.e. 0.31 nm in the zig-zag direction (0°, 60°, ...) and 0.54 nm in the armchair direction (30°, 90°, ...). Increased likelihood of higher-order jumps is observed when the angle deviates from those angles (Figure 6.12b-g). Consequently, the distances between force peaks become much larger along those lines, the

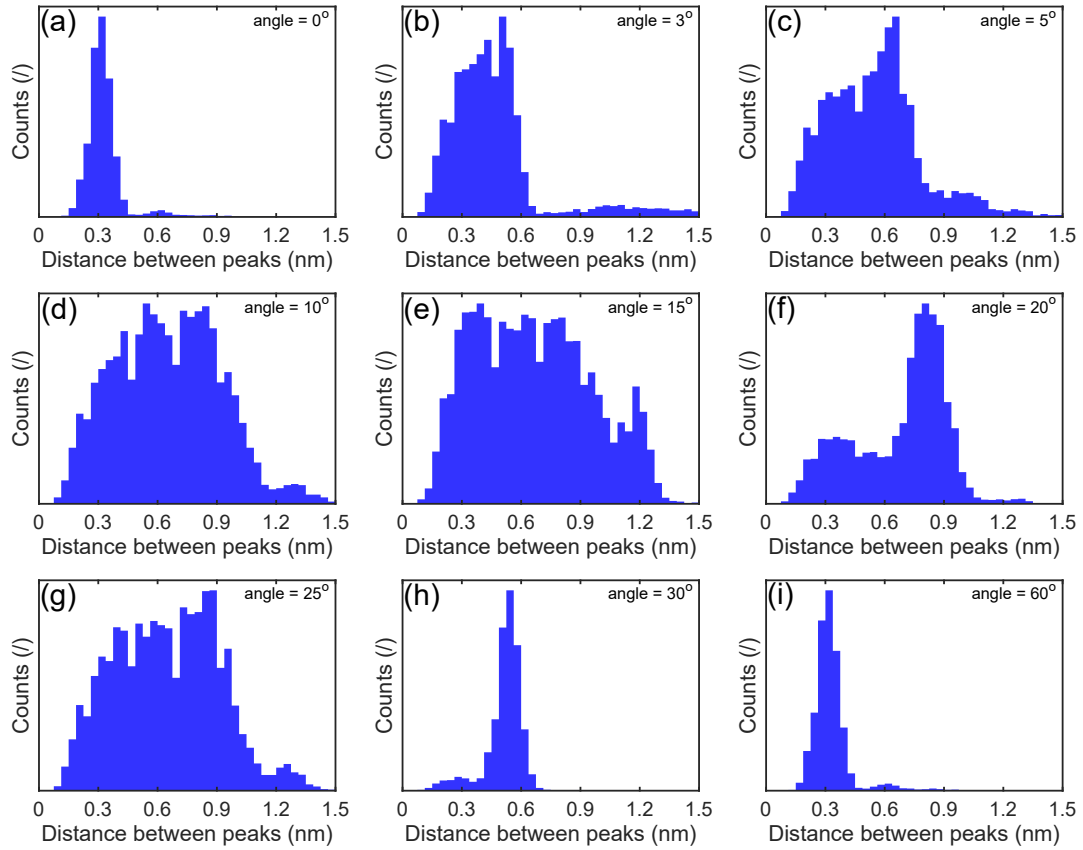

Figure 6.13: Distances between the peaks on single lines of the calculated force map with included noise rotated by a certain angle. Note that the histograms are scaled to the highest bar at each angle.

distributions broaden, and the specific peaks in the distributions become more difficult to identify.

Adding noise to the force maps further results in peak widening and produces more realistic distributions that closely resemble the distributions seen on the measured data, as shown in Figure 6.13. To distinguish between the actual peaks and noise, the minimum peak prominence in the peak detection algorithm is specified as double the maximum noise magnitude. With added noise, the specific peaks corresponding to jumps over single, double, triple or quadruple lattice constants are more easily distinguishable.

Furthermore, finite cantilever stiffness in the y-direction could cause the probe to jump towards the minima that are not directly in a line, which would have an additional impact on the final behaviour and therefore result in even wider peaks and an increased probability of higher-order jumps, as was observed in the measured data.

Figure 6.14 displays the average distance between two neighbouring peaks at different angles. The data was generated in 1° increments. The average distances between the force peaks range from 0.31 nm at 0° to 0.61 nm at 20° (0.67 at 22° considering noise).

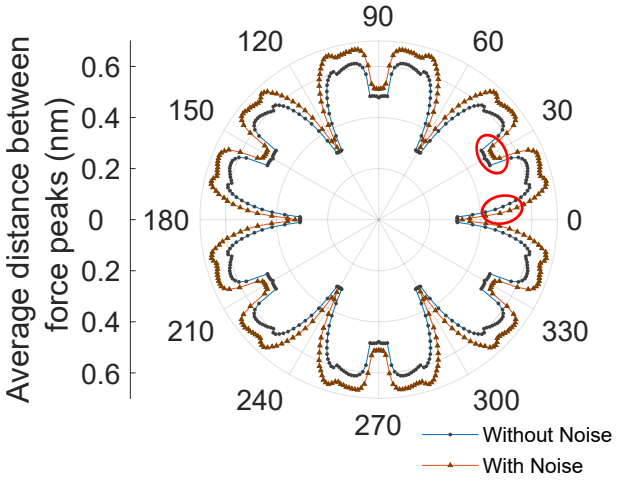

Figure 6.14: Variation of the average distance between the force peaks with the rotation angle.

The average event distances for the experimental stick-slip data were between 0.47 nm and 0.51 nm (see Table 6.1), whereas the leading peaks in the histograms were between 0.39 nm and 0.43 nm. Comparing these values with the data in Figure 6.14 allows us to determine the scanning direction to be rotated by either 2° - 7° or around $30° \pm 4°$ against the sample lattice orientation. Note that the analysis here has only been focused on the first 60°, but the same applies to the rest of the angles, considering six-fold symmetry.

Furthermore, another reason for the observed wide distributions of stick-slip distances could also be a polycrystalline structure of the sample or a heavily distorted crystal lattice. The polycrystalline structure is less likely as no grain boundaries were observed on the sample. On the other hand, lattice distortions are possible in CVD deposited samples (224).

6.3.5 Quantification of the atomic-scale frictional behaviour at the atomic-scale

Up to now, we have only looked at the geometrical features observed in the friction maps. After having determined the location of the events we can further examine the magnitude of the friction signal and (i) quantify the average peak heights, (ii) determine the average friction force and dissipated energy per unit cell (see Eq. (2.29)) and (iii) obtain the actual spring constant of the system during each event. These parameters are then used as input parameters (alongside the mean distance between events) when fitting the data to the Prandtl-Tomlinson model.

A schematic of a single scan line is shown in Figure 6.15. The average friction force $\overline{F_f}$ is determined as an average difference between the signal and the baseline

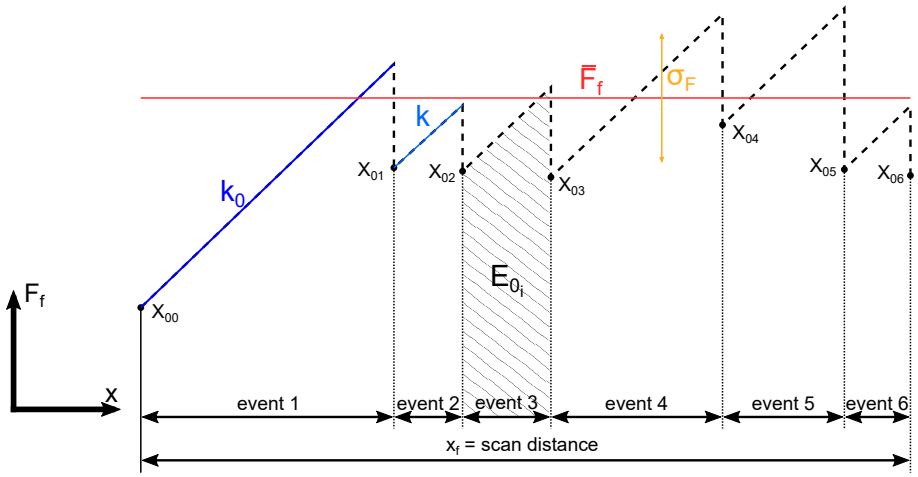

Figure 6.15: A schematic representation of a single line exhibiting stick-slip behaviour, with the corresponding points used in the algorithm for data evaluation.

$F_0 = (F_{trace}+F_{retrace})/2$, from the first event onward. The standard deviation of the resulting averaged friction corresponds to the magnitude of the stick-slip events in the analysed scan. The spring constants are obtained by fitting a line on the data between the previous minimum and the maximum of the I-th event. The slope of the fitted line corresponds to the spring constant k_I in $\mathrm{N\,m^{-1}}$. The slope of the first event on each line k_0 is collected separately and is not included in the average. Dissipated energy per unit cell can either be obtained by integrating over every event, which gives actual values of dissipated energy in each event, or by integrating over the entire scan distance and dividing the total energy by the number of events in the line (35).

The extracted data is collected in Table 6.2. Additional measurements at 0, 3.2, 12.8 and 19.2 nN, which were not included in the above analysis, are also presented for a more complete analysis of the load-dependent behaviour. The corresponding friction maps, histograms and probability density functions are given in Appendix C (Figure C.3, Figure C.4 and Figure C.5). Besides the expected increase of friction with load, the effective lateral spring constant of the system increases too, thus indicating the non-linear behaviour of the cantilever when the forces are below 10 nN. The values of dissipated energy per unit cell are comparable to similar systems in literature (35).

Figure 6.16a displays the load-dependent atomic-scale frictional response of the analysed system. Interestingly, the frictional behaviour follows the Hertz-plus-offset model closely, despite measuring on a multilayer, thus displaying a different frictional mechanism than the measurements in Chapter 5. However, as discussed in Chapter 5, the main reason for the altered behaviour observed on the multilayer systems is the large adhesion between the probe and the layer. Due to performing the measurements in water and, therefore, significantly reducing attractive forces between the probe and the layer, the behaviour reverts to the Hertzian $^2/_3$ power law. The magnitude of the friction force is roughly one-half of the monolayers presented in Chapter 4, which

Table 6.2: Average friction, spring constant and dissipated energy

$\overline{F_n}$ (nN)	v (nm/s)	F_f (nN)	σ_{F_f} (nN)	k (N/m)	σ_k (N/m)	E_0 (J)	σ_{E0} (J)
0	6.6	0.228	0.438	0.729	1.519	2.4E-19	2.4E-19
3.2	6.6	0.597	0.562	1.178	1.505	4.5E-19	1.5E-19
6.4	6.6	0.832	0.629	2.212	2.142	4.0E-19	1.5E-19
12.8	6.6	1.372	0.725	2.701	2.393	6.2E-19	2.1E-19
19.2	6.6	1.697	0.686	2.756	1.776	9.1E-19	2.0E-19
26	6.6	2.089	0.776	3.122	1.958	9.5E-19	2.2E-19
32	6.6	2.336	0.812	3.203	2.409	1.1E-18	2.8E-19
32	15	2.462	0.814	3.111	1.984	1.2E-18	2.6E-19
32	25	2.020	0.910	3.196	2.345	1.1E-18	2.2E-19
48	6.6	2.741	0.848	3.147	2.515	1.3E-18	3.1E-19

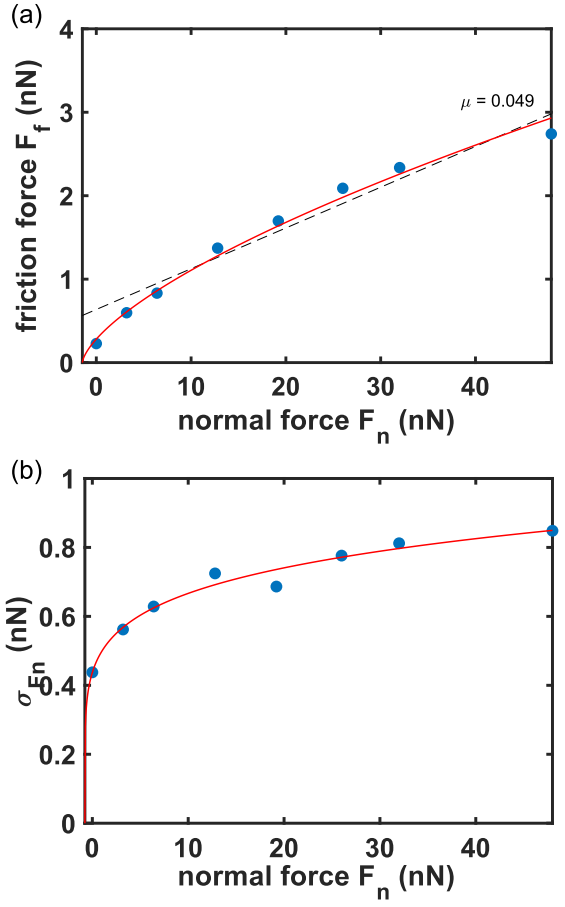

Figure 6.16: Frictional response of the measured multilayer WS_2 sample (a) and corresponding standard deviation of the signal (b).

agrees well with the reported data on other 2D materials from the literature (228, 229).

The standard deviation of the friction force is shown in Figure 6.16b and corresponds to the magnitude of the jumps rather than noise. As expected, the magnitude of the jumps increases with load, and the increase is most prominent at low load. Despite an incommensurate sliding system, due to lattice mismatch between the tip (Si, ⟨100⟩

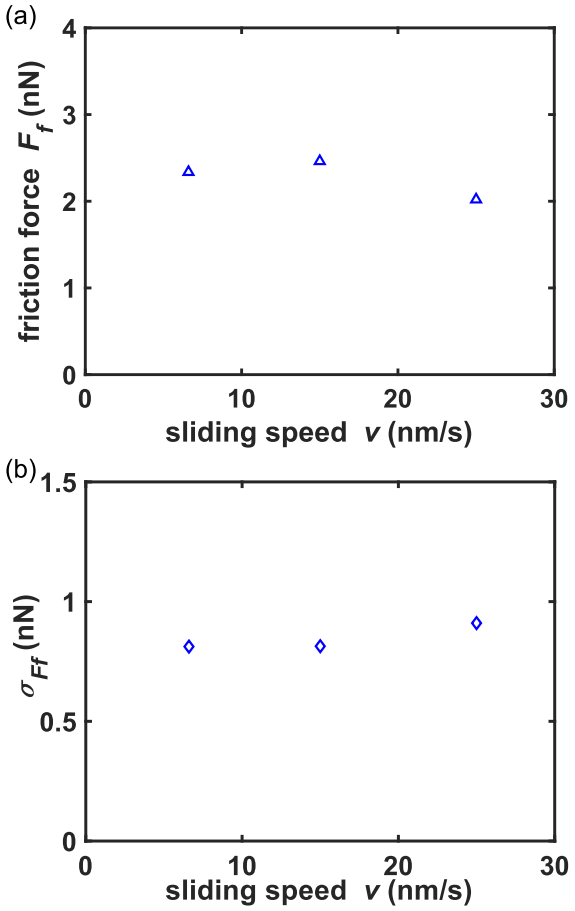

Figure 6.17: Frictional response in relation to sliding speed (a) and corresponding standard deviation of the signal (b).

orientation[3]) and the sample, the jumps do not disappear at zero load, showing that superlubricity, as defined in Section 2.1.3, was not reached.

Speed-dependent frictional behaviour at 32 nN is shown in Figure 6.17a. Similar to Chapter 4, only minor differences in friction are seen across analysed speeds. Friction at the highest sliding speed is slightly lower; however, the difference is not large enough to support any conclusions. Similarly, the standard deviation of friction in relation to sliding speed in Figure 6.17b does not show substantial differences between the friction values. In contrast to the magnitude of friction force, the standard deviation increases slightly at the highest speed.

6.3.6 Fitting of the stick-slip data to thermally activated Prandtl-Tomlinson model using a machine learning approach

As an alternative to the classical analysis presented above, some of the data was extracted from the scans and then used as input parameters in machine learning,

[3]Manufacturer specification

alongside computer-generated synthetic experiments. This subsection is a summary of the collaboration with Paola Torche, who performed machine learning fitting of the experimental data to the thermally activated Prandtl-Tomlinson (PT) model. The manuscript is currently in preparation.

The stochastic nature of FFM experiments is a major challenge for estimating the PT parameters using the analytical relations of the (non-thermal) PT model. Traditional least-square fitting with the objective function being the entire thermal PT model would be possible; however, it is computationally expensive and, therefore, not feasible in practice. As an alternative, we explore a potential estimation method based on techniques used in statistical learning for estimating the lattice spacing a, the energy of interaction E_0, and lateral stiffness k_L from FFM experiments at finite temperature.

In the analytical approach in the previous sections, we have extracted the parameters directly from the data and then averaged the results over the entire data set, which was sufficient to explain some aspects of the measured signal but could not explain why the observed distribution was much wider than expected from a purely geometrical perspective. In the presence of thermal fluctuations, on the other hand, shorter peak distances can be observed due to thermal activation, or longer, due to transitions to non-nearest neighbours. Thus the precision of the analytical estimation can be highly affected by these thermal fluctuations and noise.

Instead, we use the averaged parameters $\langle F_f \rangle$, σ_F, k, $\langle d \rangle$ and σ_d from the analytical analysis as input parameters during machine learning. Alongside we train the model with a set of computer-generated synthetic experiments. A total of 224659 labelled synthetic experiments were produced by thermal PT model at finite temperature ($T = 300$ K), constant speed $V = 6.6\,\mathrm{nm\,s^{-1}}$, over 10 nm length and varied rest of parameters, distributed as shown in Figure 6.18.

Machine learning offers an improvement over averaging approach for assessing the lattice constant in Table 6.1. It predicts the lattice constant at 0.31 ± 0.02 nm, which complies with the expected lattice constant of WS_2. Machine learning predicted more than two-fold higher spring constants than those obtained directly from the data (Table 6.2). On the other hand, the predicted dissipated energy deviated from the data only marginally.

6.4 Discussion

Reducing the scale to the atomic level results in different frictional behaviour. Atomic-scale friction shares some characteristics with nano-scale behaviour (the

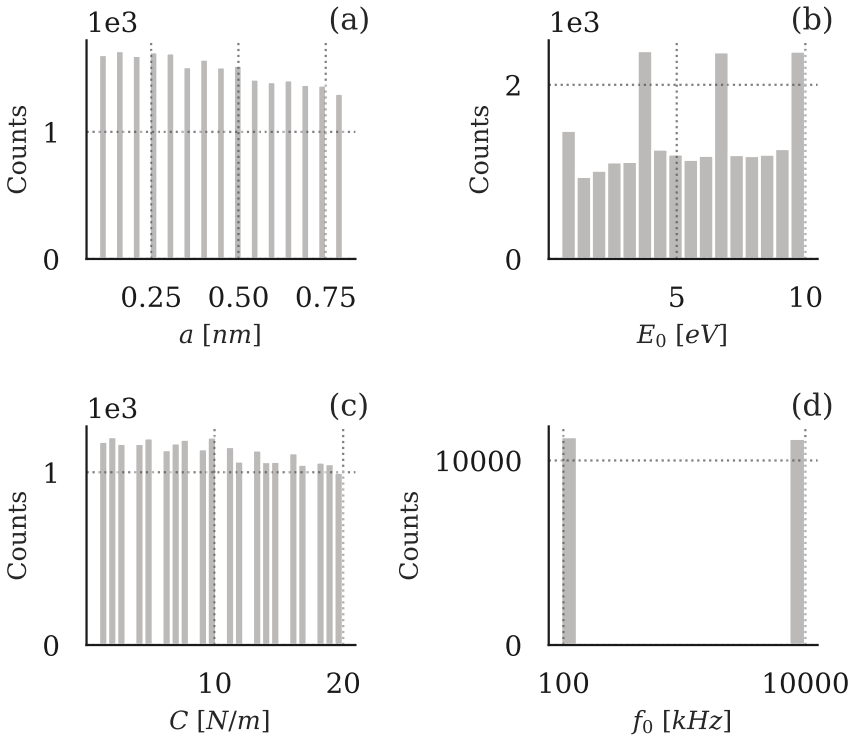

Figure 6.18: Distribution of the PT parameters a, E_0, C, f_0 of the 224659 synthetic experiments used for training and testing the regression models. (Original author of the figure: Paola Torche; reused with permission).

magnitude of the friction forces) but exhibits non-linear stick-slip motion, which is governed by the crystal lattice of the sample. The boundary between the nano-scale and the atomic scale is not strictly defined, and, as we have shown in this chapter, can even be governed by the environment in which a certain contact is operated.

Considering the similarities in absolute values of the magnitude of the friction force between the two systems, we can deduce that local stick-slip motion probably still exists at the nano-scale as the probe shape deviates from an ideal spherical shape and can therefore contain some nano-asperities. This, combined with increased adhesion can result in the tip appearing to move more continuously as a result of a superposition of several smaller atomic-scale contacts, similar to the macro-scale tribological behaviour, where the friction results from the contributions of a relatively small proportion of the real contact area.

Apart from a single measurement, the scans did not display clear atomic lattice patterns, as is usually displayed in literature (35, 129, 197, 235). In our case, the lack of a clear pattern was a consequence of several factors, including low friction, flake orientation, high probability of jumps over multiple lattice constants due to thermal activation, jumps to the out-of-line minima due to low probe stiffness, and hydrodynamic effects from the aqueous environment. As the pattern was not visible,

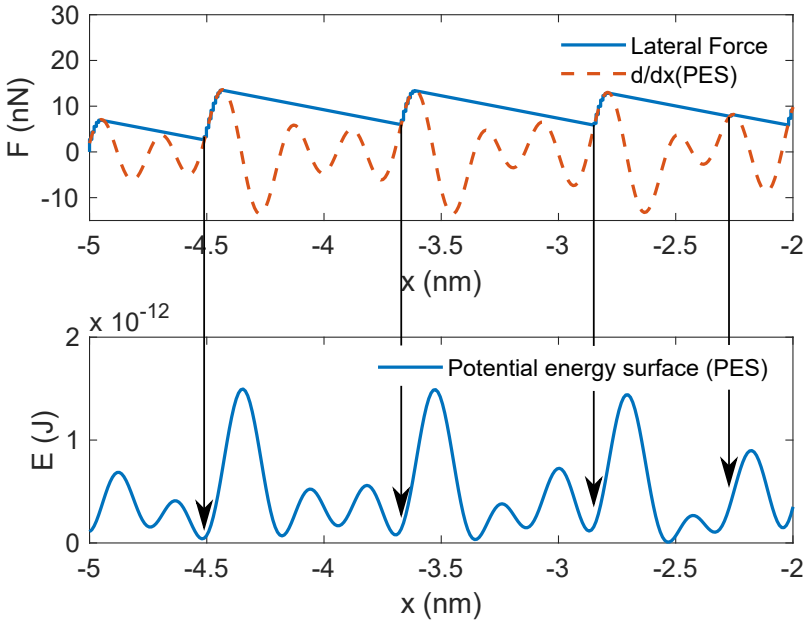

Figure 6.19: Lateral force (top) and potential energy surface (bottom) along a single line, showing the location of stick-slip events

the exact orientation of the underlying lattice could not be obtained. The distances between the events displayed wide distributions of the events, with distinguishable jumps over a single or multiple lattice constants.

We compared the measured distributions to the artificially generated force profiles from the potential energy surface, which showed that the sharp distributions would only be expected when the sample and the sliding direction are aligned at specific angles ($\theta = 0°, 30°, 60°, 90°$). This means that our scanning direction was likely not aligned with the lattice, which was the principal origin of the observed wide distributions. Consequently, jumps over multiple lattice distances are more likely when the two are not aligned due to an increased number of neighbouring peaks being of different heights (Figure 6.19). When the tip overcomes a high peak its potential energy is likely so high that it does not stop in the next minimum, but it jumps over a few lower peaks before the force reduces enough to stop. Similarly, from friction experiments and simulations it is known that friction of TMDs exhibits strong anisotropy (225, 226), where friction decrease/increase is observed at specific angles that correspond to zigzag or armchair directions.

Despite an obvious improvement of machine learning fitting over averaging the event distances when predicting the lattice constant from a noisy friction map, the 1D model used in machine learning does not take into account the potential rotation of the flake. As we have shown, a more in-depth analytical approach with deconstructing the distribution histogram into individual peaks instead of taking simple averages,

alongside additional optical and topographical images of the measured area, can provide more accurate information about the sample structure and orientation. Due to the flake rotation against the sliding direction at a certain angle $\theta > 0$, we can no longer expect all the jumps to be of the same length and both the median and average jump lengths to deviate from the lattice constant.

6.5 Conclusions

The presented algorithm in this chapter offers a straightforward method of qualitatively evaluating the measured atomic-scale friction data. It does not provide any information about the frictional behaviour itself, but it allows quick evaluation of the data validity before a more detailed analysis using more complex atomic-scale frictional models.

The atomic-scale frictional measurements on multilayer WS_2 have resulted in wide event distance distributions. The rotation of the flake has a significant impact on the resulting stick-slip signal, both in magnitude and event distances. Furthermore, finite stiffness of the probe in the perpendicular direction to the scanning might result in the probe jumping to a minimum outside of the scanning line. Actual lattice constant jumps would only be observed when the scanning direction is aligned with the sample lattice orientation, and the probe would be infinitely stiff in the perpendicular direction. These factors, combined with thermal activation due to finite temperature, were the main cause of the wide event distance distributions presented in this chapter.

Machine learning fitting of the measured signal to a 1D thermally activated Prandtl-Tomlinson model returned the accurate value of the lattice constant of the WS_2 sample, despite the average length of a stick-slip event deviating significantly from the expected value. This indicated promising results; however, it would require additional testing with different samples to unambiguously confirm the validity of the approach.

Chapter 7

Nanotribology of W-S-C coating wear tracks

7.1 Introduction

So far, we have only looked at the nano-scale frictional properties of fully crystalline TMD nano-flakes. Whereas nano-flakes are starting to gain attention, their applications remain limited to nano-scale applications. TMD thin-film coatings, on the other hand, have been widely studied and used in practical macro-scale systems. The coatings can either have a nanocrystalline or amorphous structure, and the tribofilm is formed by recrystallisation/reorientation of TMD basal planes. Only a limited number of studies using atomic force microscopy on TMD coatings and wear tracks exist (28, 37, 38, 238). Considering the nano-scale properties of the nano-flakes, we can correlate the nano-scale behaviour of the coatings and the wear tracks to the behaviour of the crystalline nano-flakes, thus providing additional insight into tribofilm formation mechanism and the correlation between frictional properties at different scales.

The increasing presence of man-made mechanical systems in space requires the use of highly developed technical materials, which include the lubrication of moving components. For example, the high vapour pressure of most liquid lubricants (239, 240) can limit their applicability in space applications. The two most researched replacements are solid lubricants (4, 18) and ionic liquids (239). Whereas ionic liquids can provide sufficient tribological performance due to their low vapour pressure (241), their main drawbacks are tribo-corrosion (242), toxicity to the environment (243), rapid decomposition (244), and limited temperature range (244). On the other hand, most solid lubricants offer better performance and exhibit decreasing friction with increasing contact stress. Their lubricating properties mainly arise from a low shear

transfer film between the surface material and the counter body, which is often formed by tribo-chemical reactions on the surface (18). Consequently, the performance of solid lubricants is highly dependent on the working environment. Therefore, research in recent years has focused on improving the tribological and mechanical properties of solid lubricants to achieve favourable performance in a wider range of environments (21, 146, 179).

In this chapter, we present a study of the W-S-C coating and wear track properties, focused on nanotribology techniques to analyse nano-scale frictional properties of TMD thin films. The use of the AFM in contact mode, as opposed to other standard techniques for the analysis of wear tracks, such as Raman spectroscopy, electron microscopy and spectroscopy or X-Ray methods, allows us to specifically study the interface between the sliding body and the sample. As the conventionally used methods employ some form of electro-magnetic (EM) radiation (visible light, X-rays) or electron beams to probe the sample, the resulting signal from those methods would always contain some information from below the surface, which can mask the properties at the interface (245). Additionally, the energy introduced into the system by the measurement procedure can also induce changes in the crystal structure.

Furthermore, we examine the multi-scale surface mapping approach to wear track analysis, combining different techniques, including optical profilometry, scanning electron microscopy (SEM), transmission electron microscopy (TEM), atomic force microscopy, and spectral Raman mapping to examine the characteristics of the wear tracks. Since single point analysis is, in most cases, insufficient to qualitatively distinguish localised effects in non-homogeneous systems, such as wear tracks, surface mapping provides a much broader insight into the origins of friction. For example, TEM analysis is limited to analysing only tens of nanometres at one time, and conventional micro-Raman analysis is usually limited to a few single points with a diameter of around one micrometre. As a case study, we employ a composite W-S-C coating to investigate how the nano-scale properties compare across different sections of the sample and correlate them with their frictional behaviour at the macro-scale.

The work presented in this chapter was a collaboration with the *Czech Technical University in Prague* and the *University of Coimbra*. The samples were deposited by Prof Albano Cavaleiro's group (*University of Coimbra*). Macro-scale tribotests, SEM topography and Raman mapping measurements were performed by Dr Kosta Simonovic (*Czech Technical University in Prague*). TEM and high-resolution SEM were performed by Dr Teodor Huminiuc (*University of Southampton*). This chapter includes the work that has been published in *ACS Applied Materials & Interfaces* (Ref. (246)).

7.2 Methodology

7.2.1 Coating and wear track characterisation

Chemical characterisation of the as-deposited W-S-C coatings on the WC substrate was performed using Raman spectroscopy ($\lambda_{laser} = 532\,\text{nm}$; XPlora, Horiba Scientific, France), energy dispersive spectroscopy (EDS; EDAX SDD Octane Super, Ametek, United States) and X-ray photoelectron spectroscopy (XPS; Thermo Scientific Theta Probe XPS, UK).

After the macroscopic friction tests, a 3D white-light optical profilometer (Zygo NV7200, United States) was used to characterize the macroscopic wear patterns of the coatings. Eight points over the wear track were measured, and the results were averaged and reported as the total wear volume, together with the average width of the wear track for each load.

Raman spectroscopy was used to perform spectral Raman mapping of the wear tracks over a large area (50 x 10 µm). A total of 561 points (51 x 11) per sample were recorded, with a separate Raman spectrum obtained for each point. Raman maps were compiled by determining the local height of the corresponding WS_2, WO_3 and carbon peaks at 408 cm^{-1} (A_{1g} mode), 798 cm^{-1} and 1568 cm^{-1} (G-peak), respectively. A detailed description of the methodology for compiling the Raman maps is given in Appendix B. The average Raman spectra for each sample were obtained by averaging over all 561 measurements comprising the maps. The resulting spectra were then normalised to a comparable scale between the samples. The resolution of the Raman signal was kept low (2 cm^{-1}) to reduce the required acquisition time, as we were mainly interested in the distribution of carbon and WS_2 across the wear tracks, rather than the very detailed convolution of the peaks. Raman mapping experiments were performed overnight due to the long times required to acquire the data (over 9 hours) and to minimise the amount of interference from the surrounding light.

The SEM imaging of the wear tracks was performed on FEI Verios 460L (Thermo Fisher Scientific, United States). Additional SEM imaging and focused ion beam (FIB) specimen preparation were performed using an FEI Helios Nanolab electron microscope. The high-resolution transmission electron microscopy (TEM) micrographs were acquired using an FEI Titan Themis Cubed operating at 300 kV acceleration voltage and equipped with an image aberration corrector.

7.2.2 Macroscopic tribology tests

Macro-scale tribological tests were performed in the unidirectional, rotational ball-on-disc configuration with the custom-built vacuum tribometer, VacTrib03 (Advanced Materials Group, Czech Republic). The counter body was a 6 mm 100Cr6 ball for all the tests. Four tests were performed at normal loads of 2, 8, 10, and 20 N, respectively. Each test ran for 5000 cycles at a linear speed of 5 cm/s. The steady-state coefficient of friction (μ_{macro}) was determined as the average value of the friction coefficient from the final 30% of the test.

7.2.3 Nanotribology

Atomic force microscopy (AFM, Agilent 5500, USA) was used in contact mode to obtain topography and friction maps and perform load-dependent friction measurements on the coatings and the wear tracks. Topography and friction maps were obtained simultaneously by applying constant force during the measurement.

Load-dependent friction measurements were performed by incrementally increasing contact load every 25 lines over the 250 x 250 nm area. A total of 10 different loads were applied, including negative loads, used to observe the behaviour in the adhesive regime. Pull-off force, $F_{pull-off}$ ($\approx F_{adh}$), was measured just before each friction experiment, and the minimum load F_{min} was selected accordingly. More precisely, the minimum load was determined empirically for each measurement, as the lowest load at which the tip would not lose contact with the surface during continuous sliding. The minimum and maximum loads applied during each measurement are summarised in Table 7.1. A custom script was utilised to precisely control the loads in the experiment. Sliding speed was kept constant at 1 ln/s.

Table 7.1: Nanotribology measurement parameters

Scan region	F_{min} (nN)	F_{max} (nN)	F_{adh} (nN)
as-deposited - low friction	-4.1	30	6.9
as-deposited - high friction	-1.5	30	7.5
wear track - low friction	-6.5	30	10.9
wear track - high friction	-6.1	30	12.1

Nanosensors^{TM} PPP-LFMR (NanoWorld AG, Switzerland) probes with nominal spring constant 0.2 N m^{-1} were used for all measurements. The actual normal spring constant (k = 0.19 N m^{-1}) was determined in-situ by a built-in thermal noise method (199). Lateral forces were calibrated according to wedge calibration procedure (95) using a commercial TGF11 (µMasch, Bulgaria) calibration grating. The obtained lateral calibration coefficient was $\alpha = 434$ nN V^{-1}.

7.3 Results

7.3.1 As-deposited coating characterisation

The chemical composition of the as-deposited coating as determined by the EDS is shown alongside the values of hardness and elastic modulus in Table 7.2.

Table 7.2: Elemental composition of the as-deposited coating

W (at.%)	S (at.%)	C (at.%)	O (at.%)	hardness (GPa)	E_r (GPa)
18	35	40	7	7.6 ± 0.6	87 ± 4

Three distinct regions are evident from the Raman spectrum of the as-deposited coating in Figure 7.1. First, the carbon G and D peaks, representing different sp^2 hybridisation, are located at 1568 cm^{-1} and 1411 cm^{-1}, respectively (247). After the deconvolution of the spectra, the intensity ratio of the two carbon peaks (I_D/I_G) was calculated as 2.05. According to the 3-stage model of the carbon structures presented by A. Ferrari et al. (248), I_D/I_G ratio represents the amount of the sp^2 bonded carbon in the investigated material. According to the obtained value ($I_D/I_G = 2.05$), the carbon matrix was noncrystalline, with more than 80% of the sp^2 structure composed of aromatic clusters with long ordered C-C chains (248). Secondly, the two main peaks of the WS_2 structure (249) were identified (Figure 7.1); A_{1g} peak at 411 cm^{-1} and E_{2g} peak at 354 cm^{-1}. The intensity ratio between the two WS_2 peaks $I_{A_{1g}}/I_{E_{1g}}$ was calculated as 0.88. Thus, the shear vibration mode of the WS_2 structure is dominant (250). Moreover, the lower intensity of the A_{1g} peak indicates a low number of WS_2 monolayers on the surface of the coating (251). Finally, tungsten oxides (WO_x) were

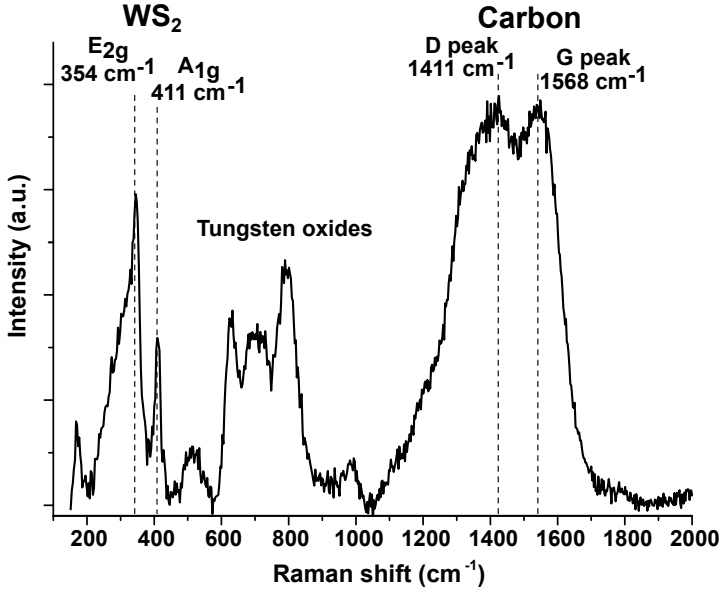

Figure 7.1: Raman spectrum of the as-deposited coating.

identified in the range between 500 and 1000 cm^{-1}, which were formed as a consequence of the WS_2 oxidation (151, 252).

7.3.2 Macroscopic tribotests

The coefficient of friction, wear volume and wear track width for the investigated loads are summarised in Table 7.3. The coefficient of friction decreases initially with the increase of normal load (from 2 N to 8 N) and increases afterwards for higher loads (10 N and 20 N). The wear, on the other hand, does not follow the same behaviour. Namely, wear volume remains constant until the sharp increase at 20 N load, while the wear track width increases steadily with the increase of load.

Table 7.3: Summary of the relevant macro-tribology results

load (N)	μ_{macro} (/)	wear volume (mm^3)	wear track width (µm)
2	0.039	0.9	107.6
8	0.023	0.9	150.7
10	0.032	0.9	160.4
20	0.044	2.9	211.1

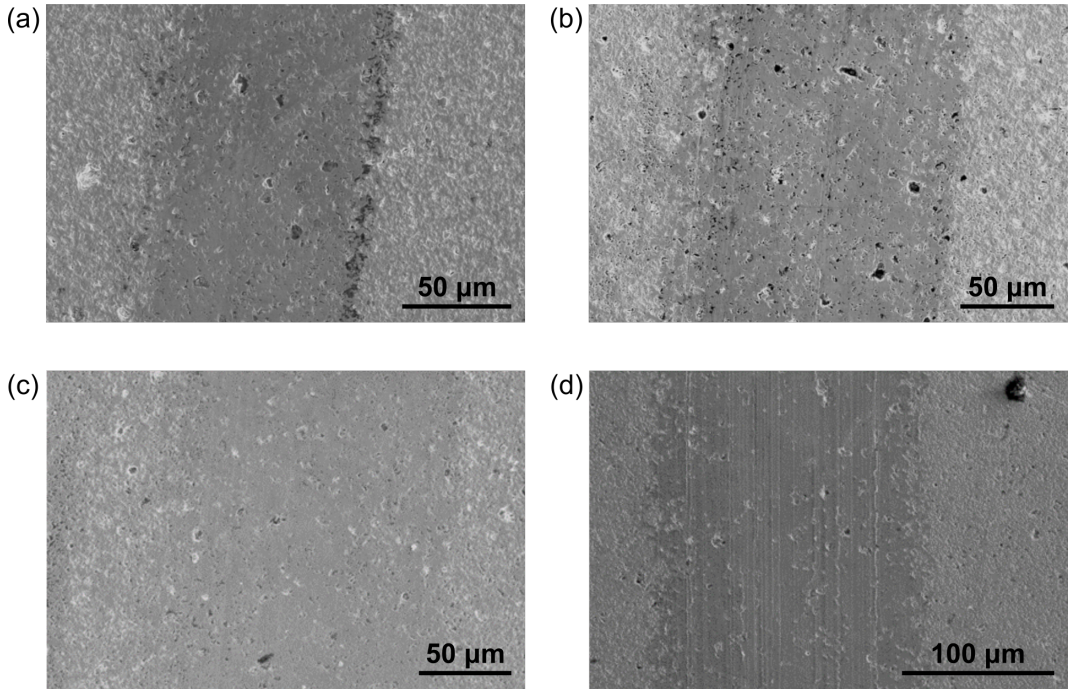

Figure 7.2: SEM images of the investigated wear tracks: a) 2 N, b) 8 N, c) 10 N and d) 20 N.

Figure 7.2 shows representative SEM images of the wear tracks for all investigated loads. At lower normal loads (Figure 7.2a-c), the wear mechanism is predominantly polishing wear, and the damage to the coating is only superficial. At 20 N

(Figure 7.2d), traces of abrasive wear are evident, which may be partially responsible for the increase of the coefficient of friction (Table 7.3).

Overall, friction and wear measurements, or SEM images are not enough to explain the behaviour of the friction coefficient. Hence, it was necessary to go beyond the macro-scale and use AFM and spectral Raman mapping to further investigate the basic tribological mechanisms. The approximate areas in the wear track used for analysis with different analytical techniques are marked in the optical profile map of the 2 N wear track in Figure 7.3a. For comparison, the profile maps for the other wear tracks are also provided (Figure 7.3b-d). The progressive transition from polishing to abrasive wear and increasing wear track depth and width are evident.

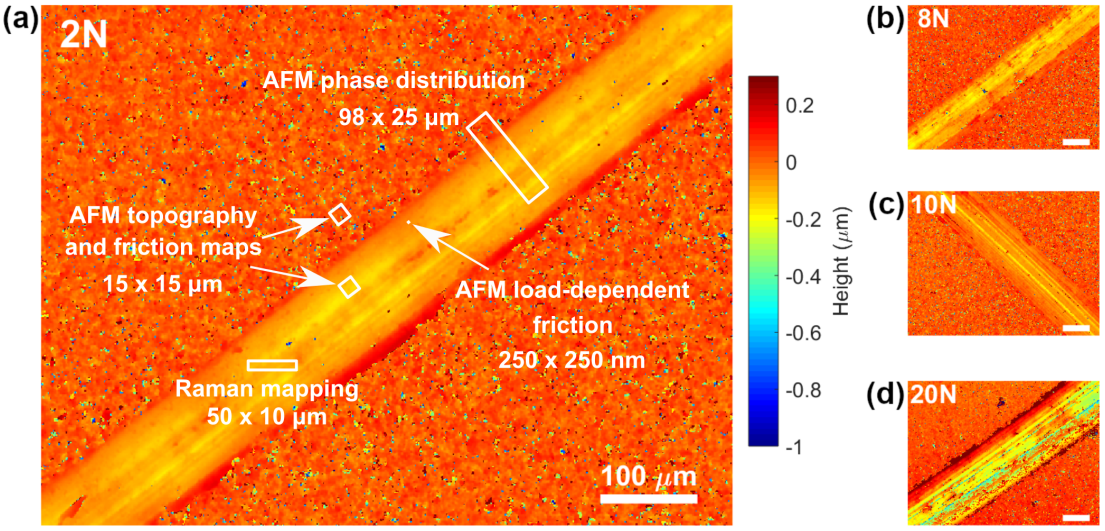

Figure 7.3: 3D optical profilometry of the investigated wear tracks. (a) The wear track obtained at 2 N with marked example areas analysed in this paper. (b-d) 8 N, 10 N and 20 N wear tracks, showing increasingly higher wear and progressive transition from polishing to abrasive wear. Scale bars correspond to 100 µm, the height colour bar applies to all.

7.3.3 Raman and spectral Raman mapping

Averaged Raman spectra over 561 points on each of the analysed areas are shown in Figure 7.4; the curves were normalised by the average intensity of each measurement. At first, a large difference is observed in the tungsten oxide region (500-1000 cm^{-1}) (151, 252). The wear tracks contain lower amounts of oxides than the as-deposited coating, meaning that most of the oxidation occurred either during the deposition or, most likely, during the coating storage and not during the tribotests. The oxide peaks on the 2 N and 10 N samples are much weaker than those at 8 N and 20 N, having the only prominent oxide peak at $\approx$ 800 cm^{-1}, resembling WO_3 (151).

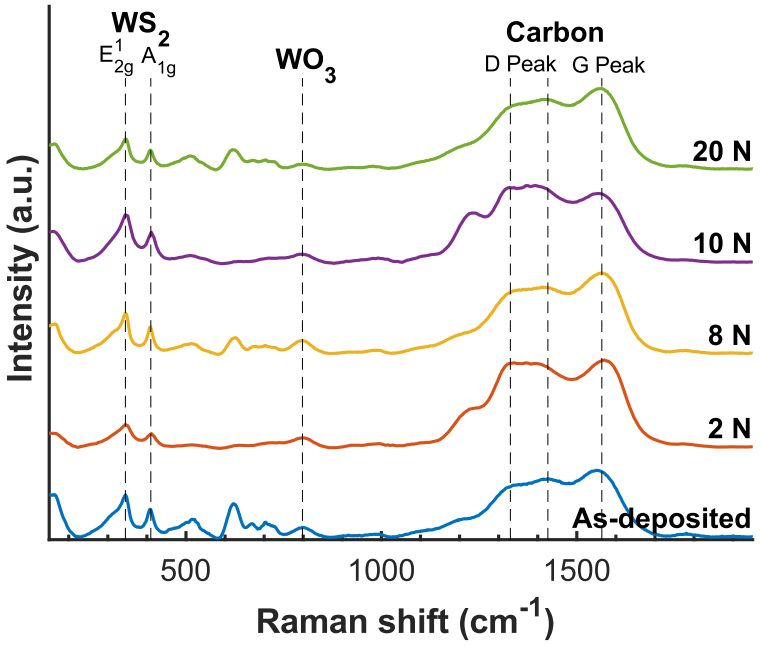

Figure 7.4: Averaged Raman spectra of the as-deposited coating and the investigated wear tracks.

Table 7.4: Peak ratios and frequency difference from the averaged Raman spectra

sample	WS_2 peak ratio ($I_{A_{1g}}/I_{E^1_{2g}}$)	WS_2 frequency difference ($f_{A_{1g}} - f_{E^1_{2g}}$)	carbon peak ratio (I_D/I_G)
as-deposited	0.68	65	0.81
2 N	0.61	67	0.97
8 N	0.68	65	0.80
10 N	0.64	67	1.12
20 N	0.65	65	0.86

As discussed by A. Ferrari and J. Robertson (248), either the maximum peak height or the area under the peak can be used to determine the peak ratios. The two can be used interchangeably for disordered systems, while peak broadening in the amorphous systems requires considering the maximum peak height to include the information about less distorted aromatic rings. All peak ratios reported here were calculated from maximum peak heights. The average WS_2 peak intensity ratio, $I_{A_{1g}}/I_{E^1_{2g}}$, is between 0.61 and 0.68 for all spectra (Table 7.4), indicating no difference in crystallinity with increasing wear. The frequency difference between the peaks is between 65 and 67 cm^{-1}, which is within the measurement resolution. This indicates that there is no significant difference in the WS_2 thickness and structure between different analysed samples. From the frequency difference, we can assume the average layer thickness of WS_2 to be at least three layers (approx. 2 nm) (200). All samples show a strong carbon signal. The I_D/I_G ratios are between 0.80 and 1.12, where the highest ratio can be observed in the 10 N sample and the lowest in the 8 N sample (Table 7.4), indicating

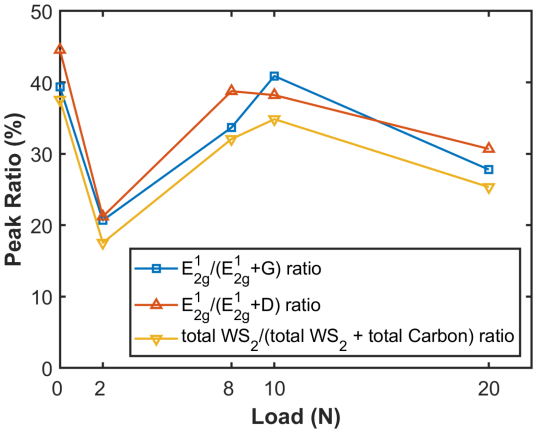

Figure 7.5: Raman peak ratios between WS_2 and carbon.

the highest amount of graphitic structure in the 8 N wear track. Since those two samples experienced similar frictional behaviour, we can conclude that the observed difference in this range was either not significant or that the chemical structure of carbon does not have an observable effect on the coefficient of friction.

A significantly lower intensity of WS_2 peaks in the 2 N wear track can be observed when compared to the ones obtained at higher loads; the highest I_{WS_2}/I_C peak ratio was observed in the 10 N wear track (Figure 7.5); in fact, the intensity at 10 N is comparable with the as-deposited coating. The low intensity of WS_2 at 2 N can be attributed to preferential wear of WS_2 and continuous transfer of WS_2 to the sliding body at lower contact pressures. At low loads, the tribological properties are driven by the constant removal of WS_2 from the surface, while carbon provides structural stability and prevents excessive wear. There is also lower energy input to the contact interface, which can slow the formation of the protective tribo-film. On the other hand, wear increases significantly above 10 N, resulting from higher material removal due to abrasion. Furthermore, the insufficient time for the formation of the tribo-film, or its instantaneous removal from the contact, results in accelerated wear of the coating. Consequently, we observe a slight decrease in WS_2 peak intensity at 20 N compared to 10 N.

Threshold Raman maps, shown in Figure 7.6, represent the intensity of the WS_2 (A_{1g} mode, blue), carbon (G peak, red) and WO_3 (798 cm^{-1}, green) peaks in each measured point. Threshold maps were compiled from the intensity maps of each peak. The relative peak intensity (i.e. the difference between the absolute counts in the peak and the nearest local minimum) was used to generate the initial intensity maps. The threshold was then set at 50% of the average intensity of the five highest peaks on the map, which assured that we could distinguish between the trace peak and actual peak intensity while not being influenced by a single high-intensity peak. The colour gradients indicate the intensities of the selected peaks in each point between the

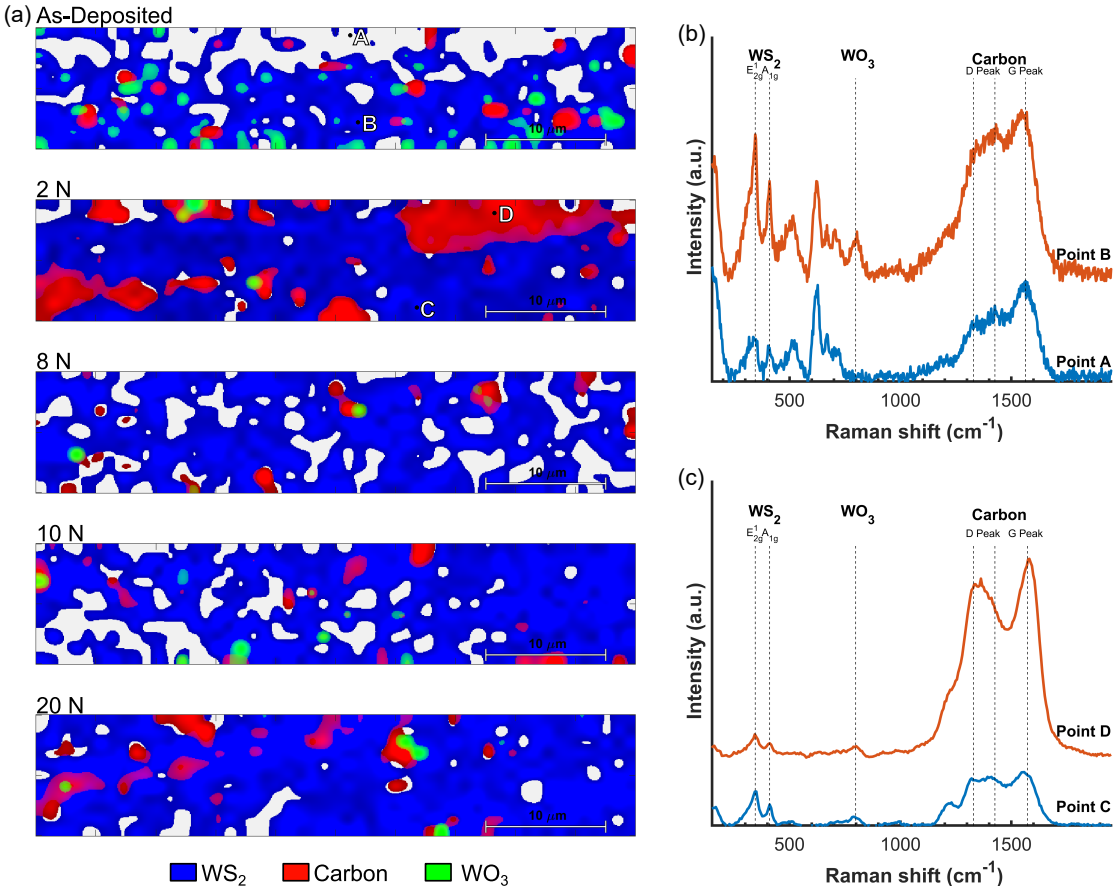

Figure 7.6: Threshold Raman maps, showing the peak intensities of WS_2 (blue), carbon (red) and WO_3 (green).

threshold and the maximum intensity. The white patches indicate that neither of the three peaks has a high enough intensity to pass the threshold. A more detailed explanation of the method used to generate the maps is given in Appendix B.

The threshold maps indicate the presence of all three compounds on all samples; however, their distribution differs significantly. WS_2 appears very uniformly distributed on all the wear tracks, indicating no large differences in crystallinity. The WS_2 signal on the as-deposited sample is more patchy. The large areas without any signal above the threshold could indicate excessive oxidation, lower signal due to surface roughness, sample tilt or different crystallinity. The single spectra obtained in points A and B, as marked in Figure 7.6, show a much lower intensity of WS_2 and C peaks in point A and no WO_3 peak at 798 cm^{-1}. The rest of the tungsten oxide peaks (580 - 750 cm^{-1}) are similar and indicate no excessive oxidation. Furthermore, no additional peaks can be detected in point A. The difference in intensity is, therefore, due to topographical differences or different crystallinity. Considering that there is no large difference in intensity of the 580 - 750 cm^{-1} peaks the difference probably indicates a two-phase structure of the coating.

Substantial amounts of WO_3 are detected in only a few spots across the samples, thus

suggesting very local oxidation; more extensive coverage with WO_3 is only observed on the as-deposited sample, further confirming that most of the oxidation happened during sample deposition or storage before the tribotests. The four wear tracks show very comparable coverage with WO_3.

The largest difference between the samples can be observed in the carbon signal. All wear tracks contain larger patches of carbon than the as-deposited sample. The 2 N wear track, in particular, contains the largest patches of carbon. The total carbon coverage is also substantially higher. This further shows that WS_2 is either worn preferentially at lower loads or is not formed in a sufficient amount, leaving behind larger patches of pure carbon. Spectra in points C and D represent areas rich in WS_2 and carbon, respectively.

The maps in Figure 7.7 show the $I_{A_{1g}} / I_{E^1_{2g}}$ ratio and frequency difference between the corresponding Raman peaks of the A_{1g} and E^1_{2g} vibrational modes. The threshold mask from Figure 7.6 is applied to the maps, so only the data where the WS_2 signal is strong enough is considered. A higher number of layers results in a larger difference between the peaks (200, 253, 254) and increased intensity of the E^1_{2g} peak. The results indicate a very similar structure between the as-deposited surface, 8 N wear track and 20 N wear track, indicating consistent and continuous wear of all the components of the coating at 8 N and 20 N. The highest frequency difference and the lowest intensity ratio can be observed on the 2 N wear track, indicating the thickest tribo film.

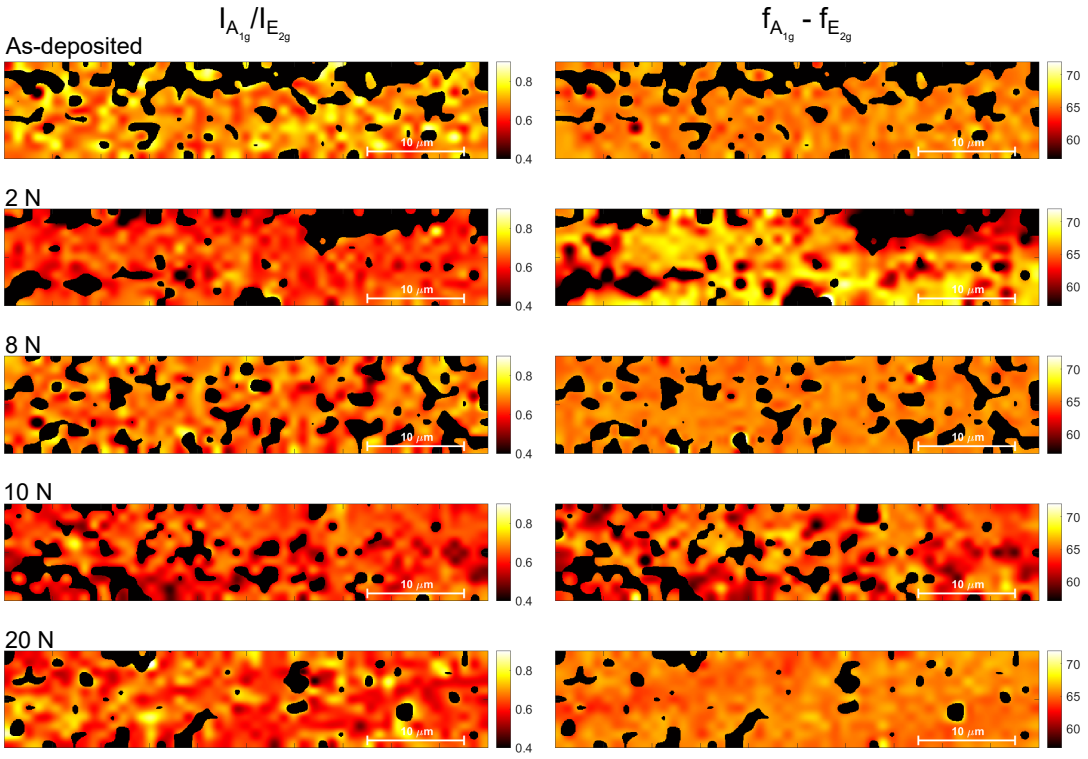

Figure 7.7: Intensity ratio and frequency difference between the main WS_2 peaks.

Similarly, the result on the 10 N wear track indicated a better tribo film coverage than 8 N; the wear rates are very similar between the two, however, the increased energy input at 10 N can speed up tribo film growth.

7.3.4 Nanoscale characterisation

The surface topography of the as-deposited W-S-C coating indicates compact columnar morphology (see Figure 7.8), with a significant amount of deep holes. The depth of the hole visible in Figure 7.8a is 1.75 µm, which is deeper than the coating thickness and might therefore indicate coating discontinuity or surface damage. However, the cross-section obtained by the SEM (see Figure 7.9d) reveals that the holes actually originate from the high substrate roughness, and the coating is uniformly aligned with the substrate topography. For nanotribological studies, we tried to avoid the holes and measure only on the flat surfaces, except where this was not possible (e.g. large friction maps, where the analysed area was much larger than the occurrence of holes on the surface).

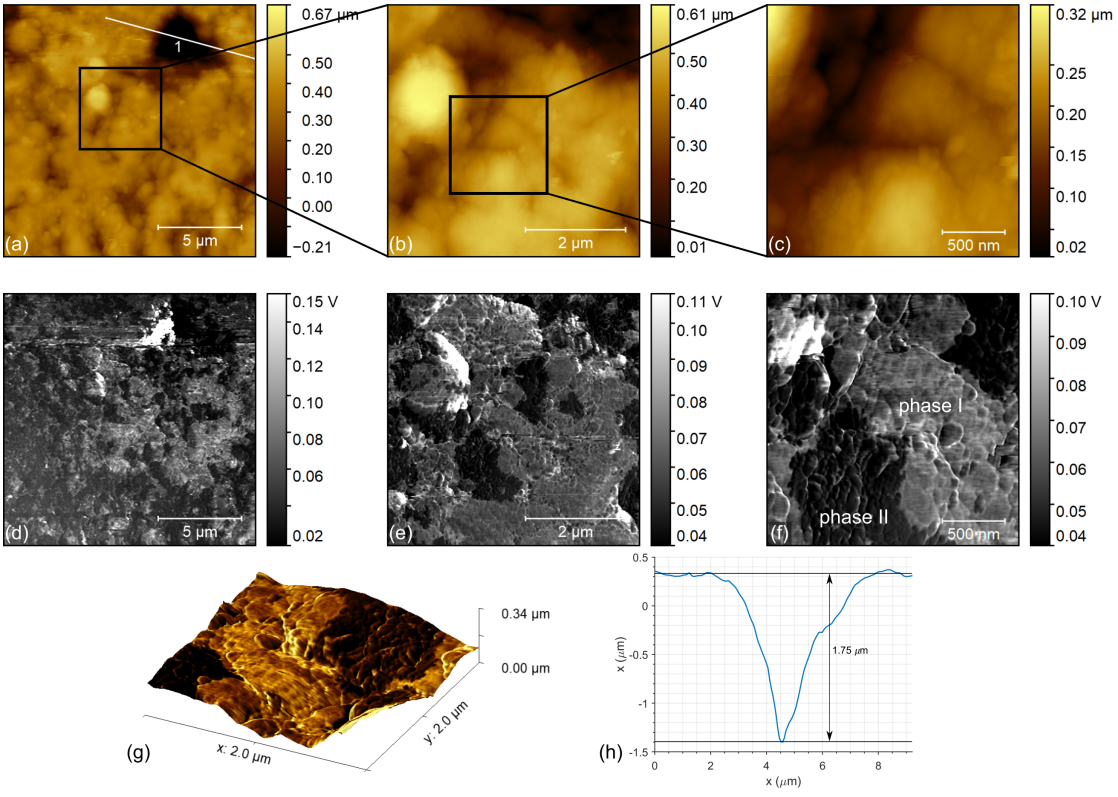

Figure 7.8: Structure of the as-deposited W-S-C coating. Topography measured at: (a) 15 µm, (b) 5 µm and (c) 2 µm scan size. (d-f) The corresponding friction maps. (g) 3D topography overlayed by the friction signal at 2 µm scan size. (h) Profile of the hole obtained along line 1.

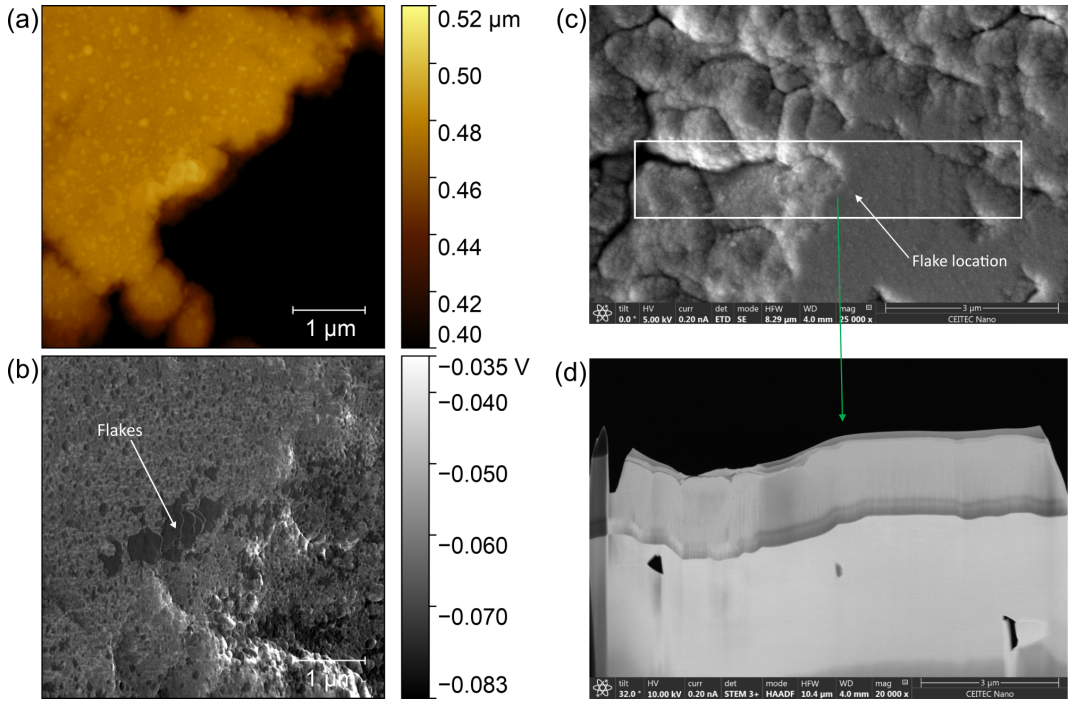

Figure 7.9: The same area on the edge of the wear track analysed by AFM and SEM. (a) AFM topography of the coating – the scale is adjusted to increase the contrast of the flat area. (b) Friction map. (c) SEM topography displaying the location of the cut. The SEM image is rotated by 145°, compared to the AFM scans. (d) SEM cross-section.

The topography and corresponding friction maps of the as-deposited coating in Figure 7.8 were obtained in the same spot at three different scan areas (15 x 15 µm, 5 x 5 µm, 2 x 2 µm), effectively zooming in on the surface to increase the resolution of the measured structures. The friction maps reveal the presence of two separate phases with contrasting frictional properties: the high-friction phase (phase I) and the low-friction phase (phase II). As evident from the overlay of the frictional signal and topography (Figure 7.8g), these differences in friction do not follow the topography, meaning that the frictional contrast is not due to topographical effects and the two phases are uniformly embedded within the coating surface. The distribution of the phases in Figure 7.8 appears to be uneven across the analysed areas, as the periodicity of the features is larger than the scanning area (see a large scan in Figure 7.10a and b). Note that the large friction map in Figure 7.10b includes areas with much higher friction than the rest of the coating, indicating frictional discontinuity due to the surface topography (see the deep hole on the left side of the map where there is a large spot with high friction). Nonetheless, the boundaries between the low and the high-friction phases are still distinguishable and, therefore, allow the determination of the ratios between the phases.

On the larger scans (Figure 7.10), each phase accounts to an almost equal amount of the surface area. Three methods in total were used to determine the exact ratios between the coverage of the phases. The first method, which uses a combination of

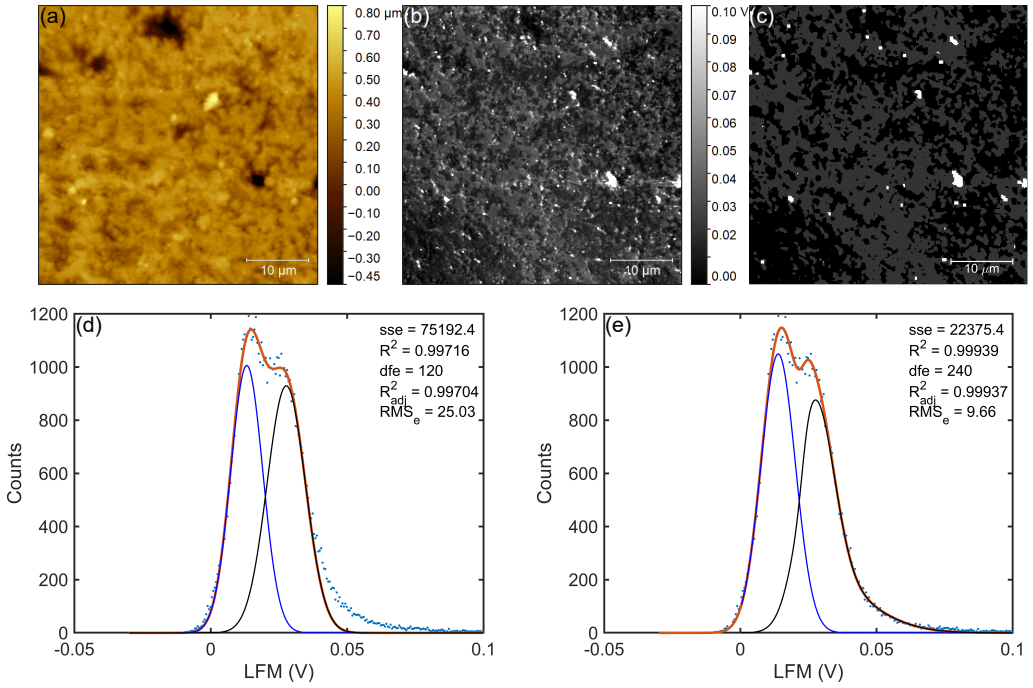

Figure 7.10: Large scan at a 45 x 45 µm scan area. (a) topography, (b) the corresponding friction map and (c) the calculated threshold map including the low-friction phase (black), high-friction phase (grey) and frictional discontinuity due to surface roughness (white). (d) The distribution of values on the friction map, including a dual Gaussian fit. (e) Alternative fitting model, with a better description of the tail at higher friction values.

thresholds and local smoothing to assign the phase in each point unambiguously, is demonstrated in Figure 7.10c. The thresholds for the low-friction phase (black), the high-friction phase (grey) and regions with frictional discontinuity (white) were below 0.022 V, between 0.022 V and 0.1 V and above 0.1 V, respectively. According to this method, 47.8% of the surface is covered with the low-friction phase.

In addition, a histogram with the number of incidences of each value on the map was obtained. The distribution in Figure 7.10d shows two prominent peaks, corresponding to normally distributed values on low and high-friction phases. Comparing the areas under the peaks yields that 47.5% of the surface corresponds to the low-friction phase, similar to the first method.

However, from the shown distribution it is evident that the tail above 0.05 V is not represented correctly by the normal distribution, which is due to an unavoidable influence of surface roughness on friction. Furthermore, the overlap of the two peaks shows that the two phases share some of the values, yielding the 1_{st} method invalid. A combination of normal and skew distributions resulted in a much better representation of the tail (Figure 7.10e), where the normal distributions determine the distribution of phases on the flat parts of the sample and the skew distribution corrects for the influence of roughness. This combined model results in a much better overall

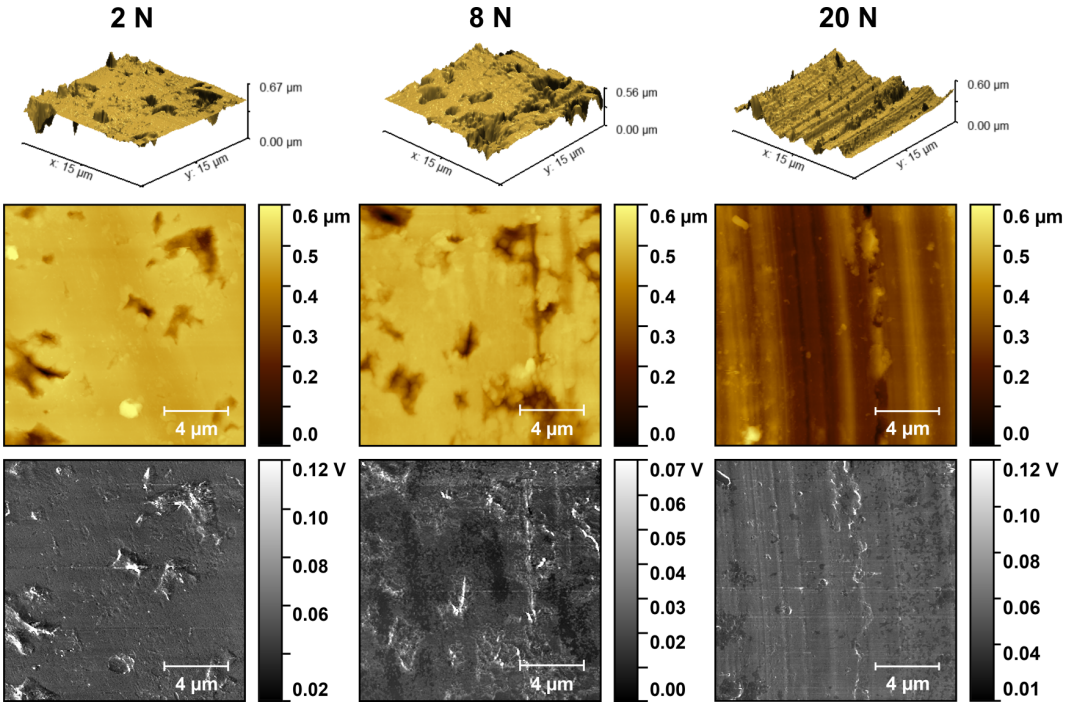

Figure 7.11: Surface structure (top: 3D representation, middle: surface topography, bottom: friction maps) of the wear track on the 2 N (left), 8 N (middle) and 20 N (right) samples. Flattening of the sample is visible on the 2 N and 8 N samples, whereas 20 N shows abrasive wear behaviour.

fit (R^2 = 0.99939, compared to R^2 = 0.99704) and a better agreement with the points corresponding to the low-friction phase. The ratio between the phases according to this method is 49.1%, which is still comparable with the other two methods.

Observation of the surface structure at the smaller scale (Figure 7.8c and f) indicates that the low-friction phase consists of 100 - 200 nm patches, which are clustered together to form a single phase. Similarly, the high-friction phase of the sample also contains some smaller patches, but the general structure is less uniform. This shows that the low-friction phase is likely nanocrystalline, whereas the high-friction phase is amorphous.

Analysing the surface topography of the measured wear tracks (Figure 7.11, top and middle rows) confirms the observation by SEM and optical profilometry (Figure 7.2 and Figure 7.3). At lower and intermediate loads, namely at 2 N and 8 N, we observe polishing wear, whereas at high loads (20 N), the wear behaviour transitions into abrasive. The surface morphology shows that 2 N and 8 N wear tracks still contain the same amount of deep holes as the as-deposited coating, indicating generally low levels of wear. The roughness on the flat plateaus is comparable between 2 N and 8 N wear tracks (Table 7.5). On the other hand, there are no visible deep holes in the 20 N sample as the wear rates were much higher.

Further inspection of the wear track topography revealed the presence of multilayered

Table 7.5: Nano-scale roughness parameters of the wear tracks in Figure 7.11

	2 N Wear track	8 N Wear track
S_a (nm)	5.905	5.639
S_q (nm)	7.570	7.216
Skew	-0.526	0.724
Kurtosis	0.440	0.615

flat structures parallel to the underlying surface and sliding direction, such as the ones shown in Figure 7.12. The layered features, which are much flatter than the surrounding coating and exhibit low friction, were only found within the wear tracks, indicating that they were produced during macroscopic sliding. Their shape strongly resembles the WS_2 ordered tribo-film formed during tribo-reactions while sliding (255). We identified structures with different shapes and sizes (ranging from 0.5 – 2.5 µm). Furthermore, the shape of some of the multilayered flakes, such as the central one seen on the 2 N wear track in Figure 7.12b, even resembles triangular geometry, which is a characteristic shape of a TMD crystal growth in a controlled environment (see Chapter 4, (256, 257)). Although present in all wear tracks, these fully crystalline flakes are very sparsely distributed.

A similar wide multilayered flake can also be seen in Figure 7.9, near the edge of the flat top surface. The same feature, however, could not be observed either by the SEM or by TEM. We performed TEM on the cross-section (Figure 7.13a) cut by FIB from the

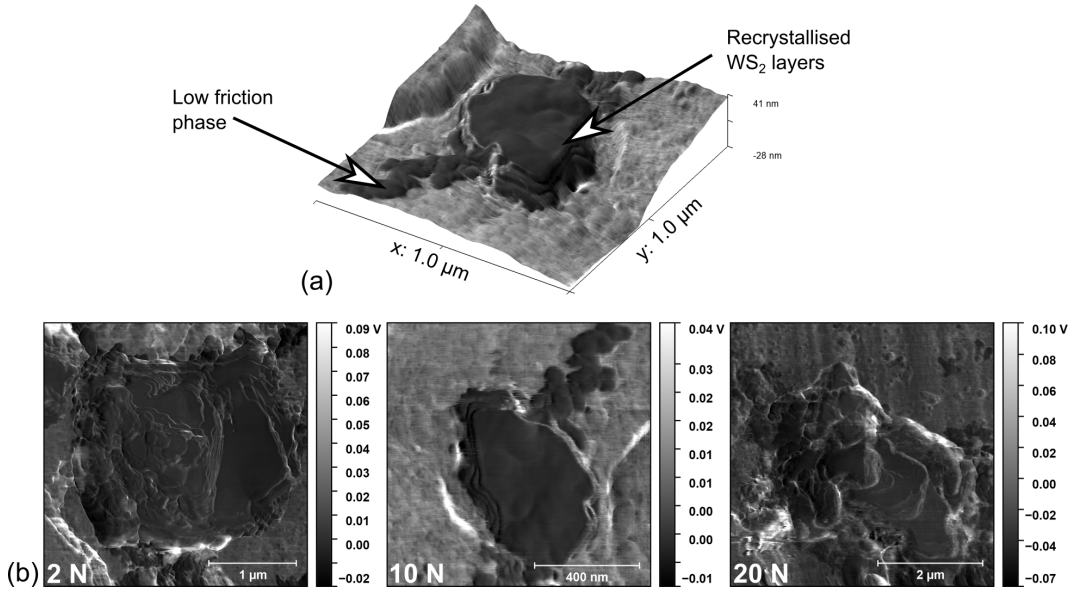

Figure 7.12: Tribo-film formation: (a) 3D view of a flake observed on the 10 N wear track, showing the difference in structure between the low-friction phase and layered tribo-film. The image is overlayed with raw friction signal. (b) Friction maps showing layered structures – flakes, found on the surface of different wear tracks, which indicate the formation of ordered TMD tribo-film in the sliding contact.

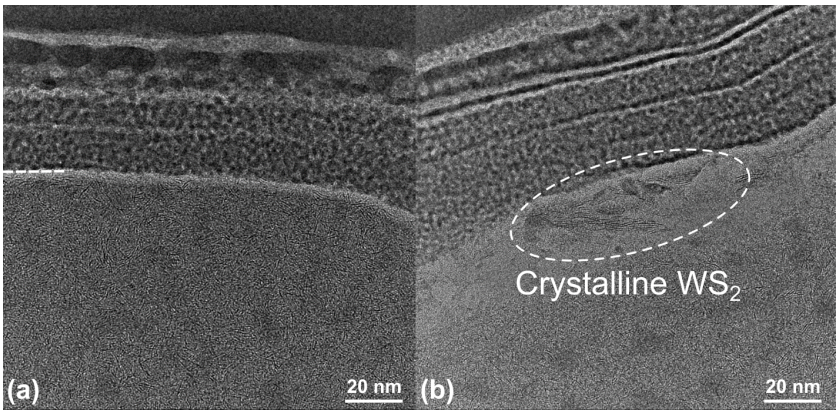

Figure 7.13: Cross-sectional TEM images of the wear track: (a) the region from Figure 7.9, (b) the other edge of the same wear track. The coating surface is shown by the dashed white line (centre left).

flat area but could not detect the observed feature from the AFM. Some randomly oriented ordered structures can be seen below the surface, but they are on a much smaller scale, measuring only a few nanometres (nanocrystalline structure). However, it is worth mentioning that the flat areas are very small, and it is likely we were not able to extract the sample exactly from the spot. In fact, clear traces of a larger ordered structure oriented parallel to the surface can be seen on another part of the wear track (Figure 7.13b), which was not analysed by AFM.

Figure 7.14a shows the frictional response on the high and low-friction phases of the coating. The results reveal a substantial difference between the two analysed regions, as the high-friction phase exhibits approximately ten times higher friction than the low-friction phase. Both phases exhibit similar linear behaviour, indicating either quasi-flat (i.e. the contact area remains constant) or multi-asperity contact. This can be attributed to tip wear and flattening during the initial large-area topography scans. As

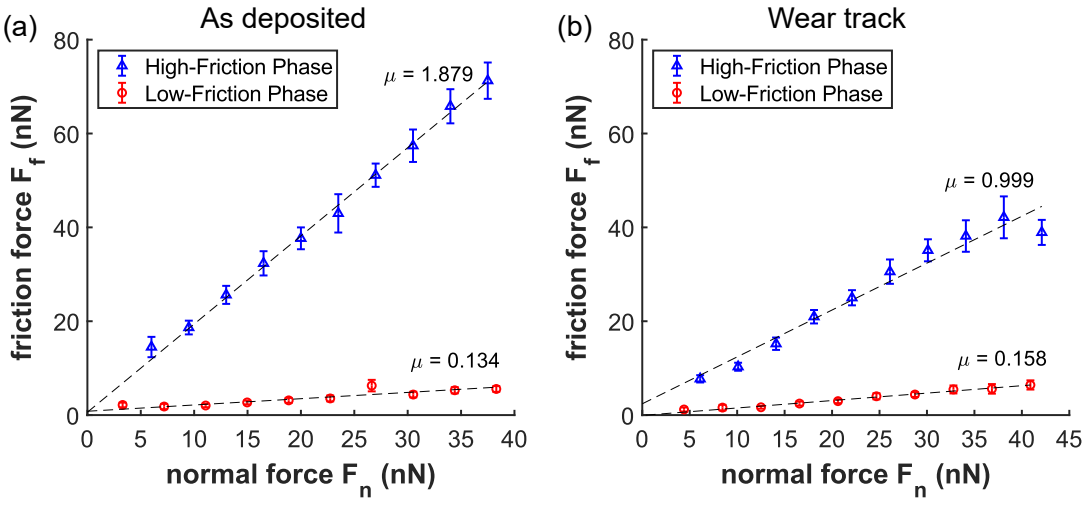

Figure 7.14: Nano-scale frictional behaviour of the two phases: Low and high-friction phases on the as-deposited W-S-C coating (a) and in the wear track (b).

reported by J. Liu et al. (97) and D.S. Grierson et al. (223), the sharp apex of the Si tip could fracture almost immediately after contact with the surface and further flatten during continuous scanning. No topographic changes were observed on the coating surfaces after the scanning, which shows that no wear occurred during the friction experiment.

The frictional behaviour inside the wear track is shown in Figure 7.14b. The values of frictional force of the low-friction phase are comparable to the ones of the bare coating, with no observable difference in behaviour or magnitude. On the other hand, the absolute friction values and behaviour on the high-friction phase reduce significantly, which can be attributed to the flattening of the surface due to polishing wear. For example, the nano-scale surface roughness of the high-friction phase, obtained over a 225 x 225 nm area, decreased from 2.31 nm on the bulk coating to only 0.54 nm within the wear track (see Table 7.6). Furthermore, sliding at reasonably low loads (that would result in polishing wear) may also contribute to the passivation of some dangling bonds on the surface, thus further reducing nano-scale frictional response.

Table 7.6: Nano-scale roughness parameters of the areas selected for the tribotest

	As deposited		Wear track	
	low friction	high friction	low friction	high friction
S_a (nm)	3.058	2.312	1.919	0.536
S_q (nm)	3.818	3.111	2.575	0.675
Skew	0.05	0.51	0.65	0.38
Kurtosis	-0.262	1.2	1.31	0.136

The amount of the low-friction phase across the width of the wear track is displayed in Figure 7.15. The measurements were performed perpendicular to the macroscopic sliding direction, and the coordinate system was placed on the edge of the wear track for all three of the analysed samples. Figure 7.15a and Figure 7.15b show the topography and the frictional map of the 8 N wear track, on which the ratios were obtained. The dashed line represents the location of the edge of the wear track. The low-friction phase corresponds to dark-blue points and the high-friction phase to the lighter blue. Regions with higher values of friction (green, yellow, red) are a consequence of surface topography or surface contamination. These regions directly correspond to the holes on the topography scan. In contrast, the boundaries between the two phases are not visible in the topography image. The presented ratios were determined as the amount of the low-friction phase against the total corresponding area along the width of the wear track. A threshold was selected between the values of the two phases and the points below the threshold were attributed to the low-friction phase.

Comparing the distributions on the wear tracks obtained at low (2 N), intermediate (8 N) and high (20 N) normal loads in Figure 7.15c reveals significantly different

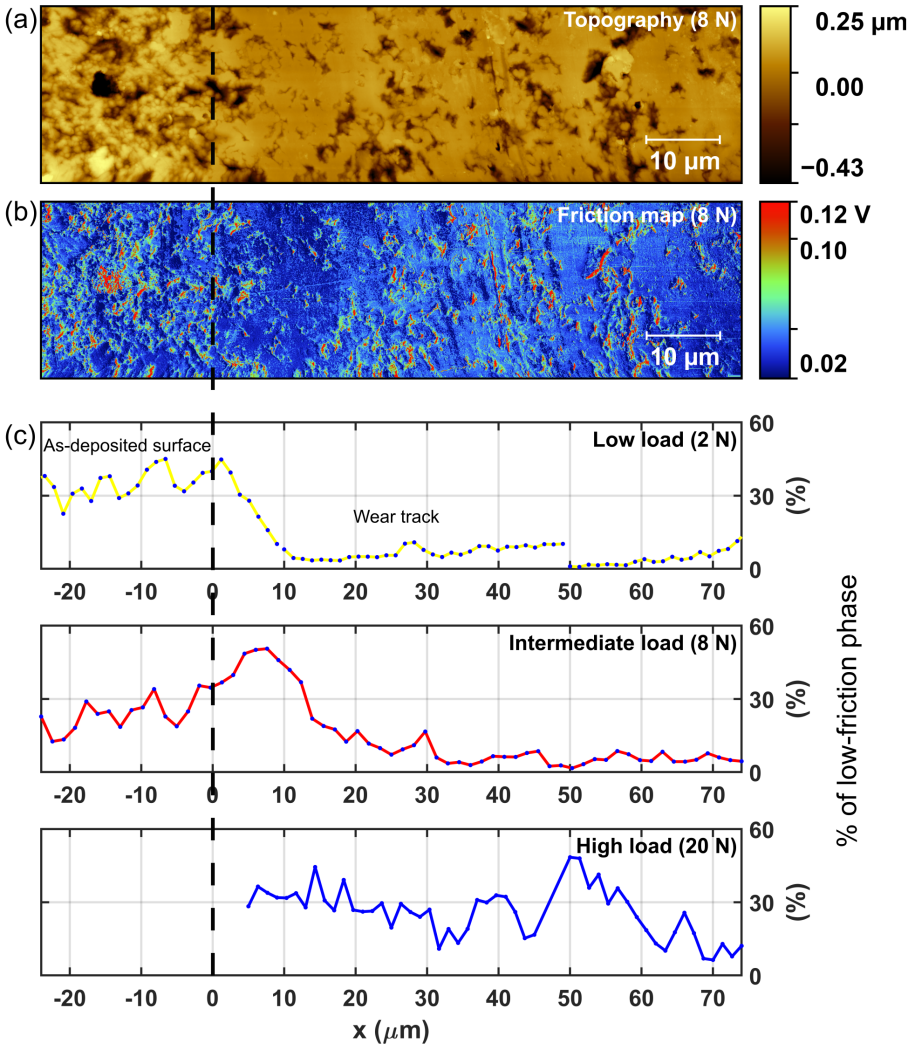

Figure 7.15: The amount of the low-friction phase across the wear track. (a) 98 x 15 µm topography scan of the 8 N wear track. (b) The corresponding friction map. (c) The ratios of low-friction phase for 2 N, 8 N and 20 N wear tracks.

characteristics. As expected, there is no observable difference in the regions outside of the wear tracks, with the low-friction phase remaining between $20 - 40\%$ in all the measured points. The other edge of the wear track was not reached on any of the samples, due to wear tracks being wider than the AFM scan size limit of 100 µm (see Figure 7.3).

At low loads (2 N), the amount of the low-friction phase drops immediately at the edge of the wear track and remains low until the end. There are some slight local increases in a few points, but the amount stays below 10%. At intermediate loads (8 N), we can observe an increased amount of low-friction phase up to 50% within the first 15 µm of the wear track, indicating transfer and accumulation of the low-friction phase towards the sides. The concentration then decreases to $15 - 20\%$ until 30 µm and finally drops to below 10%, reaching similar distribution to low loads.

On the other hand, significantly different behaviour can be observed in the last wear track obtained at 20 N. The amount of the low-friction phase is much higher than in the other two, and it even increases to almost 50% towards the centre of the wear track. This suggests that at higher contact loads, both phases wear at similar rates.

7.4 Discussion

Firstly, we must note that some of the friction measurements with different probes of the same type followed the $^2/_3$ power law (Figure 7.16), thus indicating adhesive behaviour according to the Hertz-plus-offset model (73), similar to previously reported results by J. Zekonyte et al. (37, 38) on W-S-C and W-S-C-Cr coatings. However, the probe shape can strongly influence the resulting contact properties (258). To accurately analyse the samples and minimise the potential error arising from the probe shape, all the quantitative friction measurements reported here were performed using the same probe, which had undergone pre-wearing during the initial topography tests. This assured minimum wear during the frictional experiments and, therefore, consistent probe shape throughout the measurements.

The observed columnar topography (Figure 7.8) of the as-deposited W-S-C coatings is comparable to the previously reported structures of similar coatings (21, 259). The coating thickness is uniform, but the overall surface roughness is high compared to the thickness. As shown in the cross-section (Figure 7.9), the surface roughness is a consequence of the substrate roughness, rather than coating non-uniformity. Nevertheless, surface roughness did not affect the tribological performance.

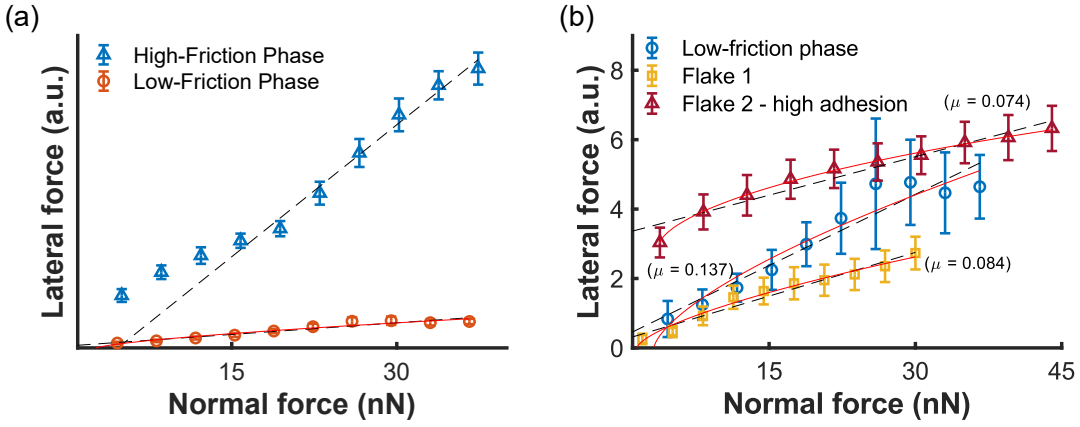

Figure 7.16: Another measurement on the same sample with a different tip, showing the same trend but slightly different frictional behaviour (a). A comparison of frictional response on the low-friction phase and on two flakes (b). Much higher adhesion was detected on flake 2.

The as-deposited coating surface consists of two separate phases, with contrasting nano-scale frictional properties: (i) high-friction phase, with a coefficient of friction above 1, indicating the onset of chemical bonding between the tip and the surface, and (ii) low-friction phase, exhibiting easy sliding with a coefficient of friction of approximately 0.15. The size and the shape of the observed phases are without clear order. Their relative distribution on the as-deposited surface reveals that the two phases attribute to approximately equal amounts across the entire coating. Our results show that the phases are completely separated, with clearly defined borders in between. The feature sizes (i.e. the size of a single continuous low-friction section) can range anywhere from 100 nm to over 10 µm. According to E. Serpini et al. (260), nano-scale friction of pure sputtered amorphous TMD films is reported to be significantly higher than that of the crystalline material. Similarly, amorphous carbon also exhibits high nano-scale friction (261), especially under ambient conditions (73). From our observations, we can conclude that the high-friction phase corresponds to a highly disordered solution of WS_2 and carbon, while low friction represents locally nanocrystalline WS_2. The highly disordered structure likely contains high amounts of dangling bonds, thus resulting in chemical bonding with the tip during sliding and consequently increased nano-scale friction.

Frictional response within the wear tracks shows some degree of friction reduction of the high-friction phase, compared to the respective measurement on the as-deposited bulk coating. This reduction may be linked to flattening of the surface due to polishing wear and passivation of dangling bonds during sliding. We can again identify the two separated phases; however, their distribution is changed and shows load dependence. Whereas the as-deposited coating shows a reasonably even distribution of the phases over the entire coating surface, the distribution across the wear track profiles varies at different loads. This indicates uneven wear of the two phases. At low loads, the low-friction phase wears preferentially, leaving a much higher concentration of the high-friction phase on the wear track. A similar case is observed at 8 N, but the amount of the low-friction phase is slightly higher, particularly closer to the edge of the wear track. On the other hand, at 20 N, high and abrasive wear results in continuous removal of the material. Therefore, the ratio of high and low-friction phases is similar to that of the as-deposited surface.

Furthermore, we have observed traces of fully recrystallised WS_2 tribo-film being formed in the wear tracks in the form of multilayered flakes. The coverage of the wear tracks with such crystalline features is low, and they occur randomly across the analysed areas. This is somewhat contradictory to the previously believed sliding mechanisms of TMD and TMD-C coatings (21, 31) and indicates that the tribo-film formation is very local within the wear tracks. Likely, the structural transformation (from amorphous W-S-C coating into crystalline WS_2 tribo-film) occurs only at the asperities in the contact where the energy input is the highest; in fact, the real contact

area represents only a fraction of the total apparent contact area. The tribo-film is only formed when enough energy is introduced in the contact, rather than being formed continuously. Therefore, even low coverage by WS_2 tribo-film can still provide a significant reduction of friction. It is worth noting that low amounts and sparse distribution of such crystalline layers may also present a challenge in the observation of tribo-film formation by TEM; for coatings with low amounts of tribo-film in the wear track, these areas can easily be missed. As seen from the example in this chapter, the thickness of the formed flakes is only a few layers, and they could easily be removed or damaged during sample preparation or further handling. Furthermore, the inability to detect the exact location of the flake by SEM requires relying on the reference AFM scans to identify the suitable area for analysis.

The observed nano-scale frictional properties, namely the coefficient of friction, differ substantially from the measurements at the macro-scale; nevertheless, they can be understood by the same principles. Since the AFM tip represents a single asperity (32) and the ratios between the phases on the as-deposited coating surface are close to 1:1, it follows that, on average, only half of the asperities in the macro scale contact would initially interact with the potentially chemically reactive high-friction phase. Interaction between the reactive surface and the sliding body results in immediate passivation of the surface dangling bonds and, therefore, a rapid reduction of the friction force.

Furthermore, some material transfer to the sliding body can occur, thus further modifying the interface structure. The actual sliding interface is, therefore, established within the coating, rather than between the sliding body and the coating, meaning that the frictional properties are mainly driven by the shear strength of the coating material. Furthermore, the tribo-film, which is formed when the introduced energy to the contact could damage the coating, can further protect the surface and reduce friction.

Finally, we have shown that using the AFM to identify the presence of crystalline tribo-film and study its structure is a very powerful alternative to standard wear track analysis with TEM. It does not require specific sample preparation and has a much lower energy input during the measurement, thus preventing the sample from potential alterations, which can occur with other beam-based characterisation techniques.

7.5 Conclusions

AFM analysis of W-S-C coatings revealed a two-phase structure. The phases exhibit notably different frictional characteristics, with an order of magnitude difference in

absolute values of lateral forces between them. Raman analysis has revealed obvious contrast between the regions either rich in carbon or rich in WS_2 and with varying crystallinity across the analysed area, leading to a conclusion that the two phases correspond to an amorphous solution of WS_2 and C (high-friction) and nanocrystalline WS_2 (low-friction) regions.

Frictional mapping within the wear tracks has unveiled different distributions of low and high-friction phases across the wear tracks according to the applied loads during the macro-scale tribotests. At low loads, only the high-friction phase remained, indicating preferential wear of the low-friction phase. At intermediate loads, the low-friction phase was abundant near the edges but almost depleted towards the centre of the wear track. At high loads, we observed a completely different distribution; the amount of the low-friction phase was higher than at lower loads but remained constant across the measured area. It can be correlated to considerably higher wear rates that were observed at 20 N. We can conclude that the high-friction phase provides good wear resistance and structural stability, while the low-friction phase provides good sliding properties.

Large, flat, and multilayered WS_2 flakes were identified within the wear tracks by AFM analysis. The high resolution of AFM allows a very detailed examination of the surface and can reveal features that would be impossible to identify with other techniques. Up to now, the crystallinity of the TMD tribo-film has mostly been examined by TEM. However, our analysis shows very low coverage of the wear track with the fully crystalline tribo-film. Performing TEM analysis on rough coatings such as those presented in this study would be challenging without precisely knowing the location of the crystalline tribo-film. Additionally, the low coverage of the wear tracks with the flakes indicates very local recrystallisation of WS_2 where the contact conditions (pressure, temperature) exceed the threshold of energy input required for structural transformation.

Chapter 8

Discussion: frictional properties of 2D materials across multiple scales

In this work, we assessed the origins of low friction of transition metal dichalcogenides (TMDs) across different scales by combining the experimental techniques from nanotribology, macrotribology and computational simulations. Friction was assessed on a number of crystalline systems (monolayer MoS_2, $MoSe_2$ and mono and multilayer WS_2 and WSe_2), manufactured by chemical vapour deposition (CVD), and on TMD based sputtered thin-film coatings with amorphous (MoS_2) and two-phase (W-S-C) structure. Chemical composition, crystallinity, crystalline orientation and surface contamination were found to have a substantial effect on the nano-scale friction. In contrast, the contact sizes at the macro-scale are larger than realistic crystal sizes, making amorphous and nanocrystalline structures more favourable. A low friction interface at the larger scales is then established within the contact when the conditions exceed the required crystallisation energy. However, due to resulting high contact pressures and arising internal stresses stretching beyond the coating-substrate interface, coating adhesion to the substrate is one of the main factors limiting the tribological performance of the system.

Focusing on the nano-scale performance of the monolayers, we have found that all the analysed samples exhibited similarly low friction. The differences in frictional response between the samples were below the quantitative precision of the experimental set-up, and the only way to meaningfully compare the behaviour of different materials was to measure all the samples in a single session and limit contact conditions to prevent excessive wear of the tip. Completing all the measurements in a single session removed a significant level of uncertainty arising from contact geometry and calibration (95). The ranking of the frictional responses of the analysed materials ($WS_2 > MoSe_2 > WSe_2$) was similar to previously reported results on MoS_2 and $MoSe_2$ monolayers (196). The outlier was the measurement on MoS_2, which contained

an adsorbed contamination layer on the surface after deposition, despite measuring multiple samples. Nevertheless, the measured friction on MoS_2 was still in the same order of magnitude as the rest. However, the comparison with the others was not possible due to differences in frictional behaviour, indicating different processes occurring within the tip-MoS_2 contact.

Different orientations of a number of WS_2 and WSe_2 flakes revealed observably different friction, thus showing that frictional anisotropy on TMDs can also be observed in environmental conditions and at larger tip radii. As expected, the effect of flake orientation was less pronounced than in a vacuum (226) due to the unavoidable presence of environmental adsorbents present on the sliding bodies. As reported in the literature (225, 226, 262), the frictional anisotropy of TMDs is expected to be high and can result in a significant change in friction even at small angle variations. A larger number of data points and more precise angle control would be required to extract more meaningful information from our samples; however, that was not possible due to limitations of the available equipment.

A shift in behaviour can be observed when we compare the measurements on the mono and multilayered samples. The friction on the monolayer flakes follows an accepted Hertz-plus-offset model, thus indicating a similar behaviour to bulk materials; a single layer with sufficient adhesion to the substrate only modifies the magnitude of lateral force and does not introduce any additional behavioural changes in the contact. On the other hand, a substantial deviation from the model was observed on the multilayered WSe_2 samples; the friction was larger at very low loads and lower at higher loads when compared to the corresponding monolayer. Only WSe_2 was used in the analysis due to the higher consistency of flakes containing at least two layers with a high-quality structure. Nonetheless, similar behaviour is expected to apply to the other 2D materials.

When analysing layer dependence, it is important to distinguish between supported and unsupported layers, as they experience a significantly different response to loading. The elastic deformation of a thin supported layer is predominantly governed by the elastic deformation of a substrate, as long as the thickness of the layer is significantly lower than the interaction depth of the internal stresses ($d << \delta$). Conversely, the initial deformation of the suspended layer is driven only by the elastic properties of the layer and the surrounding geometry, i.e. the dimensions of the hole in the substrate across which the layer is deposited. With the increase in the number of layers, the stiffness of the unsupported layer increases linearly (35), whereas the more complex composite stiffness of the substrate-layer system in the supported layers becomes increasingly affected by the layer properties. Nevertheless, both systems are expected to approach the bulk properties of the layered material when the total thickness of the sample becomes significantly larger than the interaction depth.

Consequently, contact area and frictional behaviour can differ significantly between the two systems.

The environment in which the measurements are performed can have a significant influence on adhesion between the probe and the surface, and can consequently influence friction and induce changes in the frictional behaviour. For example, measurements performed in ambient environmental conditions are expected to have higher adhesion due to the formation of meniscus forces around the contact area (263–265). In contrast, the majority of the adsorbed water would evaporate in a vacuum. Similarly, a reduction in adhesion can be expected in aqueous environments, as the meniscus can not form around the contact. The environment and experimental conditions are one of the main reasons why the behaviour we observe here differs from the reported results in the literature (35, 36, 228, 229, 266) and why the results in literature can be inconsistent (35, 36). Some of the reported measurements were performed in vacuum (35, 228, 229) or ambient air (36, 266). Furthermore, two publications only report results at a single load (35, 36), and one publication analysed only a very narrow range of forces (266). As shown in our results, selecting the results at a single load would be insufficient and could be the reason for the discrepancies in the literature (35, 36). Filleter et al. (228, 229) have shown frictional behaviour over a large range of forces; however, the behaviour they observed was different from ours as they performed the measurements in a vacuum.

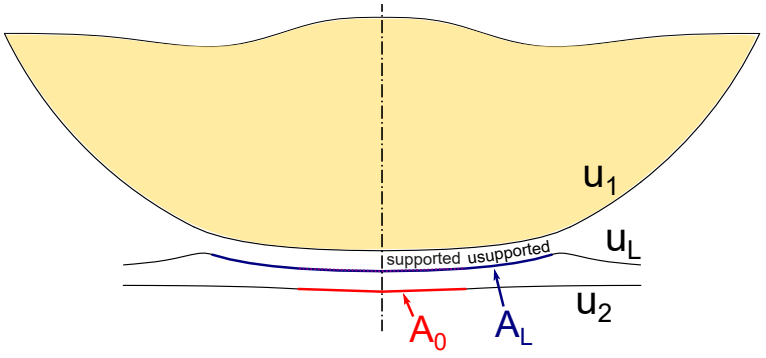

Figure 8.1: A schematic of the contact conditions showing supported and unsupported regions of the layer.

Based on our observations and the comparison of the results with the literature, we proposed a new mechanism describing the contact and sliding properties of atomically thin layered materials. For the conditions when the adhesion between the probe and the top layer is larger than the cohesive force between the layers, the top layer would locally detach from the rest of the layers and form a lip around the initial contact area with the tip, thus increasing the total size of the contact. The final contact area would therefore contain a combination of supported and unsupported areas, as shown in Figure 8.1. The unsupported area behaves as a monolayer and has a corresponding contact shear strength equal to an unsupported monolayer, whereas the supported area behaves as a multilayer, for which it was reported to experience

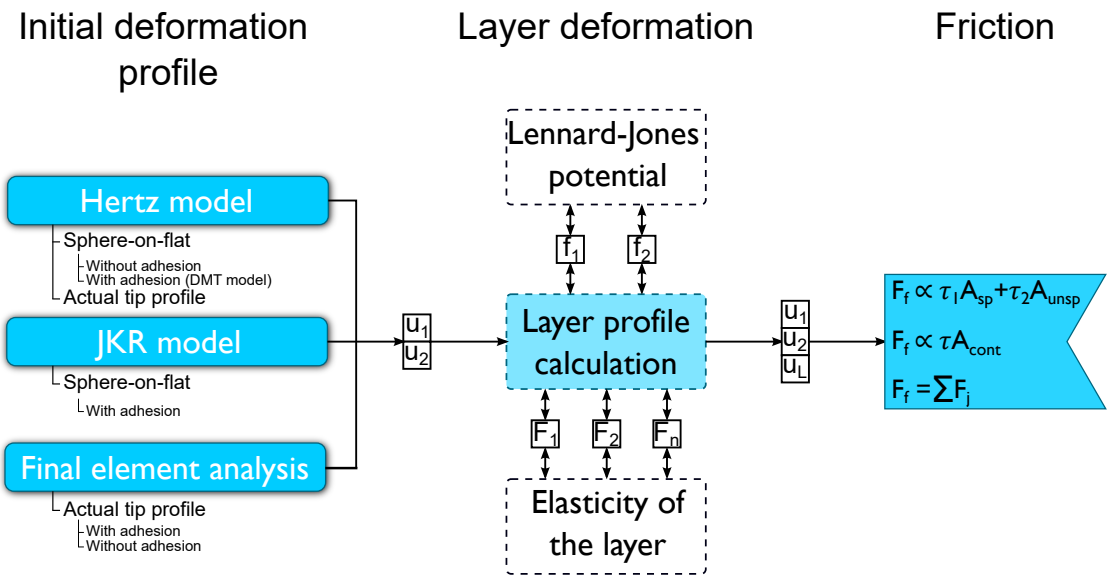

Figure 8.2: A schematic of the numerical model, displaying modular structure and parameters that are shared between individual modules.

lower friction due to phonon coupling between the layers. The combined effect of the two phenomena can explain the behaviour we observe in our results, which we have confirmed with a custom numerical model of the contact.

The numerical model used was based on the initial deformation profile, obtained using the standard Hertz model for a sphere-on-flat contact. The layer was then introduced between the two contacting bodies; in the initial position, the layer was fully in contact with the deformed flat surface. The atoms in the layer follow the actual lattice configurations: hexagonal, rhombical or square. The forces between the layer atoms and the surrounding surfaces were modelled by Lennard-Jones potential (LJP), whereas the forces between the atoms within the layer were approximated by linear springs. Lateral forces were then calculated as a function of the contact area, where the two areas, corresponding to supported multilayer and unsupported monolayer, were evaluated separately. The resulting evolution of frictional force with load was in good agreement with the experimental observation within the analysed range.

In our numerical model, we used a simple formulation for the initial deformation according to the Hertz model. The tip apex shape was approximated as a perfect sphere, which was a good enough approximation in our case, as any deviation from the spherical shape should show as a deviation from the $^2/_3$ power law on the monolayer. However, this might not provide a general solution for an arbitrary shape of the probe. As shown in Figure 8.2, the model is composed of independent modules. Therefore, changing the method to calculate the initial deformation profile with a more specific method can easily be done and would not affect the performance of the rest of the model. Furthermore, friction could also be evaluated differently. As the positions of the atoms are known precisely, a more complex method, combining the

individual contributions to friction from each atom, could be used instead. Similarly, the Lennard-Jones potential can be swapped with any other inter-atomic potential. Whereas any of these corrections would provide some degree of improvement over the results presented in Chapter 5, they would come at an additional computational cost, which might not be feasible to perform. However, the purpose of the presented model was not to predict the exact values of friction of the chosen system but to support an explanation of the behaviour observed in multilayer systems, for which the simplifications were sufficient.

Based on the observations from the numerical model, we proposed a modification to the Hertz-plus-offset model for fitting the data obtained on the multilayer systems. The resulting two-component model was based on the same principles as the numerical model: the contact area constitutes of two regions with different contact shear strengths. The model provides a good fit and an improvement over the existing models, including the m-power law (73), which does result in a mathematically sufficient fit but returns the wrong value of the contact shear strength and a false interpretation of the origin of the observed behaviour. The ambiguity of the power coefficient m as a factor to account for the discrepancy in the probe shape (73) does not provide a sensible explanation for the frictional behaviour of the multilayers. The contact shear strength for the bilayer sample calculated by our model was 195.6 MPa, which is 25% lower than monolayer and complies with the literature. In contrast, the m-model predicted the contact shear strength of the multilayer as 640.2 MPa.

A different case was observed at the atomic scale, where the measurement on the multilayer still followed the $^2/_3$ power law, indicating no influence of adhesion on frictional behaviour. As the atomic scale measurements were performed in water, this significantly reduced adhesion between the tip and the top layer, resulting in the top layer remaining firmly attached to the layers below. A sharper tip further results in a larger gap between the slider and the top layer and, consequently, a reduced pull on the top layer by the probe. This particularly highlights the importance of the environment and the scale on the resulting frictional behaviour and how the specific samples' nano and atomic-scale properties can only be considered valid in the environments they were tested in. Furthermore, this points to the meniscus forces having the largest effect on the frictional behaviour, which could indicate a possibility of a different model besides LJP to obtain the layer profile.

Moving to the larger scales and non-crystalline samples, we have analysed two different thin-film systems, a composite W-S-C (Chapter 7) and a pure MoS_2 (Appendix D). W-S-C coating was identified to exhibit a two-phase structure with significantly different frictional properties. The nanocrystalline WS_2 phase experienced low friction, similar in magnitude to the TMD flakes in Chapter 4, whereas the amorphous solution of WS_2 and carbon experienced high friction due to

the high amount of dangling bonds on the surface of the coating. On the other hand, the structure of the MoS_2 surface is more homogeneous and experiences high friction, which indicates the coating is amorphous. Both coatings show the formation of a crystalline low-friction tribofilm during the tribotest in a vacuum; however, the WS_2 tribofilm on W-S-C coatings was larger and better defined as MoS_2.

The distribution of low and high friction phases on the W-S-C coating has changed after sliding. Different distributions could be observed at different loads of the tribotest. At the lowest loads, very low amounts of low friction phase remained, whereas, at the highest load, the distribution was comparable to the bare coating surface, indicating preferential wear of nanocrystalline WS_2 at lower loads. The sliding mechanism at low loads is, therefore, guided by the nanocrystalline WS_2 phase providing low friction and the amorphous W-S-C phase providing structural stability and wear resistance. As the coverage of the wear tracks with the fully crystalline features was sparse, we have concluded that the tribo-film is formed locally in the contact only when the load conditions exceed the formation threshold energy. The higher hardness of W-S-C coatings, when compared to MoS_2, promotes higher energy concentration in the contact, which can explain the better defined WS_2 flakes.

Comparing the measurements performed on the same MoS_2 coatings across different scales displayed the trend of reduction of the coefficient of friction with increasing scale. The graph can be extended to include the remaining measurements on other samples from this work, as presented in Figure 8.3. Note that the friction coefficients obtained by AFM measurements performed with different probes can vary substantially (95). Therefore, minor differences between the samples that exhibit friction in the same order of magnitude can only be analysed using the same probe, as reported in Chapter 4. Nonetheless, the graph in Figure 8.3 displays clear trends, as friction can be decreased by improving sample crystallinity or increasing the scale.

First, the crystallinity of the samples has an immediate impact on friction at the same scale, which can be directly correlated with the amount of dangling bonds at the surface (amorphous as-deposited $>$ amorphous wear track $>$ nanocrystalline $>$ monolayer $\approx$ tribofilm $>$ multilayer). The amorphous structures have the highest amount of dangling bonds at the surface, thus significantly influencing single asperity friction; instead of continuous sliding, the bonds between the tip and the sample are constantly formed and broken (stiction). Therefore, the lateral force needs to be large enough to break the bonds and can even result in friction coefficients above 1. Furthermore, higher friction observed on the as-deposited sample can be attributed to a higher degree of surface oxidation and, to some extent, dangling bond termination during sliding. The nanocrystalline structure already experiences considerably lower nano-scale friction at $\mu \sim 0.15$, an order of magnitude lower than amorphous. Due to the crystalline nature, the faces of the grains are almost fully terminated and the

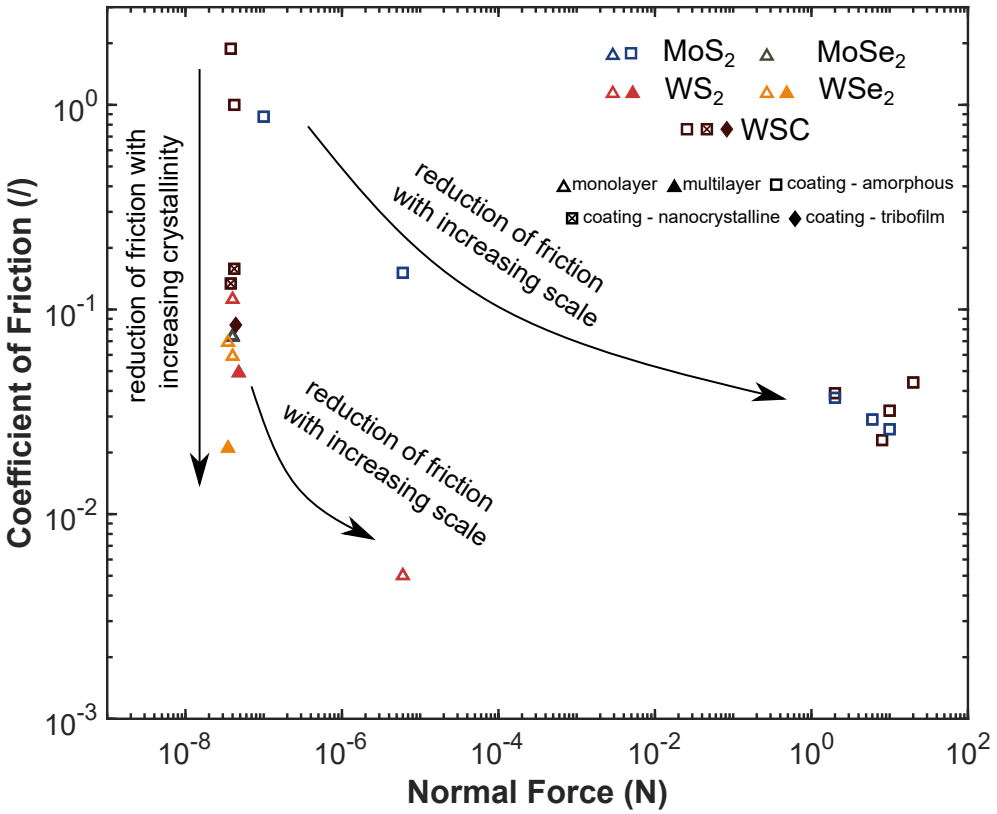

Figure 8.3: A collection of all friction measurements included in this work, displaying the correlation between different scales. The arrows show the direction of friction reduction with either increasing scale or improving crystallinity.

dangling bonds only exist at the boundaries between the grains. Furthermore, the CVD deposited monolayers experience even lower friction. The size of a single layer (single grain) is larger than the measured area, thus eliminating the influence of dangling bonds at the layer edges. Even lower friction was observed on the multilayers (at higher loads), which was attributed to a better coupling between the layers and consequently more efficient energy dissipation. The tribofilms, however, despite displaying multilayer structure, exhibit friction in magnitude closer to monolayers. The reasons for that are poorer crystal quality than CVD deposited, which were formed in a controlled environment, lower sample cleanliness and transfer of material to the probe.

Second, the scale has an enormous effect on the coefficient of friction, and already transitioning from the nano-scale to the intermediate micro-scale decreases the coefficient of friction of amorphous systems to ~ 0.15. Furthermore, similar values to those observed on the fully crystalline samples at the nano-scale can be observed on the coatings at the macro-scale. As the contact loads increase, the contact area increases at a slower rate; furthermore, it is a well-known fact that the real contact area of macro-scale systems is always smaller than the apparent nominal contact area due

to surface roughness, as only a small proportion of surface asperities are actually in contact with another surface. Consequently, the proportion of the formed bonds between the two bodies is much lower than at the nano-scale, and the transfer of material from the coating to the slider can result in the sliding interface forming within the coating material, thus further promoting the reorientation of the crystallite basal planes. Furthermore, higher energy input in the contact promotes local recrystallisation of TMD flakes, which further decreases friction.

The lowest coefficient of friction among all measurements was observed on the crystalline sample at the intermediate scale, displaying a similar trend of friction reduction to the amorphous coatings. This further shows the impact of the contact area increasing slower than load. If the same effect continues towards the macro-scale, this could present large-scale TMD crystals as potential extremely-low friction materials in any environment. However, the main challenge in using crystalline TMDs at the macro-scale would be to manufacture large-scale single grain and defect-free crystals, as any defect in the crystal would cause the layer to tear and peel off instantly. As we have shown, defect-free layers can prevent wear when scratched with a sharp AFM tip at even very high contact pressures. Therefore, achieving a low-defect criterion would be imperative to attain good performance. Macro-scale friction using MoS_2 flakes deposited on DLC has recently been highlighted by Yu et al. (267). The flakes were deposited by the evaporation of an ethanol-MoS_2 dispersion, which formed a thick film of individual flakes on top of the substrate. They achieved macro-scale friction coefficients in the humid air as low as 0.005, which are significantly lower than in sputtered systems. Similar observations were made when graphene films were used in combination with nanodiamond particles (268) or using a combination of graphene and MoS_2 flakes (269).

Ultimately, nano-scale friction of TMDs can be devised into two categories: amorphous structures, which experience high nano-scale friction and for which the energy introduced by the AFM probe is not sufficient to form easy sliding tribofilm, and crystalline flakes, which experience a very low coefficient of friction and include nanocrystalline structures. The obvious influences on the frictional response are also roughness, sample quality, presence of defects (e.g. nanocrystalline samples experience slightly higher frictional response compared to their fully crystalline counterparts, see Figure 7.14 and Figure 4.3), sliding orientation (see Figure 4.9) and thickness of layers (see Figure 5.2).

Chapter 9

Conclusions

All the analysed TMD monolayers exhibit low friction properties, with only minor but still observable differences between the samples. Generally, the selenides were shown to exhibit lower friction than the sulphides. TMD monolayers were shown to prevent wear beyond the plastic deformation limit of the Si probes used. Furthermore, sliding orientation had some effect on friction, but the observed difference was even smaller than the difference between different samples, whereas sliding speed had no effect on friction within the analysed range. The friction of monolayers is significantly affected by sample contamination, as displayed by MoS_2 samples. Therefore, when selecting a specific TMD monolayer it is most important to prevent sample contamination during deposition and assure good crystal quality.

A difference in frictional behaviour was observed between monolayers and multilayers, which was attributed to a combination of increased contact area due to adhesion, and more effective energy dissipation due to the coupling between the layers. With this, we displayed the importance of performing load-dependent measurements at the nano-scale instead of single-load. The difference in the behaviour was backed up by a numerical simulation.

The atomic-scale measurements have displayed clear stick-slip behaviour; however, the event distances showed a broad distribution and consequently, a clear pattern could only be observed on a very small area. We have shown that the rotation of the flake would significantly impact the event distances. The additional thermal activation and finite probe stiffness in the slow scan direction can further mask the patterns in the friction maps. Nonetheless, the required parameters could be extracted from the measurements and were later used in the machine learning fitting algorithm.

The nanotribological analysis of W-S-C coatings has demonstrated the complexity of a macro-scale frictional problem. The W-S-C coating itself consists of two separate phases, where the phase with high friction corresponds to an amorphous solution of

WS_2 and carbon and low friction to nano-crystalline WS_2. The low friction phase experiences preferential wear at low loads. The two-phase structure provides favourable macro-scale tribological characteristics, as the amorphous phase assures structural stability, and the nano-crystalline low friction phase promotes easy sliding. Furthermore, multilayered WS_2 flakes were identified within the wear track, which showed that AFM could be used instead of TEM to identify tribo-film and its properties. In the specific case of W-S-C coatings, the coverage with such features was low, meaning that recrystallisation only occurs locally within the contact and only when the contact conditions exceed the recrystallisation energy threshold, i.e. when the energy input is high enough to damage the coating. Similar features, albeit smaller, were also observed in the wear tracks of amorphous MoS_2 coatings.

To conclude, we found that friction decreases with increasing scale and with improved crystallinity and crystal quality. The contact area between a sphere and a flat surface increases at a slower rate than load. The contact condition also transitions from single asperity contact at the nano-scale to multi asperity contact at the macro-scale, meaning that only a small proportion of the apparent contact area is actually in contact with the sample and contributes to friction. The main factor contributing to the friction of a single asperity on an amorphous structure was attributed to chemical bonds forming between the asperity and the dangling bonds of the sample. At the nano-scale, the force required to break these bonds is relatively high and can result in coefficients of friction well above 1. At the macro-scale, however, these bonds contribute to only a fraction of the normal load. Likewise, better crystallinity and crystal quality decrease the amount of dangling bonds interacting with the sliding body, thus resulting in low friction at the nano-scale.

Appendix A

AFM Probe Characterisation

A.1 Introduction

Measuring nano-tribological properties of materials requires a good understanding of the properties of the AFM probe. Whereas determining the shape of a counter-body in a macro-scale contact can be relatively straightforward, the shape of the AFM probe is more irregular and rarely has an ideally spherical apex (73). Furthermore, nano-scale wear, which typically occurs in an atom by atom fashion (98), can significantly alter the shape of the probe during the measurements and therefore change the detected frictional behaviour significantly.

Similarly, an accurate description of forces at a small scale is not a trivial task. The thickness of an AFM cantilever can be lower than 1 µm, making the determination of elastic properties based on the methods of classical mechanics very challenging due to manufacturing tolerances. Furthermore, coupling of the cantilever deflection with the optical and electronic system can make the quantitative interpretation of the actual forces in the contact even more complicated. Methods based on cantilever oscillation or scanning a calibration grating are therefore preferred methods for the calibration of normal and lateral spring constants, respectively.

Here we present the methods for the tip shape determination, normal and lateral calibration, and an example of the results obtained on one of the probes. The presented procedure needs to be performed for every quantitative frictional measurement with an AFM.

A.2 Methodology

A.2.1 Determination of the probe shape

As mentioned above, the shape of the AFM probe tip is rarely ideal, therefore the final image would always contain some distortions related to the probe geometry (222). If the shape of the tip is known, we can correct for such distortions. Furthermore, understanding the exact geometry of the tip allows us to correctly apply the suitable contact model for the description of nano-scale frictional properties of the measured material (73).

D. J. Keller and F. S. Franke (222) presented an envelope reconstruction method for the determination of the probe geometry. The method is an easy way of determining the probe shape, as it does not require solving complex derivatives. It computes the reconstructed image of the sample surface as an envelope of a larger set of probe-surface functions and is also applicable to the data that contains relatively high levels of noise, i.e. it filters out any fluctuations that are below a certain critical dimension. A summary of the method and the corresponding equations are presented below.

$z(x, y)$ is an obtained probe microscope image, where z is the height of the image surface at each position (x, y) and $t(x, y)$ is a function that describes the surface of the probe tip. The coordinate system is positioned so that the sample is below the probe, meaning that the tip surface would be downward pointing and has a well-defined minimum – the end-point of the tip. The axis of the tip is defined to be parallel to the z-axis of the sample and passes through the end-point. It is usually convenient to position the origin of $t(x, y)$ in the end-point. As shown in Figure A.1 the resulting reconstructed sample surface $r(x, y)$ is the envelope formed by all tip surfaces.

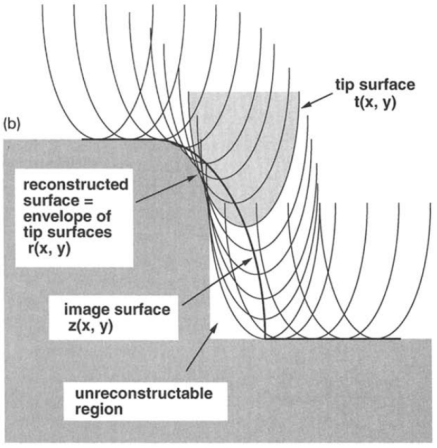

Figure A.1: Envelope reconstruction (222).

To formalise the problem, we define an image surface $z(x, y)$, which is defined in the region R of the xy plane. The surface of the probe is given as $t(x, y)$. (x, y) and (x',y') are two points in the xy plane. We can define a function:

$$w(x, y; x', y') = z(x', y') + t(x - x', y - y'), \tag{A.1}$$

where $w(x, y; x', y')$ is a tip function with its axis located in (x', y'), and the end-point raised to $z(x', y')$. Therefore, the reconstructed surface $r(x, y)$ would be the minimum of all functions $w(x, y; x', y')$, namely:

$$r(x, y) = minimum\{z(x', y') + t(x - x', y - y'),\ all\ (x', y')\ in\ R\}, \tag{A.2}$$

for each point (x, y) in R. The same definition can be applied when the data is only a single line and not the entire image. In that case, we substitute all instances of (x, y) with a single axis (x). Strictly speaking, the procedure above is used for the determination of the original sample surface based on the scanned image and known probe geometry. However, the same procedure can be applied to determine the probe shape, provided that we know the exact shape of the sample surface. Overall, if we only know two out of three surfaces (image surface, tip surface or sample surface) we can determine the third by switching around the roles of each image.

To determine the probe shape, we need a well-defined sample surface. We use TGT1 (ND-MDT, Russia) calibration grating, consisting of sharp tips with a tip angle of 50°±10° and a tip radius of 10 nm. We assign the role of the tip to the reference sample. Therefore, we place a set of inverted sample surfaces on top of the measured image surface. We invert the sample surface so that it points downward, as the tip would in a normal procedure. As a result, we get an inverted shape of the tip $-t(x, y)$:

$$-t(x, y) = minimum\{z(x', y') - s(x - x', y - y'),\ all\ (x', y')\ in\ R\}, \tag{A.3}$$

for all (x, y) in R.

A.2.2 Normal force calibration

Normal stiffness k (spring constant) of the cantilever is defined by the general expression (270):

$$F_n = k\Delta z, \tag{A.4}$$

where Δz is cantilever deflection and F_n is the normal force acting on the cantilever.

A wide array of analytical and experimental methods exist and are summarised in (270). The two methods that apply to our system and were used in this work are presented in the following section.

A.2.2.1 Thermal noise method

A harmonic oscillator, which is in equilibrium with its surroundings, will oscillate in response to the thermal noise (199). Thermal fluctuations of a relatively soft AFM cantilever are in the order of 3 Å at room temperature, which indicates that we can approximate the AFM cantilever as a simple harmonic oscillator with the Hamiltonian (199):

$$H = \frac{p^2}{2m} + \frac{1}{2}m\omega_0^2 q^2, \tag{A.5}$$

where p is the momentum, m is the oscillating mass, q is the displacement of the cantilever, and ω_0 is the resonant angular frequency of the system. According to the equipartition theorem, the average value of each quadratic term in the Hamiltonian is $k_B T/2$, where k_B is Boltzmann's constant and T is the temperature. This results in (199):

$$\left\langle \frac{1}{2}m\omega_0^2 q^2 \right\rangle = \frac{1}{2}k_B T. \tag{A.6}$$

Thermal noise data is collected in the frequency domain. As the area of the peak in the power spectrum is equal to the mean square of the fluctuations, the equation for the spring constant becomes (199):

$$k = \frac{k_B T}{P}, \tag{A.7}$$

where P is the area of the power spectrum of thermal fluctuations.

The method eliminates the need for the dimensions and the mechanical properties of the cantilever and is, therefore, less prone to experimental uncertainties. Thus, it is accurate and relatively simple to perform, but usually requires additional equipment that can collect the thermal noise data (270). The main limitation of the method is that it is most suitable for the calibration of soft cantilevers (for the cantilevers with the expected spring constant $k < 1\ \mathrm{N\,m^{-1}}$) (270). The thermal noise method is already built into our AFM system and therefore does not require the manual acquisition of thermal noise data and calculation of the spring constant.

However, L. Heim and M. Kappl (271), and J. Hutter (272) pointed out that all the previously reported force measurements according to the above method may have been underestimated by up to 20%, due to possible cantilever tilt. They have proposed a modification of the above equation by a correction factor based on the cantilever angle.

A.2.2.2 Resonance (Sader) method

For stiffer cantilevers (where the expected $k > 1\ N\,m^{-1}$), an alternative method, which is based upon measurement of the resonant frequency of the cantilever, is more applicable (270). The method was developed by J. E. Sader et al. (273) for the calculation of the cantilever spring constant in a vacuum. J. E. Sader et al. (233) have later extended the method to the operation in any viscous fluid. The stiffness of the cantilever can be obtained by:

$$k_z = 0.1906\rho_f b^2 L Q \omega_f^2 \Gamma_i(\omega_f), \tag{A.8}$$

where ρ_f is the density of the fluid, b is cantilever width, L is cantilever length, Q and ω_f are the quality factor and angular resonant frequency of the cantilever, and Γ_i is the imaginary part of the hydrodynamic function.

Hydrodynamic function for a rectangular cantilever $\Gamma_{rect}(\omega)$ is expressed as an empirical correction of the exact analytical result for a circular cantilever $\Gamma_{circ}(\omega)$ (274):

$$\Gamma_{rect}(\omega) = \Omega(\omega)\Gamma_{circ}(\omega), \tag{A.9}$$

where $\Omega(\omega)$ is an empirical correction function. $\Gamma_{circ}(\omega)$ can be calculated from:

$$\Gamma_{circ}(\omega) = 1 + \frac{4iK_1(-i\sqrt{i\mathrm{Re}})}{\sqrt{i\mathrm{Re}}K_0(-i\sqrt{i\mathrm{Re}})}, \tag{A.10}$$

where $Re = \rho\omega b^2/(4\eta)$ is the Reynolds number and the functions K_1 and K_0 are modified Bessel functions of the third kind. The correction function $\Omega(\omega)$ is expressed as $\Omega(\omega) = \Omega_r(\omega) + i\Omega_i(\omega)$ and is valid in the range $\mathrm{Re} \in [10^{-6}, 10^4]$. Real and imaginary parts of the correction function are expressed in terms of $\tau = log_{10}(Re)$ as:

$$\Omega_r = \frac{0.91324 - 0.48274\tau + 0.46842\tau^2 - 0.12886\tau^3 + 0.044055\tau^4 - 0.0035117\tau^5 + 0.00069085\tau^6}{1 - 0.56964\tau + 0.48690\tau^2 - 0.13444\tau^3 + 0.045155\tau^4 - 0.0035862\tau^5 + 0.00069085\tau^6} \tag{A.11}$$

$$\Omega_i = \frac{-0.024134 - 0.029256\tau + 0.016294\tau^2 - 0.00010961\tau^3 + 0.000064577\tau^4 - 0.00004451\tau^5}{1 - 0.59702\tau + 0.55182\tau^2 - 0.18357\tau^3 + 0.079156\tau^4 - 0.014369\tau^5 + 0.0028361\tau^6}. \tag{A.12}$$

The method is suitable for the calibration of AFM probes in air, where the main criterion $Q >> 1$ is satisfied. Q and ω_f can be obtained either from the thermal noise spectra or by driving the cantilever close to its fundamental mode resonant frequency. Good accuracy can be achieved for rectangular cantilevers with aspect ratios L/b exceeding 3 (233).

A.2.3 Lateral force calibration

For the assessment of frictional forces in the AFM contact, an accurate measurement of lateral forces acting on the tip is required. When a lateral force F_y is applied on the AFM tip this results in bending of the cantilever in the y-direction and torsion along the cantilever axis (270). Lateral stiffness k_Φ ($M = k_\Phi \Phi$, where Φ is the angular deflection of the cantilever and M is the torsional moment) of the cantilever with a rectangular cross-section is defined as (270):

$$k_\Phi = \frac{Gbt^3}{3L}, \tag{A.13}$$

where G is the shear modulus of the cantilever and t is the cantilever thickness.

What we experimentally measure from an AFM is the voltage (or current, depending on the system) output from the photo-detector F_o, where the subscript "o" indicates the raw value of lateral force measured in Volts or nano-Amperes. We then need to determine a correlation factor α to obtain the lateral force F:

$$F = \alpha F_0. \tag{A.14}$$

Currently, a generally accepted technique for the determination of lateral forces does not exist. The majority of existing analytical and experimental techniques are summarised in (270). The method used usually depends on the design of the AFM system and the calibration gratings available. The wedge calibration method (95) and its improvement (275) are the most commonly implemented methods for lateral calibration (276) and are therefore presented in more detail in the following section.

A.2.3.1 Wedge calibration method

The wedge calibration method is an in-situ technique for an experimental determination of a lateral calibration factor α. Presented by D.F. Ogletree et al. (95), the method focuses on measuring lateral and normal force signals on a sloped surface

with a known angle. The obtained calibration factor includes all the factors involved in the detection of lateral forces – lateral force constant, the deflection of the laser beam as a function of lateral tip displacement and sensor angular sensitivity.

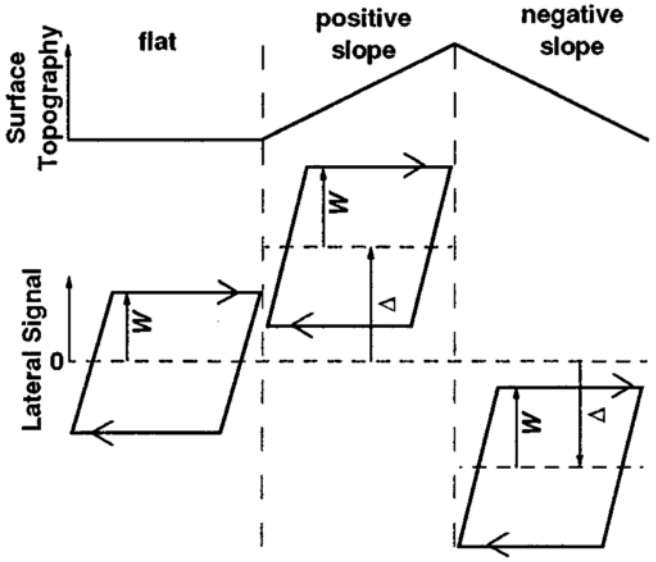

Figure A.2: LFM signals in forward and backward scanning directions for flat surface, positive slope and negative slope. W is the actual friction signal, independent from the slope, and Δ is the offset due to slope (95).

Figure A.2 shows forward and backward scans (trace and retrace) on flat, positively sloped, and negatively sloped surfaces. The frictional force W is characterised as the half-width of the friction loop and changes only slightly with slope. On the other hand, the offset Δ depends greatly on the applied load and the tilt angle – for a flat surface, it is ideally equal to zero.

During the calibration procedure, values of Δ and W are measured at different loads L. From measured values, we calculate the slopes $\Delta' = d\Delta/dL$ and $W' = dW/dL$, which are expected to be independent of the load. Using slopes instead of absolute values eliminates the effects of adhesion and any possible offset in the photodiode sensor. The slopes are equal to:

$$\alpha\Delta_0^{'} = \Delta^{'} = \frac{(1+\mu^2)\sin\theta\cos\theta}{\cos^2\theta - \mu^2\sin^2\theta} \tag{A.15}$$

and:

$$\alpha W_0^{'} = W^{'} = \frac{\mu}{\cos^2\theta - \mu^2\sin^2\theta}, \tag{A.16}$$

where μ is the coefficient of friction between the tip and the surface. By combining the two equations, we get the following expression for the determination of μ:

$$\mu + \frac{1}{\mu} = \frac{2\Delta_0^{'}}{W_0^{'} \sin 2\theta} \tag{A.17}$$

Once μ is known, we can use it to find the value of α. The above equation, however, yields two mathematically equally valid results for the coefficient of friction, which in turn results in two different values of α. Considering that μ is less than one or using another method to estimate α can help resolve this ambiguity.

One of the main concerns in the wedge calibration procedure is the cross-talk between normal and lateral forces, as even a slight misalignment between the laser or the cantilever and the detector can result in a significant contribution of the normal signal to the lateral force signal. The cross-talk in regular LFM experiments can simply be avoided by measuring the friction loop W, as it mainly affects the friction loop offset Δ. In the calibration experiment, however, the values of the lateral force offset are an important parameter.

The effect of the cross-talk can be reduced by performing a measurement on two different slopes and using the values of $\Delta'_{02} - \Delta'_{01}$, W'_{01} and W'_{02} during the calculations. The equations for the two-slope calibration using 103 and 101 planes of $SrTiO_3$ surface are presented in (95). As we are using a different calibration grating to the one presented in (95), the exact equations for the used grating were derived using the procedure given by the authors.

The authors (95) have only reported the ratios between the lateral and normal force calibration factors, as they were not able to obtain a good experimental value for the normal force constant. The published results for different cantilevers show the lateral force constant to be 19 – 51 times higher than the normal calibration constant.

The expected reproducibility of the method is within 10% for the same tip on different parts of the calibration sample. There may be significant variations among the cantilevers produced from the same Si wafer, and the tip geometry plays a significant role in the lateral force response. Experimental force calibration should therefore be performed for each probe separately (95).

A.2.3.2 Improved wedge calibration method

M. Varenberg et al. (275) have pointed out a few drawbacks of the original wedge calibration method. The original method is limited to integrated probes with sharp tips only and requires a complex specially prepared calibration sample. The authors

presented an improved wedge calibration method, which uses a more commercially available grating TGF11. It takes into account the effect of tip radius of curvature (radius of up to 2 μm), eliminates the need for multiple measurements over a higher range of applied loads and includes the effect of adhesion which is assumed to be equal to the pull-off force (275). However, the method is dependent on the applied load (276).

Figure A.3 shows a schematic of a calibration grating TGF11, which is made of silicon and consists of flat (100) and sloped (111) surfaces. The angle between the surfaces is equal to 54.75^o. Using a calibration grating with a flat facet results in an accurate friction loop offset on the sloped surface. As the friction loop on a flat surface may not be equal to zero this results in $\Delta_0 = \Delta_0^* - \Delta_0^{flat}$.

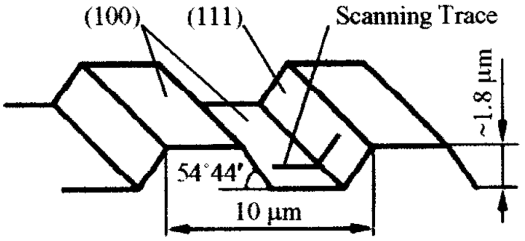

Figure A.3: TGF11 grating (275).

The correlations between the measured friction loop half-width and offset and the corresponding forces are defined by:

$$\alpha W_0 = W = \frac{\mu(L + F_{pull-off}\cos\theta)}{\cos^2\theta - \mu^2\sin^2\theta} \tag{A.18}$$

and:

$$\alpha\Delta_0 = \alpha(\Delta *_0 - \Delta_0^{flat}) = \Delta = \frac{\mu^2\sin\theta(L\cos\theta + F_{pull-off}) + L\sin\theta\cos\theta}{\cos^2\theta - \mu^2\sin^2\theta} \tag{A.19}$$

The pull-off force $F_{pull-off}$ is measured on the flat portion of the grating and is used to represent the adhesion at all loads. Dividing the above equations results in a quadratic equation:

$$\sin\theta(L\cos\theta + F_{pull-off})\mu^2 - \frac{\Delta_0^* - \Delta_0^{flat}}{W_0}(L + F_{pull-off}\cos\theta)\mu + L\sin\theta\cos\theta = 0. \tag{A.20}$$

The above equation yields two values of μ, which in turn yields two different values of α. The real solution for μ needs to be smaller than $1/\tan\theta$. If both values satisfy the criterion, we end up with two possible values for α, and for each value of α, we have two friction coefficient values μ^a and μ^{flat} on the sloped and flat surfaces, respectively. The friction coefficient on the flat surface can be obtained from the above equation, by using $\theta = 0$ and $W_0 = W_0^{flat}$:

$$\mu^{flat} = \frac{\alpha W_0^{flat}}{L + F_{pull-off}}. \tag{A.21}$$

The two coefficients of friction may differ slightly, but they should be close enough to each other. This means that we should select the calibration factor that results in the coefficients of friction closer to each other.

The reported results in (275) are given for three applied loads – 0.25, 1 and 3 μN. Those values of applied normal forces are relatively high and cannot be achieved by standard contact mode AFM probes. No notion of validity of the method outside of the reported range is given. The calibration coefficient varies with load and is valid only for a given applied load; thus, a separate calibration calculation is required for each applied load.

A.3 Results: Example of probe characterisation

The results presented in this section are for the same probe. The probe used was a commercial PPP-LFMR (Nanosensors, USA), a standard contact mode probe with increased lateral sensitivity. Additionally, lateral force calibration of a much stiffer PPP-NCHR probe is presented as well, showing the wide range of applicability of the presented calibration techniques.

A.3.1 Determination of the probe shape according to the envelope method

We have performed the envelope method on a scan performed on a single feature of the TGT1 grating, using a used LFMR probe. The shape of the grating was modelled as a hyperboloid with a tip radius of 10 nm and a slope of 65°, as per the grating data-sheet. The probe was measured after a nano-tribology experiment to determine the tip radius. A reconstructed surface of the probe is shown in Figure A.4.

A radius of any continuous curve in any point is equal to:

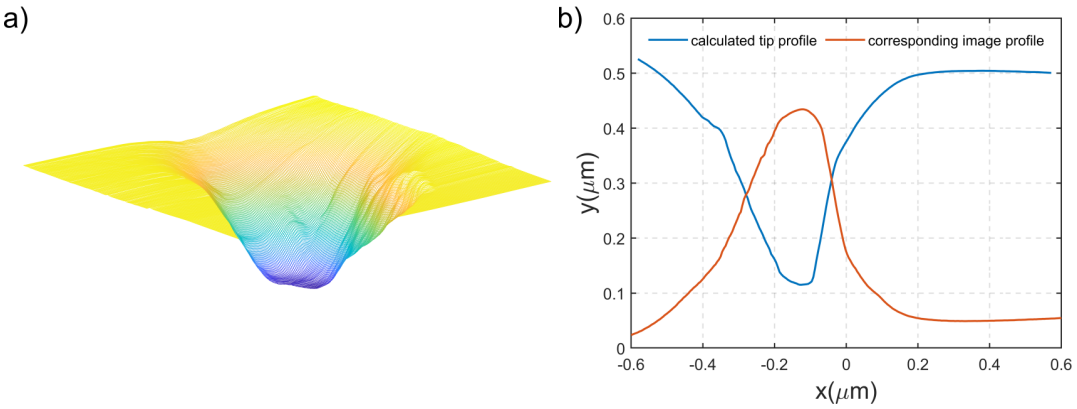

Figure A.4: The result of the performed envelope method. (a) 3D representation of the probe shape; (b) A single line profile of the probe shape (blue) and the measured surface image (red).

$$R = \frac{\left[1 + \left(\frac{dy}{dx}\right)^2\right]^{2/3}}{\frac{d^2y}{dx^2}} \tag{A.22}$$

We choose the line profile with the lowest point (Figure A.4b) and apply the above equation in the lowest point of the curve. The resulting radius is $R_{probe} = 33.4\,\text{nm}$. We assume the obtained radius as the closest approximation of the tip radius, despite potential deviation from a perfectly spherical shape. The assumption works well due to small loads and, therefore, small deformations in the contact.

A.3.2 Normal force calibration

Since the AFM system (Agilent AFM5500, United States) we are using already contains a thermal noise calibration module, no specific procedure is required to calibrate the normal force – the value is evaluated internally in the software. Therefore, we can directly enter the set-point in nN as an input parameter during our measurements. The normal spring constant of the probe was $0.153\,\text{N}\,\text{m}^{-1}$. The corresponding thermal spectrum is given in Figure A.5.

A.3.3 Lateral force calibration

TGF11 grating (Figure A.6) was used to calibrate the lateral calibration constant of the used cantilevers. The grating consists of (111) and (100) crystallographic planes of silicon. The slope of the angled region is $54°44'$ (275). The scan size was 0.5 x 0.5 µm (1 µm for the PPP-NCHR probe), with a resolution of 512 x 512 px and the scan speed was 1 ln/s (1 µm/s for PPP-LFMR and 2 µm/s for PPP-NCHR). The normal force was

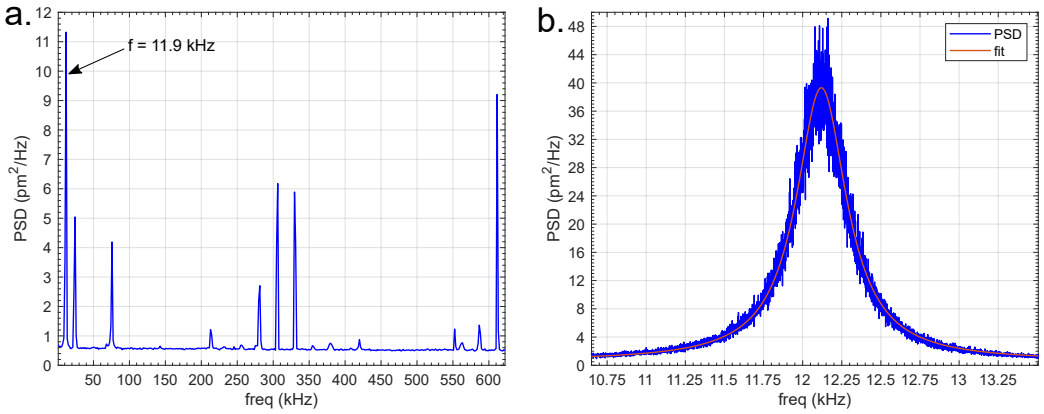

Figure A.5: Normal force calibration. (a.) The whole thermal spectrum with the peak corresponding to the probe marked, and (b.) fitting a curve on the thermal noise peak to obtain the spring constant.

increased in 20 increments, between the lowest and the highest forces, according to the linear region of the force-distance (FD) curve.

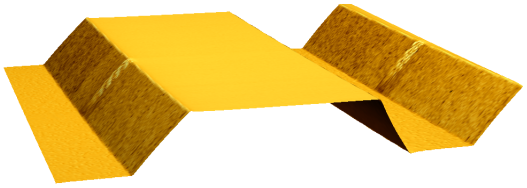

Figure A.6: TGF11 grating in 3D.

Two measurements were performed (increasing and decreasing normal load) with the same parameters for each probe. The value of the adhesion force was obtained from the FD curve before the calibration experiment. The calibration parameters are presented in Table A.1, alongside the resulting calibration factors according to two calibration methods – the presented error is defined as the standard deviation of the two repeated measurements in the same spot with the same probe. As the 'improved wedge calibration method' yields a separate factor α for every applied force, only one value is reported in Table A.1. According to Figure A.7, the 'improved wedge calibration method' only yields reasonable results when the applied load is high enough; therefore, a value at a high-enough load was chosen for comparison. The values at higher loads seem to converge towards the value calculated by the 'original wedge calibration method', whereas at lower loads the method yields complex values of the calibration factor. Thus, the 'improved wedge calibration' can only be used with higher contact loads, which are close to or above the maximum applied load for most nanotribological experiments. The discrepancy between the subsequent measurements on the same sample implies up to 20% repeatability of quantification of lateral forces, and the agreement between the methods is $\sim$ 21% for the soft probe and $\sim$ 7% for the stiff probe. The values are slightly higher than those reported in the literature (95), but they are still within the acceptable levels.

Table A.1: Input parameters and resulting calibration factors

Probe (No)	PPP-LFMR (9)	PPP-NCHR (7)
F_{min} (nN)	0	0
F_{max} (nN)	30	7000
$F_{adhesion}$ (nN)	5.6	124
$\alpha_{Ogletree}$ (nN/V)	110 ± 20	14372.5 ± 784.5
$\alpha_{Varenberg}$ (nN/V)	139 ± 10 @$(F_n = 30nN)$	15347 ± 245 @$(F_n = 7000nN)$

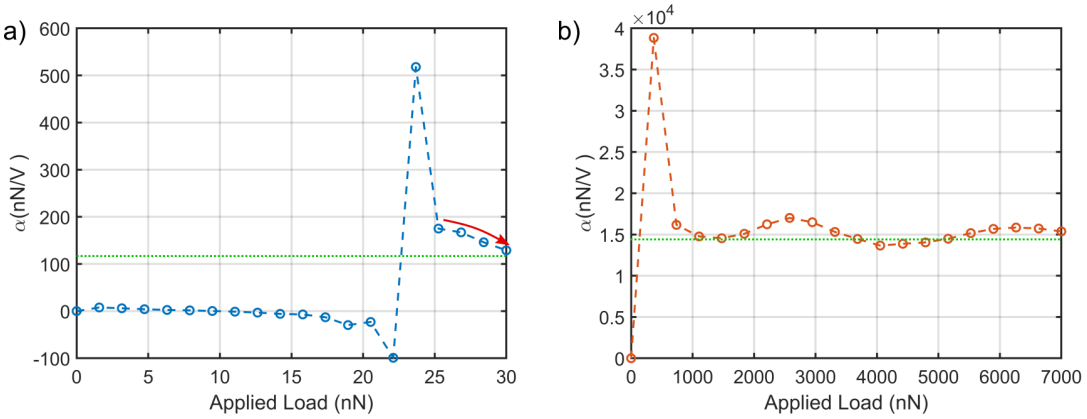

Figure A.7: Comparison between the lateral calibration values from the wedge calibration (a) and improved wedge calibration (b) procedures. The values of improved calibration method approach original calibration method with load.

A.4 Conclusions

We have presented and summarised the three methods used for the calibration of AFM probes, which are necessary when performing any LFM experiment that requires a quantitative evaluation of lateral forces.

Both methods for lateral calibration yield comparable results for the calibration factor, but the 'original wedge calibration method' shows lower error across the entire measured range. The 'original wedge calibration method' was developed with the specific custom-made calibration gratings; we show here that it can be successfully applied to the commercial grating TGF11 as well. Furthermore, the calibration factor, calculated according to the 'original wedge calibration method', can be applied across the entire usable range of the probe, which gives this method an advantage over the 'improved calibration method'. We observed that the 'improved method' fails at lower loads (see Figure A.7) and converges towards the value of the original method at higher normal loads. Therefore, the 'original Wedge calibration method' has been used to calibrate most of the probes that were used in the experiments presented in this work. Nevertheless, the calibration factors were also obtained according to the 'improved calibration method', which served as an additional check for the validity of the obtained results. Due to uneven tip wear, contaminant adsorption and slight

discrepancies in probe geometry, there is a considerable probability that one of the methods returns abnormal results. Therefore, performing calculations according to both methods from the same data set allows choosing the appropriate based on the nature of the data.

A relatively high error in determining the lateral force calibration factor indicates that even by quantifying the values of frictional forces, it is difficult to compare the values between different systems or even between different probes on the same system. Furthermore, we have observed that just moving the probe in the mount can further influence the value of lateral forces, by mainly increasing 'cross-talk' between normal and lateral signals. Therefore, the only valid procedure for comparative studies is by using the same probe on all the samples, without removing it between the measurements.

Since the measurements on the silicon grating can wear the tip faster than TMD samples, it is essential to perform the calibration of lateral forces and reconstruction after completing all the main measurements.

Appendix B

The method for generating the Raman maps

B.1 Introduction

Raman analysis requires some degree of data post-processing to make it suitable for interpretation. The effects such as fluorescence, interference and surrounding light have a large effect on the final shape of the signal and manifest as a background signal (i.e. non-specific shape across a wide range of frequencies). Additionally, despite the best efforts to shield the sample from the surroundings, the cosmic rays can occasionally enter the detector, which shows up as a very high and narrow spike. The usual approach to minimise these detrimental effects is to increase the acquisition times, measurement resolution, and average over multiple scans at the same point, which significantly increases the total time for the experiment, but it is still feasible when performing point analysis. However, when performing surface mapping one needs to find a good balance between the acquisition time, final resolution and quality of the signal. For example, the experiments presented in Chapter 7 took between nine and fourteen hours, despite keeping the resolution relatively low. The experiments were performed overnight to minimise the impact of surrounding light influencing the measurements.

The data acquisition software contains options to exclude the spikes and a built-in algorithm for background removal. The spike reduction option was used during the data acquisition, but some spikes remained in the final measurements and had to be removed afterwards. The data was collected without background removal and a custom multi-parameter algorithm was implemented during the analysis instead.

The original software offers only a basic map creation, by selecting the spectral range

to plot the map. This is sufficient for an initial observation of the surface, however, the method in the software is quite limited in terms of control. Therefore, a custom environment was created in MATLAB®, including four different methods to compile the maps.

This chapter includes a description of the algorithms for spike removal and background extraction, an overview of the methods for the extraction of the maps from the spectra, as well as the methodology used to create the threshold maps.

B.2 Spikes removal

Because the spikes are only temporal phenomena (i.e. an event when a cosmic ray hits the detector), they only appear as one or two high-intensity points and can therefore be easily identified (see Figure B.1). Due to internal averaging by the data acquisition software and a limited spike filtering algorithm, the spikes that remain in the raw collected data can sometimes manifest over multiple points. Nonetheless, they are still easy to detect and remove in most cases.

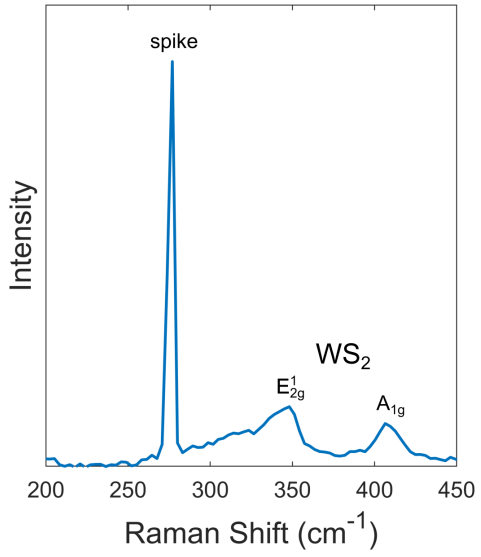

Figure B.1: An example of a cosmic spike.

The spike removal follows a simple algorithm. The spikes are first identified by finding disproportionately large differences between two neighbouring points. The intensity in that point is then replaced by a weighted average over the surrounding points (a total of 6 points are used). The algorithm works well on single-point spikes on the 1st pass, but it requires multiple passes for the spikes that span multiple points. As shown in Figure B.2a, the spike is already significantly reduced after the first pass. However, it takes up to 5 passes to reduce the spike down to the noise level, which is

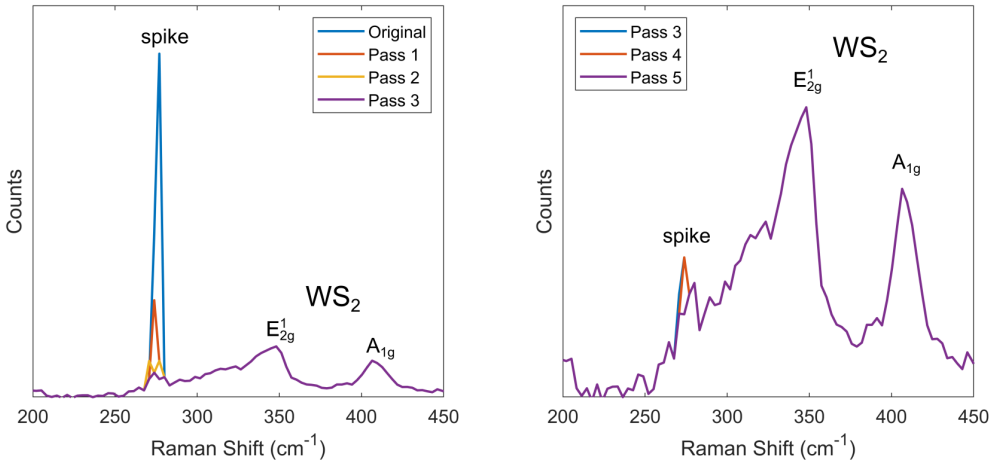

Figure B.2: The procedure for removing a spike.

shown in Figure B.2b. Special attention needs to be paid to the threshold when performing the algorithm. The threshold needs to be set low enough so it can detect the spikes, however, it should not affect any peaks or noise. A value of threshold $= 5\overline{I_{sp}}$, where $\overline{I_{sp}}$ is the average intensity of the entire spectrum, was found to satisfy both criteria sufficiently.

B.3 Background removal

B.3.1 Method 1: 2nd degree polynomial

Averaged raw data, i.e. averaged data over all 561 spectra on one sample, in Figure B.3a shows decreasing background with increasing Raman shift. The apparent shape of the curve indicates a 2nd degree polynomial to be a good first approximation for the background. Manually fitting a 2nd degree polynomial yields a sufficient result as shown in Figure B.3b. The fitting was performed using the same function parameters on all spectra of the sample, which assures that the shape of the averaged data is preserved. However, it does not take into account potential differences in the background across different points on the sample, as well as the background changing with time and temperature fluctuations. Furthermore, the valley at $\sim$100cm^{-1} and the region between 600 and 1000 cm^{-1} might still contain significant levels of background, which could follow a more complex curve. For these reasons, this method may not be suitable for detailed analysis and the creation of surface maps. It is, however, good for quick initial analysis of the samples due to its fast processing time and simplicity.

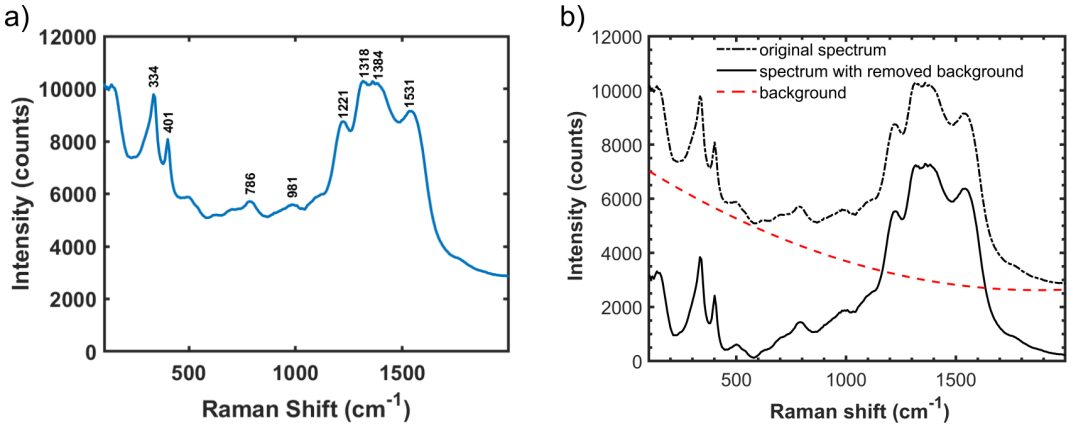

Figure B.3: Averaged spectrum before removing the background (a). Spectrum after removing the background (b).

B.3.2 Method 2: Envelope method

The envelope method removes the need for the exact analytical functional formulation of the background. The background is instead calculated numerically and therefore consists of a collection of independent, albeit continuous points. The main target of the envelope is to fit the background to the local minima on the spectrum.

Imagine a concave parabola being dragged below the spectrum, so that it just touches the data when it is in the highest position at each point. The parabola has a local shape $y(x,t) = x - a(x-t)^2$, for every $t \in X$. Finding the maximum value of the expression in each point yields the envelope of the data, which is then attributed to the background. A dual pass of the algorithm is a default option, and the coefficients can be selected separately for each of the passes, which allows the use of wider parabolas and minimises the risk of altering the data. From testing the algorithm, it follows that it is better to use a lower coefficient, i.e wider parabola, for the first pass.

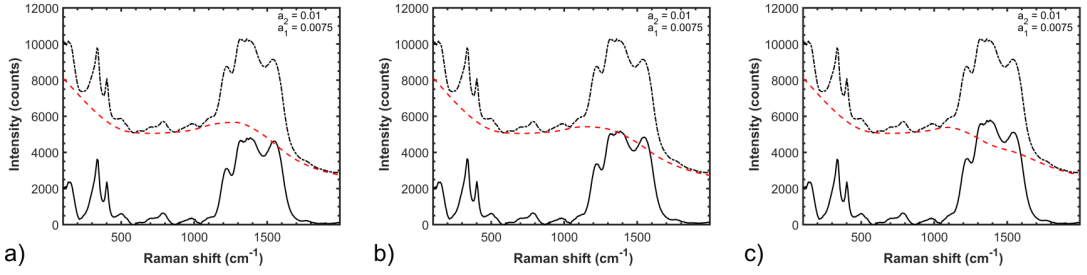

Figure B.4: Comparison of three available functions for the coefficient a. (a) constant (b) linear (c) Gaussian filter.

Additionally, three different options for the coefficient a are available: (i) constant a across the whole range, (ii) a changing according to a pre-defined function, and (iii) constant a across the whole range, with an added Gaussian filter to reduce a around a selected region. Option (ii) has the added benefit of adding additional weight to

higher or lower values of Raman shift, whereas option (iii) is useful when the spectrum contains a combination of sharp and wide peaks. The examples of the differences between the methods are shown in Figure B.4.

Figure B.5 displays the removed background of the measurements from Chapter 7. The envelope method was used to remove the background on all the samples, and the constant a was used for consistency.

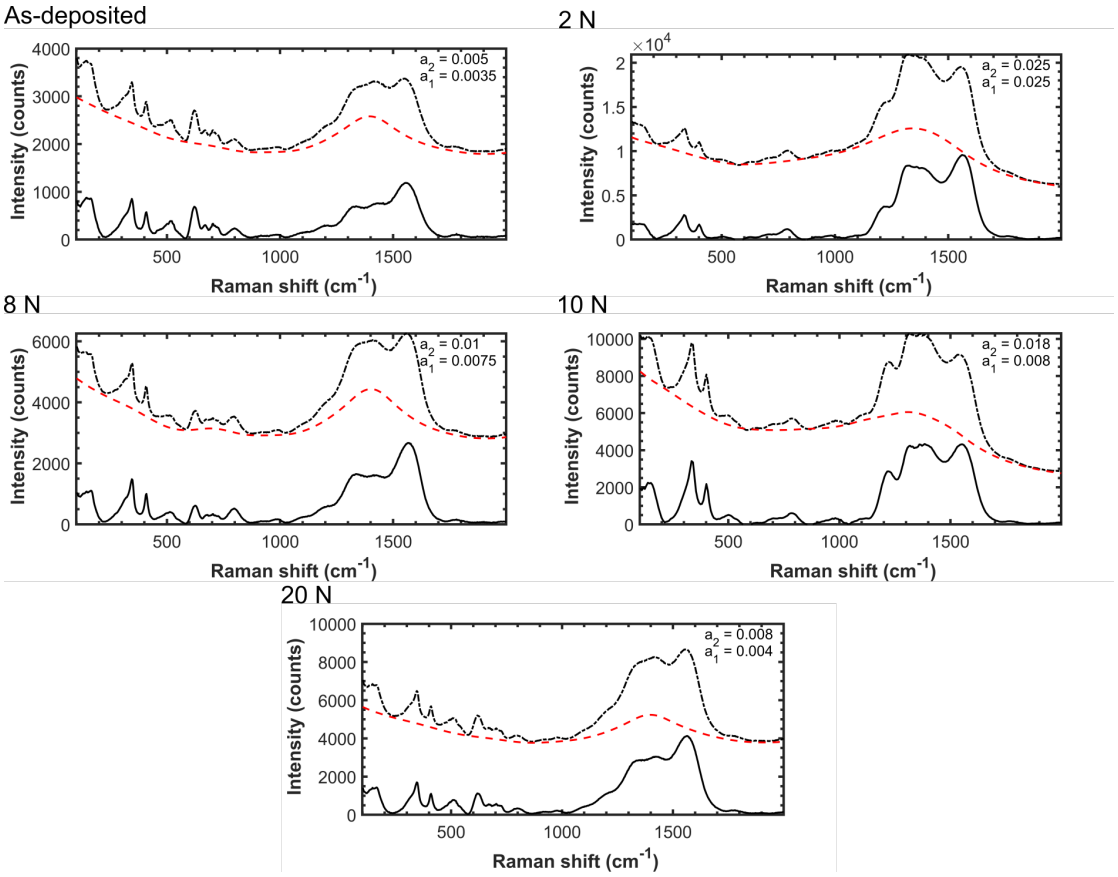

Figure B.5: Averaged spectra after removing the background.

B.4 Map extraction from the spectra

Four different methods for generating Raman maps were implemented. The methods require the input of one or two points (S1 and S2), representing the position/range of Raman shift chosen for analysis. The points S1 and S2 can be selected by the sliders or inserted in a text-box (see Figure B.6).

Absolute intensity of the signal at S1: abs(S1): The most straightforward method for generating the maps is by displaying the absolute intensity at the selected Raman shift (S1) for each point. The first method for map generation is the simplest. The absolute intensity at the selected Raman shift (S1) is displayed in the points on the map.

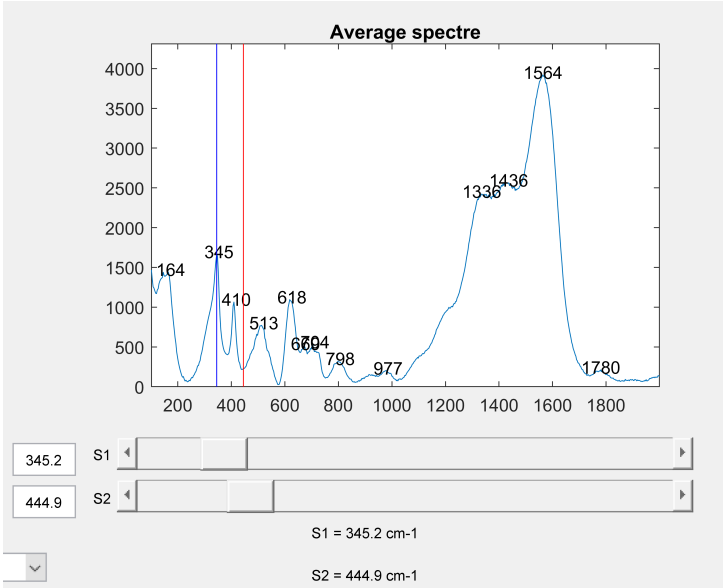

Figure B.6: Selecting the input wavelengths.

Background removal needs to be performed without a single mistake for this method to be effective; otherwise, the resulting map can depict the scans with a high residual background as a high signal, as displayed by the example in Figure B.7. In this example, the manual polynomial fitting method was used to remove the background; as evident from the spectra of point B, the background was not removed correctly in that point, which caused a seemingly high WS_2 signal on the map.

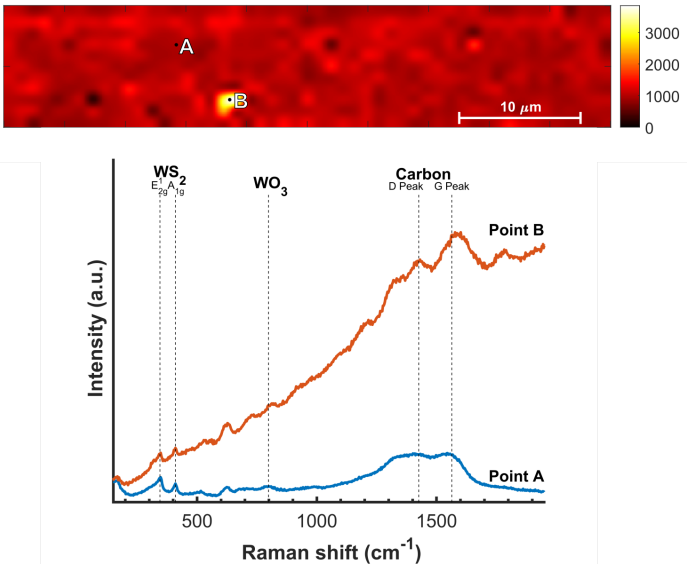

Figure B.7: Absolute intensity of the signal at S1.

The difference between the average values in two points: S1-S2: This method maps the signal as the relative intensity of the selected peak, consequently reducing the potential errors introduced by the background removal. As displayed in Figure B.8, removing the background only changes the absolute values on the map, and it does

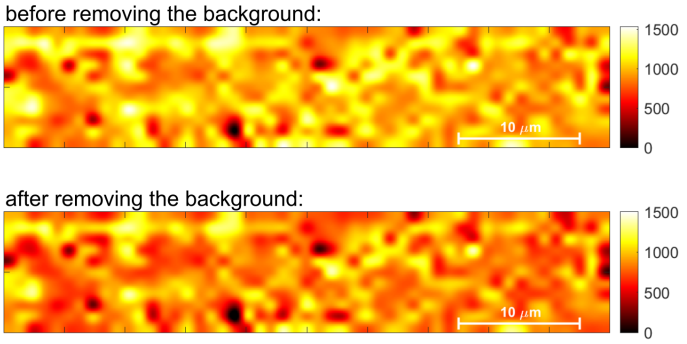

Figure B.8: The difference between the average values in two points: S1-S2

not induce any artefacts with this method. The displayed map was generated at the same peak like the one in Figure B.7.

The difference between the maximum and minimum values on the interval between the two points (min-max: [S1 S2]): This method yields similar results as the one offered by the commercial Raman software. Instead of fixing the location of the peak of interest, a range is selected and the algorithm finds the difference between the highest and lowest points. The obvious benefit of this method is that it allows accurate inclusion of shifted peaks, which would otherwise appear as lower intensity. However, this method has a major drawback, as it is sensitive to any spikes not being removed accurately; if a spike is present within the interval and its intensity is higher than the peak, it would result in an artefact. Despite using a spike filter during the data acquisition, some spikes are still present in the final data, as shown in Figure B.9. Additional spike removal corrects the map, and the resulting map is very similar to the second method; however, one of the spikes is still visible in the final map after three passes of the spike removal algorithm.

The ratio between the absolute intensities of two peaks (S1/S2): The last method takes the absolute values of the selected peaks and therefore requires accurate background removal. This method can be used to compare the relative distributions of two compounds on the map. It is, therefore, best illustrated on the 2 N sample (see Chapter 7, Section 7.3.3), which displays large contrast between the regions rich in WS_2 and carbon. The top map in Figure B.10 shows the ratios between the WS_2 A_{1g} peak and carbon G peak, clearly showing the boundaries between the regions. On the other hand, the ratio between the two WS_2 peaks remains uniform across the entire map.

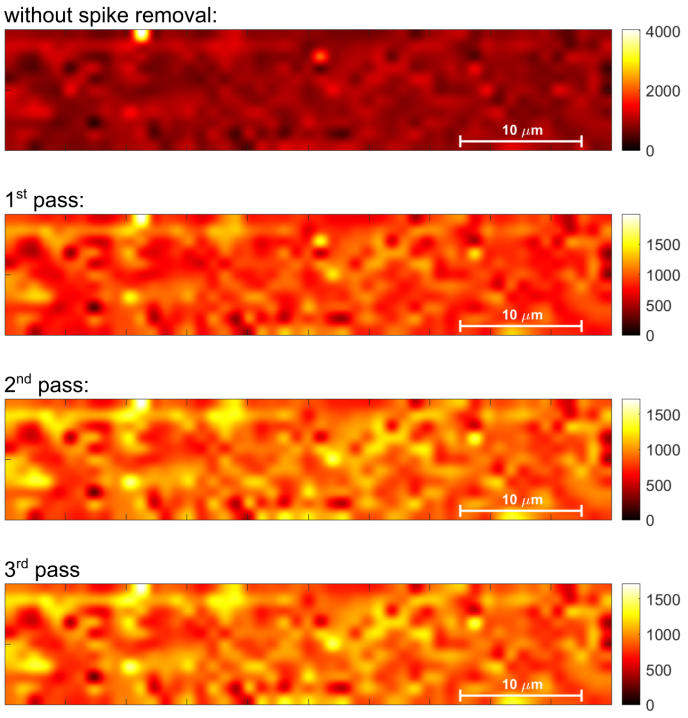

Figure B.9: The difference between the maximum and minimum values on the interval between the two points (min-max: [S1 S2]).

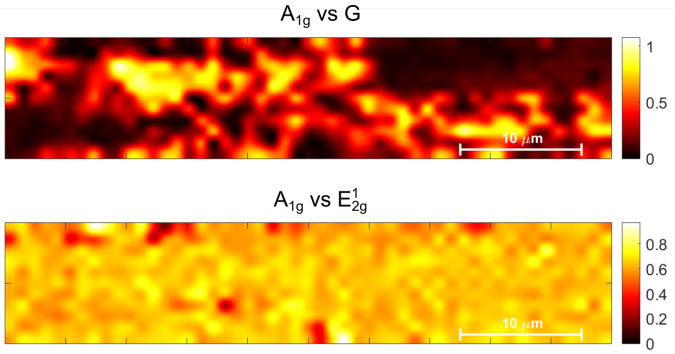

Figure B.10: The ratio between the absolute intensities of two peaks (S1/S2).

B.5 Extraction of threshold maps from single maps

B.5.1 Step 1: Single compound extraction

Instead of presenting single maps of each compound, it is better and more intuitive to transform the maps into the so-called threshold maps. Instead of displaying the whole range of intensities, only the data that passes the threshold remains on the map. Such threshold maps can then be combined into one map and present the data more compactly.

A threshold was set as 50% of the average intensity of the highest five points on the map. This allowed distinguishing between the actual signal and trace. Due to the high Raman activity of carbon and its high content in the sample, as well as potential contamination of the optical system, some carbon signal is commonly detected in all points of the sample. Taking the average of the highest five points reduces the influence of a single very high-intensity point.

The software can keep the maps of up to three materials in memory at the time. The three materials are assigned separate colours: blue, red and green.

B.5.2 Step 2: Combining the extracted maps

The three maps are then combined into a single map, by transferring each map to one channel in the RGB space. Additionally, the intensities are mapped onto each channel through the brightness of each point. The intensities of blue and red channels are reduced in the overlapping points instead of linear combination, to preserve the continuity of colours in the RGB space; the result is transparent overlaying that

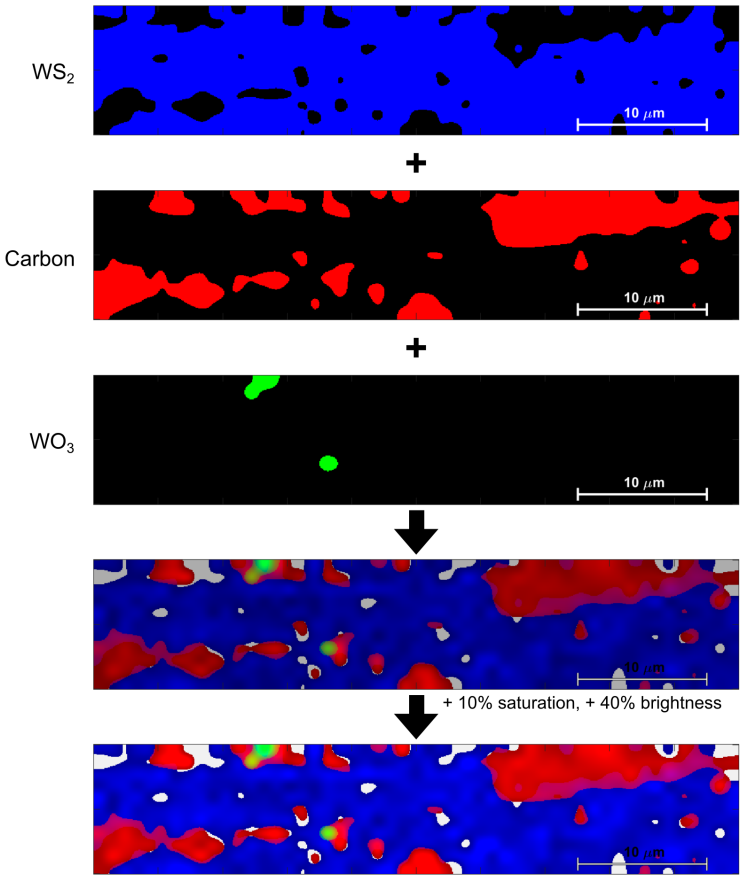

Figure B.11: Combined maps of the measurement in the 2 N wear track.

produces visually intuitive maps while maintaining mathematical consistency. It is, therefore, advisable to assign the blue channel to the compound that covers the largest area, and the green channel to the smallest. An example of combining the maps is shown in Figure B.11.

B.6 Map resolution resizing

As evident from the presented Raman maps above, the resolution of the presented images is much higher than the acquisition resolution (51 x 11 points). As discussed in the previous sections, the long acquisition times require reducing the overall resolution to finish the measurements in reasonable time frames. Furthermore, the wavelength of the laser beam and the finite beam-sample interaction area limit the spatial resolution of Raman spectroscopy to about 1 µm[1]. Consequently, the resulting Raman map appears very small and pixelated, as shown in Figure B.12.

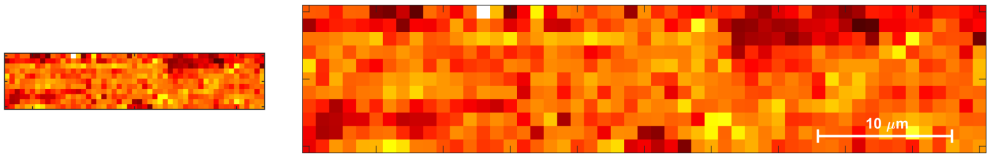

Figure B.12: Original resolution of the map.

Despite all the collected data being presented, such a map is very difficult to interpret and extract useful information from. Therefore, an increase in resolution is required, which is achieved by interpolating over the points around the observed point. Bi-cubic interpolation was used, which is based on calculating the weighted average over the nearest 4x4 square of points. Bi-cubic interpolation preserves the features on the surface (e.g. a single point maps into a circle) but can result in some values falling outside of the original range.

The different levels of resizing are presented in Figure B.13. Doubling the resolution already provides much better detail of the scanned image. At N = 5 (N is a resizing factor), the shape of the features is already clearly visible, and further increasing to N = 15 reduces the pixelation even further. Increasing the resolution to N = 50 does not result in a significant improvement over N = 15.

[1]The diffraction limit of a 532 nm laser with a 100x objective is 361 nm, but due to the complexity of technical processes in Raman spectroscopy, the diffraction limit is only rarely reached.

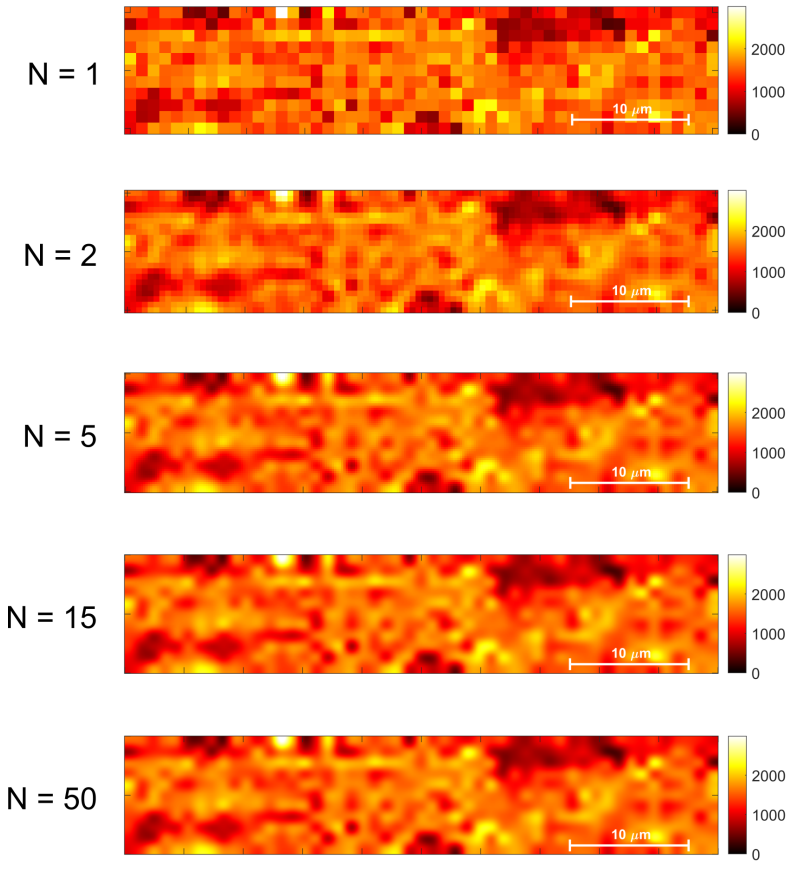

Figure B.13: Up-sampling the resolution by a factor N.

B.7 Conclusions

The presented methods for the analysis and plotting of Raman maps were all incorporated into an easy-to-use GUI (graphical user interface), which helps guide the user through the steps required to generate the desired maps. For the data presented in this thesis, only some of the available methods were used, and the data was analysed using the most appropriate procedure. The background was removed using the envelope method, and all the maps were generated using the difference between the average values of two points - a combination that has proven the most consistent across different measurements and samples.

Appendix C

Additional figures for Chapter 6

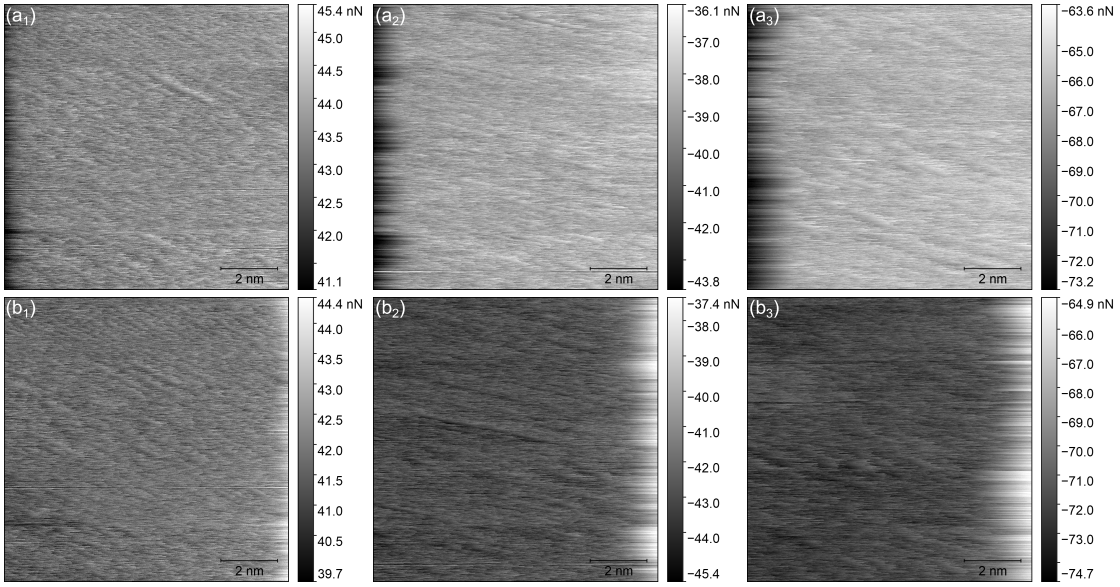

Figure C.1: Original friction maps for Figure 6.2

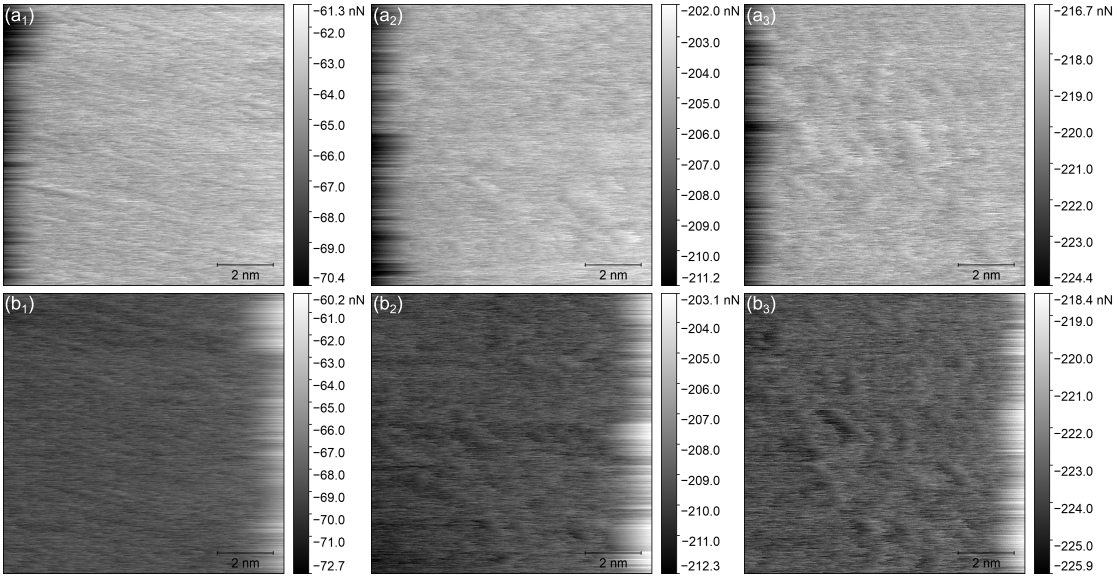

Figure C.2: Original friction maps for Figure 6.3

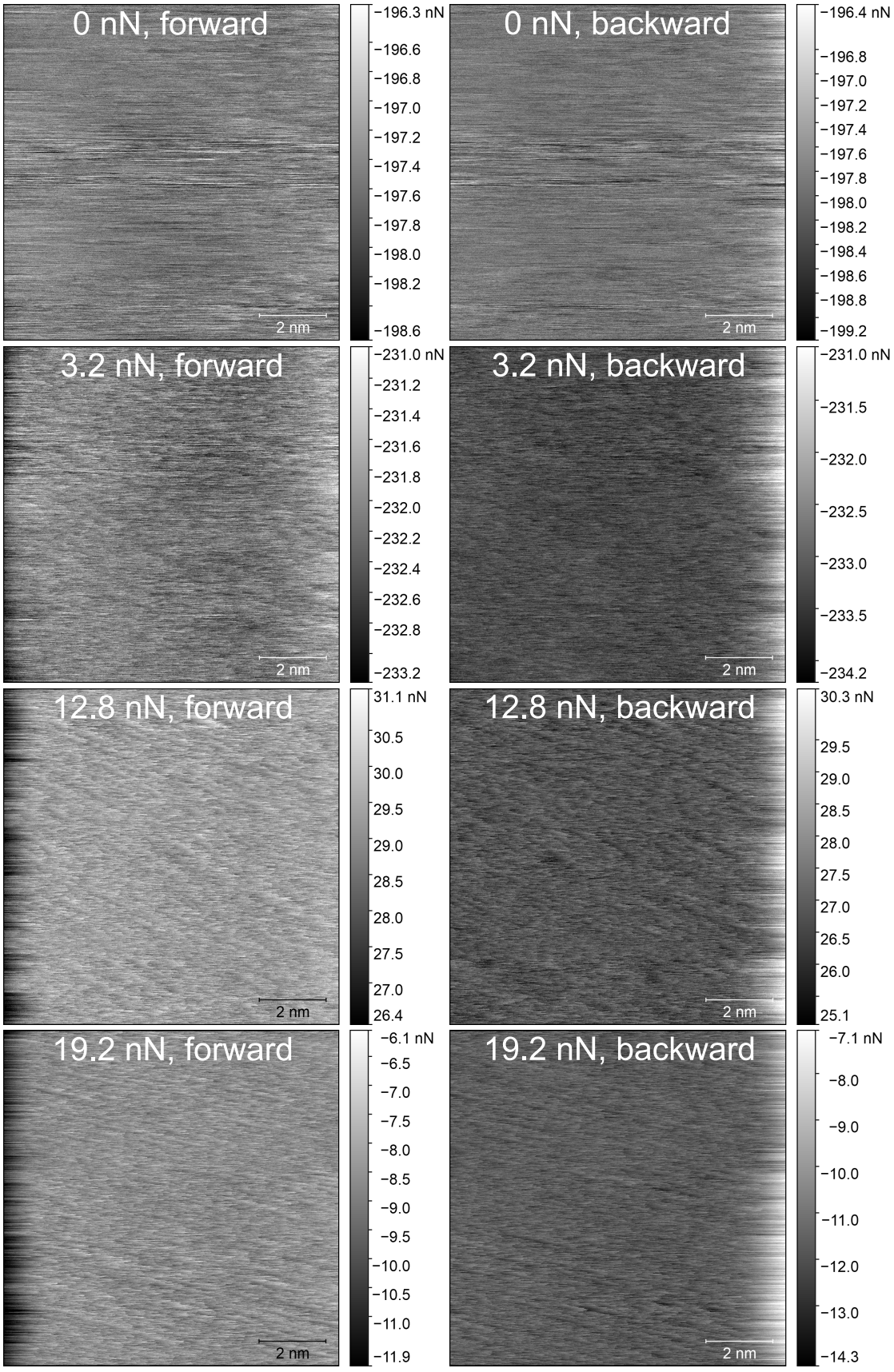

Figure C.3: Additional friction maps for Table 6.2 and Figure 6.16

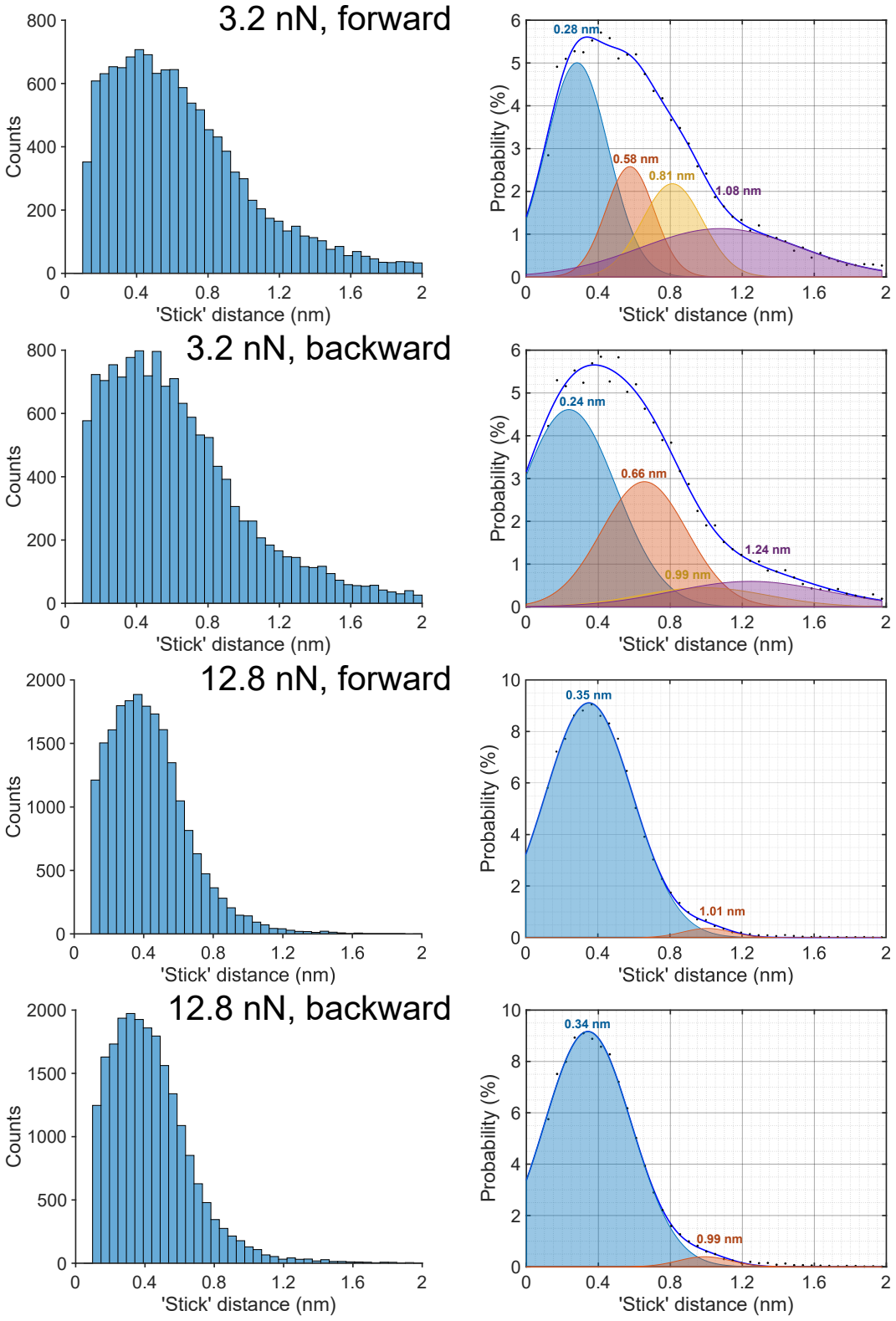

Figure C.4: Additional histograms and probability density functions for Table 6.2 and Figure 6.16; 3.2 nN and 12.8 nN

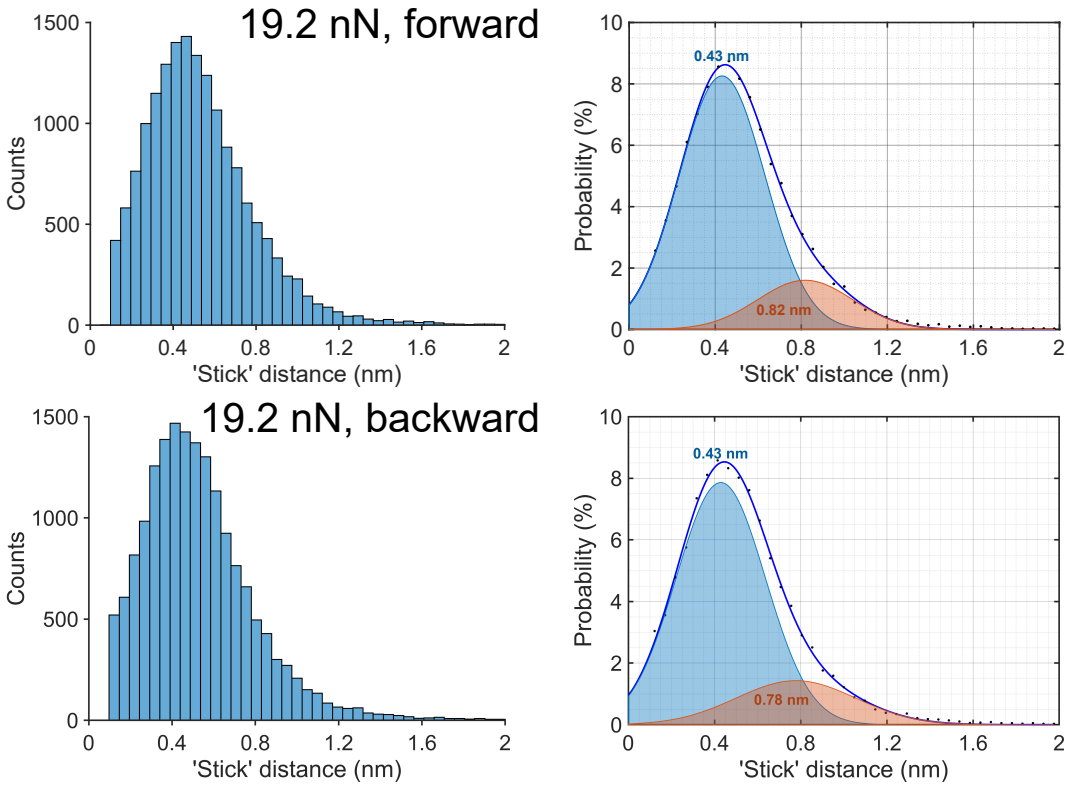

Figure C.5: Additional histograms and probability density functions for Table 6.2 and Figure 6.16; 19.2 nN

Appendix D

Multi-scale tribological characterisation of sputtered MoS_2 coatings

In this section, we look at approaching the analysis of tribological properties of sputtered MoS_2 coatings from three different points of view (scales), thus expanding upon the results from Chapter 7. In contrast to Chapter 7, we use pure MoS_2, which eliminates the effect of carbon on the sliding properties. Besides the macro-scale and nano-scale friction tests, we also perform the measurements in the intermediate micro-Newton regime.

D.1 Methodology

Similar to the majority of the analyses in this work, nano-scale friction was analysed by atomic force microscope (Agilent 5500). Measurements were performed in air using PPP-LFMR probes (Nanosensors, Switzerland) with a nominal spring constant of 0.2 N/m. Friction maps and topography were obtained simultaneously. For friction measurements, the load was incrementally increased every 25 lines to a total of 10 different loads. A custom script was utilised to control the normal forces during the experiment.

D.2 Macro-scale tribology

Macro-scale tribotests on thin-film MoS_2 coatings were performed in a custom made vacuum tribometer (CTU, Czech Republic) at various loads and sliding speeds (see Table D.1). 100Cr6 balls with a diameter of 6 mm were used as sliding counter bodies.

Table D.1: Macro-scale tribology

No of cycles	Loads	Sliding speeds
2000	2 N	2.5 cm/s
2000	6 N	1, 2.5, 4 cm/s
2000	10 N	2.5 cm/s

Macro-scale coefficients of friction as low as 0.025 and the reduction of the coefficient of friction with increasing load were observed (see Figure D.1), which is in good agreement with the literature (21, 22, 179). Wear rates (Figure D.2a) at 6N normal load do not show a significant dependence on sliding speed. On the other hand, a significant decrease of specific wear rate is observed with increasing load in Figure D.2b. A total of two measurements, with a total sliding distance of 56 m and 31 m, were averaged at each value of load and sliding speed. High values of standard deviation are due to poor adhesion of the coating to the substrate – we have observed very uneven wear within the same wear track, and some coatings experienced random peeling off.

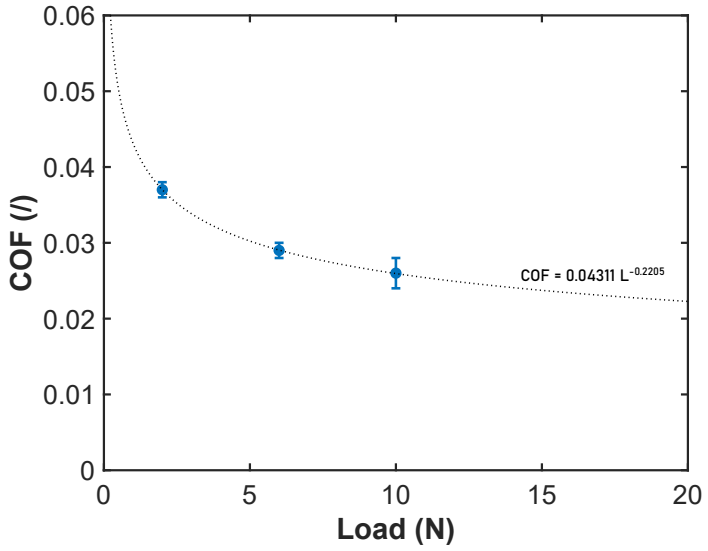

Figure D.1: Dependence of the coefficient of friction on normal load.

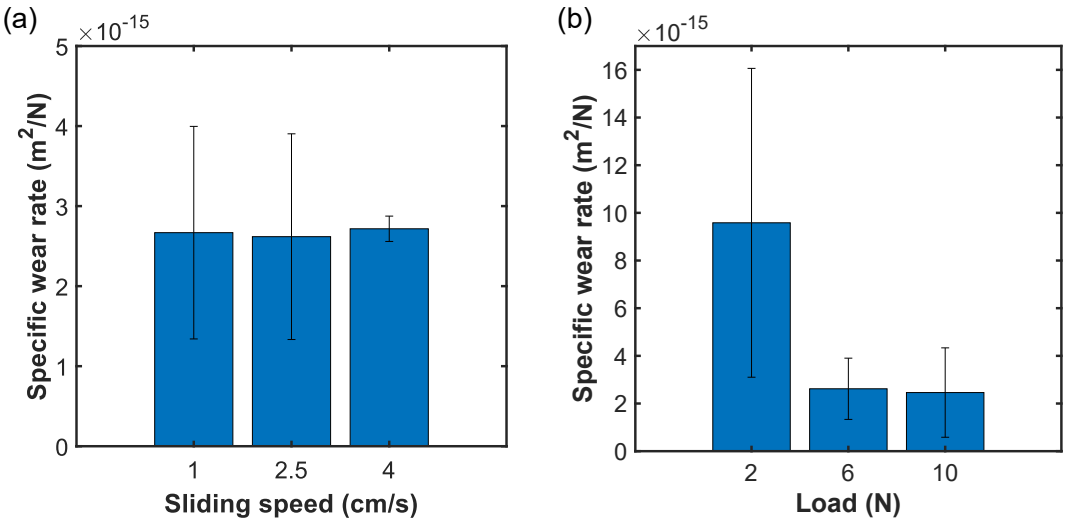

Figure D.2: Dependence of the specific wear rate on sliding speed (a) and normal load (b).

D.3 Wear track imaging

Figure D.3 shows the 3D topography of the wear track edge (a) and an overlay of the friction signal over the topography of the wear track (b). We have identified regions with significantly different nano-frictional characteristics within the wear track. The distribution of the observed regions presented in Figure D.3 is non-homogeneous across the entire wear track and indicates a multi-phase structure of the coating after sliding, similar to W-S-C coatings presented in Chapter 7.

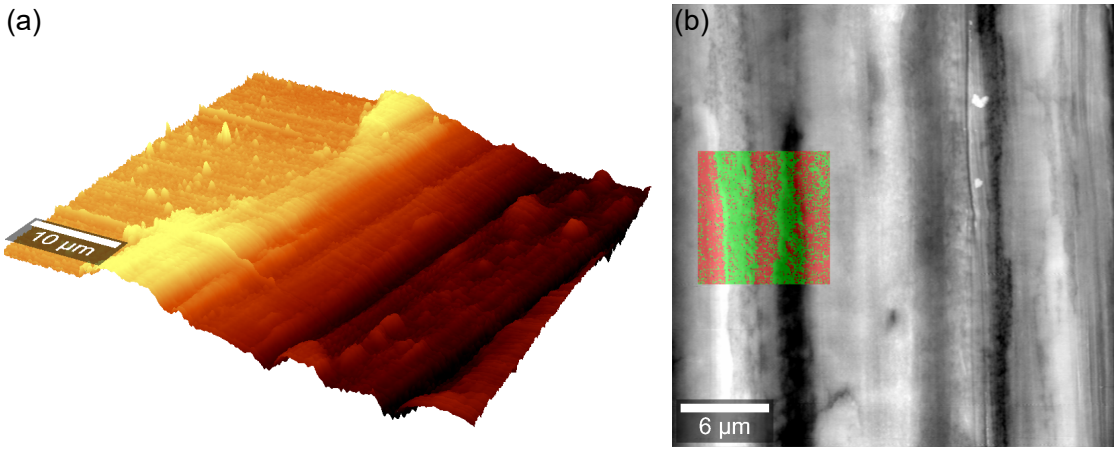

Figure D.3: 3D topography of the wear track (a) and an overlay of the friction signal (red-green) on the topography (b). Green regions indicate regions with lower lateral force.

Another topography scan of the wear track structure is displayed in Figure D.4. More detailed friction maps in Figure D.4b and d show a granular structure with different friction within the grains, indicating different degrees of crystallinity within the wear track, which backs up the conclusion from Chapter 7.

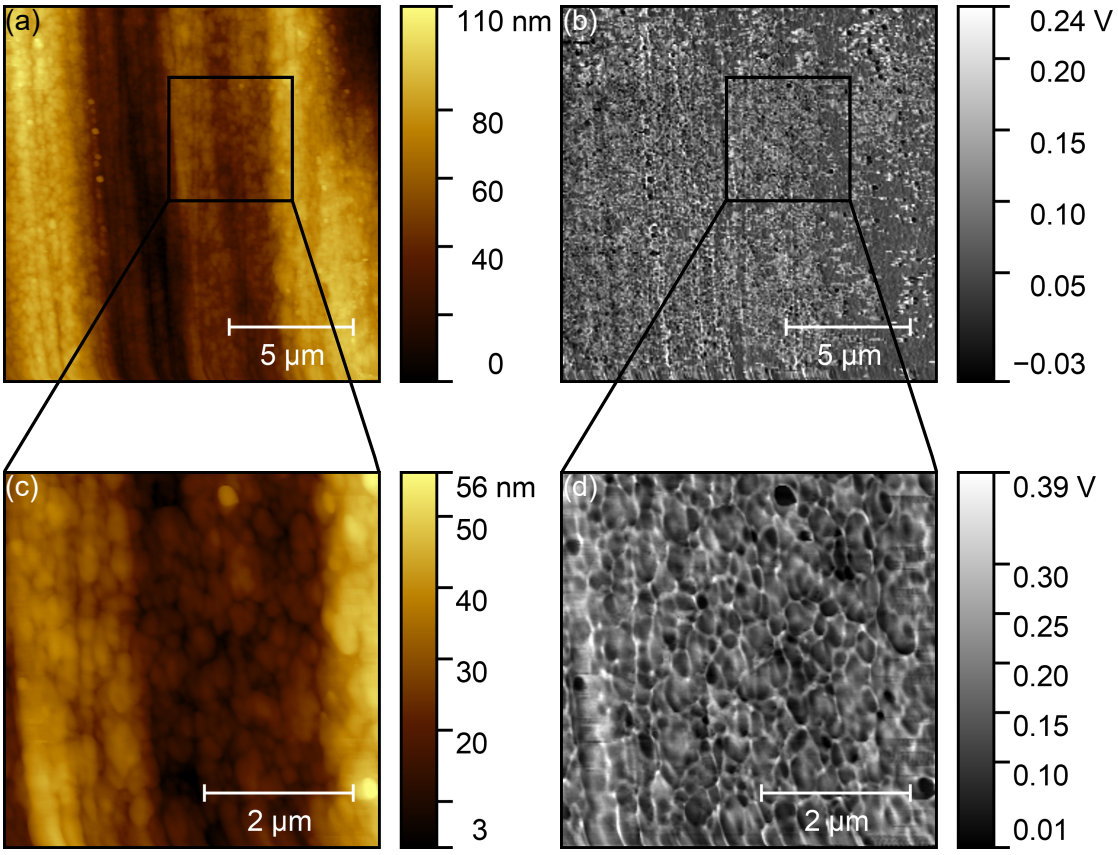

Figure D.4: Topography (a) and corresponding friction map (b) of the wear track. Detailed topography (c) and detailed friction map (d).

Furthermore, Figure D.5 displays a few crystalline flakes, which were identified within one of the wear tracks. The structure of the flakes is strongly reminiscent of the flakes presented in Chapter 7. Similar to WS_2 flakes identified in the W-S-C coatings, the MoS_2 flakes here exhibit much lower friction than the surrounding areas and appear much flatter.

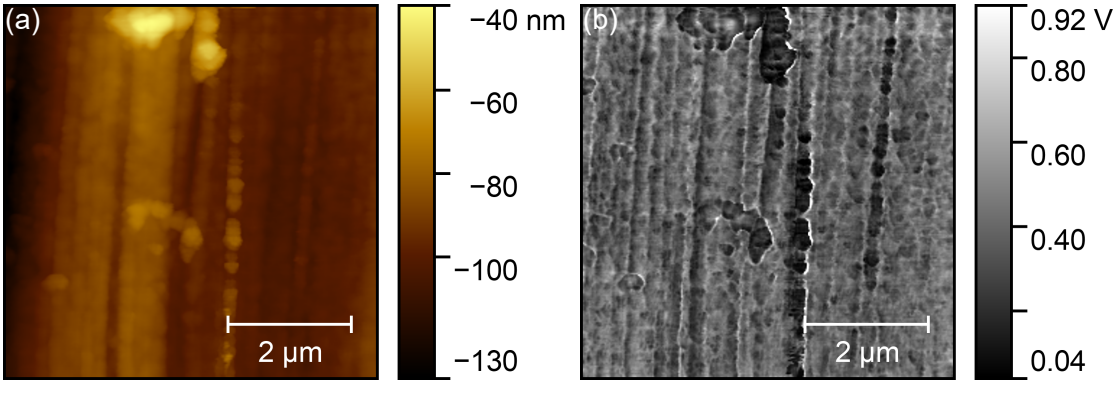

Figure D.5: Topography (a) and corresponding friction map (b) of the MoS_2 flake identified in the wear track.

D.4 Nanotribology

D.4.1 Friction

Figure D.6 displays the frictional behaviour of the coatings at the nano-scale. The nano-scale behaviour is almost linear within the measured range. The linear behaviour corresponds well with the expected response of the measured sample – finite roughness, soft material and surface contamination. The slope of the line was used to determine a nano-scale coefficient of friction (COF = 0.875). Such a high coefficient of friction at the nano-scale can be attributed to the amorphous structure of the coating. The high amounts of dangling bonds on the surface cause very high adhesive friction during sliding, while the energy introduced to the system by sliding and frictional dissipation is not enough to promote the recrystallisation and reorientation of the basal planes, which are the main sources of low friction at the macro-scale. This result agrees well with the high-friction phase from Chapter 7 and therefore further shows that the high friction phase was an amorphous structure. The high force of adhesion ($F_{adh} = 76$ nN) arose due to the tip wear and the transfer of particles from the sample to the tip. If we compare the measurement with the values obtained for fully crystalline samples in Chapter 4, we see that the amorphous material experiences completely different behaviour. Furthermore, the Hertz-plus offset model produces a sufficiently good fit, with a very low offset.

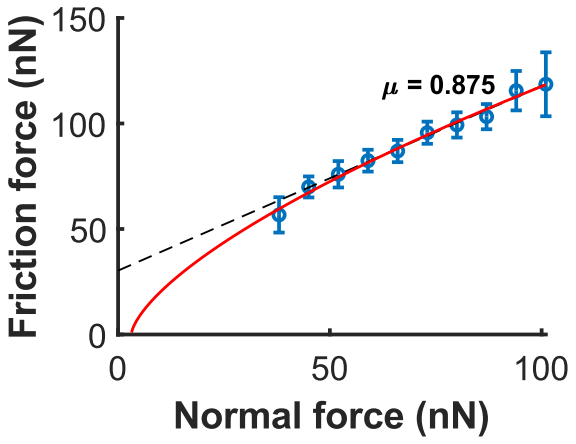

Figure D.6: Load dependent frictional behaviour of the MoS_2 sample measured in the wear track. $F_{adh} = 76$nN.

D.4.2 Nano-wear

To assess the nano-wear performance of the material we have performed high load ($F_n = 6$ µN) AFM measurements. The same 2 x 2 µm^2 surface was repeatedly scanned for a total of 250 cycles (125 up and 125 down). Figure D.7a displays a wear scar after

the measurement. The friction map in Figure D.7b displays a spot with significantly lower friction, indicating possible traces of tribofilm formation in the AFM contact. A similar observation has been made before by J. Zekonyte et al. (37, 38), who observed traces of crystalline tribofilm present on the AFM tip after performing nano-wear tests on W-S-C coatings.

Wear depth was determined every 50 cycles (Figure D.7d), by performing a larger area scan at a lower load, and the coefficient of friction was recorded for each scan (Figure D.7c). Wear depth follows a power law, showing the highest degree of wear at low loads and reaching almost 250 nm after 250 cycles, which is about 1/4 of the coating thickness. The coefficient of friction experiences a slight constant increase, which can be attributed to continuous tip wear. The average value of friction coefficient over the entire measurement is 0.151, which is significantly lower than on the nano-scale, but still noticeably higher than at the macro-scale.

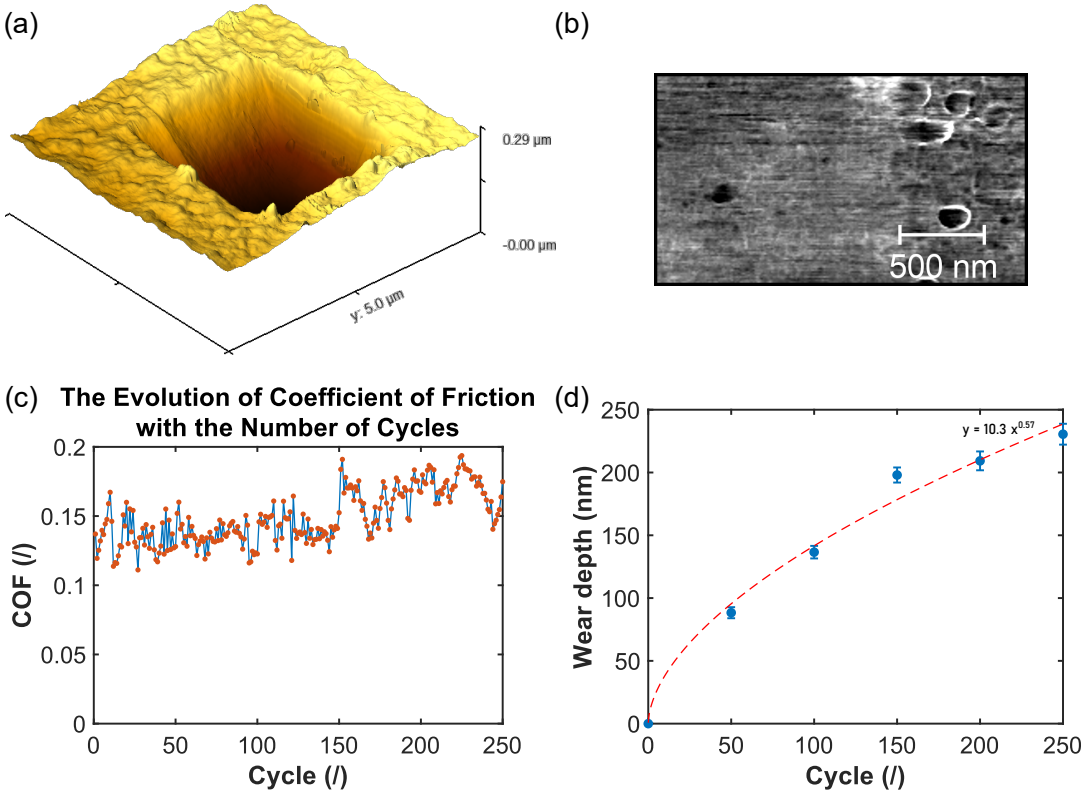

Figure D.7: Nano-wear of MoS_2. (a) Wear scar. (b) Low friction grains in the wear scar after the experiment. (c) The evolution of the coefficient of friction with the number of cycles. (d) The evolution of wear depth with the number of cycles.

D.5 Comparison of frictional behaviour across different scales

A collective comparison between the three scales is shown in Figure D.8. Friction follows the same trend of friction reduction with increasing load as observed at the

macro scale. The intermediate coefficient of friction measured at 6 µN can be attributed to very high contact pressures, resulting from a relatively high load applied on a very small nano-scale contact. Such high pressures induce high concentrations of energy in a very small volume during sliding, which can already start promoting the recrystallisation and reorientation of the coating and, therefore, decrease friction from the nano-scale. This is also confirmed by low-friction wear debris and low friction spots in the wear scar, which are formed during the experiment (Figure D.7b) and are similar to the features formed during the macro-scale tests (Figure D.5).

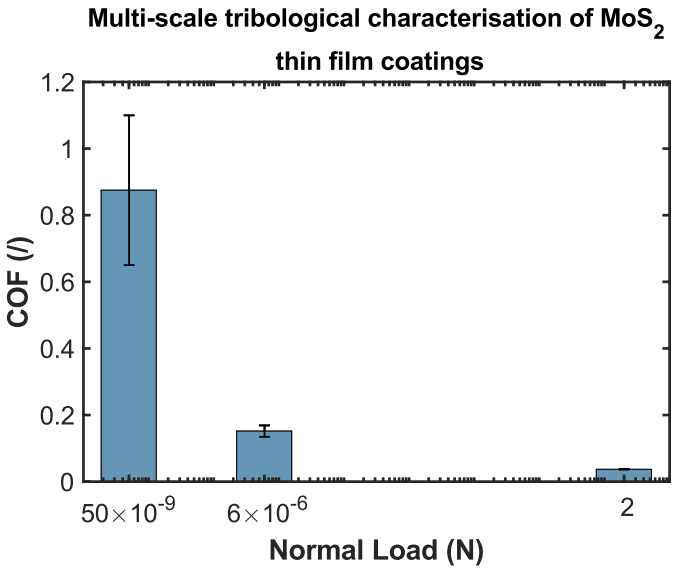

Figure D.8: Comparison of the frictional response of the coating on three different scales, showing significant reduction of friction with increasing the contact size and load.

References

[1] The European Parliament and T. C. o. t. E. Union, "REGULATION (EU) 2019/631 OF THE EUROPEAN PARLIAMENT AND OF THE COUNCIL of 17 April 2019 setting CO2 emission performance standards for new passenger cars and for new light commercial vehicles, and repealing Regulations (EC) No 443/2009 and (EU) No 510/201," *Official Journal of the European Union*, no. L 111, pp. 13–53, 2019.

[2] K. Holmberg and A. Erdemir, "Influence of tribology on global energy consumption, costs and emissions," 2017.

[3] R. W. Carpick, A. Jackson, W. G. Sawyer, N. Argibay, P. Lee, A. Pachon, and R. M. Gresham, "The tribology opportunities study: Can tribology save a quad?," *Tribology and Lubrication Technology*, vol. 72, no. 5, pp. 44–45, 2016.

[4] E. W. Roberts, "Thin solid lubricant films in space," *Tribology International*, vol. 23, no. 2, pp. 95–104, 1990.

[5] J. Krim, D. H. Solina, and R. Chiarello, "Nanotribology of a Kr monolayer: A quartz-crystal microbalance study of atomic-scale friction," *Physical Review Letters*, vol. 66, pp. 181–184, 1 1991.

[6] J. Krim, "Atomic-Scale Origins of Friction," *Langmuir*, vol. 12, pp. 4564–4566, 1 1996.

[7] C. M. Mate, G. M. McClelland, R. Erlandsson, and S. Chiang, "Atomic-scale friction of a tungsten tip on a graphite surface," *Physical Review Letters*, vol. 59, no. 17, pp. 1942–1945, 1987.

[8] J. Krim and A. Widom, "Damping of a crystal oscillator by an adsorbed monolayer and its relation to interfacial viscosity," *Physical Review B*, vol. 38, pp. 12184–12189, 12 1988.

[9] J. Israelachvili and D. Tabor, "The shear properties of molecular films," *Wear*, vol. 24, pp. 386–390, 6 1973.

[10] N. X. Randall, "Experimental methods in tribology," in *Tribology for Scientists and Engineers: From Basics to Advanced Concepts*, vol. 9781461419457, pp. 141–175, Springer New York, 7 2013.

[11] B. Bhushan, "Nanotribology and nanomechanics," *Wear*, vol. 259, no. 7-12, pp. 1507–1531, 2005.

[12] S. H. Yang and E.-S. Yoon, "Nanotribology," in *Tribology for Scientists and Engineers*, pp. 525–553, New York, NY: Springer New York, 2013.

[13] M. de Boer and T. Mayer, "Tribology of MEMS," *MRS Bulletin*, vol. 26, pp. 302–304, 4 2001.

[14] W. H. Soe, S. Srivastava, and C. Joachim, "Train of single molecule-gears," *Journal of Physical Chemistry Letters*, vol. 10, no. 21, pp. 6462–6467, 2019.

[15] H.-J. Kim and D.-E. Kim, "Nano-scale friction: A review," *International Journal of Precision Engineering and Manufacturing*, vol. 10, pp. 141–151, 4 2009.

[16] D. Brown, T. O. Walker, J. A. Blanco, R. W. Ives, H. T. Ngo, J. Shey, and R. Rakvic, "Detecting firmware modification on solid state drives via current draw analysis," *Computers and Security*, vol. 102, pp. 1–18, 2021.

[17] M. H. Kryder and C. S. Kim, "After hard drives-what comes next?," *IEEE Transactions on Magnetics*, vol. 45, no. 10, pp. 3406–3413, 2009.

[18] T. W. Scharf and S. V. Prasad, "Solid lubricants: A review," *Journal of Materials Science*, vol. 48, no. 2, pp. 511–531, 2013.

[19] E. Rabinowicz, "The determination of the compatibility of metals through static friction tests," *ASLE Transactions*, 1971.

[20] D. Berman, A. Erdemir, and A. V. Sumant, "Graphene: a new emerging lubricant," *Materials Today*, vol. 17, pp. 31–42, 1 2014.

[21] T. Polcar and A. Cavaleiro, "Review on self-lubricant transition metal dichalcogenide nanocomposite coatings alloyed with carbon," *Surface and Coatings Technology*, vol. 206, no. 4, pp. 686–695, 2011.

[22] T. Polcar and A. Cavaleiro, "Self-adaptive low friction coatings based on transition metal dichalcogenides," *Thin Solid Films*, vol. 519, no. 12, pp. 4037–4044, 2011.

[23] J. Robertson, "Diamond-like amorphous carbon," *Materials Science and Engineering: R: Reports*, vol. 37, no. 4-6, pp. 129–281, 2002.

[24] P. H. Mayrhofer, C. Mitterer, L. Hultman, and H. Clemens, "Microstructural design of hard coatings," *Progress in Materials Science*, vol. 51, pp. 1032–1114, 11 2006.

[25] T. Polcar, M. Evaristo, and A. Cavaleiro, "The tribological behavior of W-S-C films in pin-on-disk testing at elevated temperature," *Vacuum*, vol. 81, no. 11-12, pp. 1439–1442, 2007.

[26] A. Gupta, T. Sakthivel, and S. Seal, "Recent development in 2D materials beyond graphene," *Progress in Materials Science*, vol. 73, pp. 44–126, 2015.

[27] P. Nicolini and T. Polcar, "A comparison of empirical potentials for sliding simulations of MoS2," *Computational Materials Science*, vol. 115, pp. 158–169, 2016.

[28] T. Polcar, M. Evaristo, R. Colaço, C. Silviu Sandu, and A. Cavaleiro, "Nanoscale triboactivity: The response of Mo–Se–C coatings to sliding," *Acta Materialia*, vol. 56, pp. 5101–5111, 10 2008.

[29] Y. Rai, A. Neville, and A. Morina, "Transient processes of MoS 2 tribofilm formation under boundary lubrication," *Lubrication Science*, vol. 28, pp. 449–471, 11 2016.

[30] B. Bhushan and B. K. Gupta, *Handbook of Tribology: Materials, coatings, and surface treatments*. McGraw-Hill, 1991.

[31] J. Moser and F. Levy, "Crystal Reorientation and Wear Mechanisms in Mos2 Lubricating Thin-Films Investigated By TEM," *Journal of Materials Research*, vol. 8, no. 1, pp. 206–213, 1993.

[32] I. Szlufarska, M. Chandross, and R. W. Carpick, "Recent advances in single-asperity nanotribology," *Journal of Physics D: Applied Physics*, vol. 41, p. 123001, 6 2008.

[33] M. Dienwiebel, G. S. Verhoeven, N. Pradeep, J. W. Frenken, J. A. Heimberg, and H. W. Zandbergen, "Superlubricity of graphite," *Physical Review Letters*, vol. 92, no. 12, pp. 1–4, 2004.

[34] L. Y. Lin, D. E. Kim, W. K. Kim, and S. C. Jun, "Friction and wear characteristics of multi-layer graphene films investigated by atomic force microscopy," *Surface and Coatings Technology*, vol. 205, no. 20, pp. 4864–4869, 2011.

[35] C. Lee, Q. Li, W. Kalb, X. Z. Liu, H. Berger, R. W. Carpick, and J. Hone, "Frictional Characteristics of Atomically Thin Sheets," *Science*, vol. 328, pp. 76–80, 4 2010.

[36] L. Fang, D.-M. Liu, Y. Guo, Z.-M. Z.-M. Liao, J.-B. J.-B. Luo, and S.-Z. S.-Z. Wen, "Thickness dependent friction on few-layer MoS2, WS2, and WSe2," *Nanotechnology*, vol. 28, p. 245703, 6 2017.

[37] J. Zekonyte, A. Cavaleiro, and T. Polcar, "Frictional properties of self-adaptive chromium doped tungsten-sulfur- carbon coatings at nanoscale," *Applied Surface Science*, vol. 303, pp. 381–387, 2014.

[38] J. Zekonyte and T. Polcar, "Friction Force Microscopy Analysis of Self-Adaptive W-S-C Coatings: Nanoscale Friction and Wear," *ACS Applied Materials and Interfaces*, vol. 7, no. 38, pp. 21056–21064, 2015.

[39] C. Lee, H. Yan, L. Brus, T. Heinz, J. Hone, and S. Ryu, "Anomalous lattice vibrations of single-and few-layer MoS2," *ACS nano*, vol. 4, no. 5, pp. 2695–700, 2010.

[40] E. Liu, B. Blanpain, J. P. Celis, and J. R. Roos, "Comparative study between macrotribology and nanotribology," *Journal of Applied Physics*, vol. 84, no. 9, pp. 4859–4865, 1998.

[41] J. R. Lince and P. D. Fleischauer, "Crystallinity of rf-sputtered MoS2 films," *Journal of Materials Research*, vol. 2, pp. 827–838, 12 1987.

[42] J. S. Zabinski, M. S. Donley, and S. V. Prasad, "Synthesis and Characterization of Tungsten Disulfide Films Grown By Pulsed-Laser Deposition," *Journal of Materials Science*, vol. 29, no. 18, pp. 4834–4839, 1994.

[43] A. A. Voevodin and J. S. Zabinski, "Supertough wear-resistant coatings with 'chameleon' surface adaptation," *Thin Solid Films*, vol. 370, no. 1, pp. 223–231, 2000.

[44] P. J. Blau, "The significance and use of the friction coefficient," *Tribology International*, vol. 34, pp. 585–591, 9 2001.

[45] Y. Mo, K. T. Turner, and I. Szlufarska, "Friction laws at the nanoscale," *Nature*, vol. 457, no. 7233, pp. 1116–1119, 2009.

[46] B. N. J. Perrson, *Sliding Friction: Physical Principles and Applications*. Heidelberg: Springer, 2nd ed., 2010.

[47] F. P. Bowden and D. Tabor, *The Friction and Lubrication of Solids*. Oxford: Clarendon Press, 1st ed., 1950.

[48] A. Vanossi, N. Manini, M. Urbakh, S. Zapperi, and E. Tosatti, "Colloquium: Modeling friction: From nanoscale to mesoscale," *Reviews of Modern Physics*, vol. 85, pp. 529–552, 4 2013.

[49] E. Liamas, S. D. Connell, S. N. Ramakrishna, and A. Sarkar, "Probing the frictional properties of soft materials at the nanoscale," *Nanoscale*, vol. 12, no. 4, pp. 2292–2308, 2020.

[50] M. Weiss and F. J. Elmer, "A Simple Model for Wearless Friction: The Frenkel-Kontorova-Tomlinson Model," in *Physics of Sliding Friction*, pp. 163–178, Dordrecht: Springer Netherlands, 1996.

[51] L. Prandtl, "Ein Gedankenmodell zur kinetischen Theorie der festen Körper," *ZAMM - Zeitschrift für Angewandte Mathematik und Mechanik*, vol. 8, no. 2, pp. 85–106, 1928.

[52] G. Tomlinson, "CVI. A molecular theory of friction," *The London, Edinburgh, and Dublin Philosophical Magazine and Journal of Science*, vol. 7, pp. 905–939, 6 1929.

[53] J. Frenkel and T. Kontorova, "On the theory of plastic deformation and twinning," *J. Phys. USSR*, vol. 1, pp. 137–149, 1939.

[54] M. Hirano and K. Shinjo, "Superlubricity and frictional anisotropy," *Wear*, vol. 168, no. 1-2, pp. 121–125, 1993.

[55] M. Hirano, "Atomistics of superlubricity," *Friction*, vol. 2, no. 2, pp. 95–105, 2014.

[56] Q. J. Wang and Y.-W. Chung, eds., *Encyclopedia of Tribology*. Boston, MA: Springer US, 2013.

[57] M. Hirano, "Atomistics of superlubricity," in *Superlubricity*, pp. 1–19, Elsevier, 2021.

[58] J. Li and J. Luo, "Advancements in superlubricity," *Science China Technological Sciences*, vol. 56, no. 12, pp. 2877–2887, 2013.

[59] K. L. Johnson, K. Kendall, and A. D. Roberts, "Surface Energy and the Contact of Elastic Solids," *Proceedings of the Royal Society A: Mathematical, Physical and Engineering Sciences*, vol. 324, no. 1558, pp. 301–313, 1971.

[60] P. Prokopovich and V. Starov, "Adhesion models: From single to multiple asperity contacts," *Advances in Colloid and Interface Science*, vol. 168, no. 1-2, pp. 210–222, 2011.

[61] K. L. Johnson, "Mechanics of adhesion," *Tribology International*, vol. 31, no. 8, pp. 413–418, 1998.

[62] G. G. Adams and M. Nosonovsky, "Contact modeling - forces," *Tribology International*, vol. 33, no. 5, pp. 431–442, 2000.

[63] V. V. Pokropivny and V. V. Skorokhod, "Classification of nanostructures by dimensionality and concept of surface forms engineering in nanomaterial science," *Materials Science and Engineering C*, vol. 27, no. 5-8 SPEC. ISS., pp. 990–993, 2007.

[64] B. V. Derjaguin, V. M. Muller, and Y. P. Toporov, "Effect of contact deformations on the adhesion of particles," *Journal of Colloid And Interface Science*, vol. 53, no. 2, pp. 314–326, 1975.

[65] R. Bradley, "LXXIX. The cohesive force between solid surfaces and the surface energy of solids," *The London, Edinburgh, and Dublin Philosophical Magazine and Journal of Science*, vol. 13, pp. 853–862, 4 1932.

[66] B. Derjaguin, "Untersuchungen über die Reibung und Adhäsion, IV," *Kolloid-Zeitschrift*, vol. 69, pp. 155–164, 11 1934.

[67] C. M. Mate, "Tribology on the Small Scale," *Tribology on the Small Scale: A Bottom Up Approach to Friction, Lubrication and Wear*, vol. 16, no. February 2015, pp. 1–15, 2007.

[68] D. Tabor, "Surface forces and surface interactions," *Journal of Colloid and Interface Science*, vol. 58, pp. 2–13, 1 1977.

[69] V. M. Muller, V. S. Yushchenko, and B. V. Derjaguin, "On the influence of molecular forces on the deformation of an elastic sphere and its sticking to a rigid plane," *Journal of Colloid and Interface Science*, vol. 77, no. 1, pp. 91–101, 1980.

[70] D. Maugis, "Adhesion of spheres: The JKR-DMT transition using a dugdale model," *Journal of Colloid And Interface Science*, vol. 150, no. 1, pp. 243–269, 1992.

[71] D. Dugdale, "Yielding of steel sheets containing slits," *Journal of the Mechanics and Physics of Solids*, vol. 8, no. 2, pp. 100–104, 1960.

[72] K. Johnson and J. Greenwood, "An Adhesion Map for the Contact of Elastic Spheres," *Journal of Colloid and Interface Science*, vol. 192, pp. 326–333, 8 1997.

[73] U. D. Schwarz, O. Zwörner, P. Köster, and R. Wiesendanger, "Quantitative analysis of the frictional properties of solid materials at low loads. I. Carbon compounds," *Physical Review B*, vol. 56, pp. 6987–6996, 9 1997.

[74] U. D. Schwarz, O. Zwörner, P. Köster, and R. Wiesendanger, "Quantitative analysis of the frictional properties of solid materials at low loads. II. Mica and germanium sulfide," *Physical Review B - Condensed Matter and Materials Physics*, vol. 56, no. 11, pp. 6997–7000, 1997.

[75] R. W. Carpick, D. Ogletree, and M. Salmeron, "A General Equation for Fitting Contact Area and Friction vs Load Measurements," *Journal of Colloid and Interface Science*, vol. 211, pp. 395–400, 3 1999.

[76] U. D. Schwarz, "A generalized analytical model for the elastic deformation of an adhesive contact between a sphere and a flat surface," *Journal of Colloid and Interface Science*, vol. 261, no. 1, pp. 99–106, 2003.

[77] L. Kogut and I. Etsion, "Adhesion in elastic-plastic spherical microcontact," *Journal of Colloid and Interface Science*, vol. 261, no. 2, pp. 372–378, 2003.

[78] L. Wenning and M. H. Müser, "Friction laws for elastic nanoscale contacts," *Europhysics Letters*, vol. 54, no. 5, pp. 693–699, 2001.

[79] M. Mishra and I. Szlufarska, "Analytical model for plowing friction at nanoscale," *Tribology Letters*, vol. 45, no. 3, pp. 417–426, 2012.

[80] D. K. Ward, D. Farkas, J. Lian, W. A. Curtin, J. Wang, K. S. Kim, and Y. Qi, "Engineering size-scaling of plastic deformation in nanoscale asperities," *Proceedings of the National Academy of Sciences of the United States of America*, vol. 106, no. 24, pp. 9580–9585, 2009.

[81] H. Klein, D. Pailharey, and Y. Mathey, "Friction force studies on layered materials using an Atomic Force Microscope," *Surface Science*, vol. 387, no. 1-3, pp. 227–235, 1997.

[82] H. K. Wickramasinghe, "Scanned-Probe Microscopes," *Scientific American*, vol. 261, no. 4, pp. 98–105, 1989.

[83] G. Binnig, C. F. Quate, and C. Gerber, "Atomic Force Microscope," *Physical Review Letters*, vol. 56, pp. 930–933, 3 1986.

[84] G. Binnig, H. Rohrer, C. Gerber, and E. Weibel, "Tunneling through a controllable vacuum gap," *Appl. Phys. Lett.*, vol. 40, no. September 1981, pp. 178–180, 1982.

[85] G. Binnig, H. Rohrer, C. Gerber, and E. Weibel, "Surface studies by scanning tunneling microscopy," *Physical review letters*, vol. 49, no. 1, pp. 57–61, 1982.

[86] F. J. Giessibl, "Advances in atomic force microscopy," *Reviews of Modern Physics*, vol. 75, no. 3, pp. 949–983, 2003.

[87] M. Hirano and K. Shinjo, "Atomistic locking and friction," *Physical Review B*, vol. 41, no. 17, pp. 11837–11851, 1990.

[88] A. I. Vakis, V. A. Yastrebov, J. Scheibert, L. Nicola, D. Dini, C. Minfray, A. Almqvist, M. Paggi, S. Lee, G. Limbert, J. F. Molinari, G. Anciaux, R. Aghababaei, S. Echeverri Restrepo, A. Papangelo, A. Cammarata, P. Nicolini, C. Putignano, G. Carbone, S. Stupkiewicz, J. Lengiewicz, G. Costagliola, F. Bosia, R. Guarino, N. M. Pugno, M. H. Müser, and M. Ciavarella, "Modeling and simulation in tribology across scales: An overview," *Tribology International*, vol. 125, no. February, pp. 169–199, 2018.

[89] J. Gao, B. Li, J. Tan, P. Chow, T. M. Lu, and N. Koratkar, "Aging of Transition Metal Dichalcogenide Monolayers," *ACS Nano*, vol. 10, no. 2, pp. 2628–2635, 2016.

[90] C. B. Prater, H. J. Butt, and P. K. Hansma, "Atomic force microscopy," *Nature*, vol. 345, pp. 839–840, 6 1990.

[91] D. Sarid, *Scanning Force Microscopy*. New York: Oxford University Press, 1991.

[92] P. C. Braga and D. Ricci, *Atomic Force Microscopy*, vol. 242. New Jersey: Humana Press, 10 2003.

[93] F. Gołek, P. Mazur, Z. Ryszka, and S. Zuber, "AFM image artifacts," *Applied Surface Science*, vol. 304, pp. 11–19, 2014.

[94] B. Voigtländer, *Atomic Force Microscopy*. NanoScience and Technology, Cham: Springer International Publishing, 2019.

[95] D. F. Ogletree, R. W. Carpick, and M. Salmeron, "Calibration of frictional forces in atomic force microscopy," *Review of Scientific Instruments*, vol. 67, no. 9, pp. 3298–3306, 1996.

[96] J. K. Huang, J. Pu, C. L. Hsu, M. H. Chiu, Z. Y. Juang, Y. H. Chang, W. H. Chang, Y. Iwasa, T. Takenobu, and L. J. Li, "Large-area synthesis of highly crystalline WSe2 monolayers and device applications," *ACS Nano*, vol. 8, no. 1, pp. 923–930, 2014.

[97] J. Liu, J. K. Notbohm, R. W. Carpick, and K. T. Turner, "Method for characterizing nanoscale wear of atomic force microscope tips," *ACS Nano*, vol. 4, no. 7, pp. 3763–3772, 2010.

[98] B. Gotsmann and M. A. Lantz, "Atomistic wear in a single asperity sliding contact," *Physical Review Letters*, vol. 101, no. 12, pp. 1–4, 2008.

[99] G. Meyer and N. Amer, "Simultaneous measurement of lateral and normal forces with an optical beam deflection atomic force microscope," *Appl. Phys. Lett.*, vol. 57, no. 1990, p. 2089, 1990.

[100] O. Marti, J. Colchero, and J. Mlynek, "Combined scanning force and friction microscopy of mica," *Nanotechnology*, vol. 1, p. 141, 1990.

[101] N. N. Gosvami, J. A. Bares, F. Mangolini, A. R. Konicek, D. G. Yablon, and R. W. Carpick, "Mechanisms of antiwear tribofilm growth revealed in situ by single-asperity sliding contacts," *Science*, vol. 348, no. 6230, pp. 102–106, 2015.

[102] N. Gosvami, I. Lahouij, J. Ma, and R. Carpick, "Nanoscale in situ study of ZDDP tribofilm growth at aluminum-based interfaces using atomic force microscopy," *Tribology International*, vol. 143, p. 106075, 3 2020.

[103] W. Choi, N. Choudhary, G. H. Han, J. Park, D. Akinwande, and Y. H. Lee, "Recent development of two-dimensional transition metal dichalcogenides and their applications," *Materials Today*, vol. 20, no. 3, pp. 116–130, 2017.

[104] K. S. Novoselov, A. K. Geim, S. V. Morozov, D. Jiang, Y. Zhang, S. V. Dubonos, I. V. Grigorieva, and A. A. Firsov, "Electric Field Effect in Atomically Thin Carbon Films," *Science*, vol. 306, pp. 666–669, 10 2004.

[105] A. K. Geim and K. S. Novoselov, "The rise of graphene," *Nature Materials*, vol. 6, pp. 183–191, 3 2007.

[106] D. Akinwande, C. J. Brennan, J. S. Bunch, P. Egberts, J. R. Felts, H. Gao, R. Huang, J.-s. Kim, T. Li, Y. Li, K. M. Liechti, N. Lu, H. S. Park, E. J. Reed, P. Wang, B. I. Yakobson, T. Zhang, Y.-W. Zhang, Y. Zhou, and Y. Zhu, "A Review on Mechanics and Mechanical Properties of 2D Materials - Graphene and Beyond," *Extreme Mechanics Letters*, vol. 13, pp. 42–77, 2016.

[107] C. Lee, X. Wei, J. W. Kysar, and J. Hone, "Measurement of the Elastic Properties and Intrinsic Strength of Monolayer Graphene," *Science*, vol. 321, pp. 385–388, 7 2008.

[108] J. M. Martin, C. Donnet, T. Le Mogne, and T. Epicier, "Superlubricity of molybdenum disulphide," *Physical Review B*, vol. 48, pp. 10583–10586, 10 1993.

[109] M. R. Vazirisereshk, A. Martini, D. A. Strubbe, and M. Z. Baykara, "Solid Lubrication with MoS2: A Review," *Lubricants*, vol. 7, p. 57, 7 2019.

[110] M. Lotya, P. J. King, U. Khan, S. De, and J. N. Coleman, "High-concentration, surfactant-stabilized graphene dispersions," *ACS Nano*, vol. 4, no. 6, pp. 3155–3162, 2010.

[111] S. Mohammadi, Z. Kolahdouz, S. Darbari, S. Mohajerzadeh, and N. Masoumi, "Graphene formation by unzipping carbon nanotubes using a sequential plasma assisted processing," *Carbon*, vol. 52, pp. 451–463, 2013.

[112] K. S. Kim, Y. Zhao, H. Jang, S. Y. Lee, J. M. Kim, K. S. Kim, J. H. Ahn, P. Kim, J. Y. Choi, and B. H. Hong, "Large-scale pattern growth of graphene films for stretchable transparent electrodes," *Nature*, vol. 457, no. 7230, pp. 706–710, 2009.

[113] P. W. Sutter, J. I. Flege, and E. A. Sutter, "Epitaxial graphene on ruthenium," *Nature Materials*, vol. 7, no. 5, pp. 406–411, 2008.

[114] S. W. Lee, C. Mattevi, M. Chhowalla, and R. M. Sankaran, "Plasma-assisted reduction of graphene oxide at low temperature and atmospheric pressure for flexible conductor applications," *Journal of Physical Chemistry Letters*, vol. 3, no. 6, pp. 772–777, 2012.

[115] Q. H. Wang, K. Kalantar-Zadeh, A. Kis, J. N. Coleman, and M. S. Strano, "Electronics and optoelectronics of two-dimensional transition metal dichalcogenides," *Nature Nanotechnology*, vol. 7, no. 11, pp. 699–712, 2012.

[116] M. S. Fuhrer and J. Hone, "Measurement of mobility in dual-gated MoS2 transistors," *Nature Nanotechnology*, vol. 8, no. 3, pp. 146–147, 2013.

[117] G. Tai, T. Zeng, J. Yu, J. Zhou, Y. You, X. Wang, H. Wu, X. Sun, T. Hu, and W. Guo, "Fast and large-area growth of uniform MoS2 monolayers on molybdenum foils," *Nanoscale*, 2016.

[118] A. Antonelou, G. Syrrokostas, L. Sygellou, G. Leftheriotis, V. Dracopoulos, and S. N. Yannopoulos, "Facile, substrate-scale growth of mono- and few-layer homogeneous MoS2 films on Mo foils with enhanced catalytic activity as counter electrodes in DSSCs," *Nanotechnology*, 2015.

[119] A. K. Geim, "Graphene: Status and Prospects," *Science*, vol. 324, pp. 1530–1534, 6 2009.

[120] O. Lopez-Sanchez, D. Lembke, M. Kayci, A. Radenovic, and A. Kis, "Ultrasensitive photodetectors based on monolayer MoS 2," *Nature Nanotechnology*, vol. 8, no. 7, pp. 497–501, 2013.

[121] S. Bertolazzi, J. Brivio, and A. Kis, "Stretching and breaking of ultrathin MoS 2," *ACS Nano*, vol. 5, pp. 9703–9709, 12 2011.

[122] J. Pu, Y. Yomogida, K. K. Liu, L. J. Li, Y. Iwasa, and T. Takenobu, "Highly flexible MoS 2 thin-film transistors with ion gel dielectrics," *Nano Letters*, vol. 12, no. 8, pp. 4013–4017, 2012.

[123] H. Li, Z. Yin, Q. He, H. Li, X. Huang, G. Lu, D. W. H. Fam, A. I. Y. Tok, Q. Zhang, and H. Zhang, "Fabrication of single- and multilayer MoS 2 film-based field-effect transistors for sensing NO at room temperature," *Small*, vol. 8, no. 1, pp. 63–67, 2012.

[124] A.R. Lansdown, *Molybdenum Disulphide Lubrication*. Elsevier, 1st ed., 1999.

[125] M. B. Elinski, Z. Liu, J. C. Spear, and J. D. Batteas, "2D or not 2D? the impact of nanoscale roughness and substrate interactions on the tribological properties of graphene and MoS2," *Journal of Physics D: Applied Physics*, vol. 50, no. 10, 2017.

[126] A. Smolyanitsky, J. P. Killgore, and V. K. Tewary, "Effect of elastic deformation on frictional properties of few-layer graphene," *Physical Review B*, vol. 85, p. 035412, 1 2012.

[127] Q. Li, C. Lee, R. W. Carpick, and J. Hone, "Substrate effect on thickness-dependent friction on graphene," *Physica Status Solidi (B) Basic Research*, vol. 247, no. 11-12, pp. 2909–2914, 2010.

[128] G. S. Verhoeven, M. Dienwiebel, and J. W. M. Frenken, "Model calculations of superlubricity of graphite," *Physical Review B*, vol. 70, p. 165418, 10 2004.

[129] K. Miura and S. Kamiya, "Observation of the Amontons-Coulomb law on the nanoscale: Frictional forces between flakes and surfaces," *Europhysics Letters*, vol. 58, p. 610, 2002.

[130] P. Gallagher, M. Lee, F. Amet, P. Maksymovych, J. Wang, S. Wang, X. Lu, G. Zhang, K. Watanabe, T. Taniguchi, and D. Goldhaber-Gordon, "Switchable friction enabled by nanoscale self-assembly on graphene," *Nature Communications*, vol. 7, 2 2016.

[131] M. Park, J. Im, M. Shin, Y. Min, J. Park, H. Cho, S. Park, M. B. Shim, S. Jeon, D. Y. Chung, J. Bae, J. Park, U. Jeong, and K. Kim, "Highly stretchable electric circuits from a composite material of silver nanoparticles and elastomeric fibres," *Nature Nanotechnology*, vol. 7, no. 12, pp. 803–809, 2012.

[132] W. Zheng, W. Huang, F. Gao, H. Yang, M. Dai, G. Liu, B. Yang, J. Zhang, Y. Q. Fu, X. Chen, Y. Qiu, D. Jia, Y. Zhou, and P. Hu, "Kirigami-Inspired Highly Stretchable Nanoscale Devices Using Multidimensional Deformation of Monolayer MoS2," *Chemistry of Materials*, vol. 30, no. 17, pp. 6063–6070, 2018.

[133] J. A. Rogers, T. Someya, and Y. Huang, "Materials and mechanics for stretchable electronics," *Science*, vol. 327, no. 5973, pp. 1603–1607, 2010.

[134] J. H. Ahn and J. H. Je, "Stretchable electronics: Materials, architectures and integrations," *Journal of Physics D: Applied Physics*, vol. 45, no. 10, 2012.

[135] S. Jung, J. H. Kim, J. Kim, S. Choi, J. Lee, I. Park, T. Hyeon, and D. H. Kim, "Reverse-micelle-induced porous pressure-sensitive rubber for wearable human-machine interfaces," *Advanced Materials*, vol. 26, no. 28, pp. 4825–4830, 2014.

[136] T. Yamada, Y. Hayamizu, Y. Yamamoto, Y. Yomogida, A. Izadi-Najafabadi, D. N. Futaba, and K. Hata, "A stretchable carbon nanotube strain sensor for human-motion detection," *Nature Nanotechnology*, vol. 6, no. 5, pp. 296–301, 2011.

[137] C. Pang, G. Y. Lee, T. I. Kim, S. M. Kim, H. N. Kim, S. H. Ahn, and K. Y. Suh, "A flexible and highly sensitive strain-gauge sensor using reversible interlocking of nanofibres," *Nature Materials*, vol. 11, no. 9, pp. 795–801, 2012.

[138] X. Liu, T. Ma, N. Pinna, and J. Zhang, "Two-Dimensional Nanostructured Materials for Gas Sensing," *Advanced Functional Materials*, vol. 27, no. 37, pp. 1–30, 2017.

[139] C. Ataca, H. Şahin, and S. Ciraci, "Stable, single-layer MX 2 transition-metal oxides and dichalcogenides in a honeycomb-like structure," *Journal of Physical Chemistry C*, vol. 116, no. 16, pp. 8983–8999, 2012.

[140] E. Bergmann, G. Melet, C. Müller, and A. Simon-Vermot, "Friction properties of sputtered dichalcogenide layers," *Tribology International*, vol. 14, no. 6, pp. 329–332, 1981.

[141] D. Shtansky, T. Lobova, V. Fominski, S. Kulinich, I. Lyasotsky, M. Petrzhik, E. Levashov, and J. Moore, "Structure and tribological properties of WSex, WSex/TiN, WSex/TiCN and WSex/TiSiN coatings," *Surface and Coatings Technology*, vol. 183, pp. 328–336, 5 2004.

[142] S. Dominguez-Meister, A. Justo, and J. Sanchez-Lopez, "Synthesis and tribological properties of WSex films prepared by magnetron sputtering," *Materials Chemistry and Physics*, vol. 142, pp. 186–194, 10 2013.

[143] S. Domínguez-Meister, M. Conte, A. Igartua, T. C. Rojas, and J. C. Sánchez-López, "Self-Lubricity of WSe x Nanocomposite Coatings," *ACS Applied Materials and Interfaces*, vol. 7, pp. 7979–7986, 4 2015.

[144] T. Polcar, M. Evaristo, and A. Cavaleiro, "Friction of self-lubricating W-S-C sputtered coatings sliding under increasing load," *Plasma Processes and Polymers*, vol. 4, no. SUPPL.1, pp. 541–546, 2007.

[145] A. Nossa and A. Cavaleiro, "The influence of the addition of C and N on the wear behaviour of W–S–C/N coatings," *Surface and Coatings Technology*, vol. 142-144, pp. 984–991, 7 2001.

[146] A. A. Voevodin, J. P. O'Neill, and J. S. Zabinski, "Nanocomposite tribological coatings for aerospace applications," *Surface and Coatings Technology*, vol. 116-119, pp. 36–45, 1999.

[147] T. Spalvins and J. S. Przybyszewski, "Deposition of sputtered molybdenum disulphide films and friction characteristics of such films in vacuum," *Vacuum*, vol. 18, p. 496, 8 1968.

[148] L. Shi, C. Sun, and W. Liu, "Electrodeposited nickel-cobalt composite coating containing MoS2," *Applied Surface Science*, vol. 254, no. 21, pp. 6880–6885, 2008.

[149] M. F. Cardinal, P. A. Castro, J. Baxi, H. Liang, and F. J. Williams, "Characterization and frictional behavior of nanostructured Ni-W-MoS2 composite coatings," *Surface and Coatings Technology*, vol. 204, no. 1-2, pp. 85–90, 2009.

[150] T. Kubart, T. Polcar, L. Kopecký, R. Novák, and D. Nováková, "Temperature dependence of tribological properties of MoS2 and MoSe2 coatings," *Surface and Coatings Technology*, vol. 193, no. 1-3 SPEC. ISS., pp. 230–233, 2005.

[151] S.-s. Xu, L.-j. Weng, Y.-z. Liu, K.-h. Kang, C.-L. Kim, and D.-e. Kim, "Microstructure evolution and enhanced vacuum tribological performance of

Ni-doped WS 2 composite coating," *Surface and Coatings Technology*, vol. 325, pp. 81–88, 9 2017.

[152] J. R. Lince, "Doped MoS2 Coatings and Their Tribology," in *Encyclopedia of Tribology* (Q. J. Wang and Y.-W. Chung, eds.), pp. 782–785, Boston, MA: Springer US, 2013.

[153] W. O. Winer, "Molybdenum Disulpide As a Lurricant: a Review of Fundamental Knowledge," *Wear*, vol. 10, pp. 422–452, 1967.

[154] G. Stachowiak and A. Batchelor, *Engineering Tribology*. Elsevier, 2006.

[155] R. L. Johnson, D. H. Buckley, and M. A. Swikert, "Studies of Lubricating Materials in Vacuum," tech. rep., NATIONAL AERONAUTICS AND SPACE ADMINISTRATION, 1964.

[156] T. Spalvins, "Friction characteristics of sputtered solid film lubricants," *NASA Tech. Memo. TM X- 52819*, 1970.

[157] N. W. Price and C. R. D. Priestland, "Sputtered molybdenum disulphide as a lubricant for instrument slip rings," *Thin Solid Films*, vol. 11, no. 1, pp. 191–193, 1972.

[158] T. Spalvins, "Coatings for wear and lubrication," *Thin Solid Films*, vol. 53, no. 3, pp. 285–300, 1978.

[159] K. Reichelt and G. Mair, "The structure and composition of rf reactively sputtered MoS x films," *Journal of Applied Physics*, vol. 49, pp. 1245–1247, 3 1978.

[160] H. Dimigen, H. Hübsch, P. Willich, and K. Reichelt, "Stoichiometry and friction properties of sputtered MoSx layers," *Thin Solid Films*, vol. 129, no. 1-2, pp. 79–91, 1985.

[161] W. E. Jamison and S. L. Cosgrove, "Friction Characteristics of Transition-Metal Disulfides and Diselenides," *A S L E Transactions*, vol. 14, pp. 62–72, 1 1971.

[162] M. Evaristo, T. Polcar, and A. Cavaleiro, "Synthesis and properties of W–Se–C coatings deposited by PVD in reactive and non-reactive processes," *Vacuum*, vol. 83, pp. 1262–1265, 6 2009.

[163] M. Evaristo, T. Polcar, and A. Cavaleiro, "Can W-Se-C coatings be competitive to W-S-C ones?," *Plasma Processes and Polymers*, vol. 6, no. SUPPL. 1, pp. 92–95, 2009.

[164] S. Grigoriev, V. Fominski, R. Romanov, and M. Volosova, "Structural modification and tribological behavior improvement of solid lubricating WSe¡inf¿x¡/inf¿coatings during pulsed laser deposition in buffer He-Gas," *Journal of Friction and Wear*, vol. 34, no. 4, pp. 262–269, 2013.

[165] C. Donnet, J. Martin, T. Le Mogne, and M. Belin, "Super-low friction of MoS2 coatings in various environments," *Tribology International*, vol. 29, pp. 123–128, 2 1996.

[166] B. C. Stupp, "Synergistic effects of metals co-sputtered with MoS2," *Thin Solid Films*, vol. 84, pp. 257–266, 10 1981.

[167] T. Spalvins, "Frictional and morphological properties of Au-MoS2 films sputtered from a compact target," *Thin Solid Films*, vol. 118, pp. 375–384, 8 1984.

[168] D. Teer, J. Hampshire, V. Fox, and V. Bellido-Gonzalez, "The tribological properties of MoS2/metal composite coatings deposited by closed field magnetron sputtering," *Surface and Coatings Technology*, vol. 94-95, pp. 572–577, 10 1997.

[169] V. C. Fox, N. Renevier, D. G. Teer, J. Hampshire, and V. Rigato, "The structure of tribologically improved MoS2-metal composite coatings and their industrial applications," *Surface and Coatings Technology*, vol. 116-119, pp. 492–497, 1999.

[170] X. Wang, Y. Xing, S. Ma, X. Zhang, K. Xu, and D. G. Teer, "Microstructure and mechanical properties of MoS2/titanium composite coatings with different titanium content," *Surface and Coatings Technology*, vol. 201, no. 9-11 SPEC. ISS., pp. 5290–5293, 2007.

[171] X. Qin, P. Ke, A. Wang, and K. H. Kim, "Microstructure, mechanical and tribological behaviors of MoS2-Ti composite coatings deposited by a hybrid HIPIMS method," *Surface and Coatings Technology*, vol. 228, pp. 275–281, 2013.

[172] S. Xu, X. Gao, M. Hu, J. Sun, D. Wang, F. Zhou, L. Weng, and W. Liu, "Morphology evolution of Ag alloyed WS2 films and the significantly enhanced mechanical and tribological properties," *Surface and Coatings Technology*, vol. 238, pp. 197–206, 2014.

[173] A. Nossa, A. Cavaleiro, N. J. Carvalho, B. J. Kooi, and J. T. M. De Hosson, "On the microstructure of tungsten disulfide films alloyed with carbon and nitrogen," *Thin Solid Films*, vol. 484, no. 1-2, pp. 389–395, 2005.

[174] T. Polcar, M. Evaristo, M. Stueber, and A. Cavaleiro, "Synthesis and structural properties of Mo-Se-C sputtered coatings," *Surface and Coatings Technology*, vol. 202, no. 11, pp. 2418–2422, 2008.

[175] T. B. Yaqub, T. Vuchkov, M. Evaristo, and A. Cavaleiro, "DCMS Mo-Se-C solid lubricant coatings – Synthesis, structural, mechanical and tribological property investigation," *Surface and Coatings Technology*, vol. 378, no. September, p. 124992, 2019.

[176] T. B. Yaqub, K. Hebbar Kannur, T. Vuchkov, C. Pupier, C. Héau, and A. Cavaleiro, "Molybdenum diselenide coatings as universal dry lubricants for terrestrial and aerospace applications," *Materials Letters*, vol. 275, p. 128035, 9 2020.

[177] T. B. Yaqub, T. Vuchkov, P. Sanguino, T. Polcar, and A. Cavaleiro, "Comparative Study of DC and RF Sputtered MoSe2 Coatings Containing Carbon—An Approach to Optimize Stoichiometry, Microstructure, Crystallinity and Hardness," *Coatings*, vol. 10, p. 133, 2 2020.

[178] T. Vuchkov, T. B. Yaqub, M. Evaristo, and A. Cavaleiro, "Synthesis, microstructural and mechanical properties of self-lubricating Mo-Se-C coatings deposited by closed-field unbalanced magnetron sputtering," *Surface and Coatings Technology*, vol. 394, no. May, p. 125889, 2020.

[179] T. Polcar, M. Evaristo, and A. Cavaleiro, "Comparative study of the tribological behavior of self-lubricating W-S-C and Mo-Se-C sputtered coatings," *Wear*, vol. 266, no. 3-4, pp. 388–392, 2009.

[180] T. B. Yaqub, S. Bruyere, J. F. Pierson, T. Vuchkov, and A. Cavaleiro, "Insights into the wear track evolution with sliding cycles of carbon-alloyed transition metal dichalcogenide coatings," *Surface and Coatings Technology*, vol. 403, no. August, p. 126360, 2020.

[181] T. Vuchkov, M. Evaristo, T. B. Yaqub, and A. Cavaleiro, "The effect of substrate location on the composition, microstructure and mechano-tribological properties of W-S-C coatings deposited by magnetron sputtering," *Surface and Coatings Technology*, vol. 386, no. February, p. 125481, 2020.

[182] T. Hudec, M. Mikula, L. Satrapinskyy, T. Roch, M. Truchlý, P. Švec, T. Huminiuc, and T. Polcar, "Structure, mechanical and tribological properties of Mo-S-N solid lubricant coatings," *Applied Surface Science*, vol. 486, no. March, pp. 1–14, 2019.

[183] T. Hudec, T. Roch, M. Gregor, L. Orovčík, M. Mikula, and T. Polcar, "Tribological behaviour of Mo-S-N solid lubricant coatings in vacuum, nitrogen gas and elevated temperatures," *Surface and Coatings Technology*, vol. 405, no. November 2020, pp. 1–7, 2021.

[184] T. Hudec, V. Izai, L. Satrapinskyy, T. Huminiuc, T. Roch, M. Gregor, B. Grančič, M. Mikula, and T. Polcar, "Structure, mechanical and tribological properties of MoSe2 and Mo-Se-N solid lubricant coatings," *Surface and Coatings Technology*, vol. 405, no. August 2020, 2021.

[185] K. Hebbar Kannur, T. Huminiuc, T. B. Yaqub, T. Polcar, C. Pupier, C. Héau, and A. Cavaleiro, "An insight on the MoS2 tribo-film formation to determine the

friction performance of Mo-S-N sputtered coatings," *Surface and Coatings Technology*, vol. 408, no. October 2020, 2021.

[186] S. Watanabe, J. Noshiro, and S. Miyake, "Tribological characteristics of WS2/MoS2 solid lubricating multilayer films," *Surface and Coatings Technology*, vol. 183, no. 2-3, pp. 347–351, 2004.

[187] S. Watanabe, J. Noshiro, and S. Miyake, "Friction properties of WS2/MoS2 multilayer films under vacuum environment," *Surface and Coatings Technology*, vol. 188-189, pp. 644–648, 11 2004.

[188] A. Reina, X. Jia, J. Ho, D. Nezich, H. Son, V. Bulovic, M. S. Dresselhaus, and K. Jing, "Large area, few-layer graphene films on arbitrary substrates by chemical vapor deposition," *Nano Letters*, vol. 9, no. 1, pp. 30–35, 2009.

[189] Q. Yu, J. Lian, S. Siriponglert, H. Li, Y. P. Chen, and S. S. Pei, "Graphene segregated on Ni surfaces and transferred to insulators," *Applied Physics Letters*, vol. 93, no. 11, pp. 1–4, 2008.

[190] J. C. Spear, B. W. Ewers, and J. D. Batteas, "2D-nanomaterials for controlling friction and wear at interfaces," *Nano Today*, vol. 10, no. 3, pp. 301–314, 2015.

[191] R. Maboudian and R. T. Howe, "Critical review: Adhesion in surface micromechanical structures," *Journal of Vacuum Science and Technology B: Microelectronics and Nanometer Structures*, vol. 15, no. 1, pp. 1–20, 1997.

[192] R. Maboudian, W. R. Ashurst, and C. Carraro, "Tribological challenges in micromechanical systems," *Tribology Letters*, vol. 12, no. 2, pp. 95–100, 2002.

[193] B. Bhushan, "Nanotribology and nanomechanics of MEMS/NEMS and BioMEMS/BioNEMS materials and devices," *Microelectronic Engineering*, vol. 84, no. 3, pp. 387–412, 2007.

[194] W. Guo, J. Yin, H. Qiu, Y. Guo, H. Wu, and M. Xue, "Friction of low-dimensional nanomaterial systems," *Friction*, vol. 2, pp. 209–225, 9 2014.

[195] D. Berman, A. Erdemir, and A. V. Sumant, "Approaches for Achieving Superlubricity in Two-Dimensional Materials," *ACS Nano*, vol. 12, no. 3, pp. 2122–2137, 2018.

[196] M. R. Vazirisereshk, K. Hasz, M. Q. Zhao, A. T. Johnson, R. W. Carpick, and A. Martini, "Nanoscale friction behavior of transition-metal dichalcogenides: Role of the chalcogenide," *ACS Nano*, vol. 14, no. 11, pp. 16013–16021, 2020.

[197] X. Zhou, Y. Liu, X. Hu, L. Fang, Y. Song, D. Liu, and J. Luo, "Influence of elastic property on the friction between atomic force microscope tips and 2D materials," *Nanotechnology*, vol. 31, no. 28, 2020.

[198] A. Rapuc, H. Wang, and T. Polcar, "Nanotribology of transition metal dichalcogenide flakes deposited by chemical vapour deposition: The influence of chemical composition and sliding speed on nanoscale friction of monolayers," *Applied Surface Science*, vol. 556, p. 149762, 8 2021.

[199] J. L. Hutter and J. Bechhoefer, "Calibration of atomic-force microscope tips," *Review of Scientific Instruments*, vol. 64, no. 7, pp. 1868–1873, 1993.

[200] A. Berkdemir, H. R. Gutiérrez, A. R. Botello-Méndez, N. Perea-López, A. L. Elías, C. I. Chia, B. Wang, V. H. Crespi, F. López-Urías, J. C. Charlier, H. Terrones, and M. Terrones, "Identification of individual and few layers of WS2 using Raman Spectroscopy," *Scientific Reports*, vol. 3, pp. 1–8, 2013.

[201] Y. Lv, F. Huang, L. Zhang, J. Weng, S. Zhao, and Z. Ji, "Preparation and Photoluminescence of Tungsten Disulfide Monolayer," *Coatings*, vol. 8, p. 205, 5 2018.

[202] H. Martinez, A. Benayad, D. Gonbeau, P. Vinatier, B. Pecquenard, and A. Levasseur, "Influence of the cation nature of high sulfur content oxysulfide thin films MO S (M=W, Ti) studied by XPS," *Applied Surface Science*, vol. 236, pp. 377–386, 9 2004.

[203] M. Cattelan, B. Markman, G. Lucchini, P. K. Das, I. Vobornik, J. A. Robinson, S. Agnoli, and G. Granozzi, "New Strategy for the Growth of Complex Heterostructures Based on Different 2D Materials," *Chemistry of Materials*, vol. 27, no. 11, pp. 4105–4113, 2015.

[204] F. Reale, P. Palczynski, I. Amit, G. F. Jones, J. D. Mehew, A. Bacon, N. Ni, P. C. Sherrell, S. Agnoli, M. F. Craciun, S. Russo, and C. Mattevi, "High-Mobility and High-Optical Quality Atomically Thin WS 2," *Scientific Reports*, vol. 7, no. 1, pp. 1–10, 2017.

[205] J. C. Shaw, H. Zhou, Y. Chen, N. O. Weiss, Y. Liu, Y. Huang, and X. Duan, "Chemical vapor deposition growth of monolayer MoSe2 nanosheets," *Nano Research*, vol. 7, pp. 511–517, 4 2014.

[206] J. Xia, X. Huang, L. Z. Liu, M. Wang, L. Wang, B. Huang, D. D. Zhu, J. J. Li, C. Z. Gu, and X. M. Meng, "CVD synthesis of large-area, highly crystalline MoSe2 atomic layers on diverse substrates and application to photodetectors," *Nanoscale*, vol. 6, no. 15, pp. 8949–8955, 2014.

[207] M. O'Brien, N. McEvoy, D. Hanlon, K. Lee, R. Gatensby, J. N. Coleman, and G. S. Duesberg, "Low wavenumber Raman spectroscopy of highly crystalline MoSe 2 grown by chemical vapor deposition," *physica status solidi (b)*, vol. 252, pp. 2385–2389, 11 2015.

[208] J. Huang, H. Liu, B. Jin, M. Liu, Q. Zhang, L. Luo, S. Chu, S. Chu, and R. Peng, "Large-area snow-like MoSe 2 monolayers: synthesis, growth mechanism, and efficient electrocatalyst application," *Nanotechnology*, vol. 28, p. 275704, 7 2017.

[209] Y. Zhao, H. Lee, W. Choi, W. Fei, and C. J. Lee, "Large-area synthesis of monolayer MoSe2 films on SiO2/Si substrates by atmospheric pressure chemical vapor deposition," *RSC Adv.*, vol. 7, no. 45, pp. 27969–27973, 2017.

[210] B. Wang, K. Ostrikov, T. Van Der Laan, K. Zheng, R. Shao, M. Zhu, and S. Zou, "Growth and photoluminescence of oriented MoSe2 nanosheets produced by hot filament CVD," *RSC Advances*, vol. 6, no. 43, pp. 37236–37245, 2016.

[211] A. Roy, H. C. P. Movva, B. Satpati, K. Kim, R. Dey, A. Rai, T. Pramanik, S. Guchhait, E. Tutuc, and S. K. Banerjee, "Structural and Electrical Properties of MoTe2 and MoSe2 Grown by Molecular Beam Epitaxy," *ACS Applied Materials & Interfaces*, vol. 8, pp. 7396–7402, 2016.

[212] X. Wang, Y. Gong, G. Shi, W. L. Chow, K. Keyshar, G. Ye, R. Vajtai, J. Lou, Z. Liu, E. Ringe, B. K. Tay, and P. M. Ajayan, "Chemical vapor deposition growth of crystalline monolayer MoSe2," *ACS Nano*, vol. 8, no. 5, pp. 5125–5131, 2014.

[213] H. Li, G. Lu, Y. Wang, Z. Yin, C. Cong, Q. He, L. Wang, F. Ding, T. Yu, and H. Zhang, "Mechanical exfoliation and characterization of single- and few-layer nanosheets of WSe2, TaS2, and TaSe2," *Small*, vol. 9, no. 11, pp. 1974–1981, 2013.

[214] J. Huang, L. Yang, D. Liu, J. Chen, Q. Fu, Y. Xiong, F. Lin, and B. Xiang, "Large-area synthesis of monolayer WSe2 on a SiO2/Si substrate and its device applications," *Nanoscale*, vol. 7, no. 9, pp. 4193–4198, 2015.

[215] H. Li, Q. Zhang, C. C. R. Yap, B. K. Tay, T. H. T. Edwin, A. Olivier, and D. Baillargeat, "From bulk to monolayer MoS 2: Evolution of Raman scattering," *Advanced Functional Materials*, vol. 22, no. 7, pp. 1385–1390, 2012.

[216] A. Splendiani, L. Sun, Y. Zhang, T. Li, J. Kim, C. Y. Chim, G. Galli, and F. Wang, "Emerging photoluminescence in monolayer MoS2," *Nano Letters*, vol. 10, no. 4, pp. 1271–1275, 2010.

[217] P. Liu, T. Luo, J. Xing, H. Xu, H. Hao, H. Liu, and J. Dong, "Large-Area WS2 Film with Big Single Domains Grown by Chemical Vapor Deposition," *Nanoscale Research Letters*, vol. 12, no. 1, p. 558, 2017.

[218] Q. Fu, W. Wang, L. Yang, J. Huang, J. Zhang, and B. Xiang, "Controllable synthesis of high quality monolayer WS2 on a SiO2/Si substrate by chemical vapor deposition," *RSC Adv.*, vol. 5, no. 21, pp. 15795–15799, 2015.

[219] R. Ghosh, J.-S. Kim, A. Roy, H. Chou, M. Vu, S. K. Banerjee, and D. Akinwande, "Large area chemical vapor deposition growth of monolayer MoSe2 and its controlled sulfurization to MoS2," *Journal of Materials Research*, pp. 1–6, 2016.

[220] Y.-h. Chang, O. W. Zhang, O. Y. Zhu, Y. Han, J. Pu, J.-k. Chang, and W.-t. Hsu, "Monolayer MoSe2 Grown by Chemical Vapor Deposition for Fast Photodetection," *ACS Nano*, vol. 8, no. 8, pp. 8582–8590, 2014.

[221] W. Liu, J. Kang, D. Sarkar, Y. Khatami, D. Jena, and K. Banerjee, "Role of metal contacts in designing high-performance monolayer n-type WSe2 field effect transistors," *Nano Letters*, vol. 13, no. 5, pp. 1983–1990, 2013.

[222] D. J. Keller and F. S. Franke, "Envelope reconstruction of probe microscope images," *Surface Science*, vol. 294, pp. 409–419, 9 1993.

[223] D. S. Grierson, J. Liu, R. W. Carpick, and K. T. Turner, "Adhesion of nanoscale asperities with power-law profiles," *Journal of the Mechanics and Physics of Solids*, vol. 61, no. 2, pp. 597–610, 2013.

[224] Z. Lin, B. R. Carvalho, E. Kahn, R. Lv, R. Rao, H. Terrones, M. A. Pimenta, and M. Terrones, "Defect engineering of two-dimensional transition metal dichalcogenides," *2D Materials*, vol. 3, no. 2, 2016.

[225] V. E. Claerbout, T. Polcar, and P. Nicolini, "Superlubricity achieved for commensurate sliding: MoS2 frictional anisotropy in silico," *Computational Materials Science*, vol. 163, pp. 17–23, 6 2019.

[226] M. R. Vazirisereshk, K. Hasz, R. W. Carpick, and A. Martini, " Friction Anisotropy of MoS 2 : Effect of Tip–Sample Contact Quality ," *The Journal of Physical Chemistry Letters*, vol. 11, no. 16, pp. 6900–6906, 2020.

[227] B. Bhushan, *Modern Tribology Handbook*. CRC Press, 7 2001.

[228] T. Filleter, J. L. McChesney, A. Bostwick, E. Rotenberg, K. V. Emtsev, T. Seyller, K. Horn, and R. Bennewitz, "Friction and dissipation in epitaxial graphene films," *Physical Review Letters*, vol. 102, no. 8, pp. 1–4, 2009.

[229] T. Filleter and R. Bennewitz, "Structural and frictional properties of graphene films on SiC(0001) studied by atomic force microscopy," *Physical Review B - Condensed Matter and Materials Physics*, vol. 81, no. 15, pp. 1–7, 2010.

[230] K. L. Johnson, *Contact Mechanics*. Cambridge University Press, 5 1985.

[231] J. E. Lennard-Jones, "Cohesion," *Proceedings of the Physical Society*, vol. 43, pp. 461–482, 9 1931.

[232] H. M. Westergaard, *Theory of Elasticity and Plasticity*. Harvard University Press, 12 2013.

[233] J. E. Sader, J. W. M. Chon, and P. Mulvaney, "Calibration of rectangular atomic force microscope cantilevers," *Review of Scientific Instruments*, vol. 70, pp. 3967–3969, 10 1999.

[234] H. Wang, C. C. Huang, and T. Polcar, "Controllable Tunneling Triboelectrification of Two-Dimensional Chemical Vapor Deposited MoS2," *Scientific Reports*, vol. 9, no. 1, pp. 1–8, 2019.

[235] T. Schimmel, J. Küppers, and M. Lux-Steiner, "Lattice-resolution AFM on the layered dichalcogenide WSe2 in the sliding regime," *Thin Solid Films*, vol. 264, pp. 212–216, 8 1995.

[236] W. J. Schutte, J. L. De Boer, and F. Jellinek, "Crystal structures of tungsten disulfide and diselenide," *Journal of Solid State Chemistry*, vol. 70, no. 2, pp. 207–209, 1987.

[237] K. Luo, J. Wu, H. L. Yi, L. H. Liu, and H. P. Tan, "Hexagonal convection patterns and their evolutionary scenarios in electroconvection induced by a strong unipolar injection," *Physical Review Fluids*, vol. 3, no. 5, 2018.

[238] J. Martin, H. Pascal, C. Donnet, T. Le Mogne, J. Loubet, and T. Epicier, "Superlubricity of MoS2: crystal orientation mechanisms," *Surface and Coatings Technology*, vol. 68-69, pp. 427–432, 12 1994.

[239] X. Fan and L. Wang, "Highly conductive ionic liquids toward high-performance space-lubricating greases," *ACS Applied Materials and Interfaces*, vol. 6, no. 16, pp. 14660–14671, 2014.

[240] C. J. Reeves, P. L. Menezes, M. R. Lovell, and T.-C. Jen, "Tribology of Solid Lubricants," in *Tribology for Scientists and Engineers*, vol. 9781461419, pp. 447–494, New York, NY: Springer New York, 7 2013.

[241] I. Minami, "Ionic Liquids in Tribology," *Molecules*, vol. 14, pp. 2286–2305, 6 2009.

[242] F. Zhou, Y. Liang, and W. Liu, "Ionic liquid lubricants: designed chemistry for engineering applications," *Chemical Society Reviews*, vol. 38, no. 9, p. 2590, 2009.

[243] M. Palacio and B. Bhushan, "A review of ionic liquids for green molecular lubrication in nanotechnology," *Tribology Letters*, vol. 40, no. 2, pp. 247–268, 2010.

[244] S. Kawada, S. Watanabe, Y. Kondo, R. Tsuboi, and S. Sasaki, "Tribochemical reactions of ionic liquids under vacuum conditions," *Tribology Letters*, vol. 54, no. 3, pp. 309–315, 2014.

[245] J. I. Goldstein, D. E. Newbury, P. Echlin, D. C. Joy, C. E. Lyman, E. Lifshin, L. Sawyer, and J. R. Michael, *Scanning Electron Microscopy and X-ray Microanalysis*. Boston, MA: Springer US, 2003.

[246] A. Rapuc, K. Simonovic, T. Huminiuc, A. Cavaleiro, and T. Polcar, "Nanotribological Investigation of Sliding Properties of Transition Metal Dichalcogenide Thin Film Coatings," *ACS Applied Materials & Interfaces*, vol. 12, pp. 54191–54202, 12 2020.

[247] C. Casiraghi, A. C. Ferrari, and J. Robertson, "Raman spectroscopy of hydrogenated amorphous carbons," *Physical Review B*, vol. 72, p. 085401, 8 2005.

[248] A. C. Ferrari and J. Robertson, "Interpretation of Raman spectra of disordered and amorphous carbon," *Physical Review B*, vol. 61, pp. 14095–14107, 5 2000.

[249] W. Zhao, Z. Ghorannevis, K. K. Amara, J. R. Pang, M. Toh, X. Zhang, C. Kloc, P. H. Tan, and G. Eda, "Lattice dynamics in mono- and few-layer sheets of WS2 and WSe2," *Nanoscale*, vol. 5, no. 20, pp. 9677–9683, 2013.

[250] A. Molina-Sánchez and L. Wirtz, "Phonons in single-layer and few-layer MoS2 and WS2," *Physical Review B - Condensed Matter and Materials Physics*, vol. 84, no. 15, pp. 1–8, 2011.

[251] F. Wang, I. A. Kinloch, D. Wolverson, R. Tenne, A. Zak, E. O'Connell, U. Bangert, and R. J. Young, "Strain-induced phonon shifts in tungsten disulfide nanoplatelets and nanotubes," *2D Materials*, vol. 4, no. 1, 2017.

[252] T. Polcar, F. Gustavsson, T. Thersleff, S. Jacobson, and A. Cavaleiro, "Complex frictional analysis of self-lubricant W-S-C/Cr coating," *Faraday Discussions*, vol. 156, p. 383, 2012.

[253] S. Qiao, H. Yang, Z. Bai, G. Peng, and X. Zhang, "Identifying the number of WS2 layers via Raman and photoluminescence spectrum," in *Proceedings of the 2017 5th International Conference on Mechatronics, Materials, Chemistry and Computer Engineering (ICMMCCE 2017)*, vol. 141, (Paris, France), pp. 1408–1413, Atlantis Press, 2017.

[254] A. N. Barbosa, N. S. Figueroa, M. Giarola, G. Mariotto, and F. L. Freire, "Straightforward identification of monolayer WS2 structures by Raman spectroscopy," *Materials Chemistry and Physics*, vol. 243, no. December 2019, p. 122599, 2020.

[255] F. Gustavsson, S. Jacobson, A. Cavaleiro, and T. Polcar, "Frictional behavior of self-adaptive nanostructural Mo-Se-C coatings in different sliding conditions," *Wear*, vol. 303, no. 1-2, pp. 286–296, 2013.

[256] S. M. Eichfeld, L. Hossain, Y. C. Lin, A. F. Piasecki, B. Kupp, A. G. Birdwell, R. A. Burke, N. Lu, X. Peng, J. Li, A. Azcatl, S. McDonnell, R. M. Wallace, M. J. Kim, T. S. Mayer, J. M. Redwing, and J. A. Robinson, "Highly scalable, atomically thin WSe2grown via metal-organic chemical vapor deposition," *ACS Nano*, vol. 9, no. 2, pp. 2080–2087, 2015.

[257] S. Wang, Y. Rong, Y. Fan, M. Pacios, H. Bhaskaran, K. He, and J. H. Warner, "Shape evolution of monolayer MoS2 crystals grown by chemical vapor deposition," *Chemistry of Materials*, vol. 26, no. 22, pp. 6371–6379, 2014.

[258] L. Yang, Y. S. Tu, and H. L. Tan, "Influence of atomic force microscope (AFM) probe shape on adhesion force measured in humidity environment," *Applied Mathematics and Mechanics (English Edition)*, vol. 35, no. 5, pp. 567–574, 2014.

[259] T. Polcar, M. Evaristo, and A. Cavaleiro, "Self-lubricating W-S-C nanocomposite coatings," *Plasma Processes and Polymers*, vol. 6, no. 6-7, pp. 417–424, 2009.

[260] E. Serpini, A. Rota, S. Valeri, E. Ukraintsev, B. Rezek, T. Polcar, and P. Nicolini, "Nanoscale frictional properties of ordered and disordered MoS2," *Tribology International*, vol. 136, no. March, pp. 67–74, 2019.

[261] R. Buzio, C. Boragno, and U. Valbusa, "Nanotribology of cluster assembled carbon films," *Wear*, vol. 254, no. 10, pp. 981–987, 2003.

[262] J. H. Lee, S. Lee, J. H. Jeon, D. Y. Oh, M. Shin, M. J. Lee, S. Shinde, J. H. Ahn, C. J. Roh, J. S. Lee, and B. H. Park, "Universality of strain-induced anisotropic friction domains on 2D materials," *NPG Asia Materials*, vol. 10, no. 11, pp. 1069–1075, 2018.

[263] L. R. Fisher and J. N. Israelachvili, "Direct measurement of the effect of meniscus forces on adhesion: A study of the applicability of macroscopic thermodynamics to microscopic liquid interfaces," *Colloids and Surfaces*, vol. 3, pp. 303–319, 12 1981.

[264] H. K. Christenson, "Adhesion between surfaces in undersaturated vapors—a reexamination of the influence of meniscus curvature and surface forces," *Journal of Colloid and Interface Science*, vol. 121, pp. 170–178, 1 1988.

[265] C. Gao, P. Dai, A. Homola, and J. Weiss, "Meniscus Forces and Profiles: Theory and Its Applications to Liquid-Mediated Interfaces," *Journal of Tribology*, vol. 120, pp. 358–368, 4 1998.

[266] H. Lee, N. Lee, Y. Seo, J. Eom, and S. Lee, "Comparison of frictional forces on graphene and graphite," *Nanotechnology*, vol. 20, no. 32, 2009.

[267] G. Yu, Z. Zhang, P. Tian, Z. Gong, and J. Zhang, "Macro-scale superlow friction enabled when MoS2 flakes lubricate hydrogenated diamond-like carbon film," *Ceramics International*, vol. 47, no. 8, pp. 10980–10989, 2021.

[268] D. Berman, S. A. Deshmukh, S. K. Sankaranarayanan, A. Erdemir, and A. V. Sumant, "Macroscale superlubricity enabled by graphene nanoscroll formation," *Science*, vol. 348, no. 6239, pp. 1118–1122, 2015.

[269] K. C. Mutyala, Y. A. Wu, A. Erdemir, and A. V. Sumant, "Graphene - MoS 2 ensembles to reduce friction and wear in DLC-Steel contacts," *Carbon*, vol. 146, pp. 524–527, 2019.

[270] M. L. B. Palacio and B. Bhushan, "Normal and Lateral Force Calibration Techniques for AFM Cantilevers," *Critical Reviews in Solid State and Materials Sciences*, vol. 35, pp. 73–104, 5 2010.

[271] L. O. Heim, M. Kappl, and H. J. Butt, "Tilt of atomic force microscope cantilevers: Effect on spring constant and adhesion measurements," *Langmuir*, vol. 20, no. 7, pp. 2760–2764, 2004.

[272] J. L. Hutter, "Comment on Tilt of Atomic Force Microscope Cantilevers: Effect on Spring Constant and Adhesion Measurements," *Langmuir*, vol. 21, pp. 2630–2632, 3 2005.

[273] J. E. Sader, I. Larson, P. Mulvaney, and L. R. White, "Method for the calibration of atomic force microscope cantilevers," *Review of Scientific Instruments*, vol. 66, no. 7, pp. 3789–3798, 1995.

[274] J. E. Sader, "Frequency response of cantilever beams immersed in viscous fluids with applications to the atomic force microscope," *Journal of Applied Physics*, vol. 84, pp. 64–76, 7 1998.

[275] M. Varenberg, I. Etsion, and G. Halperin, "An improved wedge calibration method for lateral force in atomic force microscopy," *Review of Scientific Instruments*, vol. 74, pp. 3362–3367, 7 2003.

[276] H. Wang and M. L. Gee, "AFM lateral force calibration for an integrated probe using a calibration grating," *Ultramicroscopy*, vol. 136, pp. 193–200, 2014.